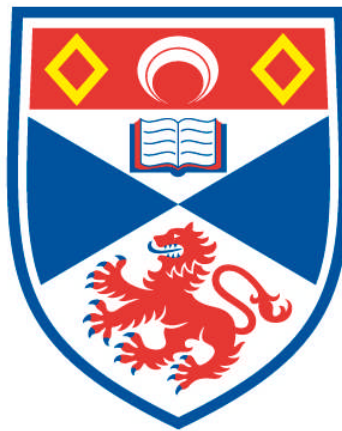


**NEGATIVE FREQUENCY WAVES IN OPTICS:
CONTROL AND INVESTIGATION OF THEIR
GENERATION AND EVOLUTION**

Joanna Siân McLenaghan

**A Thesis Submitted for the Degree of PhD
at the
University of St Andrews**



2014

**Full metadata for this item is available in
Research@StAndrews:FullText
at:**

<http://research-repository.st-andrews.ac.uk/>

Please use this identifier to cite or link to this item:

<http://hdl.handle.net/10023/6532>

This item is protected by original copyright

**This item is licensed under a
Creative Commons Licence**

Negative frequency waves in optics

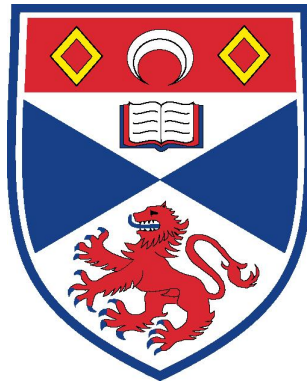
Control and investigation of their generation and evolution

by

Joanna Siân McLenaghan

School of Physics and Astronomy,

University of St Andrews



Submitted for the degree of Doctor of Philosophy

April, 2014

I. Candidate's declarations

I, Joanna McLenaghan, hereby certify that this thesis, which is approximately 44000 words in length, has been written by me, and that it is the record of work carried out by me, or principally by myself in collaboration with others as acknowledged, and that it has not been submitted in any previous application for a higher degree.

I was admitted as a research student in September 2009 and as a candidate for the degree of PhD in September 2009; the higher study for which this is a record was carried out in the University of St Andrews between 2009 and 2013.

Date

Signature of candidate

II. Supervisor's declaration

I hereby certify that the candidate has fulfilled the conditions of the Resolution and Regulations appropriate for the degree of PhD in the University of St Andrews and that the candidate is qualified to submit this thesis in application for that degree.

Date

Signature of supervisor

III. Permission for publication

In submitting this thesis to the University of St Andrews I understand that I am giving permission for it to be made available for use in accordance with the regulations of the University Library for the time being in force, subject to any copyright vested in the work not being affected thereby. I also understand that the title and the abstract will be published, and that a copy of the work may be made and supplied to any bona fide library or research worker, that my thesis will be electronically accessible for personal or research use unless exempt by award of an embargo as requested below, and that the library has the right to migrate my thesis into new electronic forms as required to ensure continued access to the thesis. I have obtained any third-party copyright permissions that may be required in order to allow such access and migration, or have requested the appropriate embargo below.

The following is an agreed request by candidate and supervisor regarding the publication of this thesis:

PRINTED COPY - *No embargo on print copy*

ELECTRONIC COPY - *No embargo on electronic copy*

Date

Signature of candidate

Date

Signature of supervisor

Abstract

This thesis is concerned with various methods for the control and investigation of pulse dynamics in a Photonic Crystal Fibre (PCF) and of the radiation driven by a short pulse. In particular the focus is on pulses in the anomalous dispersion region which would form solitons in the absence of higher order effects. Several different types of radiation can be driven by such pulses if they are perturbed by higher order dispersive and non-linear effects - for example Resonant Radiation (RR) and Negative Resonant Radiation (NRR) two dispersive waves which gain energy at the expense of the pulse.

The feature of NRR which is of particular importance is that it is the first observed example of a coupling between positive and negative frequencies in optics. This has only been possible due to recent advances in fields such as PCFs, lasers and analogue systems. As with many scientific discoveries, NRR was found by bringing together ideas and techniques from these different fields.

Both the pulse and the driven radiation are investigated using a number of different pulse and PCF parameters. These include power, chirp, polarisation and PCF dispersion. These are used to vary the wavelengths at which the driven radiation occurs as well as its generation efficiency. Furthermore the power and chirp are used to vary where in the PCF the driven radiation is generated by controlling where the driving pulse compresses and spectrally expands. This property is used to investigate different stages in the evolution of the pulse and driven radiation as well as to optimise the generation efficiency of the driven radiation.

This thesis is dedicated to my family, for their continuing encouragement and support and for putting up with me whilst I wrote this and supplying many cups of tea to keep me going

Acknowledgements

Firstly, I would like to express my sincere gratitude to my supervisor Dr. Friedrich König for his support during the years of my PhD. For his patience, availability and determination to make every result, paper or presentation as perfect as possible.

My thanks also go to the other people who have worked with me in the Experimental Quantum Optics Group: Dr. Susanne Kehr, Amul Choudhary, Sven Rohr, Imad Faruque, Matus Rybak, James Luis and Vanessa Chille. For some of the data that I have used in this thesis, for the many useful conversations and for their flexibility, patience and cheerfulness, which greatly improved the experience of working in the lab.

Further thanks are due to the former members of the theory side of the Quantum Optics group at St Andrews: Prof. Ulf Leonhardt, Dr. Thomas Philbin, Dr. Simon Horsley, Dr. Scott Robertson, Sahar Sahebdivan and William Simpson. For many fascinating group meetings and support with the theoretical background to my experiments.

Daniele Faccio and colleagues worked with us on the initial NRR paper and I would like to thank them for their input and in particular Daniele for his determination to convince the research community of the importance of NRR.

I would also like to thank Dr. Chris Kuklewicz for his work on the Labview programme used to control the monochromators for the experiments and Dr. Andrea Di Falco for his adaptations of the mode calculation programme and help in obtaining SEM images of the PCF ends.

Finally thanks go to EPSRC for the funding without which I would not have been able to devote four enjoyable years to research.

Contents

I	Literature review	17
1	Introduction	18
2	Solitons	22
2.1	Earliest discovery	22
2.2	Solitons in different systems	23
2.3	Optical solitons	24
3	Solitons in photonic crystal fibres	26
4	Radiation driven by solitons	36
4.1	Supercontinuum generation	38
4.2	Harmonic generation	42
4.3	Four wave mixing	47
5	Resonant dispersive radiation	48
5.1	Resonant Radiation	49
5.1.1	Uses for Resonant Radiation	53
5.2	Negative Resonant Radiation	56
6	Event horizon analogues	64
II	Theory	70
7	Introduction	71
8	The NLSE	71
8.1	Soliton solutions of the NLSE	73
8.2	Soliton evolution	74
8.3	Higher order effects	77
8.4	Higher order dispersion leading to Resonant Radiation	78

9	A more detailed pulse propagation equation	81
9.1	Phase matching condition	88
10	Dispersion profiles	91
III	Experimental results	97
11	Introduction	98
12	Experimental set-up	98
12.1	Input pulse power	101
12.2	Input and output polarisation	103
12.2.1	Aligning the photonic crystal fibre axis	105
12.3	Input pulse chirp	107
12.3.1	Measuring the GDD of optical elements	110
12.4	Coupling into the photonic crystal fibre	111
12.5	Output detection	116
12.6	Measuring the photonic crystal fibre properties	118
12.6.1	Method one - Resonant Radiation phase matching	118
12.6.2	Method two - external data	121
13	Results	122
13.1	Examples of RR and NRR	123
13.2	Alternative explanations for the UV peak	126
13.3	The effects of input power on pulse compression, NRR and RR	129
13.3.1	Simulation results	130
13.3.2	Experimental results	137
13.4	The effects of input chirp on pulse compression, NRR and RR	147
13.4.1	Simulation results	148
13.4.2	Experimental results	156
13.4.3	Varying chirp and PCF length	164
13.4.4	Loss calculations	174

13.5 Polarization experiments	178
IV Conclusions and outlook	185
V Appendix	189
14 Hollow core PCF guiding	190
15 Derivation of the NLSE	192
16 Equipment	203
16.1 Double chirped mirrors	203
16.2 Autocorrelator	204
References	205

Nomenclature

DCM	Double Chirped Mirrors, page 108
FOD	Fourth Order Dispersion, page 50
FWM	Four Wave Mixing, page 18
GDD	Group Delay Dispersion, page 108
GVD	Group Velocity Dispersion, page 26
HR	Hawking Radiation, page 21
HWP	Half Wave Plate, page 102
IR	Infrared, page 18
LIA	Lock in Amplifier, page 113
NLSE	Non-linear Schrödinger Equation, page 25
NRR	Negative Resonant Radiation, page 6
OAP	Off-axis Parabolic Mirror, page 111
PBC	Polarising Beam Cube, page 104
PCF	Photonic Crystal Fibre, page 6
PER	Polarisation Extinction Ratio, page 104
POL	Polariser, page 102
QWP	Quarter Wave Plate, page 111
RR	Resonant Radiation, page 6
SEM	Scanning Electron Microscope, page 31
THG	Third Harmonic Generation, page 18
TOD	Third Order Dispersion, page 34
UPPE	Uni-directional Pulse Propagation Equation, page 61
UV	Ultraviolet, page 18
XPM	Cross Phase Modulation, page 40
ZDW	Zero Dispersion Wavelength, page 27

Part I

Literature review

1 Introduction

The focus of this work is the evolution of pulses in a PCF and the radiation driven by such pulses - in particular the generation of negative frequency radiation. In the next few paragraphs I will briefly introduce these terms and over the remainder of this literature review they will be described in more detail.

The pulses are infrared (IR) electromagnetic pulses of light ranging between 7 fs and 12 fs in length. Each pulse is composed of a range of different wavelengths with a bandwidth of about 200 nm. How these pulses evolve as they pass through a medium (such as a fibre) depends on the interaction of the light with the medium. Two of the main ways in which the medium affects the pulse are via dispersion and non-linearity. Dispersion occurs because the different wavelength components of the pulse travel at different speeds in the medium. In general this leads to the pulse length increasing. Non-linearity refers to the non-linear response of the bound electrons in the medium to the electric field of the pulse. The field realigns the electrons leading to a polarisation of the medium which adds a component to the total electric flux density in the medium. Both dispersion and non-linearity will be discussed further in part II and appendix 15.

A PCF is a type of optical fibre designed to have particular dispersion properties. A pulse propagating through a PCF can evolve in different ways depending on the relative strengths of the dispersion and non-linearity. Under certain conditions dispersion and non-linearity can balance leading to a pulse which propagates without changing its shape or speed or with a periodic evolution. Such a pulse is known as a soliton. Under slightly different conditions the pulses will transfer energy to electromagnetic radiation at different wavelengths. This is typically due to higher order dispersive and non-linear effects. Types of radiation produced by such a transfer include the well known phenomena of supercontinuum generation, Third Harmonic Generation (THG), Four Wave Mixing (FWM) and RR. The focus of this work is on RR although the other phenomena will also be considered in more detail in section 4.

An example a transfer of energy from the pulse to RR can be seen in figure 1. This shows the spectrum of a pulse entering a 5 mm long PCF¹ (figure 1(a)) and the spectrum at the end of the fibre in the visible and IR (figure 1(b)) and in the ultraviolet (UV) (figure 1(c))². In this case the

¹All of the fibres used in the experiments are only a few mm long. The behaviour investigated occurs within such distances and using short fibres reduces overall loss, an issue which will be discussed in section 13.4.4.

²The IR/visible and UV spectra are presented separately as they are recorded using different detectors and the

input pulse transfers energy to signals at two different wavelengths. The first is RR and is seen at 500 nm in figure 1(b). The second is NRR and is seen at 223 nm in figure 1(c).

The RR and NRR will be discussed in more detail in sections 5.1 and 5.2 respectively. Their generation and evolution are the focus of most of the experiments described in this thesis. The NRR is of particular interest as it forms due to a conversion of positive frequencies to negative frequencies. As a brief introduction to this idea the conversion can be seen by considering the phase matching condition for the transfer of energy from the pulse to RR and NRR (both share the same phase matching condition). This is a condition which has to be obeyed in order to conserve energy and momentum. It defines the wavelengths at which the RR and NRR are generated. The condition will be derived in part II and discussed further in section 8.4. It can be expressed as a conservation of frequencies in a frame of reference moving with the pulse (i.e. Doppler shifted frequencies ω'). These frequencies are defined by

$$\omega' = \omega \left(1 - \frac{n(\omega) v_g}{c} \right), \quad (1.1)$$

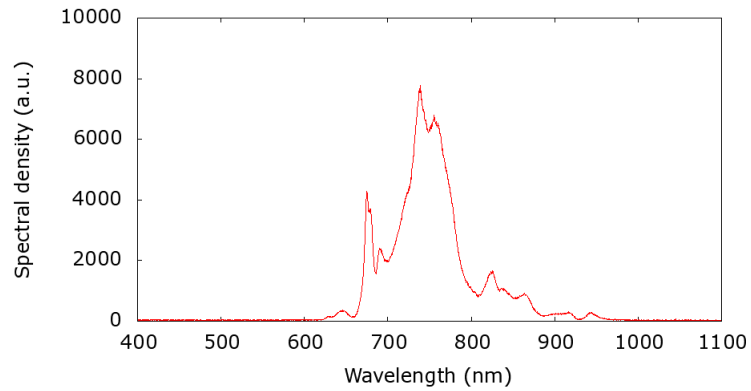
where ω is the frequency in the lab frame, v_g is the pulse group velocity, $n(\omega)$ is the frequency dependent refractive index of the fibre and c is the speed of light in a vacuum.

RR and NRR will form at wavelengths which have the same ω' as the pulse. How ω' varies with wavelength is defined by the dispersion relation of the PCF. An example dispersion relation is shown in figure 2, the y-axis shows ω' relative to ω'_s its value at the pulse wavelength. The graph includes both positive and negative wavelength branches³. As the figure shows there are two wavelengths with the same ω' as the pulse, one close to 500 nm (RR) and one in the UV with a negative wavelength (NRR). This indicates the conversion from positive to negative frequencies.

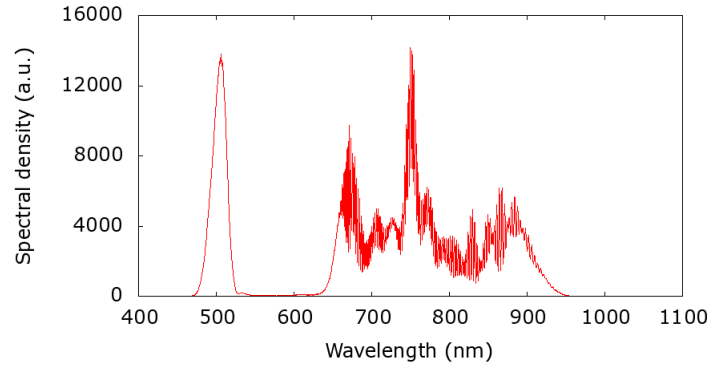
I will now outline the structure of this literature review and the key areas which will be discussed. The experiments, which will be described in section 12, show how pulse evolution and the generation of RR and NRR are controlled and investigated by varying the pulse and PCF parameters. For the majority of the work carried out the pulses under consideration would, in the absence of higher order effects (dispersive and non-linear) form a soliton. Therefore it is appropriate to begin this literature review with an overview of solitons - starting with a brief mention of the initial observations of

UV signal is orders of magnitude smaller.

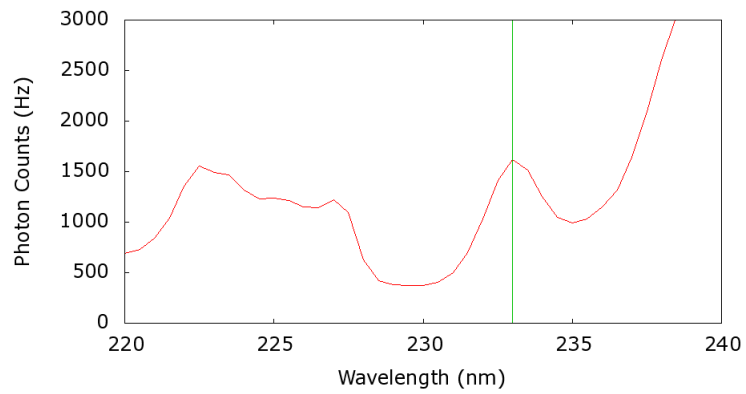
³The figure could also have been plotted with lab frame frequency (positive and negative) replacing wavelength. However as all experimental results are recorded in terms of wavelengths that is the parameter used here



(a) Input pulse spectrum



(b) Output spectrum in the visible and IR - showing the pulse between 650 nm and 950 nm and the RR at 500 nm



(c) Output spectrum in the UV - showing the NRR indicated by the vertical line

Figure 1: Input and output spectra from a 5 mm long PCF

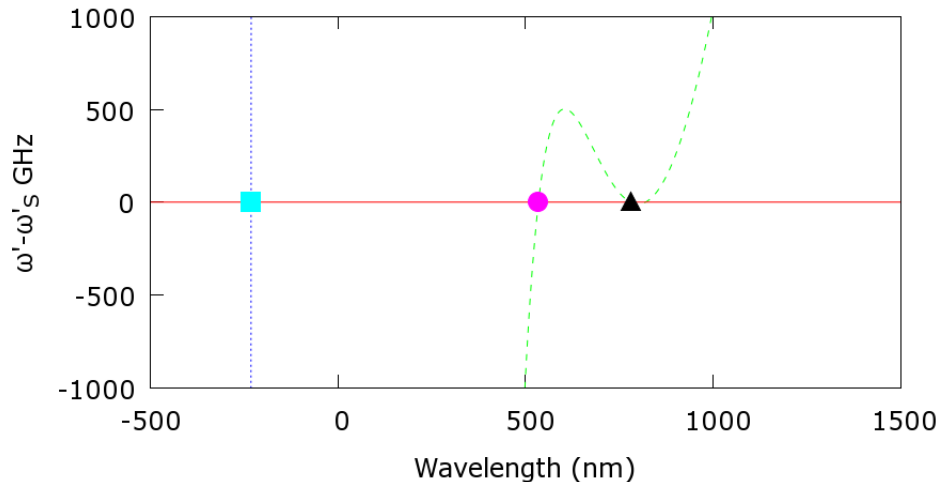


Figure 2: Dispersion relation for one of the PCFs used in the experiments. Showing the the input pulse (Δ) RR (\circ) and NRR (\square)

solitons in water waves and their subsequent theoretical description and then moving on to consider solitons in other media before reaching the early work carried out on optical solitons.

The next part of the review will look at the development of PCFs and how their properties have been used to further the research into solitons and radiation driven by solitons⁴. As a large body of research has been carried out by many different research groups over the past few decades into effects in PCFs, this literature review will only include an overview of some of the key results including supercontinuum generation, THG and FWM.

The non-linear phenomenon of RR driven by pulses will then be considered in greater detail. The new discovery of negative frequency light (NRR) arose from research into RR. As mentioned previously, the two types of radiation are both driven by short pulses and share the same phase matching condition. They differ in that RR has a frequency with the same sign as the driving pulse whilst NRR has a frequency with the opposite sign.

Finally a section will be devoted to the work on event horizon analogues in PCFs and other systems, particularly focusing on attempts to generate the optical analogue of Hawking Radiation (HR). The work of our research group in this field lead us to the idea of negative frequencies, which was necessary in developing the theory for NRR. Additionally some of the experimental

⁴A pulse which transfers energy to other radiation due to higher order effects cannot strictly be called a soliton - here I refer to pulses which would form solitons but are perturbed by higher order effects.

results indicating how the generation of NRR can be optimised may also be applicable to HR.

2 Solitons

2.1 Earliest discovery

A soliton or solitary wave is a wave which propagates without changing its shape or speed over large distances. This is possible due to the balance between non-linear and dispersive effects. Neglecting loss and higher order effects a fundamental soliton would propagate unchanged indefinitely. The phenomenon occurs naturally when water waves propagate in channels with particular properties. This led to the first in depth investigation of solitons in the 19th century. A water wave was observed propagating along the Union canal near Edinburgh by naval engineer John Scott Russell [20]. He was able to follow the wave for a distance of several miles before it gradually became too small to see.

“I was observing the motion of a boat which was rapidly drawn along a narrow channel by a pair of horses, when the boat suddenly stopped – not so the mass of water in the channel which it had put in motion; it accumulated round the prow of the vessel in a state of violent agitation, then suddenly leaving it behind, rolled forward with great velocity, assuming the form of a large solitary elevation, a rounded, smooth and well-defined heap of water, which continued its course along the channel apparently without change of form or diminution of speed. I followed it on horseback, and overtook it still rolling on at a rate of some eight or nine miles an hour, preserving its original figure some thirty feet long and a foot to a foot and a half in height. Its height gradually diminished, and after a chase of one or two miles I lost it in the windings of the channel. Such, in the month of August 1834, was my first chance interview with that singular and beautiful phenomenon which I have called the Wave of Translation.”

Russell proceeded to recreate the phenomenon in a water tank, again observing a wave that did not

change shape or speed. This contradicted the water wave theories of the day which stated that for long wavelength waves propagating in a rectangular canal even with the effect of friction neglected the waves should become steeper in the front and less steep behind. A theoretical description of solitons was provided in 1871 by Boussinesq [17] and again in 1876 by Lord Rayleigh [131]. However, in an attempt to find agreement with the standard theories of the day, Lord Rayleigh postulated that the soliton was only an approximation to a stationary wave.

The full theory of water wave solitons was developed in 1895 by Korteweg and de Vries [35]. They formulated their well known equation for waves on a shallow water surface (Korteweg-deVries equation). The solutions to this exactly solvable equation turned out to include perfectly stationary solitons - providing agreement with the experimental observations of Scott Russell.

The field of soliton research then lay almost dormant for a number of decades until the 1960s when Zabusky and Kruskal [99] demonstrated computationally the existence of solitons in a medium obeying the Korteweg-deVries equation using a finite difference numerical method. They found that interactions between solitons had almost no affect on the pulses involved.

Since that time solitons have been theoretically and computationally studied by many groups in different contexts.

2.2 Solitons in different systems

Since their first discovery solitons have been found to exist in several different systems. These can all be described by integrable differential equations. One aspect of such integrable systems is that they exhibit a number of conserved quantities leading to the observation of stable solitons. The term soliton is also used to describe topological solitons [125], which display many of the same properties as solitons from integrable systems. However these solitons are stable due to topology rather than integrability, for example they may have to obey non-trivial boundary conditions. This type of soliton is outside of the scope of this project and will not be considered further.

Solitons have been observed in water waves as well as in Bose-Einstein condensates and magnetic systems. In all of these systems the soliton is formed by a balance between non-linear and dispersive effects. Molecular solitons form in Bose Einstein condensates if a coupling exists which performs

a role analogous to second harmonic generation⁵ by forming one molecule from two atoms. This allows a coupled Bose Einstein condensate to form in which solitons can be observed [103]. A magnetic soliton is a bound state of magnons (elementary magnetic excitations) [5].

2.3 Optical solitons

One area in which solitons have received a large amount of attention is the field of fibre optics. A pulse propagating in a fibre provides a relatively simple and stable system in which to observe the effect of solitons. A coiled fibre can be many meters long allowing large propagation distances in a small laboratory space. Also large variations as well as fine tuning of the various system parameters are achievable. These parameters include, the power, shape and length of the input pulses as well as the properties of the fibre used as a propagation medium.

Solitons in fibres have been considered as carriers of information for use in telecommunications. This potential for commercial use explains the large amount of research carried out into optical solitons in the past few decades. In telecommunications the effects of non-linearity can be detrimental to signal propagation. By using solitons it is possible to make the fibre non-linearity an asset rather than a hindrance [83]. The non-linearity balances the effects of dispersion allowing stable pulses to propagate. This allows for much longer error free propagation distances than for other optical telecommunication systems. Furthermore solitons have been shown to be stable against many perturbations and to be almost totally transparent to other solitons when collisions occur [99]. This latter property makes them particularly suited to use in wavelength-division-multiplexing applications where light of different wavelengths is used to carry different signals [48]. Unfortunately various technical issues have meant that solitons have not yet been used in telecommunications systems commercially [122]. One example of such an issue is the need to compensate for loss using amplifiers. If this is not done then the balance of non-linearity and dispersion will be destroyed and the dispersion will dominate lengthening the pulses in time. The amplifiers used (for example Erbium doped fibre amplifiers) will have different dispersion characteristics to the main fibre. This must be taken into account when designing the system. Additionally amplifiers add noise to the system. This will cause the phase, and therefore carrier frequency, of the soliton to vary randomly. As

⁵Harmonic generation will be considered in more detail in section 4.2. Second harmonic generation is a non-linear optical process where two photons of the same frequency combine to produce a photon with twice that frequency.

different frequencies travel at different speeds, this will lead to a timing jitter which will in turn reduce the allowed bit rate for a particular bit error rate (probability that the soliton pulse arrives outside of its correct time slot). This effect is known as the Gordon Haus effect [50].

In this thesis the focus is on pulses of light which would form stable solitons apart from the destabilising action of higher order non-linear and dispersive effects. These are detrimental to the use of such pulses in communications - however they do allow the pulse to lose energy and drive various types of radiation. The uses of some of these types of radiation will be discussed in section 4.

The formation of solitons in optical fibres occurs, similarly to water wave solitons, due to the balance of non-linear and dispersive effects. The equivalent equation to the Korteweg-deVries equation in water waves is the Non-linear Schrödinger Equation (NLSE) [2]. This governs the propagation of light in an optical fibre in the absence of higher order dispersive and non-linear effects.

In 1972 Zakharov and Shabat showed that the NLSE was integrable using the inverse scattering transform method [153]. Soliton solutions to the equation were found in 1973 by Hasegawa and Tappert [57]. In the same year Bullough [67] working independently developed a mathematical framework to describe optical solitons and also suggested their use in telecommunications.

Over the next decade a variety of theoretical and computational studies found that optical solitons could form which were robust against perturbations. The family of soliton solutions to the NLSE was found to consist of fundamental solitons, which retain their original shape on propagation, and higher order solitons, which are stationary waves in the sense that they evolve periodically. The order of a soliton is described by

$$N^2 = \frac{L_D}{L_{NL}}, \quad (2.1)$$

where N is the soliton order, L_{NL} and L_D are the non-linear and dispersion lengths. The latter two parameters represent the length scales over which the evolution of a pulse is affected by non-linear and dispersive effects respectively. If the two are equal then the effects are balanced and a fundamental soliton will form.

Experimental verification of optical solitons had to wait until 1980. The long delay was due to

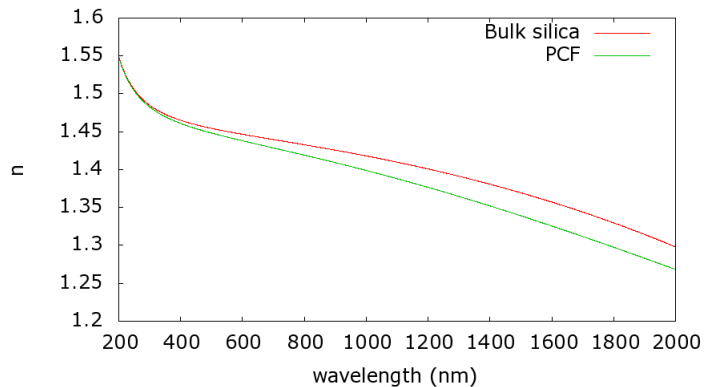


Figure 3: Refractive index n for bulk silica and for a typical PCF used in the experiments

a lack of suitable fibres and light sources. An input pulse will only form a soliton if it is in the anomalous dispersion spectral region of the fibre used (negative Group Velocity Dispersion (GVD))⁶. This allows the effects of dispersion to counteract the effects of self-phase modulation (a non-linear effect). Therefore a fibre with low loss in the anomalous dispersion region and a laser source tunable to the same wavelength range are both required.

The first experiments were carried out by Mollenauer, Stolen and Gordon [22]. They coupled infra-red pulses into a single mode optical fibre. For input power levels corresponding to higher order solitons they observed a compression in time of the input pulse followed by a splitting into a series of fundamental solitons.

3 Solitons in photonic crystal fibres

In this section I will begin by discussing conventional fibres and how the dispersion characteristics of these fibres limit the spectral regions in which solitons can form. I will then explain how dispersion in PCFs can be tailored to overcome this limit. I will also discuss in more detail the principles of waveguiding in PCFs and the advantages using this type of fibre.

As mentioned previously one limitation on the ability to produce solitons in optical fibres is the need to have low loss in the anomalous dispersion region of the fibre and a suitable laser source

⁶The terms GVD and anomalous dispersion will be explained in the next section (3). The former is a measure of how fast frequencies travelling at different speeds in a fibre will move apart. Its sign indicates whether low or high frequencies will travel faster.

in this spectral region. Dispersion occurs because different frequencies ω of light will propagate at different velocities through a medium. The velocity at which they propagate is determined by the frequency dependent refractive index of the medium $n(\omega)$. Anomalous dispersion occurs when the second order dispersion parameter ($\beta_2 = d^2(n(\omega)\omega/c)/d\omega^2$, where c is the speed of light in vacuum) is negative. The refractive index as a function of wavelength for bulk fused silica (calculated using the Sellmeier equation [2]) is shown in figure 3. From this refractive index it can be calculated that β_2 is zero at 1270 nm. This wavelength is known as the Zero Dispersion Wavelength (ZDW). For longer wavelengths the material has anomalous dispersion.

For a conventional fibre there will also be a waveguide contribution to the dispersion. At the ZDW of bulk silica the waveguide contribution to β_2 may not be zero, hence the fibre will have a non-zero overall dispersion. The fibre ZDW will occur at a wavelength where the bulk silica and waveguide contributions to the dispersion are equal and opposite in sign. This shift of the ZDW will alter the spectral region for which the fibre has anomalous dispersion and therefore the spectral region in which solitons can form. For a typical fibre the ZDW shifts to about 1310 nm [2].

The waveguide contribution arises due to the guided nature of light in the fibre. For a particular fibre there will be a discrete set of guided modes which solve the wave equation and obey the transverse resonance condition (no component propagating perpendicular to the fibre axis). Each mode will have a constant propagation constant [75] along the fibre axis determined by solving an eigenvalue equation [128]

$$\left[\frac{J'_m(\kappa a)}{\kappa J_m(\kappa a)} + \frac{K'_m(\gamma a)}{\gamma K_m(\gamma a)} \right] \left[\frac{J'_m(\kappa a)}{\kappa J_m(\kappa a)} + \frac{n_2^2 K'_m(\gamma a)}{n_1^2 \gamma K_m(\gamma a)} \right] = \left(\frac{m\beta k_0 (n_1^2 - n_2^2)}{an_1 \kappa^2 \gamma^2} \right)^2. \quad (3.1)$$

Here J_m and K_m are the Bessel and modified Bessel functions respectively, a is the fibre core radius, $\kappa = (n_1^2 k_0^2 - \beta^2)^{1/2}$, $\gamma = (\beta^2 - n_2^2 k_0^2)^{1/2}$, n_1 and n_2 are the refractive indices of the fibre core and cladding respectively, m is an integer value, $k_0 = \omega/c$ and β is the propagation constant. Solving the equation gives the propagation constants for the allowed guided modes. Each β will have a frequency dependence. This will come from the frequency dependence of the refractive indices (material dispersion) and from the frequency dependence of κ (waveguide dispersion).

The above equation is applicable to cylindrical waveguides such as an optical fibre. However the principle of waveguide dispersion is seen in a simpler way by considering a planar waveguide such

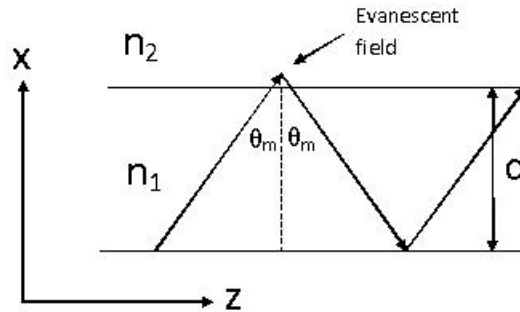


Figure 4: Ray optics picture of guided light in a planar waveguide with core refractive index n_1 and cladding refractive index n_2 .

as that shown in figure 4. As with the fibre this waveguide confines light by multiple total internal reflections at the boundary between the core and the cladding. This will occur if the refractive index of the core n_1 is greater than the refractive index of the cladding n_2 and if the angle of incidence at the cladding θ_m is greater than the critical angle $\sin\theta_c = n_2/n_1$. These two conditions suggest that waveguiding will occur for a continuum of angles greater than the critical angle. However this is not the case. There is an additional condition that guided light must have no component propagating perpendicular to the axis of the waveguide. This means that the perpendicular component of the beam must form a standing wave i.e. the total phase change after two successive reflections from the upper and lower boundaries of the waveguide must equal an integer multiple of 2π (the transverse resonance condition). Mathematically for the parameters in figure 4 this is expressed as

$$2dk_x - 2\phi(\lambda) = 2m\pi, \quad (3.2)$$

where $k_x = 2\pi/\lambda_x = 2\pi n_1 \cos\theta_m/\lambda$ is the propagation constant in the x direction (axes defined in figure 4), λ is the vacuum wavelength of the light, m is an integer and $\phi(\lambda)$ is the phase change at each boundary which occurs due to the field slightly penetrating the boundary (evanescent field).

This can be rearranged to give a condition for the ray angle θ_m

$$d \frac{2\pi n_1 \cos\theta_m}{\lambda} - \phi(\lambda) = m\pi, \quad (3.3)$$

$$\cos\theta_m = \frac{\lambda}{2\pi n_1 d} (m\pi + \phi(\lambda)). \quad (3.4)$$

This condition leads to a discrete set of allowed modes labelled by the integer m . Each mode is also characterised by n_e , the effective refractive index which is the ratio of the speed of light in a vacuum c to the phase velocity of the mode along the waveguide axis v_{pz} ,

$$n_e = \frac{c}{v_{pz}} = \frac{c}{c/(n_1 \sin\theta_m)} = n_1 \sin\theta_m. \quad (3.5)$$

The effective refractive index depends on the material via n_1 , which has a frequency dependence leading to material dispersion. The waveguide dispersion arises from the dependence of n_e on the angle θ_m , which as seen in (3.4) also has a dependence on the wavelength (frequency) of the light.

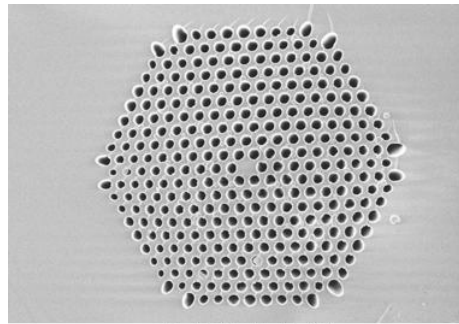
Whilst the above discussion is for the simpler case of a planar waveguide, the same principles hold for fibre waveguides. The boundary conditions allow only a discrete set of guided modes with particular angles of propagation in the ray optics picture. This introduces an additional component to the dispersion.

As mentioned previously, the effect of the waveguide dispersion is to increase the ZDW to longer wavelengths than for bulk silica (from 1270 nm for silica to about 1310 nm for a conventional fibre). This means that the anomalous dispersion region of the spectrum lies at wavelengths longer than 1310 nm, limiting the spectral region in which a soliton can form.

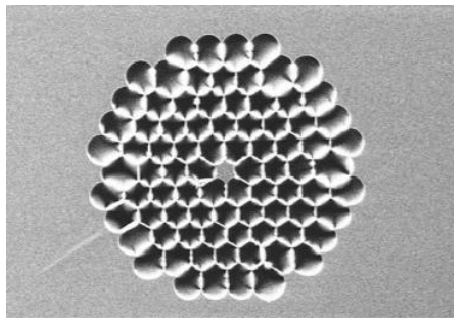
The development of PCFs [75] allowed for much greater flexibility in generating solitons at different wavelengths. The waveguide contribution to dispersion in a PCF can be much greater than in a conventional fibre and can be varied significantly to allow tailoring of the dispersion profile. The differences between the refractive index for bulk silica and for one example of a PCF can be seen in figure 3. The PCF data was obtained using the method described in section 12.6.1.

The ZDW of a PCF can be shifted to shorter wavelengths, thus moving the anomalous dispersion region to shorter wavelengths and allowing the formation of solitons from input light in the visible and near IR. At the same time that PCFs were being developed Ti:Sapphire lasers generating pulses of light in the visible and near IR were also gaining widespread use. The combination of such fibres and lasers allowed for huge advances in the study of solitons in optical fibres.

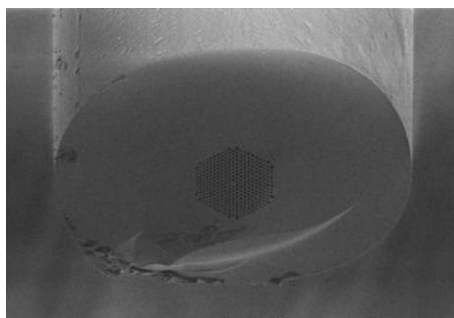
Many PCF designs have been produced but the common idea is to create a pattern of wavelength-



10.0 μm
(a) NL-1.5-590 PCF end



10.0 μm
(b) NL-1.5-670 PCF end



50.0 μm
(c) NL-1.5-590 - zoomed out image of the whole PCF end

Figure 5: Figures (a), (b) and (c) show SEM images of the ends of two different PCFs. Images recorded by Dr Di Falco and Dr Kehr at the University of St Andrews

scale air holes running the length of the PCF with either a hollow core or a missing hole at the centre leaving a solid core. To illustrate this, Scanning Electron Microscope (SEM) images of two different PCFs are shown in figure 5.

The PCFs used in the experiments are all of the solid core type shown in figure 5. These guide light in the same way as conventional fibres by total internal reflection at the core-cladding boundary. The difference is that for PCFs the optical properties of the cladding are varied by changing the pattern of air holes allowing the waveguiding properties of the PCF to be tailored. Hollow core PCFs guide light by means of a photonic band gap. For interest hollow core guiding is explained in appendix 14.

To illustrate guidance, the diagram in figure 6, shows the allowed modes for conventional fibres and for PCFs (solid and hollow core). The diagrams show the frequency ω as a function of the propagation constant along the fibre axis β (both normalised using Λ the inter-hole spacing or pitch). The different regions in the two figures indicate the range of ω and β values which can propagate in each part of the fibre. These regions are restricted by the requirement that for a particular ω the axial propagation constant β will have a maximum value $\beta_{max} = n\omega/c$. Therefore for any ω the lower the refractive index n , the smaller the cut-off value of β will be.

In the diagram for the conventional fibre there are four regions. In region 1 light can propagate in air, the silica cladding and the Ge:silica doped core. In region 2 the light cannot propagate in air where the refractive index is lowest. In region 3 the light can propagate in the core but not in the cladding which has a lower refractive index. This is equivalent to the explanation at the start of this section where it was stated that modes would be guided only if total internal reflection occurred at the core cladding boundary i.e. only if the cladding refractive index were lower than the core refractive index.

The diagram for the PCF is more complicated, in this case the fibre has a lattice of air holes, with an air filling fraction of 45%, surrounding a core (hollow or solid). The area marked 1 indicates the parameters for which light can propagate in air, the photonic crystal and a solid silica core. In area 2 the light can no longer propagate in air. In area 3 light cannot propagate in air or in the photonic crystal cladding and in area 4 it can also not propagate in a solid silica core. For the case of a solid core PCF the guided modes will be in area 3, this is considerably larger than the corresponding guided mode area for the conventional fibre. The reason for this is the much larger

difference between the effective refractive index of the photonic crystal and the larger index of the silica core compared to the difference between the conventional fibre core and cladding indices. The refractive index of the photonic crystal cladding will lie between the refractive index of silica and that of air with the value depending on the size and separation of the air holes [111].

For a hollow core PCF guided modes will occur when light can propagate in air but not in the photonic crystal cladding. This occurs for certain modes in the photonic band gap regions indicated by the black “fingers” in figure B. For the reasons explained in appendix 14 light is not able to penetrate the cladding but as indicated by the letter P it can for certain parameters propagate in air and therefore form a guided mode in the core.

The PCFs used in the experiments are all solid core PCFs and therefore they are able to guide modes in region three of figure B in figure 6. In the early stages of PCF development the technology required to produce fibres with suitable hole sizes and spacing to create photonic band gaps was not available. Therefore hollow core PCFs could not be used to guide light in the way described above. Hence the first PCF, developed by Knight et al. in 1996, had a solid core [72]. This allowed guiding without the need for a full photonic band gap.

The first PCF had a hole spacing (pitch) of $2.3\mu\text{m}$, hole diameters of $0.2\mu\text{m}$ to $1.2\mu\text{m}$ and a core diameter of approximately $4.6\mu\text{m}$. When light from the visible to the near IR was coupled into the PCF it was found to support a low loss single mode. This result resolved some uncertainty about whether a solid core PCF would be able to guide light or whether the light would be able to leave the core via the supporting struts in the cladding. The confinement in the core of a single mode is due to a property known as “mode sieving” [119], where the low index air holes act as a sieve to block propagation into the cladding. The fundamental mode has a particular shape characterised by having a single central lobe, higher order modes have more complicated multi-lobe shapes with smaller lobes. The fundamental mode is unable to escape the mode sieve formed by the air holes whereas the smaller higher order mode lobes can fit through. Some of the modes of one of the PCFs used in our experiments are shown in figure 7. The top left hand mode is the fundamental mode and the other three are a selection of higher order modes. Also shown to the same scale is the end of one of the PCFs used.

The number of modes that the PCF supports depends on the size of the air holes. The larger the holes the greater the air fill fraction and the smaller the struts between the holes. This means

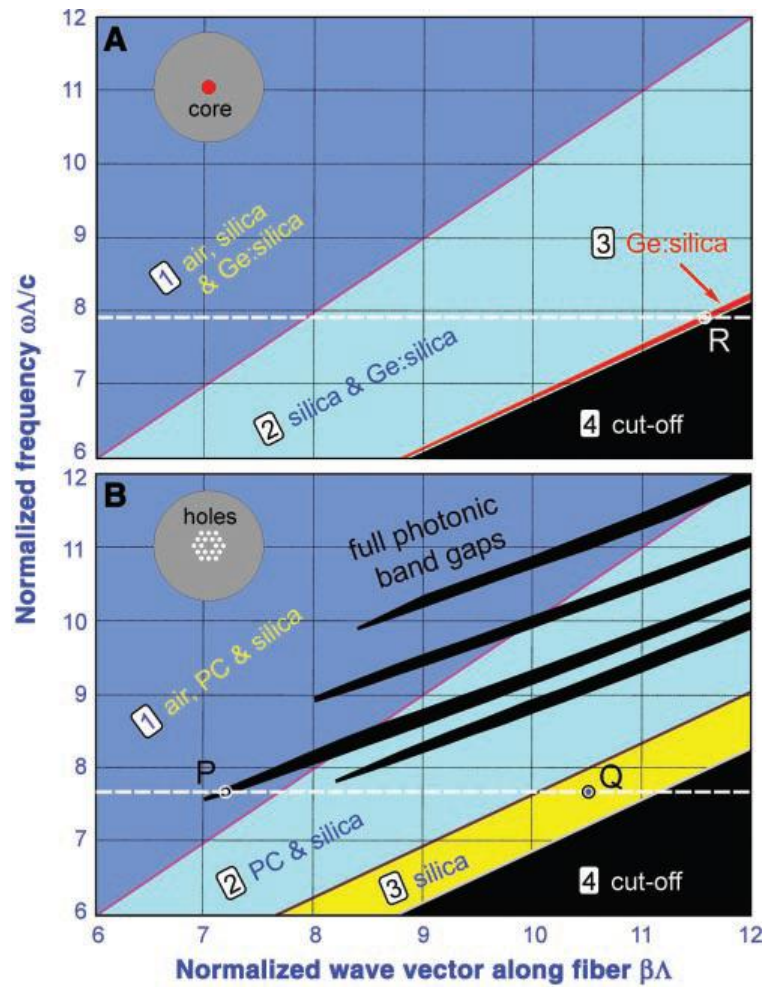


Figure 6: Figure A shows the propagation diagram (normalised ω as a function of normalised β) for a conventional single-mode fibre (Ge-doped silica core and a pure silica cladding). Figure B shows the propagation diagram for a PCF (silica glass with 45% air-filling fraction). © From Russell, Philip, *Photonic Crystal Fibers*, Science 299, 5605 (2003), pp. 358–362. Reprinted with permission from AAAS.

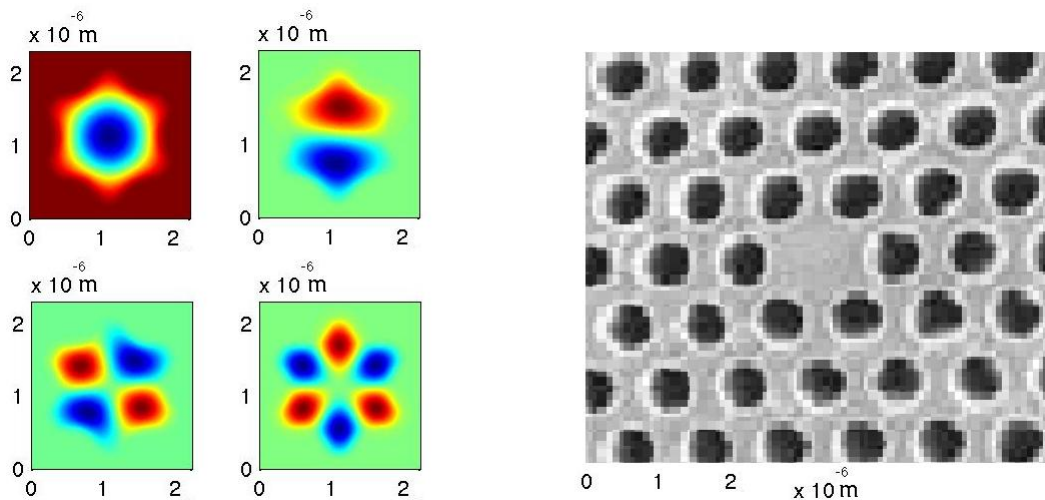


Figure 7: The fundamental and a selection of higher order modes for the NL-1.5-590 PCF used in the experiments. The mode shapes were calculated using a Matlab model with hole size and spacing parameters taken from SEM images of the PCF end. Images produced by Dr Kehr at the University of St Andrews

that the holes in the “sieve” are smaller and more of the higher order modes are trapped in the core.

As mentioned previously, one of the main advantages in using PCFs is the ability to tailor the dispersion of the fibre. This can be used to move the ZDW in order to allow soliton formation in different wavelength regions [95]. It can also be used to produce PCFs with very flat second order dispersion over a wide range of wavelengths [120, 121, 110, 42]. This has been used to suppress Third Order Dispersion (TOD) and efficiently generate a supercontinuum [108, 29].

Tailored dispersion in PCFs has been studied for its potential uses in telecommunications [90, 26, 9]. Dispersion broadens pulses limiting the distance over which they can be transmitted before requiring regeneration. If PCFs can be produced with zero second order dispersion at wavelengths used for telecommunications, then this problem is greatly reduced. Alternatively, PCFs tailored to have anomalous dispersion over a particular wavelength range are used to shorten a pulse again after it has passed through a particular length of fibre with normal dispersion. The latter solution is beneficial as the dispersed pulses will have a lower peak power and therefore be less affected by non-linearity in the fibre.

The dispersion tailoring is achieved by varying the size and separation of the air holes in the

photonic crystal cladding and the size of the core. In general the relationship is complicated and numerical calculation is required to ascertain the parameters required to achieve a particular dispersion profile or to determine the dispersion profile for a particular set of parameters. Many methods have been developed to investigate dispersion in PCFs. Some of the main ideas are described in the following publications [49, 53, 52, 96, 150].

If the air holes are large then the core can be approximated as a single strand of silica in air [13, 73]. The light will be confined in the core and, as in the case of conventional fibres, it is this confinement which adds a waveguide dispersion component to the material dispersion of the PCF. This approximation can be used to model the dispersion characteristics of the PCF. In section 12.6, I describe how we use this method to fit experimental data and find the dispersion curves for some of our fibres.

If the air holes are smaller then the silica struts in the photonic crystal cladding cannot be neglected. The cladding can be characterised by having an effective refractive index which will depend on the air filling fraction [111]. The combination of the material dispersion, the waveguide dispersion and the effective refractive index of the cladding will determine the overall dispersion.

Other properties of the PCFs are also controlled by varying their design. One such property is the range over which the PCF is single mode. As mentioned previously, this is varied by changing the size of the air holes to alter the “mode sieve.” As in the case of the first PCF, this is used to produce fibres which are single mode over a very broad range of wavelengths in the visible and IR [72]. It has been shown that only the cladding hole size and spacing are important in determining whether or not a PCF will be single mode [12] - below a particular ratio of these two properties, $d/\Lambda < 0.4$ (where d is the hole size and Λ is the spacing) the PCF will be single mode regardless of the size of the core. Therefore PCFs with large mode areas can be produced [74]. These can transmit high power beams with low intensity which are less affected by fibre non-linearity and also less susceptible to high intensity damage.

The birefringence of the PCF can also be varied. An ideal symmetric PCF should have no birefringence. However, in practice, slight asymmetries both intentional and unintentional will lead to the PCF having fast and slow optical axes. In some PCFs this effect is deliberately enhanced in order to produce polarization maintaining fibres [100, 132]. Conventional polarisation maintaining fibres are highly sensitive to temperature fluctuations as they are constructed from two different

types of glass. PCF polarisation maintaining fibres do not have this sensitivity and therefore are more useful in applications such as Sagnac interferometers [71, 155].

The field of PCFs has matured to the point where many of the fibres which were at the cutting edge of research in the late 1990s and early 2000s are now available from commercial companies. In figure 8 examples of some of these PCFs are shown.

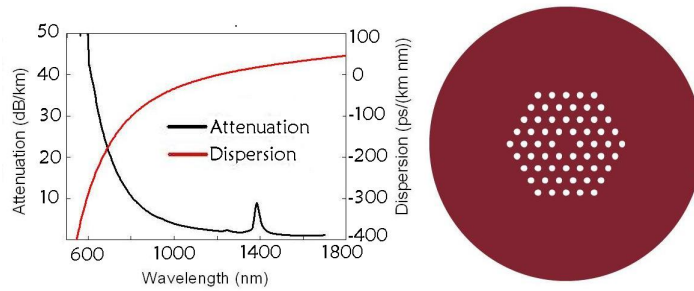
The development of PCFs allows stronger confinement than in conventional fibres and consequently larger peak pulse intensities. This leads to enhanced non-linear effects in the PCF. Hence the development of PCFs made possible a large number of experiments where solitons are perturbed by higher order non-linear effects and undergo significant changes in pulse shape, length and velocity. In addition, perturbations can lead to the transfer of energy to other types of radiation. Examples include the generation of RR, supercontinuum, FWM and higher harmonics. These will be explored in section 4. Such effects typically only occur if the pulse length is short ($T_0 < 1ps$)[2]. For longer pulses the higher order effects are small enough to allow stable solitons to form.

4 Radiation driven by solitons

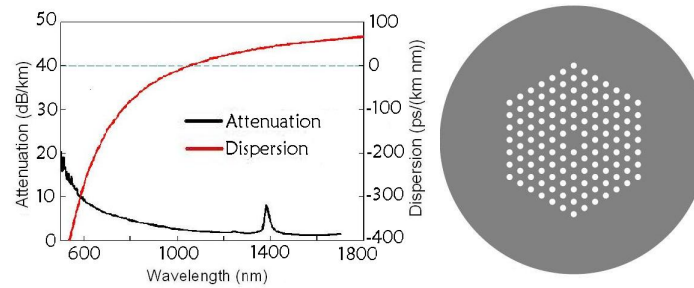
In the previous sections I discussed the early research into solitons and, in particular, optical solitons. I also explained some of the progress in soliton-related research that was made possible by the development of PCFs. In particular how tailored dispersion allows the formation of solitons over a broader range of wavelengths than in conventional fibres and how increased confinement leads to enhanced non-linear effects.

In this section I will consider various types of radiation which are driven by solitons when they are perturbed by higher order effects. Strictly a pulse driving such radiation will not be completely stable and hence cannot be referred to as a soliton. However in the following we will assume that “soliton” refers to a pulse which would, in the absence of higher order effects, propagate unchanged or with a periodic evolution.

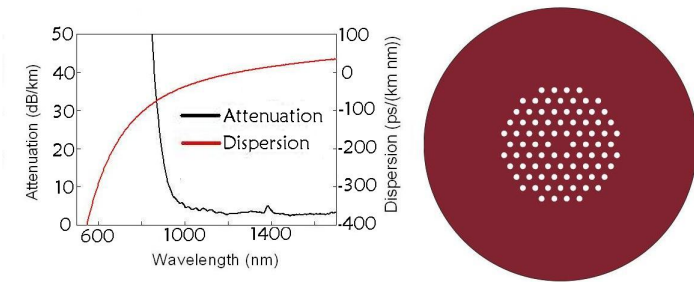
Many of the types of radiation I will discuss can be driven by pulses of light in media other than fibres, for example bulk glasses. However fibres have a number of advantages. One key benefit is the long interaction lengths that are easily possible in a fibre. In particular the use of PCFs with tailored ZDWs can minimise pulse broadening in the fibre at a particular wavelength and



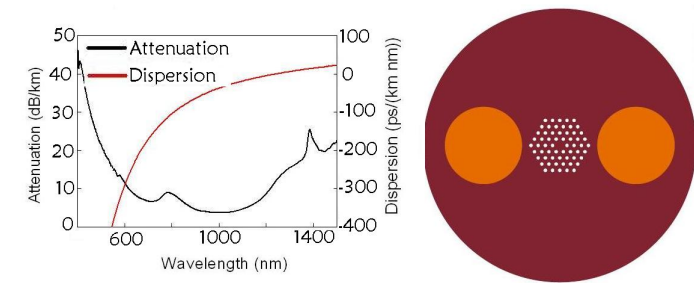
(a) Endlessly single mode PCF



(b) Large mode area PCF 5 μm core



(c) Large mode area PCF 25 μm core



(d) Polarisation maintaining large mode area PCF 5 μm core

Figure 8: A selection of PCFs produced by NKT Photonics. Including endlessly single mode PCFs (no higher order mode cut-off wavelength), large mode area PCFs and polarisation maintaining PCFs (using stress rods to introduce the birefringence). For each PCF the attenuation and dispersion as a function of wavelength are shown along with a drawing of the PCF end. Images and dispersion curves produced by NKT Photonics [105]

hence allow non-linear interactions over long distances in the PCF. A second advantage is the large intensities which are achieved for relatively low powers due to the high degree of confinement in the PCF core. This enhances non-linear effects and leads to high conversion efficiencies. As discussed previously, confinement can be particularly high for PCFs. Other advantages include the low losses which are possible over broad wavelength ranges in PCFs and the use of tailored dispersion to achieve phase matching. Mode matching can also be achieved as fibres can be made single mode over wide wavelength ranges. In addition fibre based systems can be designed to be robust, portable and small.

There are many reasons why research has been carried out into the various types of radiation that are driven by solitons and a number of these will be discussed in the following sections. One of the key reasons is the generation of new frequency components particularly in the visible and the UV. These have applications in many fields including biophotonics [139], optical coherence tomography (analogous to ultrasound or radar but using light) [10], astrocomb generation [55] and the generation of squeezed states [137].

A further reason for interest in radiation driven by solitons is that such radiation will perturb the soliton and potentially reduce its usefulness in telecommunications. As explained in section 3 it is possible to design PCFs to minimise or compensate the effects of dispersion and also to produce large mode area PCFs where the lower light intensity will reduce the effects of non-linearities.

4.1 Supercontinuum generation

Supercontinuum generation refers to the broadening of an initial spectrum to a bandwidth of several hundred nanometres [38]. The resulting light will have a low temporal coherence (weak phase relationship between components of the beam at different times but the same location) but a high spatial coherence (strong phase relationship between components of the beam at different locations but the same time) [102]. The effect can be achieved using light coupled into PCFs and occurs due to the fibre non-linearity and dispersion. Depending on the parameters of the original light, the supercontinuum is formed by different effects. One effect which helps to extend the spectrum is the generation of RR.

The main focus of the research described in this thesis is the generation and evolution of RR

and NRR. Both are types of phase matched dispersive radiation driven by solitons and, in our experiments, they lie in the visible and the UV respectively. In order to drive the RR and NRR the soliton must contain components which oscillate at their respective phase matched frequencies. This requires extreme broadening of the input pulse spectrum.

For the experiments described in this thesis, supercontinuum generation does not occur. However some of the non-linear effects, which, under different pulse and PCF conditions, would produce a supercontinuum, help to broaden the spectrum and drive the generation of RR and NRR. This justifies the inclusion of a brief description of the phenomenon of supercontinuum generation.

The original discovery of supercontinuum generation occurred in bulk glasses in 1970 [4]. In these experiments high energy (5 mJ) laser beams were used to achieve the non-linear effects necessary for supercontinuum generation. A spectrum was produced which spanned the whole of the visible range. In 1976 comparable results were achieved in conventional step-index fibres [84]. Since then considerable research, both experimental and theoretical, has been carried out in both fields.

The discovery of supercontinuum generation in solid core PCFs [109] opened up a huge new area of research. The advantages of using a PCF over a conventional fibre have been described in section 3. The high non-linearity, dispersion tailoring and long interaction lengths made possible many new advances in supercontinuum generation. Broader bandwidths with higher average powers could be produced and input sources no longer had to have the high energies required in bulk materials or conventional fibres [38]. For example the first experiment to measure supercontinuum generation in PCFs used pulses with only nJ energy and was able to produce a spectrum of over an octave in width.

A fibre generated supercontinuum has an additional advantage over using bulk materials. In a fibre the spatial shape of the light is determined by the mode characteristics of the fibre. As mentioned previously, PCFs can be made single mode over large wavelength ranges so the whole of the generated supercontinuum can have a uniform spatial profile [38]. Only temporal non-linear effects act to produce the supercontinuum. In bulk materials the supercontinuum is generated by a combination of temporal and spatial effects including pulse filamentation. This increases the difficulty in developing a theoretical description of the phenomenon and means that the broad spectrum will not have a uniform spatial profile, making it harder to use in practical applications.

Several applications for PCF generated supercontinuum have been suggested. One key use is

in the production of frequency combs for use in precise measurements of frequencies in optical metrology [34, 69, 142]. Further uses are in the fields of time-resolved absorption and excitation spectroscopy [36] and optical coherence tomography [56].

One key broadening mechanism, in both bulk materials and fibres, is self-phase modulation (SPM). This is an effect where a pulse propagating through a medium will gain an intensity dependent phase. This occurs because the refractive index of the medium will have an intensity dependent contribution. This will be seen in more detail in part II. The phase change will have the same temporal shape as the pulse

$$\phi(z, t) \propto |U(0, t)|^2 z. \quad (4.1)$$

Here $\phi(z, t)$ is the phase of the light at position z along the fibre axis and at time t . $U(0, t)$ is the amplitude of the pulse at position $z = 0$ and time t ⁷.

This dependence of the phase on time means that across the pulse the instantaneous frequency will vary [2]. This leads to the generation of new frequencies of light, with higher frequencies being produced at the back of the pulse and lower frequencies at the front. The dependence on z in (4.1) indicates that the generation of new frequencies will occur continuously as the pulse propagates.

In bulk materials the process of supercontinuum generation also depends on other non-linear effects such as space-time focusing and self-steepening [38]. As mentioned previously, the combination of spatial and temporal effects makes a theoretical description of the process complicated.

In conventional fibres supercontinuum generation is again due to several different effects. SPM and Raman scattering are the most important effects if the input light is in the normal dispersion region (positive β_2), with FWM and Cross Phase Modulation (XPM) having a smaller effect. These effects act together to form a broad, smooth spectrum. Raman scattering is due to the non-instantaneous, non-linear response of a medium to the light pulses propagating through it. The light can excite one of the vibrational modes of silica. In this process a photon in the pulse is converted to a lower energy photon and an optical phonon associated with the vibrational mode [102]. Within the spectrum of the pulse this process will amplify lower energy components at the expense of higher energy components. This results in a shifting of the pulse towards longer wavelengths, helping to create the long wavelength side of the supercontinuum. FWM will be described in more detail

⁷Fibre losses have been neglected in (4.1), inclusion of loss will affect the dependence of the phase on z

in section 4.3. It is the process whereby two input photons (which can have same frequency) are converted to two output photons at different frequencies [102]. XPM is similar to SPM however it occurs when two beams are present and the effect of one beam is to produce an intensity dependent contribution to the refractive index experienced by the second beam. As in the case of SPM this then leads to a phase change for the second beam and corresponding spectral broadening.

If the input light is in the anomalous dispersion region (negative β_2) then, as discussed previously, solitons can form. If higher order effects are neglected (a reasonable approximation for pulses with a length greater than 1 ps) then, due to a balance between non-linearity in the form of SPM and dispersion, a fundamental soliton will not change as it propagates along the fibre and a higher order soliton will undergo periodic evolution, therefore a supercontinuum will not form. However higher order effects can perturb a soliton and lead to spectral broadening. One example of this is Raman scattering which, as discussed, will shift the soliton to longer wavelengths. Another example is the generation of RR (see section 5) where the soliton is perturbed by higher order dispersion and loses energy to radiation in the normal dispersion region. Typically this helps to form the short wavelength edge of the supercontinuum.

The key effect leading to supercontinuum formation from solitons is the splitting up of a higher order soliton in a process known as soliton fission. Any higher order soliton can be described as a bound state of fundamental solitons. However the name is somewhat of a misnomer as there is no binding energy, hence the state can be easily broken apart by higher order perturbations such as Raman scattering, self steepening and two photon absorption [76]. Raman scattering has already been discussed. Self steepening is a non-linear effect that arises from the intensity dependence of the group velocity. As with SPM this is due to the intensity dependence of the refractive index of a medium. The intensity of a pulse varies across its length and the higher the intensity the larger the intensity dependent contribution to the refractive index. Therefore the slower that part of the pulse will travel. This shifts the peak of the pulse towards the trailing side creating an increasingly steep edge [2]. Two photon absorption occurs when two photons are absorbed by an atom to excite it, with the increase of the energy of the atom being equal to the sum of the two photon energies. This process is a non-linear intensity dependent process [102]. An initial pulse chirp (changing instantaneous frequency across the pulse) can also help to make a higher order soliton more prone to breaking apart [81].

Soliton fission leads to multiple fundamental solitons, all of which continue to propagate and generate new frequencies through Raman scattering or the generation of radiation in the normal dispersion region. This can lead to a smooth supercontinuum forming.

In PCFs the processes leading to supercontinuum generation are also dependent on whether the input pulse lies in the normal or anomalous dispersion region of the spectrum and also on how far away the pulse is from the ZDW. The mechanisms are the same as those described for conventional fibres but, in many cases, these effects can be enhanced or reduced by dispersion tailoring and greater confinement in the PCF core. Research into PCFs has again pointed out the importance of soliton fission [61, 63] in the formation of a supercontinuum from a soliton along with Raman scattering and the generation of radiation in the normal dispersion region [147, 86]. A smooth supercontinuum forms if the input pulse is close to the ZDW. In this case the input pulse and the radiation in the normal dispersion region will be close to each other and a smooth spectrum can form between them.

Since the first supercontinuum experiments in PCFs, the phenomenon has been explored in many ways. Both the long and short wavelength edges have been extended further using pulses in both the normal and anomalous dispersion regions [138, 25]. The sensitivity of the supercontinuum to input pulse noise has also been investigated extensively [37, 38]. This has been with a view to forming a low noise supercontinuum for use in the practical applications mentioned earlier.

In this section we have seen that supercontinuum generation in PCFs is due to a number of different effects, some of which will be discussed in more detail in the following sections. In our experiments, the pulse and PCF parameters used are not designed for the formation of supercontinuum. However the same processes that have been described will lead to spectral broadening and the generation of new types of radiation. Typically, rather than observing a smooth broad spectrum which is the sign of a supercontinuum, we will see a broadened input pulse spectrum and a number of isolated peaks due to radiation which has been driven by the pulse.

4.2 Harmonic generation

One type of radiation which can be driven by a soliton is higher harmonic radiation. This is generated at higher frequencies than the driving pulse and therefore can be used to produce light

in the visible and UV from laser sources in the IR. In particular THG can be used to generate light at a third of the wavelength of the driving pulse. This can be achieved in many different media including PCFs. Amongst other things, THG has been used to generate short wavelength light for uses in microscopy [152] and spectroscopy [124] as well as for microfabrication [39].

Higher harmonics are generated due to the fibre non-linearity. As we will see in part II the non-linearity of a fibre refers to the non-linear, intensity dependent response of the fibre to an electric field. The field will act to realign the bound electrons in the fibre inducing a polarisation which will contribute to the overall electric flux density.

The induced polarisation will have both a linear and a non-linear dependence on the electric field. Under certain conditions, which are discussed in section 15 in the appendix, this dependence can be quantified using the non-linear susceptibilities $\chi^{(n)}$,

$$\begin{aligned} \frac{\mathbf{P}(\mathbf{r}, t)}{\varepsilon_0} = & \int_{-\infty}^{\infty} \chi^{(1)}(t - t_1) \mathbf{E}(\mathbf{r}, t_1) dt_1 + \int_{-\infty}^{\infty} \int_{-\infty}^{\infty} \chi^{(2)}(t - t_1, t - t_2) \mathbf{E}(\mathbf{r}, t_1) \mathbf{E}(\mathbf{r}, t_2) dt_1 dt_2 \\ & + \int_{-\infty}^{\infty} \int_{-\infty}^{\infty} \int_{-\infty}^{\infty} \chi^{(3)}(t - t_1, t - t_2, t - t_3) \mathbf{E}(\mathbf{r}, t_1) \mathbf{E}(\mathbf{r}, t_2) \mathbf{E}(\mathbf{r}, t_3) dt_1 dt_2 dt_3 + \dots \end{aligned} \quad (4.2)$$

Here $\mathbf{P}(\mathbf{r}, t)$ is the induced polarisation and $\mathbf{E}(\mathbf{r}, t)$ is the electric field. The first term on the RHS represent the linear contribution, all other terms are non-linear contributions. In fibres the $\chi^{(2)}$ term is zero (for reasons which are discussed in section 15 in the appendix) so the first term of interest is the $\chi^{(3)}$ term. This term leads to a variety of effects. The first we will consider is the generation of THG. The higher order terms in (4.2) are responsible for the generation of higher harmonics but their effect becomes increasingly small as the order increases.

In the process radiation at one frequency ω is converted to radiation at a higher frequency 3ω . This is an example of a parametric process where the state of the fibre medium is unchanged by the radiation. Therefore the process will be instantaneous and no energy or momentum can be transferred to or from the medium. This means that energy and momentum must be conserved by the radiation conversion. We express this in a phase matching condition.

In order to conserve energy the process can occur via the mechanism $\omega + \omega + \omega = 3\omega$ or alternatively via $2\omega + 2\omega - \omega = 3\omega$, where light at ω and at the second harmonic 2ω are coupled into a fibre. Phase matching requires that the wave numbers $k = n\omega/c$ of the participating frequencies

obey the following condition for the first mechanism,

$$\begin{aligned}
 3k(\omega) &= k(3\omega), \\
 \Rightarrow 3 \frac{n(\omega)\omega}{c} &= \frac{n(3\omega)3\omega}{c}, \\
 \Rightarrow n(\omega) &= n(3\omega).
 \end{aligned} \tag{4.3}$$

Correspondingly for the second mechanism,

$$\begin{aligned}
 2k(2\omega) - k(\omega) &= k(3\omega), \\
 \Rightarrow \frac{2n(2\omega)2\omega}{c} - \frac{n(\omega)\omega}{c} &= \frac{3n(3\omega)\omega}{c}, \\
 \Rightarrow 4n(2\omega) - n(\omega) &= 3n(3\omega).
 \end{aligned} \tag{4.4}$$

These conditions require certain combinations of input light frequency and fibre dispersion curve. In our experiments we do not couple light at the second harmonic frequency into the fibre, hence we will focus on the first mechanism and its phase matching condition in (4.3).

Even with the tailored dispersion possible in a PCF it is not usually possible to satisfy the phase matching condition if only one fibre mode is considered. This is because, as seen in figure 3, typically the refractive index decreases as the wavelength increases (frequency decreases). Hence the index at the third harmonic wavelength is larger than that at the input wavelength.

However it is still possible for THG to occur if driving pulse light from one mode produces third harmonic radiation in a different mode. The guided modes of a fibre were discussed in section 3. Each mode will have a different dependence of the refractive index on frequency. Typically we couple light into the fundamental mode of the fibre and this can transfer energy to third harmonic radiation in a higher order mode. Alternatively the driving pulse light can be in one higher order mode and produce third harmonic radiation in an even higher order mode.

The higher order modes have lower refractive indices, allowing phase matching to occur. This is shown in figure 9, which shows the variation with wavelength of the refractive index for the fundamental and a selection of higher order modes for one of the PCFs used in the experiments. The modes were calculated using SEM images of the PCF end and a programme developed by Steven G. Johnson at MIT along with the Joannopoulos Ab Initio Physics group [68] and adapted

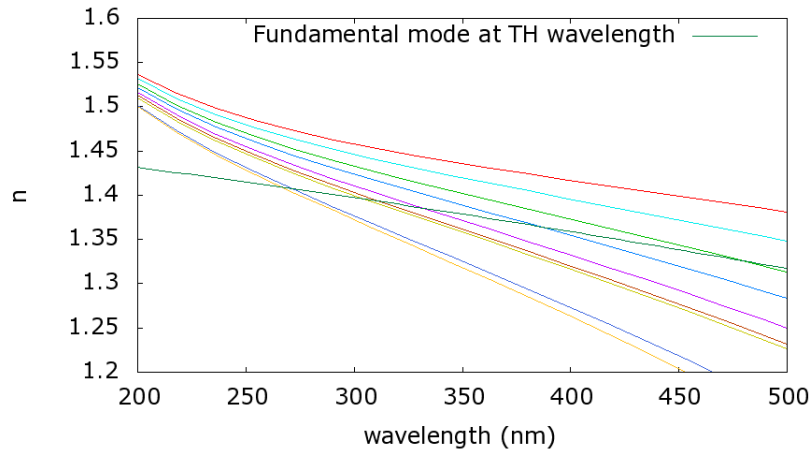


Figure 9: Refractive indices of the fundamental mode shifted to one third of the wavelength, and a selection of higher order modes for the NL-1.5-590 PCF. Possible third harmonic phase matching is indicated by the crossing points. Modes calculated by Dr Kehr at the University of St Andrews

by the group of Dr di Falco in St Andrews [33]. Some of the calculated mode shapes were shown in figure 7 in section 3.

The refractive index of the fundamental mode at one third of the wavelength is also shown in figure 9. The points where it crosses the refractive index curves for the higher order modes indicate phase matched wavelengths. In our experiments the pulses used have a bandwidth extending over 200 nm centred at 780 nm, hence the third harmonic radiation will occur in the UV.

One key experiment in harmonic generation involving higher modes was carried out by Efimov et al. [6]. They investigated coupling input light into higher order modes and producing THG in very high order modes in the UV. As in our experiments, they used IR pulses coupled into PCFs with similar dispersion curves to our fibres. The output spectra contained a number of sharp peaks in the UV which did not shift with input power. In contrast the spectrum in the IR showed large differences with varied input power. For example the extent of the soliton Raman shift increased as expected for larger input powers. Their results for one PCF are shown in figure 10. The figure shows the PCF output spectrum in the UV as the average power of the input pulse is varied. Signals can be seen to appear as the average power increases, these are believed to be due to THG.

The lack of wavelength shift in the UV was one indication that the signals were due to THG. This being the case, their position in the spectrum is determined by the phase matching condition, which is in turn determined by the PCF dispersion rather than the input wavelength. When the spectrum

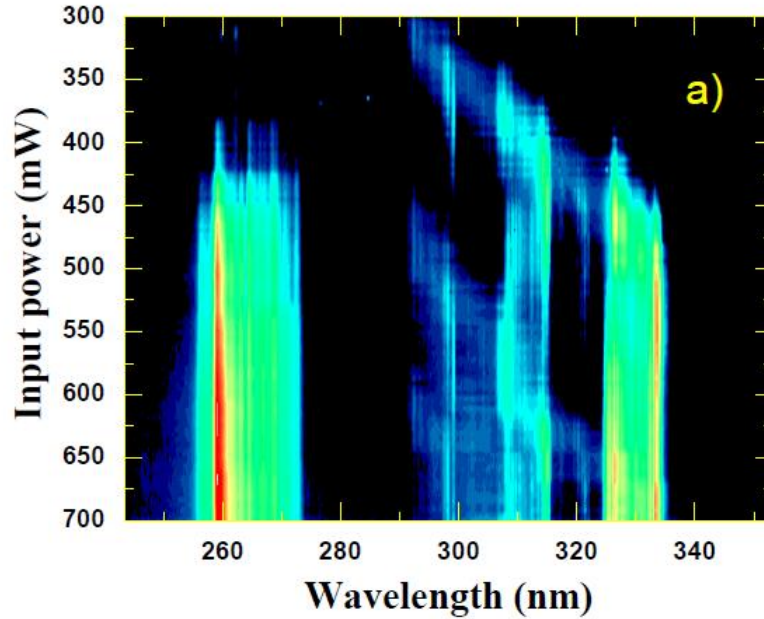


Figure 10: Figure taken from a research paper by Efimov et al. [6] showing the variation in the UV output spectrum from a PCF as the input beam average power is varied. Image © 2003 Optical Society of America

of the generated soliton overlaps with the region of the IR spectrum with a suitable refractive index for phase matching, the third harmonic will be generated. Hence the spectral position is constant even when the input light is Raman shifted. The amount of radiation generated depends on how much of the soliton spectrum overlaps with the phase matched region.

They found that they were only able to efficiently achieve THG when they coupled light into a higher order mode rather than the fundamental mode. This could be because of the different dispersion properties of higher order modes or because higher order modes have a higher proportion of their mode area propagating outside of the core. In the latter case this means that non-linear surface effects from the core-cladding boundary are more important and these may contribute to THG.

The experiments described in the Efimov paper are particularly relevant as they involve the generation of radiation in the UV, which is driven by a pulse in the IR. The NRR will be driven by a similar pulse and will occur in the same region of the UV. Firstly this means that it is important to understand where we expect to find third harmonic signals in order to distinguish them from

NRR. Secondly the techniques that we use to control and investigate the generation and evolution of NRR are also applicable to third harmonic radiation.

4.3 Four wave mixing

Four wave mixing is another mechanism leading to new frequency components in a fibre. In this section I will briefly discuss how FWM occurs. This inclusion is justified because, as in the case of THG signals, many of the experimental techniques which we have developed to study pulse evolution and RR and NRR can be extended to the study of FWM signals.

FWM can occur in many different materials. It has been demonstrated in PCFs [66] and shown to obey the expected theoretical behaviour. It can be used to produce two radiation signals one at higher frequency and one at lower frequency than a pump pulse. This mechanism can be used in optical parametric amplifiers [144] to amplify a signal frequency at the expense of the pump. It has also been used for some time in the field of spectroscopy [16].

Like THG the process of FWM arises from the $\chi^{(3)}$ non-linearity of the medium. If two frequencies ω_1 and ω_2 are coupled into a fibre then two sidebands can be produced with frequencies ω_3 and ω_4 hence the name “four wave mixing.” This process is said to be degenerate if the two input frequencies are the same. In this case two pump photons will be converted into one signal and one idler photon at ω_3 and ω_4 respectively. The process is parametric and therefore as in the case of THG it must obey a phase matching condition. Energy can be conserved via [2]

$$\omega_1 + \omega_2 = \omega_3 + \omega_4. \quad (4.5)$$

With a corresponding phase matching condition for the wave numbers $\beta = n\omega/c$, [2]

$$\begin{aligned} \beta_1 + \beta_2 &= \beta_3 + \beta_4, \\ \Rightarrow \frac{n(\omega_1)\omega_1}{c} + \frac{n(\omega_2)\omega_2}{c} &= \frac{n(\omega_3)\omega_3}{c} + \frac{n(\omega_4)\omega_4}{c}, \\ \Rightarrow n(\omega_1)\omega_1 + n(\omega_2)\omega_2 &= n(\omega_3)\omega_3 + n(\omega_4)\omega_4. \end{aligned} \quad (4.6)$$

This phase matching will have an intensity dependence as the refractive index has an intensity dependent contribution. Whether or not this phase matching condition can be satisfied will depend

on the frequency of the input light source and on the dispersion curve of the fibre used.

5 Resonant dispersive radiation

We now turn to the type of radiation which is studied in most of the experiments described in this thesis. In this section an overview will be given of the history of resonant dispersive radiation and the motivations behind its study. The theory of energy transfer from a pulse to the radiation will be explained in part II and the phase matching condition for the process will be discussed in section 8.4.

In this thesis the term resonant dispersive radiation is used to refer to both RR and NRR. Both are driven by short pulses and share the same phase matching condition but, as mentioned previously, RR has a frequency with the same sign as the driving pulse whilst NRR has a frequency with the opposite sign. Research into RR has historically been motivated by its potential uses in various fields which will be discussed in section 5.1.1. The focus has been on improving the generation efficiency of RR and on controlling the characteristics of the radiation such as its wavelength, bandwidth and stability. Our investigations into RR had the original aim of using the radiation as an indicator of pulse compression in a PCF, as the radiation is driven when the pulse compresses and its spectrum expands to overlap with the RR phase matched wavelength.

NRR is a new discovery and the first example of a coupling between positive and negative frequencies in optics [118]. As discussed before, the discovery came about through combining our research into RR with the concept of negative frequencies from the field of event horizon analogues. The latter will be discussed in section 6.

RR and NRR are generated under similar conditions to the types of radiation described in section 4, therefore it is important to briefly note the differences between both types of resonant dispersive radiation and supercontinuum, THG and FWM. As mentioned in section 4.1, RR forms the short wavelength edge of a supercontinuum. However it can also be generated without the existence of a supercontinuum. This depends on the wavelengths of the input pulse and the RR relative to the fibre ZDW. Pulses further from the ZDW will be further from the phase matched RR wavelength leading to an isolated RR peak as opposed to a smooth supercontinuum spectrum between the pulse and the RR [140]. As seen in section 4.2 (4.3) and (4.4), THG obeys a phase

matching condition. This is different to the phase matching condition for RR and NRR which, as mentioned in section 1, is a conservation of Doppler shifted frequencies in the frame co-moving with the pulse (considered in detail in part II). Likewise FWM has a different phase matching condition seen in section 4.3 (4.6). The solutions to each of these phase matching conditions depend on the pulse parameters and the dispersion profile of the fibre used. Therefore if these are known the solutions can be found and signals due to each effect can be distinguished from each other. Another important point is that THG and FWM both occur due to higher order non-linearities in the fibre whereas RR and NRR occur due to higher order dispersive effects.

5.1 Resonant Radiation

Resonant radiation is a type of radiation which arises due to the destabilisation of solitons by higher order dispersion. The soliton loses energy to a signal at a phase matched wavelength in the normal dispersion region of the spectrum. The dispersion coefficients are defined by the following equation where n is an integer, for higher order dispersion $n \geq 3$,

$$\beta_n = \frac{d^n}{d\omega^n} \left(\frac{n(\omega)\omega}{c} \right). \quad (5.1)$$

The first theoretical consideration of such radiation was in 1986 by Wai [146]. The aim of the research was to investigate the stability of solitons close to the ZDW of the fibre. As discussed previously, solitons have historically been researched for their potential uses in telecommunications where stability is critical. Close to the ZDW the effects of TOD (β_3) will be relatively larger and can lead to destabilisation of a soliton. They showed for the first time that a resonance signal in the normal dispersion region will develop as a fundamental or higher order soliton propagates in a fibre close to the ZDW. One interesting feature of this signal is that its generation efficiency is larger for higher order solitons. This is due to the spectral broadening occurring when the higher order solitons compress temporally. The increased overlap of the soliton spectrum with the resonant signal is able to stimulate its growth.

In the paper they used a split-step Fourier method to solve the NLSE (an equation describing pulse propagation in a fibre) with an initial pulse in the form of a fundamental or higher order soliton. They extended the NLSE to include the effects of loss and TOD. The results showed

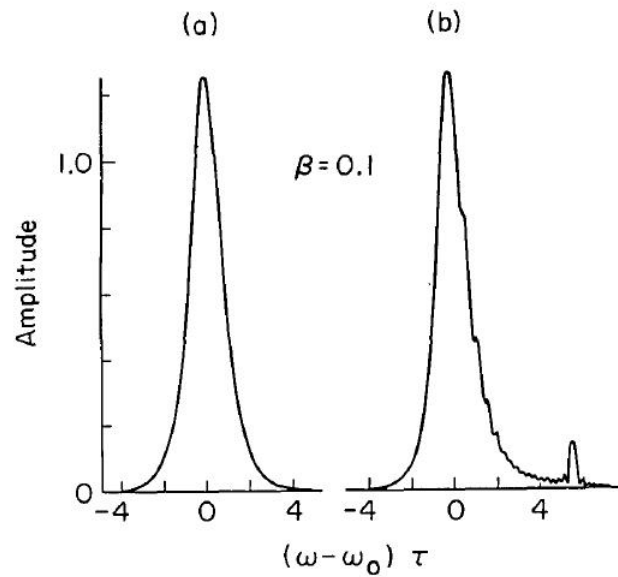


Figure 11: Figure taken from the paper by Wai [146] showing (a) the soliton amplitude as a function of frequency at the start of propagation and (b) the soliton and resonant signal after propagating a certain distance. Here β is a measure of the size of the TOD compared to the second order dispersion. Image © 1986, Optical Society of America

that, for a fundamental soliton, the resonance signal will grow steadily but leave the soliton shape approximately the same (width and height changed by only 6% and 2% respectively) even after propagation distances of over 30 km. Thus the radiation was not considered to be detrimental for the use of solitons in telecommunications. The two graphs in figure 11 show one set of results from their theoretical study. The original fundamental soliton amplitude as a function of frequency is shown along with the soliton and the resonant signal after a certain propagation distance.

A further theoretical study by Höök [59] looked at the impact on soliton stability of Fourth Order Dispersion (FOD) (β_4). This was required as new dispersion flattened fibres were being developed with large second order dispersion and negligible TOD at the pulse wavelength. In such a case FOD effects start to become significant. They found that fundamental and higher order solitons will again lose energy to resonant peaks in the normal dispersion region. In this case the resonant peaks formed two symmetric sidebands as shown in figure 12. These sidebands were shown to be equivalent to the peak due to TOD in the previously discussed 1986 paper by Wai [146].

Again they used a split-step Fourier method with an input soliton (fundamental or higher order) and the NLSE perturbed by FOD. One interesting feature of their results is that, as in the Wai

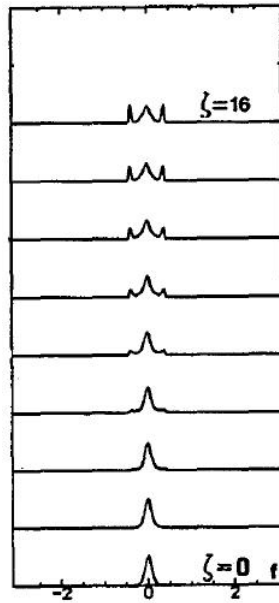


Figure 12: Figure taken from the paper by Höök [59] showing the calculated spectrum of the pulse and sidebands at different propagation distances (parametrised by ξ). The bottom axis is in units of $f = (\omega_{soliton} - \omega) / (2\pi)$. Image © 1993, Optical Society of America

paper, the soliton loses energy to the sidebands faster the greater its spectral width. However, as it loses energy, its temporal length increases and its spectrum contracts. Thus the rate of generation of the sidebands decreases with propagation.

Other studies have looked at the generation of RR in the normal dispersion region driven by solitons, using semi-analytical and numerical techniques [145, 40, 70, 77, 82]. The research focuses on both the stability of the driving soliton and the frequency and amplitude of the resonance peaks.

A simple analytic theory of RR, describing its frequency and amplitude, was first developed by Arkhmediev and Karlsson in 1995 [3]. Once again their motivation was to study perturbations to solitons. They looked at both TOD and FOD separately and found similar results to Wai and Höök [146, 59]. The TOD and FOD lead to one resonant signal and two resonant sidebands respectively and the amplitude of these signals increases with increasing overlap with the soliton spectrum.

As before they started with the NLSE and added TOD or FOD as a small perturbation. They considered solitons as being sensitive to perturbative signals with the same wavenumber, as they can transfer energy to such signals. They found a phase matching condition by equating the soliton wavenumber to the wavenumber of a linear dispersive wave and found two conditions for RR, one

for TOD

$$\omega_0 = -\frac{1}{\epsilon} \left(\frac{1}{2} + 2(\epsilon A)^2 + O((\epsilon A)^4) \right), \quad (5.2)$$

and one for FOD

$$\omega_0 = \frac{1}{\sqrt{2}\epsilon} \left(1 + (\sqrt{\epsilon}A)^2 + O((\sqrt{\epsilon}A)^4) \right). \quad (5.3)$$

Here A is the soliton amplitude, ω_0 is the frequency of the resonant signal relative to the soliton frequency and ϵ is a small parameter which quantifies the size of the perturbative TOD or FOD.

As a further interesting part of their investigation, they looked at two invariants of the perturbed NLSE - the energy conservation and the conservation of the spectral centre of mass. The former allows the soliton energy loss to be calculated and the latter leads to a spectral recoil of the soliton from the generated RR. For TOD as the soliton recoils from the RR the overlap of the pulse spectrum with the RR decreases and therefore the growth of the RR also decreases. This in turn reduces the spectral recoil until a stationary state is reached (ignoring Raman shifting). For FOD the spectral recoil from each sideband cancels out but, as in the paper by Höök [59], the loss of energy and therefore temporal broadening and spectral contraction reduce the rate of energy loss to the RR.

Further theoretical progress in the study of RR came from the field of supercontinuum research. As discussed in section 4.1, the short wavelength edge of a supercontinuum generated by pulses in the anomalous dispersion region is formed by RR. Attempts to extend this edge therefore required research into the generation of RR. One interesting paper by Husakou and Herrmann [62] focused on the breakup of higher order solitons by soliton fission and the RR generated by each of the resulting fundamental solitons. As in the paper by Arkhmediev and Karlsson [3] they found the phase matching condition for the RR by equating its phase to the phase of the soliton. In their analysis the soliton phase is given by

$$\phi_s(\omega_s) = \frac{n(\omega_s)\omega_s}{c}z + \frac{n_2 I \omega_s}{2c}z - \frac{\omega_s}{v_s}z, \quad (5.4)$$

and the RR phase by

$$\phi(\omega) = \frac{n(\omega)\omega}{c}z - \frac{\omega}{v_s}z. \quad (5.5)$$

Here z is the propagation distance, n is the intensity independent part of the refractive index, n_2

is the intensity dependent contribution to the refractive index, I is the soliton intensity (the RR intensity is assumed to be negligible) and v_s is the soliton group velocity. They used the Forward Maxwell equation to achieve the above result rather than the NLSE as the latter assumes that the pulse has a slowly varying envelope which is not true for short pulses. They found that higher order solitons can be broken apart into their constituent fundamental solitons by the action of higher order dispersion. Each of the emitted solitons will generate RR in the normal dispersion region with a frequency determined by equating the phases given in (5.4) and (5.5).

The first experimental measurement of RR could not be carried out until the development of PCFs. The small core size allowed for high light intensities in the PCF core, along with the ability to tailor the PCF dispersion which created the conditions necessary to achieve RR phase matching. In 2004 Cristiani et al. first published results directly focusing on RR [64]. They propagated a 190fs IR pulse through a PCF and measured a visible signal in the output. The wavelength of the signal matched the expected RR phase matching condition from the Husakou and Herrmann paper and followed the expected behaviour as the input pulse wavelength was varied. They also simulated the propagation of the pulse and found once again that the generation of RR only occurs when the input pulse strongly compresses in the PCF. The corresponding expansion of the pulse spectrum into the normal dispersion region produces a component at the RR phase matched wavelength which is able to drive the resonance.

Their experiments also showed that the RR signal consists of a series of signals with different group velocities. By comparing the results to simulations they concluded that the extra RR pulses are due to multiple pulse compressions occurring in the PCF. Each time the pulse compresses its spectrum extends into the visible and is able to drive the RR. The compressions became weaker and therefore the largest RR signal is driven by the first compression to occur.

5.1.1 Uses for Resonant Radiation

The early theoretical research into RR focuses on the stability of the driving soliton. Since then several potential uses for the RR itself have been suggested. One such use is as a method for conversion of short pulses to higher frequencies for use in photobiology. RR may be of particular use as it can be generated in the visible, a region of the spectrum where there are fewer suitable

laser sources than in the IR. A recent review paper by Tu and Boppart [139] looks into some of the potential uses for supercontinuum generation techniques in biophotonics. RR is one of the effects that they focus on, including how it can be incorporated into a portable and low-cost light source platform for biophotonics. Applications in other fields include using RR along with Fabry-Perot filtering cavities to produce broadband visible wavelength astrocombs for use in spectrograph calibration [24].

In addition to its practical applications RR also has interesting theoretical implications. A recent paper demonstrates that the phenomenon can be described as the scattering of pulse photons at the optical event horizon created by the pulse itself [28]. This links RR to the study of other mode conversion processes at the event horizon such as the generation of the optical analogue of HR [41].

A further large area of study related to RR is the cancellation of the Raman shift by spectral recoil [127]. Under the correct conditions this produces a wavelength locked soliton with a growing long wavelength RR peak. Such amplification of the RR along with the ability to choose its wavelength by designing the PCF dispersion curve have led to suggestions that this process could be used to produce an optical parametric amplifier [127].

Much of the recent research into RR has focused on controlling its properties in order to make it suitable for use in the practical applications mentioned in the first paragraph above. These typically require narrowband tunable light in the visible region with multi-milliWatt power levels and high stability. In order to meet these requirements the generation of RR must be carefully managed.

There are several ways to achieve the tunability requirement for practical uses of RR. One method is to use dispersion micromanaged fibres [88, 89]. These are tapered over sub- mm distances to vary the dispersion and therefore the phase matching condition for RR over the length of the fibre. This produces a broad spectrum of RR over the range of phase matched wavelengths. The central frequency and bandwidth of this spectrum can be changed by using different tapers. This method has an additional benefit in terms of noise reduction. The non-linear interactions between the pulse and the RR, which amplify the laser Schott noise, are reduced. This has been shown to reduce noise levels by 9 – 20 dB compared to fibres with longer tapers or constant core diameter fibres [89].

Another method which allows for limited tunability is to vary the input pulse polarization [94, 65]. As the fibre principal axes have slightly different dispersion profiles, input light polarized

along each axis will phase match to RR at a different wavelength. For a fibre with a modal birefringence of 1.2×10^{-3} it was shown that the RR wavelength could be shifted by up to 75 nm [94].

The widest tuning range for RR is achieved using a wavelength tunable input pulse [140]. This has been shown to allow for tuning ranges from 485 – 690 nm using an IR laser with a tuning range of 690 – 1020 nm. Many lasers now exist with broad IR tuning ranges and the ability to produce femtosecond scale pulses.

Narrow-band RR is produced by tuning the input pulse wavelength away from the fibre ZDW [140]. This suppresses the generation of supercontinuum and allows a spectrally isolated RR signal to form.

The pulse to pulse energy stability of the radiation is improved by using an all fibre set up [87, 85] or by using tapered fibres [89]. The former approach has achieved pulse to pulse energy fluctuations as low as 2.48 % using an all fibre RR source.

In order to reach milliwatt power levels, a high conversion efficiency between the pump pulse and the RR is required. To this end various groups have studied the variation in efficiency with different parameters including: pump wavelength separation from the fibre ZDW, pump pulse length, pump power, fibre core size and fibre TOD [23, 116, 141, 140]. Using these methods pump to signal conversion efficiencies of over 40 % have been achieved [23].

One crucial parameter, which will both affect the RR generation efficiency and also allow for measurements of its evolution, is the input pulse frequency chirp. To the best of our knowledge this has never been systematically studied in relation to RR. The chirp has a significant impact on how short pulses evolve in a fibre, including where and to what extent they temporally compress [80, 2, 156, 46, 134, 154, 27]. As seen in the various theoretical and experimental papers discussed in section 5.1, the compression of the pulse is critical in the generation of RR.

In the experiments described in this thesis the input pulse power and chirp will be used as tools to control the pulse compression. It is possible to vary the position in the PCF where the pulse compresses and in this way change the propagation distance to the end of the PCF for radiation generated when the pulse compresses. This allows us to investigate the evolution of such radiation without the need to cut the PCF.

5.2 Negative Resonant Radiation

The main result in this thesis is the discovery of NRR, which occurs due to a coupling between positive and negative frequencies. This is the first example of such a phenomenon in optics. This has only been possible due to some of the recent advances described in part I in various fields such as PCFs, lasers and analogue systems.

As explained in section 5, a large amount of research has been carried out into RR over the past few decades and continues to be carried out today. New developments such as tailored dispersion in PCFs and short pulsed laser systems have led to many advances in the field. However the idea of coupling to negative frequencies came from our research into event horizon analogues. In this community the concept of mixing between positive and negative frequencies is well established.

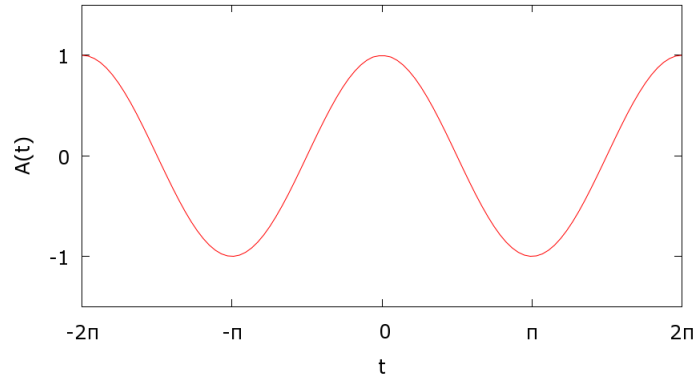
Our original research into RR had the aim of finding ways to use the radiation as a tool to measure pulse compression. By combining our knowledge of the RR phase matching condition and the idea of negative frequencies we were able to recognise that there was a further solution to the phase matching condition.

We describe the NRR as having a negative frequency as its frequency has the opposite sign to the driving soliton frequency. An electromagnetic field is real and therefore must contain both positive and negative frequencies. However the negative frequencies are typically ignored as they contain the same information as their corresponding positive frequencies. This is seen by expressing a field as the Fourier transform of its frequency spectrum

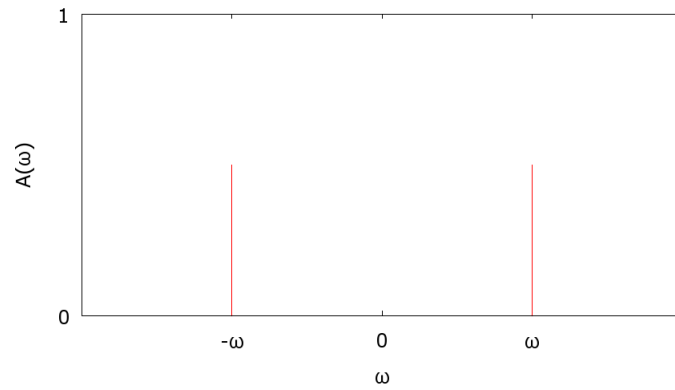
$$A(z, t) = \frac{1}{2\pi} \int_{-\infty}^{\infty} \tilde{A}(z, \omega) e^{-i\omega t} d\omega. \quad (5.6)$$

Here $\tilde{A}(z, \omega)$ has been integrated over both positive and negative frequencies. In order to look more closely at what this means we can take a simple example of a real field (we consider real fields as our electromagnetic field is real). A cosine function is a real field which can be represented in the familiar form (with no z dependence for simplicity)

$$A(t) = \cos(\omega_0 t) = \frac{1}{2} (e^{-i\omega_0 t} + e^{i\omega_0 t}). \quad (5.7)$$



(a) Cosine function in the time domain



(b) Cosine function in the frequency domain

Figure 13: The cosine function in time and frequency space

The cosine function in the time domain is shown in figure 13(a). Applying the inverse Fourier transform we can find $\tilde{A}(\omega)$ which is a measure of the amount of frequency ω in the function $A(t)$. This leads to

$$\begin{aligned}\tilde{A}(\omega) &= \int_{-\infty}^{\infty} A(t) e^{+i\omega t} dt = \frac{1}{2} \int_{-\infty}^{\infty} \left(e^{i(-\omega_0 t + \omega t)} + e^{i(\omega_0 t + \omega t)} \right) dt \\ \tilde{A}(\omega) &= \frac{1}{2} (\delta(\omega - \omega_0) + \delta(\omega + \omega_0)).\end{aligned}\tag{5.8}$$

The result $\tilde{A}(\omega)$ is plotted in figure 13(b). The two delta functions lead to two frequency components of equal size at $\pm\omega_0$. Applying the same procedure to any real field will lead to a

similar result, a symmetric graph about $\omega = 0$. This demonstrates that any real field will have both positive and negative components. For a real field $A(z, t) = A^*(z, t)$, therefore from (5.6) $\tilde{A}(z, -\omega) = \tilde{A}^*(z, \omega)$. If we only consider positive frequencies then $\tilde{A}(z, \omega)$ contains all information about the field. However, the existence of NRR demonstrates that negative frequencies play a distinct physical role and cannot be neglected.

As stated above an electromagnetic wave is real (it has a real amplitude at all points) and therefore it contains both positive and negative frequency components. Another way of expressing this is to state that it contains both positive and negative norm components. To explain this in more detail - the electromagnetic wave must solve the relevant wave equation for the system under consideration. The norm is then the scalar product of a solution of the wave equation with itself defined by [149]

$$\langle \phi_1, \phi_2 \rangle = \frac{i}{2} \int (\pi_1^* \phi_2 - \phi_1^* \pi_2) dz. \quad (5.9)$$

Here ϕ_n are complex solutions to the wave equation, π_n are the corresponding conjugate momenta and z is the propagation distance parameter. For any solution ϕ_n , to a real wave equation the complex conjugate ϕ_n^* will also be a solution. It can be shown that ϕ_n and ϕ_n^* must have opposite sign norms [112]. Therefore when an electromagnetic wave is generated it will contain both a positive and a negative norm component. It is the language of norms rather than frequencies which is typically used in the field of analogue event horizons (see section 6).

As electromagnetic waves must always contain a positive and a negative frequency (norm) component, the existence of negative frequencies (norms) is not the important point. The challenge is to find a physical situation where a conversion occurs between positive and negative frequencies (norms). This has been observed in water wave experiments, two of which will be discussed later in this section. To the best of our knowledge NRR is the first example of such a conversion in optics. The conversion occurs because the positive frequency part of the soliton transfers energy to a phase matched negative frequency (NRR). Also the complex conjugate negative frequency part of the soliton transfers energy to the complex conjugate of the NRR with a positive frequency. Thus the NRR is a real valued field with a positive and a negative frequency part.

The existence of NRR is an interesting fact in its own right and it may also have implications

for amplification processes. These implications arise as, in quantum mechanics, positive frequencies are associated with annihilation operators and negative frequencies with creation operators [91]. Therefore under the correct conditions a process mixing positive and negative frequencies can lead to amplification. This will be seen in the discussion of a recent paper by Rubino et al. later in this section. If it is the quantum vacuum which is amplified this can be considered as a particle creation process [118]. This is not the case in all experiments mixing positive and negative frequencies. In some cases the mixing leads to a conversion between positive and negative frequencies with no amplification. An example of this will be seen in the second of two water wave experiments discussed below.

To provide more insight into negative frequencies, we now briefly consider two experiments using water waves in which they have been observed. In a 2008 paper by Rousseaux et al. [115], they show analytically that, in the moving frame, water waves can have a negative frequency. They consider a wave counter-propagating against a flowing medium with speed u . The phase φ of the wave will evolve as

$$\varphi = \int (kdx - \omega dt), \quad (5.10)$$

in the lab frame, where k and ω are the wavenumber and frequency respectively. It can be shown that in the frame co-moving with the medium the phase evolves as

$$\varphi' = \int (kdx' - \omega' dt'), \quad (5.11)$$

where x' and t' are the co-moving frame coordinates and $\omega' = \omega - uk$ is the Doppler shifted frequency in the co-moving frame. Therefore, as k and ω can be related by the dispersion formula of the medium, ω' can be expressed in terms of k only. They use the following dispersion relation for water waves

$$\omega'(k)^2 = gk \tanh(kh), \quad (5.12)$$

where g is the gravitational acceleration at the water surface and h is the height of the channel of water. From this they can find the allowed ω' and k values, which obey both the Doppler relation and (5.12). They find that for fixed ω there are multiple allowed values. Under certain conditions they show that there will be a negative k value with a corresponding negative ω' value. Thus a

positive lab frame frequency can have a negative co-moving frame frequency.

In their experiment these negative ω' waves will have a negative group velocity (compared to a positive group velocity for the original generated waves). Due to the way their water tank is set up they cannot initially generate propagating waves with a negative group velocity⁸. Therefore the negative ω' waves can only be produced via a mode-conversion from positive co-moving frame frequency waves. In the paper they show that such a conversion can occur at a water wave horizon (see section 6 for more details on horizons).

In their experiments they create a water wave horizon, where the speed of the flowing medium equals the group velocity of the counter propagating waves at a particular point. Using this they are able to observe the generation of waves with negative co-moving frame frequencies. This observation is possible because, as they show, such waves will have a negative slope dt/dx for their lines of constant phase φ . By filming the waves they are able to produce space time diagrams clearly showing this negative slope.

The second water wave experiment [149], is also focussed on the water wave analogue of an event horizon. In this paper they describe a measurement of stimulated Hawking emission (see section 6) in a water tank. The basic set up is similar to the previously described experiment. They use a water tank where the speed of the flow changes depending on the position along the tank. They generate counter-propagating, shallow waves, which at one point will have a group velocity equal to the flow velocity, this is then the horizon. They show that at this horizon the incoming waves will be converted into two outgoing waves (the stimulated Hawking emission), one with positive norm and the other with negative norm. In this case the norm is defined as in (5.9). The norm can be either positive, in which case it is linked to creation operators, or negative, in which case it is linked to annihilation operators. As mentioned previously, creation (annihilation) operators are associated with negative (positive) frequencies. Thus this experiment is another example of coupling between positive and negative frequencies. As stated previously in this section, the coupling here does not lead to amplification of the quantum vacuum (particle creation), rather it is a conversion process from one mode to two others.

As in our case, the motivation for both of the above papers arose from investigations into

⁸It must be noted that this is a practical issue and that such waves could be generated initially using a different setup

analogue event horizons, more of which will be discussed in the next section.

As NRR has been discovered only recently there is currently little in the literature related to the radiation. In the recently published, first paper related to NRR, it was shown to exist in two different experimental systems. The first system, for which I carried out the experiments, is in a PCF where the compression of ultra short IR pulses is used to drive the NRR [118]. The second system is a bulk calcium fluoride sample a few centimetres in length. An IR pulse of 60 fs duration is reshaped into a Bessel beam and propagated through the sample. The beam produces an optical filament which is able to drive both an RR and an NRR signal. This work was carried out by the group of Daniele Faccio. Both experiments produced results which agreed very well with phase matching predictions based on the dispersive properties of the different media used.

In many ways NRR is expected to behave similarly to RR. For example, its amplitude is also expected to depend on the overlap of the soliton spectrum with its phase matched wavelength. This was shown both analytically and numerically in a paper by Rubino [117]. As in the paper by Choudhary [28] they treat the driving soliton as a moving refractive index perturbation which will scatter light from within the soliton itself to the RR and NRR frequencies. In a paper by Kolesik et al. the RR was analysed using this treatment and the Born scattering approximation [79]. This allowed the amplitude of the RR to be calculated. Rubino and colleagues extend the approach to find an expression for the amplitude of the NRR.

The scattering approach calculates a scattering matrix \mathbf{S} which connects all input and output modes of a process. In this case the input mode is the driving soliton and the output modes are the RR and NRR. The scattering potential is the refractive index perturbation caused by the soliton. The number of photons in each mode can be found from the scattering matrix. They use a propagation equation known as the Uni-directional Pulse Propagation Equation (UPPE) [78] to calculate a form for the scattering matrix, which leads to the following amplitudes for the RR and NRR,

$$S(z, \omega_{RR}) \approx \frac{v}{2} \hat{R}(\omega_{RR} - \omega_{IN}), \quad (5.13)$$

$$S(z, \omega_{NRR}) \approx \frac{v}{2} \hat{R}(\omega_{NRR} + \omega_{IN}). \quad (5.14)$$

Here $S(z, \omega_{RR})$ and $S(z, \omega_{NRR})$ are the elements of the scattering matrix relating to the RR and NRR respectively, v is group velocity of the moving refractive index perturbation (moving with the

soliton), \hat{R} is the amplitude of the Fourier component of the moving index perturbation and ω_{RR} , ω_{NRR} and ω_{IN} are the frequencies of the RR, NRR and soliton respectively.

Equations (5.13) and (5.14) show that the amplitudes of the RR and NRR both depend on there being a component of the spectrum of the moving index perturbation (the soliton) at $\omega_{RR} - \omega_{IN}$ and $\omega_{NRR} + \omega_{IN}$ respectively.

This matches the previously known behaviour of RR. However the phase matched wavelength of NRR is considerably further from the input pulse than the RR wavelength. Therefore a much greater spectral broadening is required to drive it and the resulting signal is expected to be much weaker. Some of the experiments described in section 13.4 describe measurements of the expansion of the pulse spectrum into the UV. Such results indicate that it is feasible for the pulse to drive NRR.

Another interesting result from their analysis connects the RR and NRR photon numbers. They use a form of the Manley-Rowe relations, which use conservation of energy to calculate the amplitude of different frequencies in a non-linear system. Using these relations adapted for the case of a moving scattering potential they are able to show that the photon numbers for RR and NRR ($|\text{RR}|$ and $|\text{NRR}|$ respectively) are related by

$$|\text{RR}|^2 - |\text{NRR}|^2 = 1. \quad (5.15)$$

Here the photon number of the input soliton has been normalised to 1. This relation indicates that the total number of photons for RR and NRR will be greater than 1 so amplification will have occurred.

They verify their results numerically using the UPPE and find good agreement with the analytical predictions. Both RR and NRR form at the predicted frequencies. Some of their results are shown in figure 14 where the temporal and spectral evolution of the soliton and the driven RR and NRR are shown. In the first plot 14(a) the pulse temporally compresses and the RR and NRR form and then fall behind the pulse as they both have a lower group velocity. In the second plot 14(b) the pulse spectrum expands, over a distance of less than 0.5mm, and drives the RR and NRR, both at higher frequencies. The simulations use bulk glass rather than a PCF to generate a soliton-like pulse but the same qualitative behaviour will apply.

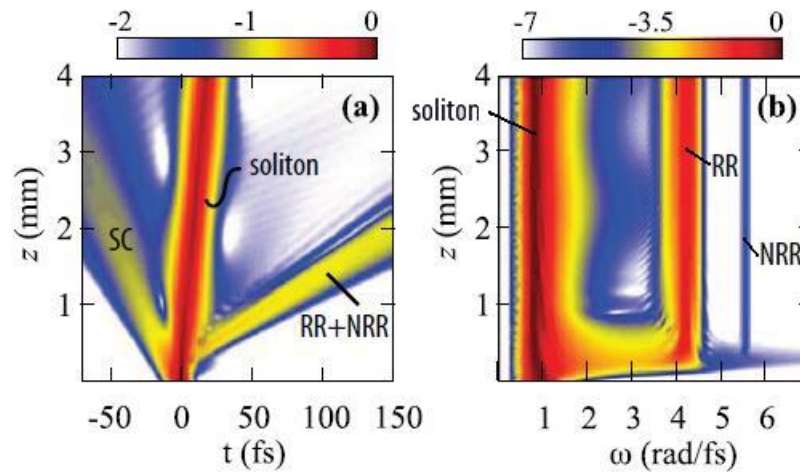


Figure 14: Figure taken from the paper by Rubino et al. [117] showing the numerically calculated temporal and spectral evolution of a soliton and the RR and NRR. Also shown is the supercontinuum (SC) (see section 4.1 for details). Image © 2012, Macmillan Publishers Limited. All rights reserved This work is licensed under a Creative Commons Attribution-NonCommercial-NoDerivs 3.0 Unported License. To view a copy of this license, visit <http://creativecommons.org/licenses/by-nc-nd/3.0/>. Labelling of the RR, NRR and soliton in figure (b) added by myself

They are also able to show numerically that it is possible to create a moving refractive index perturbation using a soliton and then scatter a weak probe into the RR and NRR modes. In this process the amplification mentioned above will occur.

Other recent work related to NRR includes two papers by Conforti et al. [92, 30]. In the first of these they seek to find theoretical support for the NRR experiments. One aim is to show that the signal attributed to NRR is not an example of radiation generated by backward propagating waves or due to FWM between the pulse and the RR. They develop an alternative envelope equation to the NLSE which can be used to find the NRR. As in the previously discussed paper they have the UPPE as a starting point. They use an envelope formation that superficially resembles that of the NLSE. However with the key difference that the slowly varying envelope approximation is not made (this approximation is discussed further in part II). Their formation splits the dynamics of the positive and negative frequency parts of the pulse spectrum. They find that positive and negative frequencies will interact via non-linear terms in their pulse propagation equation. They are able to derive the phase matching conditions for RR and NRR and find good agreement with simulation results based on pulses in bulk silica. As they start with the UPPE, which only allows

for waves propagating in one direction, it can be shown that the NRR is not radiation generated by a backwards propagating wave.

The second paper by Conforti et al. [30], describes negative frequency dispersive waves generated in quadratic media (media with second order non-linearity) via second harmonic generation. This is an important result as it shows that negative frequencies are a universal phenomenon, not restricted to media with third order non-linearities such as fibres. Another important feature of this work is that the negative frequency radiation is driven both by solitons, where dispersion and non-linearity balance each other, and by pulses in a spectral region where dispersion and non-linearity act to enforce each other. In the latter case the transfer of energy to dispersive radiation is triggered by the formation of an optical shock. An example of RR generated by pulses in a region where dispersion and non-linearity enforce each other (normal dispersion region of a PCF) has been shown recently [148], both numerically and experimentally. The Conforti paper shows numerically that NRR can also be generated from this type of pulse. As in the previous paper they use a form of the UPPE, for quadratic media, to carry out their simulations.

In this thesis some of the first experimental observations of NRR will be presented. Most of the rest of the experiments will then build on these results, looking into the conditions required for the generation of NRR. Different pulse parameters (mainly power and chirp) will be used to control and investigate the generation and evolution of the NRR.

6 Event horizon analogues

The final part of this literature review is devoted to the work on analogues of the event horizon with particular emphasis on the optical analogue of the event horizon. The work carried out in this thesis is part of a larger project of which one of the key aims is to measure the optical analogue of HR. As mentioned previously, the idea of negative frequencies came from this field. Additionally, in our experiments, the HR is predicted to lie in the UV close to the NRR wavelength. Many of the experimental results for the NRR highlight the experimental challenges in measuring UV radiation generated in our PCFs and also provide potential ways to overcome these challenges.

The connection between the experimental results in this thesis and the optical analogue of HR justifies the inclusion of a very brief introduction to analogue event horizons. The original research

into event horizons and HR arose from interest in black holes. These are astronomical objects which have collapsed to such a high density that their gravitational fields are strong enough to prevent the escape of light once it has passed over an event horizon surrounding the black hole. Such a body would be expected to only absorb radiation.

Interest in potential emission from black holes first arose from the publication of Hawking's theory in 1975 [133]. In this he showed theoretically that rather than only absorbing, a black hole could emit radiation (known as HR) as if it were a black body with a characteristic temperature T determined by the gradient of the gravitational field at the event horizon given by

$$T = \frac{\hbar c^3}{8\pi G M k_B}. \quad (6.1)$$

Here c is the speed of light in a vacuum, G is the universal gravitational constant, M is the mass of the black hole and k_B is the Boltzmann constant.

In a simplified picture the radiation occurs when spontaneous particle creation from the vacuum occurs near a black hole event horizon creating two particles. One particle can be trapped by the black hole gravitational field whilst the other is able to escape. The particles can no longer annihilate with one another thus the escaping particle can in theory be detected. A far away observer would measure the trapped particle as having negative energy in order to allow energy conservation. This is where the concept of negative frequencies arises from.

In practice the temperature of the black hole radiation is considerably lower than that of the cosmic microwave background. A stellar mass black hole has a mass of at least 10^{30} kg. Using (6.1) this gives a temperature of order nK compared to the cosmic microwave background temperature of about 3 K. Therefore measuring the radiation released from an astrophysical black hole is currently impossible and appears likely to remain so for at least the foreseeable future.

The phenomenon of HR is particularly interesting as in order to describe it quantum physics is required for spontaneous particle creation, general relativity is required as the temperature of the radiation in (6.1) is dependent on the surface gravity of the black hole and thermal physics is required for black body radiation. Thus a complete description may provide insights into the links between these areas. This consideration has motivated attempts to study HR through various analogue event horizon systems.

The field of event horizon analogues came into being in 1981 when Unruh proposed the idea for the first time in a ground breaking paper [143]. In this work he showed that the equations describing a black hole event horizon could also be used to describe a sonic horizon in a transsonic fluid flow. Thus a thermal spectrum of sound waves should be produced from such a horizon in analogy with HR.

This paper started a new field in physics which has expanded to encompass such diverse fields as water waves [149, 114], condensed matter [8], superconducting circuits [97] and optics [104, 41]. The uniting idea behind all event horizon analogues is to recreate some of the properties of an event horizon by creating a medium which travels at a velocity greater than the velocity of waves travelling within the medium.

In recent years the water wave experiments have been able to produce stimulated analogue HR [149] (this experiment was discussed in section 5.2) and a possible example of spontaneous HR has been observed in bulk optical materials [41]. The latter experiment uses a technique called ultra-short laser pulse filamentation to produce a moving refractive index perturbation in a bulk piece of glass which creates a white hole event horizon at the trailing edge of the pulse and a black hole event horizon at the leading edge. This idea is very similar to the optical fibre event horizon analogue proposed by Philbin et al. which will be discussed in detail at the end of this section. In both cases it is the gradient of the refractive index perturbation (caused by a pulse of light) which plays the role of the gradient of the gravitational field and therefore determines the temperature of the analogue HR.

The bulk optical materials experiment is interesting but it has been generally agreed to be inconclusive and it has been argued that the radiation observed does not fulfil all of the criteria to be considered spontaneous HR. I will briefly look at some of the key reasons for this as outlined in a comment on the paper by Schützhold and Unruh [123] and also at the reply to this comment by the authors of the paper [11]. This will give an overview of the requirements for a successful measurement of HR. The inclusion of this is justified as the work in this thesis is intended to assist in the further development of an experiment to measure the optical analogue of HR. As will be discussed in section 13 the results I have obtained provide insights into the dynamics of pulses in an optical fibre and in particular how their shape changes (through pulse compression). This is important as the shape of the pulse will determine the gradient of the refractive index perturbation

and therefore the temperature of the analogue HR. An understanding of how the pulse compresses should therefore allow accurate predictions of the expected temperature.

In the comment they set out five criteria for an experimental observation of the Hawking effect. The criteria are that the radiation produced is thermal, that it has a geometry dependent temperature, that the system is time independent, that at the black hole horizon a quasi exponential tearing apart (or squeezing in the case of the white hole event horizon) of wave packets leads to the production of the HR and finally that the part of the wave packet beyond the event horizon can have negative energy so that the other part can have positive energy.

The authors of the comment argue that the first four of the above criteria are not met. Firstly the system is not time independent because the pulse only lasts for a time that is shorter than a time scale set by the Hawking temperature. In the reply it is argued that the time scale is in fact several orders of magnitude shorter than the time for which the pulse filament exists and thus the system is time independent. Secondly there is no group velocity horizon (point where the group velocity of the photons under consideration changes from faster to slower than the group velocity of the pulse). Therefore there can be no tearing apart of the wave packet at the horizon. The reply argues that if the outgoing modes are traced back they can be seen to undergo the required phase divergence at the horizon and that a group velocity horizon is not necessary to produce Hawking radiation, a phase horizon is sufficient.

Thirdly in the comment it is pointed out that, as mentioned before, the temperature of the analogue HR will depend on the gradient of the change in the refractive index of the medium (induced by the ultra-short pulse). In the comment it is pointed out that the temperature of the measured signal is too high to be explained by a realistic estimate of the refractive index gradient. Likewise as the radiation is thermal the number of particles expected can be estimated from the Hawking temperature, the size of the horizon and the solid angle into which the radiation is emitted. Again realistic estimates of these quantities lead to an expected number of particles which is several orders of magnitude smaller than the number measured. In the reply it is argued that in a system with dispersion the analogue HR may not be a thermal emission and that if it is its temperature may not be related to the analogue of the gradient of the gravitational field. With regard to the number of particles detected it is argued that the differences between a stationary black hole and the experimental system mean that predictions based on the former are unlikely to be valid. They

cite two recent publications which predict numbers of HR photons similar or higher than their measurements in dispersive systems [54, 113].

As the above shows the field of analogue event horizons still contains many questions and there is considerable work to be done before a satisfactory measurement of spontaneous HR can be made.

The analogue system relevant to the results in this thesis uses PCFs. The idea was first proposed in 2008 by Philbin et al. [104]. As in the case of the bulk optical materials experiment this analogue differs from some other proposals in that rather than using a moving medium to create the event horizon, a pulse of light propagating through the medium temporarily changes the properties of the medium. Specifically a short high intensity laser pulse in a PCF will lead to an increased effective refractive index under the pulse. This means that the medium itself can be kept stationary whilst other modes propagating through the PCF will experience an effective moving medium.

Early experiments (described in [104]) using this system demonstrated that a probe beam propagating behind the intense pulse and with a higher velocity, would be slowed down as it approached the pulse by the increased refractive index. At a particular point its velocity would match that of the pulse and it would be prevented from entering the pulse. This is the time reverse of a black hole event horizon known as a white hole event horizon. The probe light would then undergo a wavelength shift as it effectively compressed against the horizon. This shift was measured and found to agree with theoretical predictions made in the supporting online material of the same paper.

In addition to the back of the pulse forming a white hole event horizon the front of the pulse forms a black hole event horizon. Both can potentially produce the optical analogue of HR by the scattering of vacuum modes from the optical event horizon [113]. The amplitude of the HR produced has been shown theoretically to depend critically on the steepness of the pulse forming the event horizon [113, 104].

The creation of photons (HR) occurs due to the mixing of positive and negative frequencies. As stated in section 5.2 an electromagnetic field will have a positive frequency component and a complex conjugate with a negative frequency. These correspond to annihilation and creation operators in quantum field theory. In the paper by Philbin et al. [104] they consider modes in the UV which will travel slower than the moving refractive index perturbation (created by the pulse) due to the shape of the PCF dispersion profile. Converting to the frame co-moving at the group

velocity of the pulse will lead to a frequency shift expressed by the Doppler formula

$$\omega' = \omega \left(1 - \frac{n(\omega)}{n_g} \right). \quad (6.2)$$

Here ω' represents the co-moving frame frequency, ω is the lab-frame frequency, $n(\omega)$ is the refractive index at frequency ω and n_g is the group index at the pulse frequency. The co-moving frame frequency will be negative if $n(\omega)$ is greater than n_g . The positive frequency component of the modes in the UV which are travelling slower than the pulse can therefore have a negative co-moving frame frequency. Similarly the negative frequency component of the UV modes can have a positive co-moving frame frequency.

Also (6.2) shows us that for every co-moving frame frequency ω' there can be two lab-frame frequencies with the opposite sign, one travelling faster than the pulse and the other slower. Mixing between positive and negative frequencies occurs because, whilst ω' is a conserved quantity for a stable pulse, it is possible for a conversion to occur between the two modes with opposite sign lab frame frequencies but the same ω' . This process can lead to amplification, either of occupied modes or of vacuum fluctuations if both modes are in their vacuum state.

As discussed previously NRR can also be described as the scattering of light from the event horizon [117]. However, the light which scatters comes from the pulse itself and scatters to a positive frequency (RR) and a negative frequency (NRR).

Therefore both phenomena (HR and NRR) involve a mixing between positive and negative frequencies. Thus the study of one may provide insights into the optical processes leading to the generation of the other and into the physical meaning of negative frequencies.

Additionally, as explained in section 5.2, the amplitude of the NRR will depend on the overlap of the pulse spectrum with its phase matched wavelength. One way to achieve the steep pulse required for HR and the broad spectrum needed for NRR is for the driving pulse to compress temporally. Therefore the experimental results described in section 12 relating to control and optimisation of pulse compression can be used to optimise the generation of both NRR and HR.

Part II

Theory

7 Introduction

Having outlined the history of research into soliton formation and propagation in optical fibres, and the different types of radiation that are driven by solitons, I now turn to a theoretical description of pulse propagation in a PCF. I start with the NLSE, the simplified equation governing the propagation of light in a fibre and the family of soliton solutions to this equation. I then describe the derivation of a more complete equation for pulse propagation, which removes some of the assumptions contained within the NLSE.

I show that both the NLSE, with higher order dispersion included and the more general pulse propagation lead to a phase matching condition for the transfer of energy from the soliton to dispersive radiation. I then focus on the PCFs used in the experiments. These all share a similar dispersion curve from which solutions to the phase matching condition are found. The shape of the curve leads to two solutions, one with a positive frequency (RR) and the other with a negative frequency (NRR).

The theory in this section is for the most part well known and is presented here for completeness. The most important part of this section is the NRR, as mentioned previously we have for the first time discovered a coupling between positive and negative frequencies in optics. The PCF dispersion curves presented in section 10 will show clearly where this coupling comes from.

8 The NLSE

The derivation of the NLSE starting from Maxwell's equations is well known and presented in many excellent books [2, 18]. For reference a detailed derivation is presented in the appendix in section 15. This outlines the assumptions made during the derivation. One key assumption is that the pulse can be separated into a rapidly varying part and a slowly varying envelope (the slowly varying envelope approximation), this is not valid for short pulses.

The NLSE does not take into account higher order effects in the fibre. These include higher order dispersion (β_3 and higher) and higher order non-linear effects such as self-steepening and Raman scattering. If these effects are negligible then a pulse coupled into the fibre will under the right conditions form a fundamental or higher order soliton. Solitons are exact solutions to the NLSE

and occur due to the balance of dispersion and non-linearity. The higher order effects mentioned above will be negligible for long pulses where the peak pulse power is low reducing the effect of non-linearities and the pulse spectral width is narrow reducing the effect of higher order dispersion. A pulse of approximately pico-second length or longer can be considered to obey the NLSE [2] and will form a soliton which would propagate with unchanged shape and velocity (fundamental soliton) or undergo a periodic evolution (higher order soliton). These soliton solutions cannot couple to dispersive radiation such as RR and NRR and therefore they cannot lose energy to such radiation.

In this section I begin by presenting the NLSE, then outline its soliton solutions and explain how dispersion and non-linearity combine to influence the evolution of fundamental and higher order solitons. I then show how the NLSE can be modified to include higher order effects and finally I focus on the effect of higher order dispersion to show how the soliton can transfer energy to dispersive radiation.

One form of the NLSE is

$$\frac{\partial A(\xi, T)}{\partial \xi} + \frac{i\beta_2}{2} \frac{\partial^2 A(\xi, T)}{\partial T^2} - i\gamma |A(\xi, T)|^2 A(\xi, T) = 0, \quad (8.1)$$

where A represents the amplitude of the electric field of the pulse, β_2 is the second order dispersion parameter or GVD parameter, γ is the non-linear parameter, T is the time co-ordinate in a frame co-moving with the pulse and $\xi = z/L_D$ is a dimensionless form of the propagation distance along the fibre axis where $L_D = T_0^2/|\beta_2|$ is the dispersion length and T_0 is the initial width of the pulse at e^{-1} of the maximum pulse intensity.

The non-linear parameter is due to the non-linear contribution to the refractive index. The total index can be expressed as $\tilde{n} = n + n_2 |E|^2$, where n is the linear refractive index and $n_2 |E|^2$ is the non-linear part. The non-linear parameter is given by

$$\gamma = \frac{n_2 \omega_0}{c A_{\text{eff}}}, \quad (8.2)$$

where ω_0 is the central frequency of the pulse and A_{eff} is a measure of the area of the mode formed by the light in the fibre.

8.1 Soliton solutions of the NLSE

In this section I will briefly outline the fundamental and higher order soliton solutions to the NLSE presented in the previous section.

The NLSE in (8.1) can be solved by means of the inverse scattering method [153]. Solitons are one family of solutions which can be found using this method. They occur due to a balance between the dispersion represented by β_2 and the non-linearity represented by γ . The fundamental soliton has the form

$$A(\xi, T) = \sqrt{P_0} \operatorname{sech}\left(\frac{T}{T_0}\right) e^{i\gamma P_0 \xi/2}, \quad (8.3)$$

where P_0 is the peak power of the soliton. As it propagates the soliton will gain a ξ dependent phase but its shape will remain the same over any propagation distance.

Whether a pulse forms a fundamental or a higher order soliton will depend on the pulse peak power and width as well as the fibre dispersion and non-linearity. The order N of the soliton was previously defined in (2.1) in terms of L_D the dispersion length defined in section 8 and $L_{NL} = (\gamma P_0)^{-1}$ the non-linear length. They represent respectively the propagation distances over which dispersive and non-linear effects are significant. The peak power is defined by $P_0 = P_{av}/T_0\nu$, where P_{av} is the average power of the input beam and ν is the repetition rate of the laser. N is then defined as

$$N^2 = \frac{\gamma P_0 T_0^2}{|\beta_2|}. \quad (8.4)$$

If the input pulse has a hyperbolic secant shape and suitable peak power and pulse length for N to equal 1, a fundamental soliton will form. If the value of N for the input pulse is less than 1 but greater than 0.5 a soliton will still form but the pulse will first broaden in time, if N is greater than 1 but less than 1.5 then the pulse will first narrow then form a soliton [2]. In both cases the pulse will lose energy as it broadens or narrows. Similarly if the input pulse has small deviations from the hyperbolic secant shape it will still evolve into a soliton after a certain propagation distance which will depend on the exact shape of the input pulse.

Higher order solitons will form if $N > 1.5$. As in the case of the fundamental soliton for non-

integer initial values of N and initial pulse shapes that deviate slightly from a hyperbolic secant, the pulse will evolve until it reaches the form of a soliton, losing energy as it does so.

8.2 Soliton evolution

In this section the stable (fundamental solitons) or periodic (higher order solitons) evolution of solitons is discussed. With a particular focus on soliton compression, which plays an important role in the generation of many types of radiation from solitons.

As discussed previously in the NLSE there are two main influences on pulses propagating in a fibre. These are dispersion governed by β_2 and non-linearity governed by γ . In many cases only one needs to be considered as its effects will be significant over a much shorter propagation distance than the other. The distances over which non-linearity and dispersion are significant are quantified by the previously defined non-linear length L_{NL} and dispersive length L_D . If L_{NL} and L_D are of the same order then non-linearity and dispersion must be considered to act together. This leads to complicated pulse evolution and in order to show the effects clearly I will initially consider each on its own and then in combination..

Non-linear effects will be most significant for short, high peak power pulses. The primary effect is SPM, this adds an extra intensity dependent phase to the electric field, thus changing the instantaneous frequency across the pulse generating low frequencies at the front of the pulse and high frequencies at the back. The pulse temporal length remains the same but the spread of frequencies increases broadening the pulse spectrum.

In the absence of dispersion we can see the effect of SPM by considering (8.1) without the β_2 term

$$\frac{\partial A(\xi, T)}{\partial \xi} - i\gamma |A(\xi, T)|^2 A(\xi, T) = 0. \quad (8.5)$$

Following the approach in Agrawal [2], this can be solved using $A(\xi, T) = V \exp(i\phi_{NL})$, where V and ϕ_{NL} are both real

$$\frac{\partial V e^{i\phi_{NL}}}{\partial \xi} - i\gamma |V e^{i\phi_{NL}}|^2 V e^{i\phi_{NL}} = 0. \quad (8.6)$$

Equating the real and imaginary parts leads to

$$\frac{\partial V}{\partial \xi} = 0, \quad (8.7)$$

$$\frac{\partial \phi_{NL}}{\partial \xi} = \gamma V^2. \quad (8.8)$$

Equation (8.7) tells us that the amplitude V does not change as the pulse propagates, hence the phase will be given by $\phi_{NL} = \gamma V^2 \xi = \gamma |A(0, T)|^2 \xi$ and the pulse amplitude at a propagation distance ξ by

$$A(\xi, T) = |A(0, T)| e^{i\phi_{NL}(\xi, T)}. \quad (8.9)$$

The effect of SPM is therefore to keep the shape of the pulse the same but to introduce a phase shift which is dependent on the pulse intensity. As the phase shift is time dependent it will vary across the pulse and therefore so will the instantaneous frequency. The difference between the instantaneous frequency and the central pulse frequency is given by[2]

$$\delta\omega = -\frac{\partial \phi_{NL}}{\partial T} = -\gamma \xi \frac{\partial}{\partial T} |A(0, T)|^2. \quad (8.10)$$

This shows that SPM generates new frequencies continually as the pulse propagates. For the case of a hyperbolic secant pulse $\delta\omega$ will be positive at the trailing edge of the pulse generating higher frequencies and negative at the front edge of the pulse generating lower frequencies.

Having seen that SPM will generate new frequencies without changing the pulse shape, we now consider how dispersion will affect the pulse. If non-linearity is negligible then (8.1) becomes

$$\frac{\partial A(\xi, T)}{\partial \xi} + \frac{i\beta_2}{2} \frac{\partial^2 A(\xi, T)}{\partial T^2} = 0. \quad (8.11)$$

Following the approach of Agrawal [2] we Fourier transform this equation using

$A(\xi, T) = (1/2\pi) \int_{-\infty}^{\infty} \tilde{A}(\xi, \omega) \exp(-i\omega T) d\omega$ leading to

$$\frac{\partial \tilde{A}(\xi, \omega)}{\partial \xi} + \frac{i\beta_2}{2} (-i\omega)^2 \tilde{A}(\xi, \omega) = 0. \quad (8.12)$$

This is solved by

$$\tilde{A}(\xi, \omega) = \tilde{A}(0, \omega) e^{\frac{i}{2}\beta_2\omega^2\xi}. \quad (8.13)$$

Hence as the pulse propagates each spectral component will gain a frequency dependent phase, this keeps the spectrum of the pulse constant whilst changing the pulse shape [2].

A solution to (8.11) can be found by taking the inverse Fourier transform of (8.13) however the calculations are not simple for the case of a soliton (hyperbolic secant pulse shape). The main result is that as the pulse propagates it develops a time dependent phase. As discussed for SPM, this means that the instantaneous frequency varies across the pulse. Similarly to the SPM case the difference between the instantaneous frequency and the central pulse frequency will increase as the pulse propagates. The difference with the SPM case is that new frequencies are not generated, rather the existing frequencies spread further in time because they all propagate at different speeds. We are interested in the case of anomalous dispersion ($\beta_2 < 0$), as in order for solitons to form the input pulse must lie in this spectral region. In this case it can be shown that due to GVD low frequencies will propagate slower than high frequencies causing the pulse to broaden in time.

We will now consider the combined effect of SPM and GVD. If SPM is not negligible then it will generate high frequencies at the back of the pulse and low frequencies at the front. Anomalous GVD will act by slowing the low frequencies relative to the high frequencies.

For fundamental solitons we have $N = 1$ and the non-linear and dispersive lengths are equal. In this case the pulse shape will remain the same over any propagation distance as GVD and SPM are balanced. The change in the instantaneous frequency due to SPM will be cancelled by the change in instantaneous frequency due to GVD. Overall there will be no change in the spectrum of the pulse.

For a higher order soliton N will be greater than 1 and L_{NL} will be shorter than L_D , hence SPM will initially be the most significant effect. In very basic terms, new frequencies will be generated causing the pulse spectrum to broaden. As the pulse propagates further the effect of dispersion will cause the pulse to temporally contract as the different frequencies in the broadened spectrum propagate at different speeds. As the pulse contracts the peak power increases and the effect of SPM also increases. This leads to a periodic evolution of the soliton where the pulse temporally contracts and expands and correspondingly its spectrum broadens and narrows.

8.3 Higher order effects

As discussed previously the NLSE in (8.1) does not include higher order dispersion and higher order non-linearities. It is these effects which lead to the different phenomena described in section 4 (i.e. supercontinuum generation, THG, FWM, RR and NRR). They destabilise the soliton solutions to the NLSE and allow different types of radiation to be generated. In the case of higher order solitons, instabilities due to higher order effects act to break up the pulse into its constituent fundamental solitons.

The key higher order effects in fibres are higher order dispersion, self-steepening and Raman scattering. These effects only become significant for short pulses where the peak power is high and the spectral width is broad. The latter two were discussed briefly in section 4.1, the former is quantified by the dispersion parameters β_n , $n > 2$, defined in (5.1). As was explained in section 5 it is the higher order dispersion which is responsible for the transfer of energy from the soliton to RR and NRR.

The NLSE given in (8.1) can be modified to include each of the above mentioned higher order effects [2]

$$\frac{\partial A}{\partial \xi} + i \frac{\beta_2}{2} \frac{\partial^2 A}{\partial T^2} - i \gamma |A|^2 A = \sum_{n \geq 3} \frac{i \beta_n}{n!} \left(\frac{i \partial}{\partial T} \right)^n A - \frac{1}{\omega_0} \frac{\partial}{\partial T} (\gamma |A|^2 A) - i T_R \gamma A \frac{\partial |A|^2}{\partial T}. \quad (8.14)$$

Here for the sake of clarity we have omitted the parameters (ξ, T) in $A = A(\xi, T)$. The derivation of the above equation is explained in detail in the book by Agrawal [2] and will not be presented here. Many of the key steps are similar to those which will be included in the derivation of the more complete pulse propagation equation in section 9.

The first term on the RHS of (8.14) represents higher order dispersion, the second self-steepening and the third Raman scattering (T_R is a measure of the size of the Raman scattering effect). As we are particularly interested in RR and NRR it is the dispersion term that is of most interest and this will be discussed in the next section. The self-steepening term arises from the intensity dependence of the refractive index of the medium. As explained in section 4.1 this causes the peak of the pulse to shift towards the trailing side creating a steep edge and can lead to the break-up

of higher order solitons. Raman scattering is due to the non-instantaneous, non-linear response of a medium to the light pulses propagating through it. As explained in section 4.1 this results in a shifting of the pulse towards longer wavelengths, which helps to create the long wavelength side of the supercontinuum.

8.4 Higher order dispersion leading to Resonant Radiation

In this section I will focus on the effect of higher order dispersion on solitons and how this leads to a transfer of energy to RR when the following phase matching condition is met

$$\sum_{n \geq 2} \frac{\beta_n}{n!} (\omega_{RR} - \omega_S)^n = \frac{(2N - 1)^2 \gamma P_0}{2N^2}. \quad (8.15)$$

Here ω_{RR} and ω_S are the RR and soliton angular frequencies respectively. The procedure is well established and can be found in different forms in many of the papers mentioned in section 5, it is presented here for reference.

The higher order dispersion will destabilise a soliton and lead to the transfer of energy to dispersive radiation. In order to show this I will start with (8.14) and set the effects of self-steepening and Raman scattering to zero in order to simplify the analysis

$$\frac{\partial A}{\partial \xi} + i \frac{\beta_2}{2} \frac{\partial^2 A}{\partial T^2} - i \gamma |A|^2 A = \sum_{n \geq 3} \frac{i \beta_n}{n!} \left(\frac{i \partial}{\partial T} \right)^n A. \quad (8.16)$$

If the RHS is set to zero then the soliton is a solution to the above equation. The size of the RHS term depends on the dispersion profile of the fibre, far from the ZDW of a fibre the higher order dispersion coefficients are typically small compared to β_2 , and the term can be treated as a small perturbation. In this case the effect of higher order dispersion can be found by substituting into the above equation the soliton solution with an additional, small dispersive wave (a dispersive wave is a non-stationary wave i.e. not a soliton),

$$A(\xi, T) = A_s(\xi, T) + a(\xi, T), \quad (8.17)$$

where $A_s(\xi, T)$ is the fundamental soliton defined in (8.3) and a is the small dispersive wave. Here

the assumption is made that the dispersive wave has a negligible affect on the soliton hence the unperturbed form is used. This leads to

$$\frac{\partial A_s}{\partial \xi} + \frac{\partial a}{\partial \xi} + i\frac{\beta_2}{2} \frac{\partial^2 A_s}{\partial T^2} + i\frac{\beta_2}{2} \frac{\partial^2 a}{\partial T^2} - i\gamma |A_s + a|^2 (A_s + a) = \sum_{n \geq 3} \frac{i\beta_n}{n!} \left(\frac{i\partial}{\partial T} \right)^n (A_s + a). \quad (8.18)$$

As the soliton is a solution to the original NLSE several terms cancel,

$$\begin{aligned} \frac{\partial a}{\partial \xi} + i\frac{\beta_2}{2} \frac{\partial^2 a}{\partial T^2} - \left(i\gamma A_s a^* + i\gamma A_s^* a + i\gamma |a|^2 \right) (A_s + a) - i\gamma |A_s|^2 a \\ = \sum_{n \geq 3} \frac{i\beta_n}{n!} \left(\frac{i\partial}{\partial T} \right)^n (A_s + a). \end{aligned} \quad (8.19)$$

Assuming that the dispersive wave will be small we can linearise in a ,

$$\frac{\partial a}{\partial \xi} + i\frac{\beta_2}{2} \frac{\partial^2 a}{\partial T^2} - i\gamma A_s^2 a^* - 2i\gamma |A_s|^2 a = \sum_{n \geq 3} \frac{i\beta_n}{n!} \left(\frac{i\partial}{\partial T} \right)^n (A_s + a). \quad (8.20)$$

We then insert the form of the fundamental soliton

$$\begin{aligned} \frac{\partial a}{\partial \xi} + i\frac{\beta_2}{2} \frac{\partial^2 a}{\partial T^2} - i\gamma P_0 \operatorname{sech}^2 \left(\frac{T}{T_0} \right) \left(e^{i\gamma P_0 \xi/2} a^* + 2a \right) \\ = \sum_{n \geq 3} \frac{i\beta_n}{n!} \left(\frac{i\partial}{\partial T} \right)^n \left(\sqrt{P_0} \operatorname{sech} \left(\frac{T}{T_0} \right) e^{i\gamma P_0 \xi/2} + a \right). \end{aligned} \quad (8.21)$$

This is then Fourier transformed using $a(\xi, T) = (1/2\pi) \int_{-\infty}^{\infty} \tilde{a}(\xi, \omega - \omega_s) \exp(-i(\omega - \omega_s)T) d\omega$ and the Fourier transform of the hyperbolic secant

$$\begin{aligned} \frac{\partial \tilde{a}(\xi, \omega - \omega_s)}{\partial \xi} - i\frac{\beta_2}{2} (\omega - \omega_s)^2 \tilde{a}(\xi, \omega - \omega_s) - (2\pi) F.T.:T \rightarrow \omega \left[i\gamma P_0 \operatorname{sech}^2 \left(\frac{T}{T_0} \right) \left(e^{i\gamma P_0 \xi/2} a^* + 2a \right) \right] \\ = \sum_{n \geq 3} (-i(\omega - \omega_s))^n \frac{i\beta_n}{n!} i^n \left(e^{i\gamma P_0 \xi/2} T_0 \sqrt{P_0} \pi \operatorname{sech} \left(\frac{\pi}{2} T_0 (\omega - \omega_s) \right) + \tilde{a}(\xi, \omega - \omega_s) \right). \end{aligned} \quad (8.22)$$

And further Fourier transformed using $\tilde{a}(\xi, \omega) = \int_{-\infty}^{\infty} \hat{a}(k, \omega) \exp(ik\xi) dk$ and the Fourier transform

of the ξ dependent part of the soliton $\exp(i\gamma P_0 \xi/2)$,

$$\begin{aligned}
& ik\hat{a}(k, \omega - \omega_s) - \sum_{n \geq 2} (\omega - \omega_s)^n \frac{i\beta_n}{n!} \hat{a}(k, \omega - \omega_s) \\
&= F.T.\xi \rightarrow k \left\{ 2\pi F.T \left[i\gamma P_0 \operatorname{sech}^2 \left(\frac{T}{T_0} \right) \left(e^{i\gamma P_0 \xi/2} a^* + 2a \right) \right] \right\} \\
&+ \sum_{n \geq 3} (\omega - \omega_s)^n \frac{i\beta_n}{n!} \left(T_0 \sqrt{P_0} \pi \operatorname{sech} \left(\frac{\pi}{2} T_0 (\omega - \omega_s) \right) \delta \left(k - \frac{\gamma P_0}{2} \right) \right). \tag{8.23}
\end{aligned}$$

We rearrange to find an expression for $\hat{a}(k, \omega - \omega_s)$

$$\begin{aligned}
\hat{a}(k, \omega - \omega_s) &= \frac{2\pi F.T \left\{ F.T \left[i\gamma P_0 \operatorname{sech}^2 \left(\frac{T}{T_0} \right) \left(e^{i\gamma P_0 \xi/2} a^* + 2a \right) \right] \right\}}{\left(ik - \sum_{n \geq 2} (\omega - \omega_s)^n \frac{i\beta_n}{n!} \right)} \\
&+ \frac{\sum_{n \geq 3} (\omega - \omega_s)^n \frac{i\beta_n}{n!} \left(T_0 \sqrt{P_0} \pi \operatorname{sech} \left(\frac{\pi}{2} T_0 (\omega - \omega_s) \right) \delta \left(k - \frac{\gamma P_0}{2} \right) \right)}{\left(ik - \sum_{n \geq 2} (\omega - \omega_s)^n \frac{i\beta_n}{n!} \right)}. \tag{8.24}
\end{aligned}$$

As an approximation we can assume that the terms in the numerator of the first fraction on the RHS are small. These terms will play a role in the phase matching however they amount to only a small shift in the phase matched wavelength under the soliton [3]

$$\hat{a}(k, \omega - \omega_s) = \frac{\sum_{n \geq 3} (\omega - \omega_s)^n \frac{i\beta_n}{n!} \left(T_0 \sqrt{P_0} \pi \operatorname{sech} \left(\frac{\pi}{2} T_0 (\omega - \omega_s) \right) \delta \left(k - \frac{\gamma P_0}{2} \right) \right)}{\left(ik - \sum_{n \geq 2} (\omega - \omega_s)^n \frac{i\beta_n}{n!} \right)}. \tag{8.25}$$

The dispersive wave $\hat{a}(k, \omega - \omega_s)$ will be large when the denominator on the RHS is zero, this leads to the phase matching condition

$$ik - \sum_{n \geq 2} (\omega - \omega_s)^n \frac{i\beta_n}{n!} = 0, \tag{8.26}$$

where from the delta function in the numerator of (8.25) we can see that $k = \gamma P_0/2$. This can be rearranged to the form of (8.15) with $N = 1$,

$$\sum_{n \geq 2} \frac{\beta_n}{n!} (\omega - \omega_s)^n = \frac{\gamma P_0}{2}. \tag{8.27}$$

A similar procedure using higher order solitons rather than the fundamental soliton will produce

the phase matching condition for $N > 1$.

Thus we have seen that by including higher order dispersion in the NLSE we can find the phase matching condition for the transfer of energy from a soliton to a dispersive wave. Equation (8.25) shows that the radiation is driven by the effect of higher order dispersion on the original soliton. It also shows that the amplitude of the radiation depends on the amplitude of the soliton at the phase matched frequency. Therefore the solutions to the phase matching condition will depend critically on pulse compression and the corresponding spectral expansion.

9 A more detailed pulse propagation equation

In the derivation of the NLSE a number of assumptions are made which limit the applicability of the equation. In particular the slowly varying envelope approximation means that its use is limited when considering short pulses ($T < 1$ ps). In this section an alternative derivation will be used to reach a less aesthetically pleasing but more representative equation. The exact form of the equation is new but the approach is similar to other methods such as the UPPE [117, 92] and the Forward Maxwell equations [62], which derive pulse propagation equations starting from Maxwell's equations. The situation we are considering is that of a short pulse propagating through a PCF.

The starting point is the same as for the NLSE and the final result will yield the same phase matching condition for dispersive waves as in section 8.4 thus showing that the analysis leading to a predicted new solution (NRR) of the phase matching condition is robust. Many of the steps are similar to those in the NLSE and they are presented in more detail in appendix 15.

We start with the wave equation derived from Maxwell's equations in an isotropic, homogeneous medium at rest

$$\nabla(\nabla \cdot \mathbf{E}) + \nabla^2 \mathbf{E} = \frac{1}{c^2} \frac{\partial^2 \mathbf{E}}{\partial t^2} + \frac{1}{\varepsilon_0 c^2} \frac{\partial^2 \mathbf{P}}{\partial t^2}, \quad (9.1)$$

where $\mathbf{E}(\mathbf{r}, t)$ is the electric field vector of the pulse, $\mathbf{P}(\mathbf{r}, t)$ is the induced electric polarisation and ε_0 is the vacuum permittivity. The electric field of the pulse causes the electrons in the fibre material to re-distribute creating a net charge density which gives rise to the induced electric polarisation

which contributes to the overall electric flux in the fibre \mathbf{D} ,

$$\mathbf{D} = \varepsilon_0 \mathbf{E} + \mathbf{P}. \quad (9.2)$$

The term $\nabla \cdot \mathbf{E}$ represents the free and bound charge densities in the medium, the former is identically zero in a fibre and the latter we assume to be negligible. It actually depends on the non-linear response of the medium to the electric field. As discussed in the appendix this will be considerably smaller than the linear response. This simplifies the wave equation to

$$\nabla^2 \mathbf{E} = \frac{1}{c^2} \frac{\partial^2 \mathbf{E}}{\partial t^2} + \frac{1}{\varepsilon_0 c^2} \frac{\partial^2 \mathbf{P}}{\partial t^2}. \quad (9.3)$$

In order to solve the wave equation we need to find a representation for the induced polarisation in terms of the electric field. We start by separating \mathbf{P} into a linear and a non-linear part

$$\mathbf{P} = \mathbf{P}_L + \mathbf{P}_{NL}. \quad (9.4)$$

The linear part can be expressed as (see the appendix for further details)

$$\mathbf{P}_L(\mathbf{r}, t) = \varepsilon_0 \int_{-\infty}^{\infty} \chi^{(1)}(t - t_1) \cdot \mathbf{E}(\mathbf{r}, t_1) dt_1, \quad (9.5)$$

where $\chi^{(1)}$ is the first order susceptibility and $\chi^{(1)}(t - t_1) = 0$ for $t < t_1$. We have assumed that the response of the medium to the electric field is local i.e. the induced polarisation at position \mathbf{r} is influenced only by the electric field at position \mathbf{r} . The above equation does not however assume an instantaneous response, the field at time t_1 can affect the polarisation at a later time t . If we assume that there is no loss in the fibre then the Fourier transform of the first order susceptibility can be expressed as $\tilde{\chi}^{(1)}(\omega) = n^2(\omega) - 1$, where $n(\omega)$ is the linear part of the medium refractive index [2].

The non-linear part of the induced polarisation can be expressed as

$$\begin{aligned} \frac{\mathbf{P}_{NL}(\mathbf{r}, t)}{\varepsilon_0} = & \int_{-\infty}^{\infty} \int_{-\infty}^{\infty} \chi^{(2)}(t-t_1, t-t_2) \mathbf{E}(\mathbf{r}, t_1) \mathbf{E}(\mathbf{r}, t_2) dt_1 dt_2 \\ & + \int_{-\infty}^{\infty} \int_{-\infty}^{\infty} \int_{-\infty}^{\infty} \chi^{(3)}(t-t_1, t-t_2, t-t_3) \mathbf{E}(\mathbf{r}, t_1) \mathbf{E}(\mathbf{r}, t_2) \mathbf{E}(\mathbf{r}, t_3) dt_1 dt_2 dt_3 + \dots, \end{aligned} \quad (9.6)$$

where $\chi^{(n)}$ are the higher order susceptibilities and again we have assumed locality. In a centrosymmetric system such as a fibre the $\chi^{(2)}$ term will be zero and the size of the susceptibilities will decrease as the order increases (see appendix 15 for more explanation of both of these points). Therefore we take into account only the third order susceptibility term. As a simplification we treat the medium response as instantaneous, leading to

$$\mathbf{P}_{NL}(\mathbf{r}, t) = \varepsilon_0 \chi^{(3)}(t) \mathbf{E}(\mathbf{r}, t) \mathbf{E}(\mathbf{r}, t) \mathbf{E}(\mathbf{r}, t). \quad (9.7)$$

If we again assume that there is no loss in the fibre then the Fourier transform of the third order susceptibility can be expressed as $\tilde{\chi}^{(3)}(\omega) = 8nn_2/3$, where n_2 is the non-linear part of the medium refractive index. The total refractive index is $\tilde{n} = n + n_2 |E|^2$ [2].

We now use a separation of variables approach and express the electric field in terms of a transverse component $F(x, y)$ and a component $\mathbf{A}(z, t)$ depending on time and position along the axis of the fibre, $\mathbf{E}(\mathbf{r}, t) = F(x, y) \mathbf{A}(z, t)$. We assume that the electric field and the induced polarisation are linearly polarized and remain so during propagation and therefore we can re-write (9.3) as

$$\frac{\partial^2 A}{\partial z^2} = \frac{1}{c^2} \frac{\partial^2 A}{\partial t^2} + \frac{1}{c^2} \frac{\partial^2}{\partial t^2} \int_{-\infty}^{\infty} \chi^{(1)}(t-t_1) A(z, t_1) dt_1 + \frac{1}{c^2} \frac{\partial^2}{\partial t^2} \chi^{(3)}(t) A(z, t)^3. \quad (9.8)$$

Where we have separated the wave equation into an equation for $A(z, t)$ and an equation for $F(x, y)$ and only considered the $A(z, t)$ equation. The equation for $F(x, y)$ allows the modal distribution of the light to be found.

In order to simplify the above equation we would like to remove the integral. This is achieved

using convolution theorem

$$\begin{aligned} \int_{-\infty}^{\infty} \chi^{(1)}(t-t_1) A(z, t_1) dt_1 &= \int_{-\infty}^{\infty} \tilde{\chi}^{(1)}(\omega) \tilde{A}(z, \omega) e^{-i\omega t} d\omega \\ \Rightarrow \int_{-\infty}^{\infty} \chi^{(1)}(t-t_1) A(z, t_1) dt_1 &= \int_{-\infty}^{\infty} (n(\omega)^2 - 1) \tilde{A}(z, \omega) e^{-i\omega t} d\omega. \end{aligned} \quad (9.9)$$

Inserting the above into (9.8) we obtain

$$\frac{\partial^2 A}{\partial z^2} = \frac{1}{c^2} \frac{\partial^2 A}{\partial t^2} + \frac{1}{c^2} \int_{-\infty}^{\infty} (n^2(\omega) - 1) \tilde{A}(z, \omega) (-i\omega)^2 e^{-i\omega t} d\omega + \frac{1}{c^2} \frac{\partial^2}{\partial t^2} \chi^{(3)}(t) A(z, t)^3. \quad (9.10)$$

We use the propagation constant $\beta(\omega)$ to obtain

$$\begin{aligned} \frac{\partial^2 A}{\partial z^2} &= \frac{1}{c^2} \frac{\partial^2 A}{\partial t^2} + \frac{1}{c^2} \int_{-\infty}^{\infty} \tilde{A}(z, \omega) \omega^2 e^{-i\omega t} d\omega - \int_{-\infty}^{\infty} \beta^2(\omega) \tilde{A}(z, \omega) e^{-i\omega t} d\omega \\ &\quad + \frac{1}{c^2} \frac{\partial^2}{\partial t^2} \chi^{(3)}(t) A^3(z, t). \end{aligned} \quad (9.11)$$

And expand the propagation constant in a Taylor series around a frequency ω_0 (the central frequency of the pulse)

$$\begin{aligned} \frac{\partial^2 A}{\partial z^2} - \frac{1}{c^2} \frac{\partial^2 A}{\partial t^2} + \frac{1}{c^2} \int_{-\infty}^{\infty} \tilde{A}(z, \omega) \frac{\partial^2}{\partial t^2} e^{-i\omega t} d\omega \\ = - \int_{-\infty}^{\infty} \left(\sum_{n=0}^{\infty} \frac{\beta_n}{n!} (\omega - \omega_0)^n \right)^2 \tilde{A}(z, \omega) e^{-i\omega t} d\omega + \frac{1}{c^2} \frac{\partial^2}{\partial t^2} \chi^{(3)}(t) A^3(z, t), \end{aligned} \quad (9.12)$$

where $\beta_n = (\partial^n \beta / \partial \omega^n)_{\omega=\omega_0}$. The integrals can now be removed

$$\frac{\partial^2 A}{\partial z^2} - \frac{1}{c^2} \frac{\partial^2 A}{\partial t^2} + \frac{1}{c^2} \frac{\partial^2}{\partial t^2} A = - \left(\sum_{n=0}^{\infty} \frac{\beta_n}{n!} \left(i \frac{\partial}{\partial t} \right)^n \right)^2 A + \frac{1}{c^2} \frac{\partial^2}{\partial t^2} \chi^{(3)}(t) A(z, t)^3. \quad (9.13)$$

Resulting in the equation

$$\frac{\partial^2 A}{\partial z^2} + \left(\sum_{n=0} \frac{\beta_n}{n!} \left(i \frac{\partial}{\partial t} \right)^n \right)^2 A = \frac{1}{c^2} \frac{\partial^2}{\partial t^2} \chi^{(3)}(t) A(z, t)^3. \quad (9.14)$$

We note that the electric field is a real field and both $\beta(\omega)$ and $\chi^{(3)}$ are also real. We chose to represent the field A in the following way

$$A(z, t) = \frac{1}{2\sqrt{A_{\text{eff}}}} (U(z, t) + U^*(z, t)). \quad (9.15)$$

Where the real part of the complex field $U(z, t)$ will solve (9.14). A_{eff} is a measure of the area of the mode described by $F(x, y)$. We insert this into (9.14) to obtain

$$\begin{aligned} \frac{\partial^2 U}{\partial z^2} + \frac{\partial^2 U^*}{\partial z^2} + \left(\sum_{n=0} \frac{\beta_n}{n!} \left(i \frac{\partial}{\partial t} \right)^n \right)^2 U + \left(\sum_{n=0} \frac{\beta_n}{n!} \left(i \frac{\partial}{\partial t} \right)^n \right)^2 U^* \\ = \frac{1}{4A_{\text{eff}}} \frac{1}{c^2} \frac{\partial^2}{\partial t^2} \chi^{(3)} \left(U^3 + 3|U|^2 U + 3|U|^2 U^* + U^{*3} \right). \end{aligned} \quad (9.16)$$

Separating this into parts dependent on U and U^* and focusing on the equation for U

$$\frac{\partial^2 U}{\partial z^2} + \left(\sum_{n=0} \frac{\beta_n}{n!} \left(i \frac{\partial}{\partial t} \right)^n \right)^2 U = \frac{1}{4A_{\text{eff}}} \frac{1}{c^2} \frac{\partial^2}{\partial t^2} \chi^{(3)} \left(U^3 + 3|U|^2 U \right). \quad (9.17)$$

We now make two transformations to simplify the maths, First we move to the rotating frame using

$$\begin{aligned} \frac{\partial}{\partial z} &\rightarrow \frac{\partial}{\partial z} + i\beta_0 \\ \frac{\partial}{\partial t} &\rightarrow \frac{\partial}{\partial t} - i\omega_0 \\ U(z, t) &= u(z, t) e^{i(\beta_0 z - \omega_0 t)}. \end{aligned}$$

This appears similar to the slowly varying envelope approximation used in the NLSE where the field is separated into a rapidly oscillating part with frequency ω_0 and a slowly varying envelope.

However here we make no assumptions about how fast the u varies. This leads to

$$\begin{aligned} & \left(-\beta_0^2 u + 2i\beta_0 \frac{\partial u}{\partial z} + \frac{\partial^2 u}{\partial z^2} \right) e^{i(\beta_0 z - \omega_0 t)} + \left(\sum_{n=0} \frac{\beta_n}{n!} \left(i \frac{\partial}{\partial t} \right)^n \right)^2 \left[u e^{i(\beta_0 z - \omega_0 t)} \right] \\ & = \frac{1}{4A_{\text{eff}}} \frac{1}{c^2} \frac{\partial^2}{\partial t^2} \chi^{(3)} \left(u^3 e^{3i(\beta_0 z - \omega_0 t)} + 3|u|^2 u e^{i(\beta_0 z - \omega_0 t)} \right). \end{aligned} \quad (9.18)$$

To simplify the time derivative terms we use the Fourier transform $u(z, t) = \frac{1}{2\pi} \int_{-\infty}^{\infty} \tilde{u}(z, \omega) e^{-i\omega t} d\omega$.

Focusing on the time derivative terms on the LHS we obtain

$$\begin{aligned} & \left(\sum_{n=0} \frac{\beta_n}{n!} \left(i \frac{\partial}{\partial t} \right)^n \right)^2 \left[\frac{1}{2\pi} \int_{-\infty}^{\infty} \tilde{u}(z, \omega) e^{-i(\omega + \omega_0)t} d\omega e^{i\beta_0 z} \right] \\ & \Rightarrow \frac{1}{2\pi} e^{i(\beta_0 z - \omega_0 t)} \int_{-\infty}^{\infty} \left(\sum_{n=0} \frac{\beta_n}{n!} (\omega + \omega_0)^n \right)^2 \tilde{u}(z, \omega) e^{-i\omega t} d\omega \\ & \Rightarrow \frac{1}{2\pi} e^{i(\beta_0 z - \omega_0 t)} \left(\sum_{n=0} \frac{\beta_n}{n!} \left(i \frac{\partial}{\partial t} + \omega_0 \right)^n \right)^2 \int_{-\infty}^{\infty} \tilde{u}(z, \omega) e^{-i\omega t} d\omega. \end{aligned} \quad (9.19)$$

This leads to

$$\begin{aligned} & \left(-\beta_0^2 u + 2i\beta_0 \frac{\partial u}{\partial z} + \frac{\partial^2 u}{\partial z^2} \right) e^{i(\beta_0 z - \omega_0 t)} + e^{i(\beta_0 z - \omega_0 t)} \beta^2 \left(i \frac{\partial}{\partial t} + \omega_0 \right) u \\ & = \frac{1}{4A_{\text{eff}}} \frac{1}{c^2} \frac{\partial^2}{\partial t^2} \chi^{(3)} \left(u^3 e^{3i(\beta_0 z - \omega_0 t)} + 3|u|^2 u e^{i(\beta_0 z - \omega_0 t)} \right). \end{aligned} \quad (9.20)$$

We make a further transformation by moving to the frame co-moving with the pulse at velocity v_g ,

$$T = t - \frac{z}{v_g} = t - \beta_1 z,$$

$$\xi = z,$$

$$\frac{\partial}{\partial z} = \frac{\partial}{\partial \xi} - \beta_1 \frac{\partial}{\partial T},$$

$$\frac{\partial}{\partial t} = \frac{\partial}{\partial T}.$$

Inserting the above into (9.20) we obtain

$$\begin{aligned}
 & \left[\left(-\beta_0^2 u + 2i\beta_0 \frac{\partial u}{\partial \xi} - 2i\beta_0 \beta_1 \frac{\partial u}{\partial T} + \frac{\partial^2 u}{\partial \xi^2} - 2\beta_1 \frac{\partial^2 u}{\partial \xi \partial T} + \beta_1^2 \frac{\partial^2 u}{\partial T^2} \right) \right] e^{i(\beta_0 \xi - \omega_0 T + \omega_0 \frac{\xi}{v_g})} \\
 & \quad + \left[\beta^2 \left(i \frac{\partial}{\partial T} + \omega_0 \right) u \right] e^{i(\beta_0 \xi - \omega_0 T + \omega_0 \frac{\xi}{v_g})} \\
 & = \frac{e^{i(\beta_0 \xi - \omega_0 T + \omega_0 \frac{\xi}{v_g})}}{4A_{\text{eff}} c^2} \left(\frac{\partial}{\partial T} - i\omega_0 \right)^2 \chi^{(3)} \left(u^3 e^{2i(\beta_0 \xi - \omega_0 T + \omega_0 \frac{\xi}{v_g})} + 3|u|^2 u \right). \quad (9.21)
 \end{aligned}$$

Cancelling the exponentials and rearranging leads to

$$\begin{aligned}
 & \left(-\beta_0^2 u + 2i\beta_0 \frac{\partial u}{\partial \xi} - 2i\beta_0 \beta_1 \frac{\partial u}{\partial T} + \frac{\partial^2 u}{\partial \xi^2} - 2\beta_1 \frac{\partial^2 u}{\partial \xi \partial T} + \beta_1^2 \frac{\partial^2 u}{\partial T^2} \right) + \beta^2 \left(i \frac{\partial}{\partial T} + \omega_0 \right) u \\
 & = \frac{1}{4A_{\text{eff}} c^2} \left(\frac{\partial}{\partial T} - i\omega_0 \right)^2 \chi^{(3)} \left(u^3 e^{2i(\beta_0 \xi - \omega_0 T + \omega_0 \frac{\xi}{v_g})} + 3|u|^2 u \right). \quad (9.22)
 \end{aligned}$$

We define the second and higher order dispersion as $D = \sum_{n \geq 2} \beta_n (i\partial/\partial T)^n / n!$

$$\beta \left(i \frac{\partial}{\partial T} + \omega_0 \right) = \sum_{n=0} \frac{\beta_n}{n!} \left(i \frac{\partial}{\partial T} + \omega_0 - \omega_0 \right)^n = \beta_0 + i\beta_1 \frac{\partial}{\partial T} + D \left(i \frac{\partial}{\partial T} \right), \quad (9.23)$$

$$\beta^2 \left(i \frac{\partial}{\partial T} + \omega_0 \right) = \beta_0^2 + 2i\beta_1 \beta_0 \frac{\partial}{\partial T} + 2\beta_0 D - \beta_1^2 \frac{\partial^2}{\partial T^2} + 2i\beta_1 \frac{\partial}{\partial T} D + D^2. \quad (9.24)$$

Using (9.24) we cancel several terms in (9.22)

$$\begin{aligned}
 & \left(\frac{\partial^2}{\partial \xi^2} + D^2 + 2\beta_0 D + 2i\beta_1 \frac{\partial}{\partial T} D - 2\beta_1 \frac{\partial^2}{\partial \xi \partial T} + 2i\beta_0 \frac{\partial}{\partial \xi} \right) u \\
 & = \frac{1}{4A_{\text{eff}} c^2} \left(\frac{\partial}{\partial T} - i\omega_0 \right)^2 \chi^{(3)} \left(u^3 e^{2i(\beta_0 \xi - \omega_0 T + \omega_0 \frac{\xi}{v_g})} + 3|u|^2 u \right). \quad (9.25)
 \end{aligned}$$

We factorise the LHS

$$\begin{aligned}
 & \left(D - i \frac{\partial}{\partial \xi} + 2 \left(\beta_0 + i\beta_1 \frac{\partial}{\partial T} \right) \right) \left(D + i \frac{\partial}{\partial \xi} \right) u \\
 & = \frac{1}{4A_{\text{eff}} c^2} \left(\frac{\partial}{\partial T} - i\omega_0 \right)^2 \chi^{(3)} \left(u^3 e^{2i(\beta_0 \xi - \omega_0 T + \omega_0 \frac{\xi}{v_g})} + 3|u|^2 u \right). \quad (9.26)
 \end{aligned}$$

To remove the derivatives we take two Fourier transforms $u(\xi, T) = \int_{-\infty}^{\infty} \hat{u}(k, T) \exp(ik\xi) dk$ and

$$\begin{aligned}
 \hat{u}(k, T) &= (1/2\pi) \int_{-\infty}^{\infty} \tilde{u}(k, \omega - \omega_0) \exp(-i(\omega - \omega_0)T) d\omega, \\
 &= -\frac{2\pi}{4A_{\text{eff}}c^2} ((\omega - \omega_0) + \omega_0)^2 F.T. \left[\chi^{(3)} \left(u_s^3 e^{2i(\beta_0\xi - \omega_0T + \omega_0 \frac{\xi}{v_g})} + 3|u_s|^2 u_s \right) \right]. \quad (9.27)
 \end{aligned}$$

This is the final form of the equation that we will use to find the phase matching condition in the next section.

9.1 Phase matching condition

We now have an equation which can be compared to (8.16) the NLSE with higher order dispersion included. The new equation (9.27) has some similarities but contains extra terms. However we will see that both lead to the same phase matching condition for dispersive radiation generated by a soliton. As in section 8.4 we do this by inserting into (9.27) a solution $u = u_s + a$, where u_s is the fundamental soliton (again assuming that to a good approximation it is unchanged by the generation of dispersive waves) and a is a small dispersive wave perturbation. We insert the solution into (9.27) and linearise in a to obtain

$$\begin{aligned}
 &(D + k + 2(\beta_0 + \beta_1(\omega - \omega_0)))(D - k)(\tilde{u}_s + \tilde{a}) = \\
 &\quad -\frac{2\pi\omega^2}{4A_{\text{eff}}c^2} F.T. \left[\chi^{(3)}(T) \left(u_s^3 e^{2i(\beta_0\xi - \omega_0T + \omega_0 \frac{\xi}{v_g})} + 3|u_s|^2 u_s \right) \right] \\
 &\quad -\frac{2\pi\omega^2}{4A_{\text{eff}}c^2} F.T. \left[\chi^{(3)} \left(3u_s^2 a e^{2i(\beta_0\xi - \omega_0T + \omega_0 \frac{\xi}{v_g})} + 6|u_s|^2 a + 3u_s^2 a^* \right) \right]. \quad (9.28)
 \end{aligned}$$

Similarly to the terms dropped from (8.24) in section 8.4, the terms in the final bracket on the RHS will only have a small effect on the solution for a . As a first order approximation they are ignored leading to the following solution for \tilde{a} ,

$$\tilde{a} = \frac{(D + k + 2(\beta_0 + \beta_1(\omega - \omega_0)))(D - k) \tilde{u}_s - \frac{2\pi\omega^2}{4A_{\text{eff}}c^2} F.T. \left[\chi^{(3)} \left(u_s^3 e^{2i(\beta_0\xi - \omega_0T + \omega_0 \frac{\xi}{v_g})} + 3|u_s|^2 u_s \right) \right]}{(D + k + 2(\beta_0 + \beta_1(\omega - \omega_0)))(D - k)}.$$

As in the case of 8.25, the dispersive wave will be phase matched when the denominator is zero i.e

$$D(\omega - \omega_0) - k = 0, \quad (9.29)$$

or

$$D + k + 2(\beta_0 + \beta_1(\omega - \omega_0)) = 0. \quad (9.30)$$

We can find the amplitude of these resonances by considering $A' = (D - k)\tilde{a}|_{D \rightarrow k}$ for the first condition and $A' = (D + k + 2(\beta_0 + \beta_1(\omega - \omega_0)))\tilde{a}|_{D \rightarrow -k - 2(\beta_0 + \beta_1(\omega - \omega_0))}$ for the second, which lead to the same form for the amplitude

$$A' = \frac{-\frac{2\pi\omega^2}{8A_{\text{eff}}c^2}F.T. \left[\chi^{(3)} \left(u_s^3 e^{2i(\beta_0\xi - \omega_0 T + \omega_0 \frac{\xi}{v_g})} + 3|u_s|^2 u_s \right) \right]}{\beta(\omega - \omega_0)}. \quad (9.31)$$

Using the form of the fundamental soliton $u_s(\xi, T)$ defined in (8.3), we obtain

$$A' = -\frac{2\pi\omega^2 P_0 \sqrt{P_0}}{8A_{\text{eff}}c^2 \beta(\omega - \omega_0)} F.T. \left[\chi^{(3)} \text{sech}^3 \left(\frac{T}{T_0} \right) e^{3i\gamma P_0 \xi/2} e^{2i(\beta_0 \xi - \omega_0 T + \omega_0 \frac{\xi}{v_g})} \right] \\ - \frac{2\pi\omega^2 P_0 \sqrt{P_0}}{8A_{\text{eff}}c^2 \beta(\omega - \omega_0)} F.T. \left[3\chi^{(3)} \left| \text{sech} \left(\frac{T}{T_0} \right) \right|^2 \text{sech} \left(\frac{T}{T_0} \right) e^{i\gamma P_0 \xi/2} \right]. \quad (9.32)$$

We take the Fourier transform $\xi \rightarrow k$,

$$A' = -\frac{2\pi\omega^2 P_0 \sqrt{P_0} \chi^{(3)}}{8A_{\text{eff}}c^2 \beta(\omega - \omega_0)} F.T. \left[\delta \left(k - \frac{3\gamma P_0}{2} - 2\beta_0 - 2\beta_1 \omega_0 \right) \text{sech}^3 \left(\frac{T}{T_0} \right) e^{-2i\omega_0 T} \right] \\ - \frac{2\pi\omega^2 P_0 \sqrt{P_0} \chi^{(3)}}{8A_{\text{eff}}c^2 \beta(\omega - \omega_0)} F.T. \left[3\delta \left(k - \frac{\gamma P_0}{2} \right) \left| \text{sech} \left(\frac{T}{T_0} \right) \right|^2 \text{sech} \left(\frac{T}{T_0} \right) \right]. \quad (9.33)$$

And the Fourier transform $T \rightarrow \omega - \omega_0$,

$$A' = -\frac{\pi\omega^2 T_0 P_0 \sqrt{P_0} \chi^{(3)}}{8A_{\text{eff}}c^2 \beta(\omega - \omega_0)} \left[\delta' \left(T_0^2 (\omega - 3\omega_0)^2 + 1 \right) \text{sech} \left(\frac{\pi T_0}{2} (\omega - 3\omega_0) \right) \right] \\ - \frac{\pi\omega^2 T_0 P_0 \sqrt{P_0} \chi^{(3)}}{8A_{\text{eff}}c^2 \beta(\omega - \omega_0)} \left[3\delta \left(T_0^2 (\omega - \omega_0)^2 + 1 \right) \text{sech} \left(\frac{\pi T_0}{2} (\omega - \omega_0) \right) \right]. \quad (9.34)$$

Here $\delta = \delta \left(k - \frac{\gamma P_0}{2} \right)$ and $\delta' = \delta \left(k - \frac{3\gamma P_0}{2} - 2\beta_0 - 2\beta_1 \omega_0 \right)$.

This leads to four resonance conditions arising from the two conditions in (9.29) and (9.30) and

the two delta functions in the above equation. From $\delta\left(k - \frac{\gamma P_0}{2}\right)$ we obtain

$$D - \frac{\gamma P_0}{2} = 0, \quad (9.35)$$

$$D + \frac{\gamma P_0}{2} + 2(\beta_0 + \beta_1(\omega - \omega_0)) = 0, \quad (9.36)$$

each with amplitude,

$$A' = -\frac{\pi\gamma\beta_0\omega^2 T_0 P_0 \sqrt{P_0} \chi^{(3)}}{\omega_0^2 \beta \chi_0^{(3)}} \left(T_0^2 (\omega - \omega_0)^2 + 1\right) \operatorname{sech}\left(\frac{\pi T_0}{2} (\omega - \omega_0)\right). \quad (9.37)$$

And from $\delta\left(k - \frac{3\gamma P_0}{2} - 2\beta_0 - 2\beta_1\omega_0\right)$ we obtain

$$D - \frac{3\gamma P_0}{2} - 2\beta_0 - 2\beta_1\omega_0 = 0, \quad (9.38)$$

$$D + \frac{3\gamma P_0}{2} + 2\beta_0 + 2\beta_1\omega_0 + 2(\beta_0 + \beta_1(\omega - \omega_0)) = 0, \quad (9.39)$$

each with amplitude,

$$A' = -\frac{\pi\gamma\omega^2 \beta_0 T_0 P_0 \sqrt{P_0} \chi^{(3)}}{3\omega_0^2 \beta \chi_0^{(3)}} \left(T_0^2 (\omega - 3\omega_0)^2 + 1\right) \operatorname{sech}\left(\frac{\pi T_0}{2} (\omega - 3\omega_0)\right). \quad (9.40)$$

For the amplitudes, $\gamma = 3\chi_0^{(3)}\omega_0 / (8n_0cA_{eff})$ and $\beta_0 = n_0\omega_0/c$.

The important point to note from this section is that the condition in (9.35) is the same as the phase matching condition derived from the NLSE with higher order dispersion. This will be considered in more detail in the next section. We also note that as in section 8.16 the amplitude of the dispersive wave solution (see (9.37)) depends on the strength of the component of the soliton spectrum at the phase matched wavelength. Therefore pulse compression and spectral broadening will be critical in driving the radiation.

The two phase matching conditions in (9.36) and (9.38) have no solutions in our PCFs if we only consider the fundamental mode. The phase matching condition in (9.39) does have a solution in our PCFs however as we can see from (9.40) the amplitude depends on the component of the third harmonic of the soliton at the phase matched frequency. As discussed in section 4.2 THG also

requires higher order modes. Therefore all of these other phase matching conditions require higher order modes and are beyond the scope of this thesis, thus they will not be considered further.

10 Dispersion profiles

In the previous sections we have seen that the same phase matching condition can be derived from the NLSE with higher order dispersion and the more complicated pulse propagation equation. In this section we look at this condition in more detail and use a typical dispersion profile from the PCFs that are used in the experiments to find solutions. From this analysis we find the well known RR solution to the phase matching condition. The more important finding is the new NRR solution which only arises when negative frequencies are taken into account.

We start with the resonance condition and find that we can express it in a simple way in terms of frequencies in the co-moving frame. The frequency in a frame moving with group velocity v_g is defined by the Doppler shift formula (non-relativistic)

$$\omega' = \omega \left(1 - \frac{n}{n_g} \right). \quad (10.1)$$

Where ω' is the co-moving frame frequency, ω is the lab frame frequency, n is the refractive index (linear and non-linear parts) defined by $n = c/v_p = c/(\omega/\beta)$, and n_g is the group index defined by $n_g = c/v_g = c/(d\omega/d\beta)$. From the phase matching condition $D - \gamma P_0/2 = 0$ we expand D and rearrange to obtain

$$\begin{aligned} \sum_{n \geq 2} \frac{\beta_n}{n!} (\omega - \omega_0)^n - \frac{\gamma P_0}{2} &= \beta(\omega) - \beta_0 - \beta_1(\omega - \omega_0) - \frac{\gamma P_0}{2} = 0 \\ \Rightarrow -\beta(\omega) + \beta_1\omega &= -\beta_0 + \beta_1\omega_0 - \frac{\gamma P_0}{2} \\ \Rightarrow -\frac{n(\omega)\omega}{c} + \frac{\omega}{v_g} &= -\frac{n(\omega_0)\omega_0}{c} + \frac{\omega_0}{v_g} - \frac{\gamma P_0}{2} \\ \Rightarrow \omega \left(1 - \frac{n(\omega)}{n_g} \right) &= \omega_0 \left(1 - \frac{n(\omega_0)}{n_g} - \frac{\gamma P_0 c}{2\omega_0 n_g} \right) \\ \Rightarrow \omega' &= \omega'_0. \end{aligned} \quad (10.2)$$

Where the third term in the bracket on the RHS is the non-linear contribution to the refractive index divided by n_g . Therefore the phase matching condition is a conservation of frequency in the

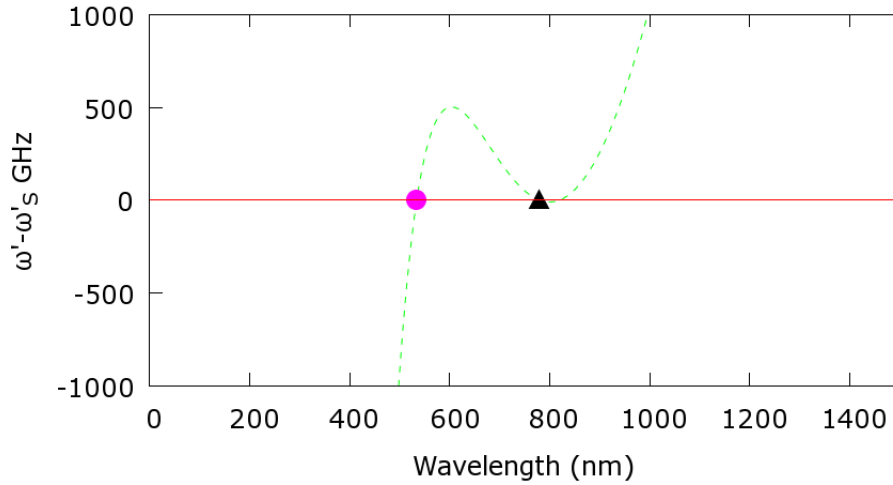


Figure 15: Dispersion profile in the co-moving frame with the soliton (\triangle) and RR (\circ) indicated

frame co-moving with the driving pulse centred at ω_0 .

In order to find solutions to these phase matching conditions we need to know the dispersion profiles of the PCFs being used. In the co-moving frame the lab frame frequency plays the role of wavenumber and hence a plot of ω' as a function of ω is the equivalent in the moving frame of a plot of ω as a function of β in the lab frame, which is the dispersion relation. For simplicity we initially consider the case of negligible pulse power hence the non-linear contribution to the refractive index is ignored.

An example of a moving frame dispersion profile for one of our PCFs is shown in figure 15. This is plotted using wavelength rather than frequency on the x-axis as in the experiments the fibre output spectra are recorded as functions of wavelength.

There are a few points of interest in the figure. The first is the soliton wavelength (represented by the triangle). This occurs at a minimum because if we take the derivative of the co-moving frame frequency with respect to lab frequency we obtain the following relation

$$\frac{d}{d\omega} (\omega') = \frac{d}{d\omega} \left[\omega \left(1 - \frac{n}{n_g} \right) \right] = 1 - \frac{n}{n_g} - \frac{\omega}{n_g} \frac{dn}{d\omega}. \quad (10.3)$$

Using the previously defined n and n_g we obtain

$$\frac{d}{d\omega}(\omega') = 1 - \frac{c\beta}{n_g\omega} - \frac{c\omega}{n_g} \left(\frac{-\beta}{\omega^2} + \frac{1}{\omega} \frac{d\beta}{d\omega} \right) = 1 - \frac{c}{n_g} \frac{d\beta}{d\omega} = 1 - \frac{n_g(\omega)}{n_g(\omega_0)}. \quad (10.4)$$

Therefore the derivative is zero at the soliton frequency (or wavelength). The maximum of the curve is known as the group velocity matched wavelength, because it will have the same group velocity as the soliton. Between the maxima and the minima is a point of inflection which represents the ZDW of the fibre, we can see this by taking the second derivative of the co-moving frame frequency with respect to lab frame frequency

$$\frac{d^2}{d\omega^2}(\omega') = -\frac{c}{n_g} \frac{d^2\beta}{d\omega^2}. \quad (10.5)$$

At the point of inflection the second derivative is zero and therefore so is the second derivative of the propagation constant i.e. $\beta_2 = 0$.

On the short wavelength side of the group velocity matched point there is a solution to the phase matching condition i.e. a point on the curve with the same ω' as the soliton (marked by the circle). This is the RR and for all of the PCFs used in the experiments it lies in the visible region of the spectrum.

As mentioned before the dispersion curve in figure 15 is plotted for negligible soliton power. If the power increases then we have to take account of the non-linear contribution to the refractive index in (10.2). This will reduce the value of ω'_0 and therefore change the wavelength of the phase matched RR. The variation in the value of the phase matched wavelength with input pulse power for one PCF is shown in figure 16. As the power increases ω' will decrease shifting the RR signal to shorter wavelengths. The same behaviour occurs for all the PCFs used.

The RR solution is well known, the important point in this section is that there is another solution to the phase matching condition, the NRR which requires us to take into account negative frequencies. This is a new result and, as previously discussed, it is to the best of our knowledge the first example of this sort of coupling between positive and negative frequencies in optics.

As explained in section 5.2 electromagnetic waves can be decomposed into positive and negative frequency parts. Therefore we consider a second branch of the dispersion curve for negative

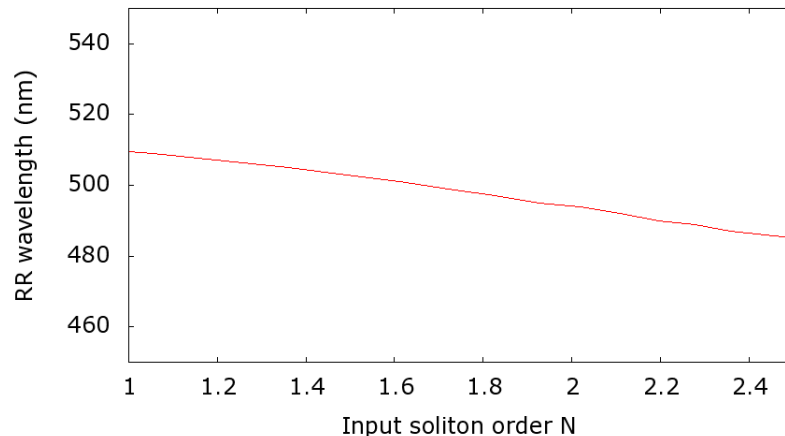


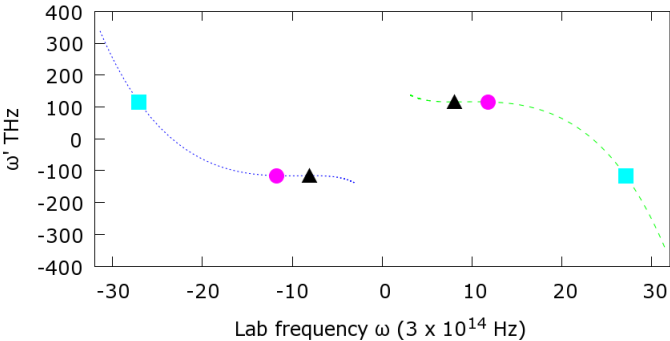
Figure 16: Phase matched RR wavelength as the input pulse power varies for the NL-1.5-590 PCF (power expressed in terms of N)

wavelengths, both positive and negative wavelength branches are shown in figure 17(a). The soliton is a real electromagnetic wave and hence we can plot both its positive frequency component and its complex conjugate negative frequency component on the dispersion curve (marked by triangles). Figure 17(b) shows only the top part of the dispersion relation for both branches (in this case the co-moving frame frequency has been plotted relative to the soliton co-moving frame frequency ω'_s). This clearly shows that there is a further solution to the condition $\omega' = \omega'_0$, which lies on the negative wavelength branch, this is the NRR. Figure 17(c) shows only the bottom part of the dispersion relation for both branches (in this case the co-moving frame frequency has been plotted relative to the co-moving frame frequency of the complex conjugate part of the soliton ω'^*_s). Again we see two solutions to the phase matching condition, the RR on the negative branch and the NRR on the positive branch.

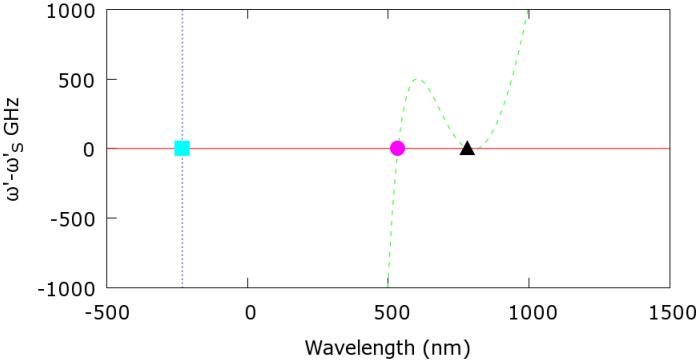
In summary there are two solutions each real electromagnetic waves with a positive frequency part and a negative frequency complex conjugate. The RR is always phase matched to the soliton component with the same frequency sign and the NRR is always phase matched to the soliton component with the opposite frequency sign.

For all of the PCFs we use the NRR lies in the UV region of the spectrum. In section 12 the properties of NRR will be discussed further in particular the similarities and differences between NRR and RR and the dependence of NRR on pulse compression. We note here, whilst the dispersion

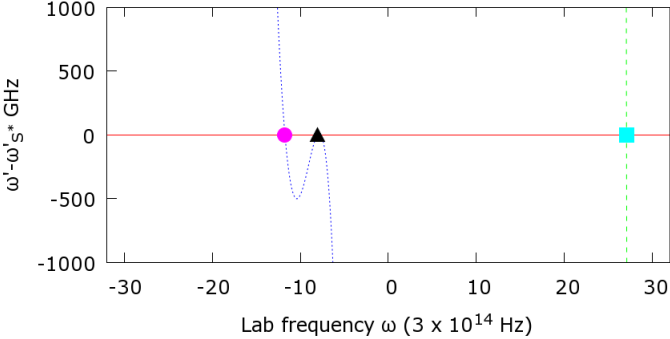
profiles are to hand, that in the UV the slope of the curve is considerably steeper than in the visible. This means that any change in the co-moving frame frequency of the soliton will have a larger effect on the wavelength of the RR than on that of the NRR. We will see this in the experimental results.



(a) Positive and negative ω'



(b) Top part of figure (a)



(c) Bottom part of figure (a)

Figure 17: Dispersion curves as a function of positive and negative lab wavelengths (frequencies). Showing the the soliton (Δ) RR (\circ) and NRR (\square)

Part III

Experimental results

11 Introduction

In the first two parts of this thesis I have discussed developments in the field of optical solitons and the types of radiation which are driven by such solitons. I have explained in more detail the theory behind solitons propagating in fibres and in particular how they transfer energy to RR and NRR. I now turn to the experiments that I have carried out. These mainly investigate the evolution of short pulses, in particular pulse compression, and the generation and evolution of RR and NRR.

In this part I will first describe the set-up used for the experiments and the parameters that could be varied. I will also explain some of the experimental procedures used and the particular challenges encountered in this project.

In the experimental results section I will present results demonstrating the first discovery of NRR in optics. The significance of this result has already been discussed in section 5.2. In brief it demonstrates the first example in optics of a mixing between positive and negative frequencies. Such a mixing can in some circumstances lead to amplification and may have links to the generation of the optical analogue of HR discussed in section 6.

Many of the other experimental results focus on the use of different pulse parameters to control pulse evolution - in particular to control pulse compression. The purpose of this control was twofold, firstly to vary the generation efficiency of the different types of radiation driven by solitons and secondly to allow for qualitative investigations into how the pulse and driven radiation evolve in the PCF. The results are compared to simulations carried out using a split step Fourier tool (RPPulse [101]), which is used to quantitatively investigate pulse evolution.

12 Experimental set-up

The majority of the experiments use a Ti:Sapphire laser (FemtoSource Rainbow). This produces hyperbolic secant pulses of approximately 7 fs duration using a Kerr lens mode-locking technique [130, 19]. The development of lasers which could produce pulses in the femtosecond range made possible many of the developments in the field of solitons and radiation driven by solitons. The short pulse lengths mean that peak powers are high for relatively low average powers allowing a variety of non-linear effects to take place. The average power of the laser in continuous wave mode

reaches up to 300 mW. Once mode-locked with a repetition rate of 77 MHz the average power is reduced to a maximum of 200 mW with a corresponding peak power of up to 370 kW.

The pulses have a bandwidth of approximately 200 nm centred at 780 nm. With a short pulse a broad bandwidth is inevitable. It can be useful, for example components of the soliton are able to drive phase matched radiation over a wide range of wavelengths. It also leads to various challenges when using the pulses, which will be discussed in sections 12.3 and 12.4. The wavelength is important to note because, in order for solitons to form, this must lie within the anomalous dispersion region of the PCF used. Equally as important, the wavelength of the input pulse will determine the wavelengths of the RR, NRR and other phase matched radiation.

The pulse spectrum produced by the laser is shown in figure 18 measured as the detector is moved horizontally across the beam cross section. The figure shows the width of the spectrum as well as the spatial shape of the pulse.

The sharp peak at approximately 670 nm is not part of the pulse spectrum and, as can be seen in the figure, it has a different spatial profile. In some of the experiments it is removed using a 695 nm long pass filter with little significant change in the results. It arises due to the mirror coatings used in the laser. These extend the laser spectrum in order to make it possible to carry out carrier envelope locking. This is a technique for fixing the offset between the maximum of the pulse envelope and the optical phase. Whilst carrier envelope locking is useful for experiments requiring a well defined, stable frequency comb, it is not used in any of the experiments described here and hence the 670 nm peak can be removed. Without the 670 nm peak, the pulse is approximately symmetric in shape. In figure 18 the centre of the beam lies at approximately 6 mm.

The pulses are coupled into solid core PCFs which were discussed in section 3. Measurements of the dispersive properties of the PCFs will be described in section 12.6. The output light is measured using either a CCD spectrometer for the visible and IR, or a monochromator and photomultiplier tube for the UV. The input pulse properties which are varied in the experiments are the pulse power, polarisation and pulse chirp.

The experimental set-up varies a little between the different experiments. The basic configuration is shown in figure 19. As mentioned the output can also be coupled into a spectrometer to detect the visible and IR. The various important features of the experimental set-up will be considered in more detail in the following sections.

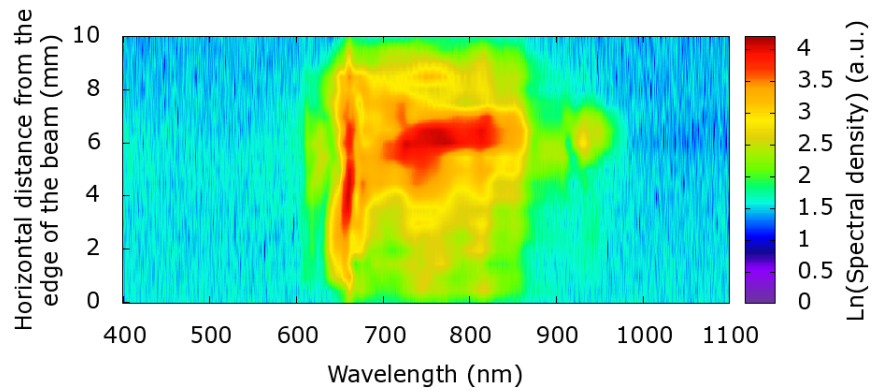


Figure 18: Input pulse spectrum (logarithmic values) for different positions moving horizontally through the cross section of the beam

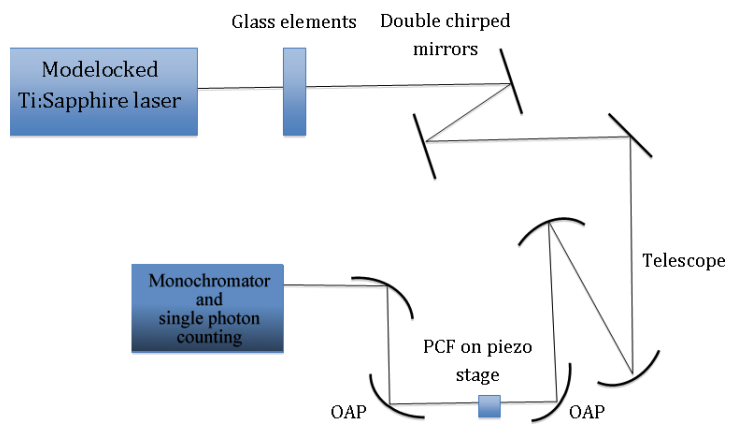


Figure 19: Basic experimental set-up

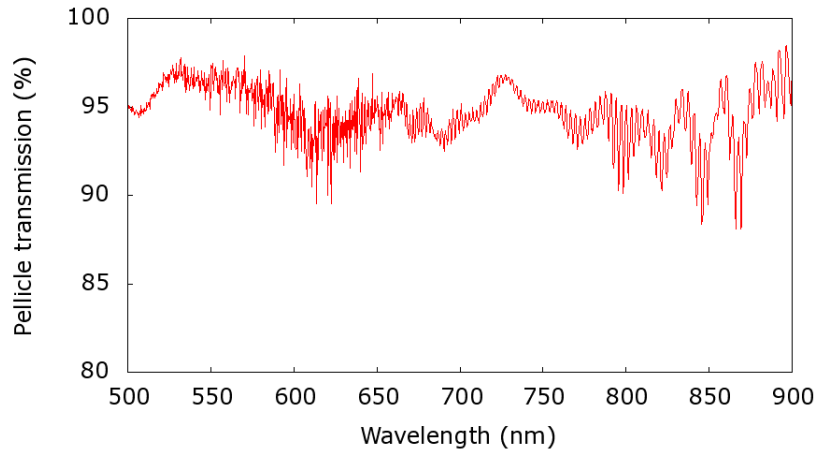


Figure 20: Transmission of the 92:8 pellicle at 45° incidence, calculated from measurements of the spectrum using the CCD spectrometer. Averaged over 200 ms i.e. over more than 15 million pulses

12.1 Input pulse power

Power is a key parameter to adjust as it can be used to control pulse compression in the PCF and the strength of non-linear effects. In all experiments it is necessary to either keep the power constant whilst varying another parameter or to be able to vary the power whilst not altering any other beam parameters such as the polarisation or the pulse chirp.

The power reaching the PCFs is adjusted using polarisation optics or pellicle beamsplitters. The latter are thin nitrocellulose membranes. Depending on the coating applied to the membrane they act as beamsplitters with different ratios for reflection and transmission. They are used in the experiments to change the power without introducing significant extra glass into the beam path and thus altering the input pulse chirp (see section 12.3 for details on pulse chirp).

The graph in figure 20 shows the measured transmission of one of the pellicles at 45° incidence, across the spectrum of the input pulse. The specified transmission is 92% and the results match this reasonably well with some small dependence on wavelength. This allows us to conclude that inserting pellicles will not distort the pulse spectrum significantly. If the incidence angle is varied the ratio of transmitted to reflected power will change slightly which can be used for small power adjustments. However large rotations introduce increasingly large fringes into the transmission

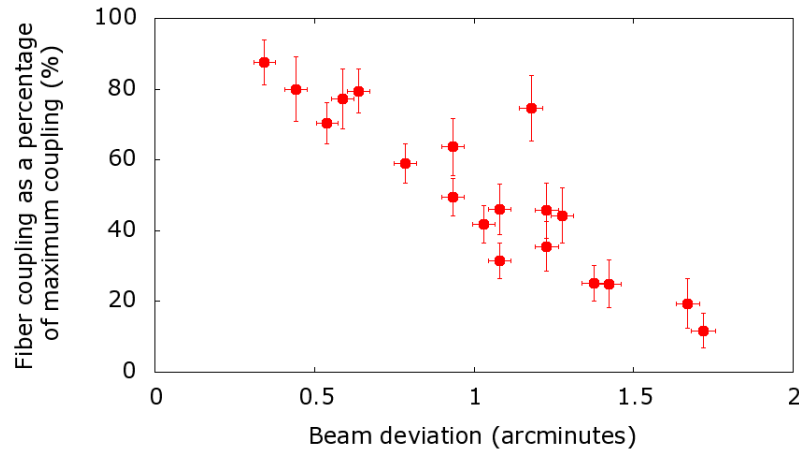


Figure 21: Change in PCF coupling as a function of angular beam deviation

spectrum which are undesirable.

For some experiments larger input pulse chirps are not detrimental and so polarisation optics are used to control the power. Specifically this involves using an achromatic Half Wave Plate (HWP) followed by an achromatic thin film Polariser (POL) in the beam path. Both are intended for use over the range 600 – 950 nm, which as seen in figure 18 includes the spectrum of the input pulses. Both elements add considerable chirp to the pulse significantly changing the pulse length. The exact values of the added chirp will be considered in section 12.3.1.

A further consideration, when using the HWP for either power or polarisation control, is that if it is at all wedged in shape it will cause slight deviations in the beam when it is rotated. This will change the coupling into the PCF which will affect the measured output. Estimates of the potential change in coupling are found by deviating the input beam using a mirror and measuring the angular deviation and the change in the power coupled into a piece of PCF. The mirror used for deviating the beam is positioned at approximately the same distance from the PCF as the HWP. The results are shown in figure 21, they show that a relatively small angular change has a large effect on the coupling. A wedge of the order of an arc-minute in the HWP would reduce the coupling by over half.

The specified wedge angle of the HWP is considerably less than an arc-minute and should therefore cause a change in coupling of much less than 50%. To test this, the HWP is placed in the beam path before the POL and rotated. The power after the POL is kept constant using pellicles

and the change in coupling is measured. Including the POL after the HWP ensures that the input beam polarisation is always aligned in the same way with respect to the PCF axes. The results indicate that the coupling varied by less than 5% over the whole rotation.

The POL consists of a polarizing coating deposited on ultra thin fused silica plates, which are mounted in such a way that lateral displacement of the beam should be perfectly compensated and rotating the POL should cause no beam deviation. This is checked in the same way as the HWP by placing the POL under test behind a second POL. Similar results to the HWP are found for the change in coupling. This indicates that rotating the HWP or POL causes minimal deviation of the beam. In this case, as seen in figure 21, minimal means that they deviate the beam by less than 0.5 arcminutes. To reduce any slight deviation the HWP and POL are placed as close to the PCF input as possible in any experiment where they have to be rotated.

12.2 Input and output polarisation

Input polarisation is an important parameter to be able to measure and control. We require the output from the laser to be linearly polarised and to be able to rotate this linear polarisation before the PCF. Additionally it must be possible to measure the polarisation of the output. As in the case of the power, any adjustments to the input polarisation should not affect the other pulse parameters such as power and chirp.

The laser output must be linearly polarised and rotatable so that it can be aligned with one principal axis of the PCF and excite only this axis. This will maximise the peak power along that axis and therefore the non-linear effects. In addition, the different PCF axes have slightly different dispersion curves and therefore radiation driven by the input pulse will be phase matched at different wavelengths. Exciting only one axis simplifies the resulting output spectra allowing easier interpretation of results. A further reason for requiring linear polarisation is that this optimises the use of some of the optical components. For example using the HWP and the POL to control the power over the widest possible range requires linearly polarised light. Another example is that some components are sensitive to the polarisation of the light. As explained in section 12.1, rotating the pellicle introduces fringes into the spectrum. This effect is more pronounced for linearly polarised light aligned vertically with respect to the optical table as compared to horizontally.

Measurements of the output polarisation allow us to see how the polarisation state changes during propagation through the PCF.

The pulse exiting the laser is expected to be linearly polarised and aligned horizontally with respect to the optical table. To test this we use a HWP and Polarising Beam Cube (PBC) (specified for use at 800 nm) to measure the Polarisation Extinction Ratio (PER) at the laser output, which gives a value of 0.99. Here I have used the following definition for the PER,

$$\text{PER} = \frac{(A - B)}{A + B}. \quad (12.1)$$

Where A and B are respectively the maximum and minimum transmitted powers through the PBC as the HWP is rotated. Using this definition, the PER would be 1 if the beam was linearly polarised and the polariser used was perfect. In this measurement the PBC is used instead of the achromatic thin film POL as the latter has a specified maximum PER of only 0.96.

Measurements of the PER at different points in the beam path before the coupling into the PCF yield similar results indicating that the input light is linearly polarised to a very good degree.

The input beam linear polarisation is rotated using the achromatic HWP. The polarisation of the output in the IR and visible can be measured using a similar HWP and the achromatic thin film POL, or the HWP and polarisers such as the PBC, with narrower operational bandwidths but higher PERs. However these elements are not designed for use in the UV - hence a different type of polariser called a Glan-Taylor polariser is used. This consists of two right angled prisms of a birefringent material fixed opposite each other with a small air gap in between. Light passing through the first prism will be totally internally reflected at the prism-air boundary if it is polarised perpendicular to the optical axis of the prism. Light polarised parallel to the optical axis will be transmitted [102]. The polarising properties of the Glan-Taylor polariser are independent of wavelength and the birefringent material used to make the polariser is selected to have high transmittance in the UV. The polariser is specified to have a PER of 0.999998 indicating that very accurate polarisation measurements should be possible.

The Glan-Taylor polariser may cause some deviation of the output beam as it is rotated. This will change the coupling into the monochromator used for detection in the UV. In order to measure the deviation two Glan-Taylor polarisers are used. The first one in the beam path is rotated whilst

the second is kept stationary to maintain the same polarisation into the detector and remove any effects due to the polarisation sensitivity of the monochromator. If the rotation of the polariser causes no effects other than the selection of different polarisations then the intensity measured by the monochromator will follow a squared sinusoidal pattern.

The results are shown in figure 22(a) along with the expected sinusoidal variation. Additionally the residuals are shown in figure 22(b). The value 0^0 indicates that the two polarisers are aligned with each other. The monochromator signal is recorded across the region in the UV where most of the signals of interest in the experiments occur.

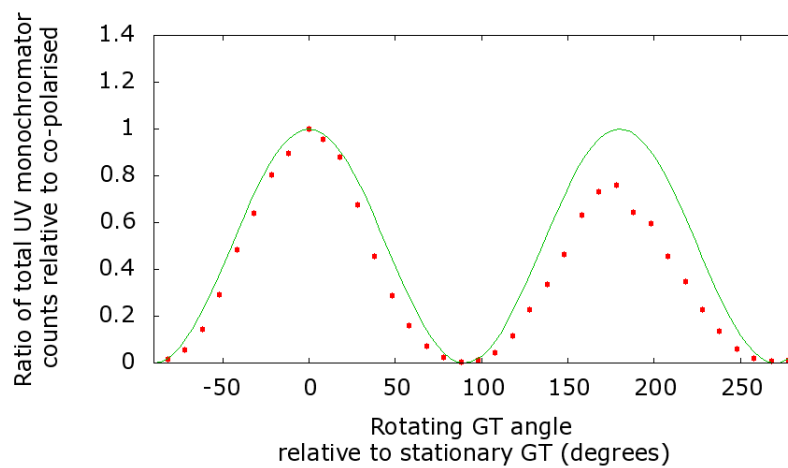
The graph in figure 22(a) shows that the measured ratios follow the expected squared sinusoidal pattern reasonably closely for a rotation over 90^0 , although the residuals indicate that there is a systematic deviation. For larger rotations the measured values are slightly lower than expected (the maximum difference from the expected value is 28%) indicating a small beam deviation. These results indicate that for precision measurements of the polarisation the Glan-Taylor polariser is not suitable. Therefore in all measurements the Glan-Taylor rotation is restricted to 90^0 to minimise deviations and additionally the polariser is positioned closer to the detector to further reduce the issue.

A further polarisation related consideration is the sensitivity of the detectors. The spectrometer used for the visible and the IR shows negligible sensitivity to polarisation. The UV detection system does have some polarisation dependence particularly for wavelengths close to the edge of the sensitivity bandwidth. This will be described in more detail in section 12.5.

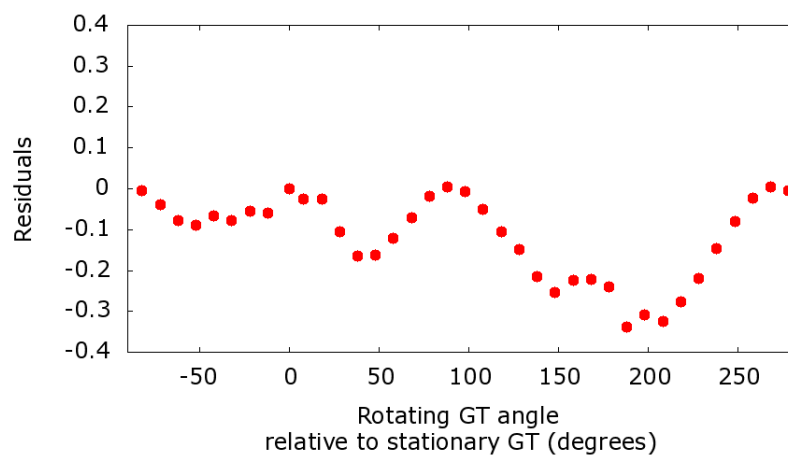
12.2.1 Aligning the photonic crystal fibre axis

As explained previously, aligning one of the principal axes of the PCF with the input polarisation ensures that only one axis is excited. This alignment is achieved by rotating the input polarisation and measuring the PER in the PCF output. This is used to determine whether the output light is linearly or elliptically polarised. If the polarisation of the input light is aligned with one PCF principal axis we expect linear polarisation in the output and therefore the highest PER.

The input polarisation is rotated using the HWP and POL. The HWP could be used on its own to rotate the polarisation. However the use of the HWP and POL allows easy control of the



(a) Ratio of the total UV output signal 230 nm to 260 nm relative to the signal for aligned polarisers as one Glan-Taylor polariser is rotated. The solid line is the expected squared sinusoidal variation



(b) Residuals - deviations of the measured ratio from the theoretical ratio as a function of the angle

Figure 22: Rotating the Glan-Taylor polariser

input power. The output polarisation is measured using another HWP and a PBC both specified for use at 800 nm. The input beam is passed through a bandpass filter of 40 nm width centred at 800 nm. This both increases the pulse length and decreases the average power (further decrease is achieved using the input HWP and POL). So the pulse peak power and hence the non-linear effects in the PCF are considerably reduced. As will be shown in section 13.5, the degree of polarisation deteriorates to a large extent during propagation through the PCF. The highest output polarisation ratios are measured for low input powers, which suggests that some of the de-polarisation is due to non-linear effects.

Once the angle of the principal PCF axes relative to horizontally polarised input light have been found the PCF is rotated. A different alignment method would be to leave the PCF and to rotate the input light using the HWP and POL. However in many of the experiments these optical elements had to be removed either to maintain a low pulse chirp or to vary the pulse chirp.

12.3 Input pulse chirp

Chirp is a key parameter to adjust as, like the power, it can be used to control pulse compression in the PCF. In all experiments it is necessary to either keep the chirp constant whilst varying another parameter or to be able to vary the chirp whilst not altering any other beam parameters, such as the power or the polarisation. I will begin this section by briefly explaining the concept of chirp and then discuss how it is controlled in the experiments.

As shown in figure 18, the width of the spectrum is approximately 200nm and therefore the pulse is extremely susceptible to frequency dispersion. Different wavelengths in the pulse will experience a different refractive index when passing through a medium, and thus propagate at different group velocities. As an example of this we can consider a piece of BK7 glass. This has a refractive index of $n = 1.51629$ at 600 nm and a refractive index of $n = 1.5090$ at 900 nm [106]. This means that if the two wavelengths of light were propagated through 1 mm of BK7 glass they would be separated in time by approximately 55 fs at the output.

This dispersion leads to a change in the temporal shape of the pulse and also a variation in the frequency at different temporal positions across the pulse (the instantaneous frequency). The pulse is then said to be “chirped”. The effect of passing through a medium such as air or bulk glass will

be to temporally broaden a previously unchirped pulse by applying a positive chirp.

A positive chirp occurs when the longer wavelengths move to the front of the pulse and the shorter wavelengths to the back, a negative chirp is produced when the opposite occurs. The sign of the chirp produced will depend on the wavelength of the input light. For example, as mentioned in section 3, bulk silica has a ZDW at 1270 nm. This means that pulses at longer wavelengths will be negatively chirped by passing through silica and pulses at shorter wavelengths will be positively chirped. The connection between chirp and dispersion will be discussed shortly.

In the wavelength region containing the pulses from the laser, most glasses (e.g. fused silica, LakL21, SF10 and BK7 [98]) and air will produce a positive chirp. In order to produce a negative chirp Double Chirped Mirrors (DCM) are used (see appendix 16.1 for details and for other methods used to produce negative chirp).

Changing the length and instantaneous frequency of a pulse has consequences for its subsequent evolution in a PCF, as will be seen in section 13.4. This is used to control the generation of dispersive radiation and also to investigate how the pulse and the radiation it drives evolve.

In order to quantify the chirp a pulse develops as it passes through a medium we begin with the propagation constant. For light of angular frequency ω in a medium with effective refractive index $n(\omega)$ this is, as before, given by $\beta = n(\omega)\omega/c$. Expanding in a Taylor series about a central pulse frequency ω_0 leads to

$$\beta = \beta_0 + \beta_1(\omega - \omega_0) + \frac{\beta_2}{2!}(\omega - \omega_0)^2 + \frac{\beta_3}{3!}(\omega - \omega_0)^3 + \dots = \sum_{n=0}^{\infty} \frac{\beta_n}{n!}(\omega - \omega_0)^n. \quad (12.2)$$

Here the β_n coefficients are as defined in (5.1).

The β_1 term is the inverse of the group velocity of the light and hence the β_2 term quantifies the difference in velocity between different frequencies and therefore the pulse chirp. If a medium has a positive β_2 then it will introduce a positive chirp to a previously unchirped pulse and if a medium has a negative β_2 it will introduce a negative chirp. The higher order terms will also have an effect, however in most media the β_2 term dominates. The β_2 term is known as the GVD parameter and, in this thesis, it will be expressed in units of $\text{fs}^2\text{mm}^{-1}$. A medium with GVD parameter β_2 and length L is said to have a Group Delay Dispersion (GDD) of $\beta_2 L$ in units of fs^2 and will introduce a chirp to the pulse of $\beta_2 L$.

Before coupling the laser beam into the PCF it is possible to vary its chirp. This is done either by increasing or decreasing the path length of the light through air or different types of glass, or by the use of DCM. In both cases to a good approximation the effect of higher order dispersion can be neglected. For example for BK7 glass the term containing β_2 in (12.2) is approximately 60 times larger than the term containing β_3 (when considering the largest separation of pulse frequency ω from the pulse central frequency).

The effect of varying the path length through a particular medium on the pulse length is easily quantified if non-linear effects in the medium are small enough to be ignored. This is a good approximation to make for propagation through glass or air in the absence of any focusing of the beam.

In this case the NLSE (see (8.1)) can be simplified further, by removing the γ term. It can then be solved using the Fourier transform method [2] to find the amplitude of the electric field of the pulse. The final result for the form of the electric field amplitude $A(z, T)$ after a propagation distance z through a medium with GVD parameter β_2 is

$$A(z, T) = \frac{1}{2\pi} \int_{-\infty}^{\infty} \tilde{A}(0, \omega) e^{(\frac{i}{2}\beta_2\omega^2 z - i\omega T)} d\omega. \quad (12.3)$$

Where T is the normalised time parameter and $\tilde{A}(0, \omega)$ is the Fourier transform of the incident field,

$$\tilde{A}(0, \omega) = \int_{-\infty}^{\infty} A(0, T) e^{(i\omega T)} dT. \quad (12.4)$$

This is readily solved for the case of a pulse with an initially unchirped Gaussian temporal profile $A_{Gauss}(0, T) = \exp(-T^2/2\tau_0^2)$, leading to

$$A_{Gauss}(z, T) = \frac{\tau_0}{(\tau_0^2 - i\beta_2 z)^{1/2}} e^{\left(-\frac{T^2}{2(\tau_0^2 - i\beta_2 z)}\right)}. \quad (12.5)$$

Here τ_0 is a measure of the initial pulse length⁹. The pulse still has a Gaussian shape but the imaginary term in the exponent leads to a phase which varies with propagation distance. This phase term produces a variation in the instantaneous frequency across the pulse i.e a pulse chirp.

⁹ τ_0 is the temporal half width of the pulse when the pulse intensity is e^{-1} of its maximum value

The form of $A_{Gauss}(z, T)$ in (12.5) leads to the following equation for the variation in the pulse length $\tau_z(z)$ ¹⁰ as a function of the propagation distance [2],

$$\tau_z(z) = \tau_0 \sqrt{1 + \left(\frac{\beta_2 z}{\tau_0^2}\right)^2}. \quad (12.6)$$

As can be seen from (12.6) the smaller the initial pulse length, the greater the effect of the same combination of z and β_2 . For both positive and negative β_2 values the length of the pulse will increase as z increases an effect known as dispersive pulse broadening.

For the hyperbolic secant pulses used in the experiments $A_{Sech}(0, T) = \text{sech}(T/T_0)$, there is not such a simple analytical form for the pulse broadening, however the qualitative behaviour is similar. The Fourier transform of the hyperbolic secant pulse is given by

$$\text{F.T.}[A(0, T)] = \tilde{A}_{Sech}(0, \omega) = \frac{T_0}{2} \text{sech}\left(\frac{\pi}{2} T_0 \omega\right). \quad (12.7)$$

Inserting this into (12.3) and solving numerically allows the pulse length to be calculated. The variation in pulse length with $\beta_2 z$ turns out to be similar to the behaviour of a Gaussian pulse so that it is possible to use the Gaussian equation for pulse broadening as an approximation.

12.3.1 Measuring the GDD of optical elements

As explained in the previous section, the variation in the pulse chirp is achieved by changing the beam path length through air or glass or by introducing DCMs into the beam path. In order to quantify the pulse chirp, the dispersive properties of the optical elements used in the beam path need to be known.

This is achieved by adding and removing optical elements from the beam path and measuring the resulting pulse length. An autocorrelator (A.P.E pulseCheck) is used for these measurements, the details of how such a device works can be found in appendix 16.2. The changes in pulse length are then fitted to (12.6) to calculate the GDD values ($\beta_2 z$) for each element. The results for various optical elements are shown in table 1. Figure 23(a) shows the theoretical variation in pulse length as the GDD is varied and a selection of the experimental data with the fitted GDD values. The

¹⁰As for τ_0 , τ_z is the temporal half width of the pulse when the pulse intensity is e^{-1} of its maximum value

Optical element	GDD (fs^2) at 780 nm
Achromatic HWP (600 – 950 nm)	74
Achromatic Quarter Wave Plate (QWP) (600 – 950 nm)	36
Achromatic thin film POL (600 – 950 nm)	45
Laser output coupler wedge per extra mm moved into the beam	1.7
Pellicle beamsplitter ($2\ \mu\text{m}$ nitrocellulose membrane)	1.1
DCM per extra double bounce	-50
Glass slide (BK7 glass, $\sim 1\ \text{mm}$ thick)	50
695 nm long pass filter (3 mm thick)	80

Table 1: Measured GDD for each of the optical elements used to vary the pulse chirp. Where unspecified the GDD is for one pass through the element

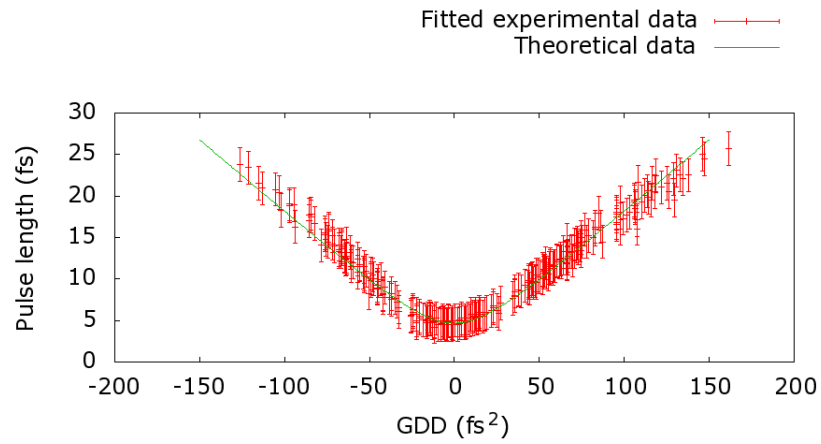
match is very good for smaller GDD values and only deviates slightly from the theory at larger values. This deviation can be seen clearly in the plot of the residuals 23(b) which are randomly distributed about zero in the central part of the graph but not at large negative or positive GDD values.

A more accurate calculation of the GDD values of the optical elements would be achieved by fitting the measured pulse length variation to numerical simulations of the hyperbolic secant pulse broadening. In addition the effect of TOD could also be included. This would improve the match between the theoretical and the measured data. However the majority of the experiments carried out using the chirp do not require such a high degree of accuracy.

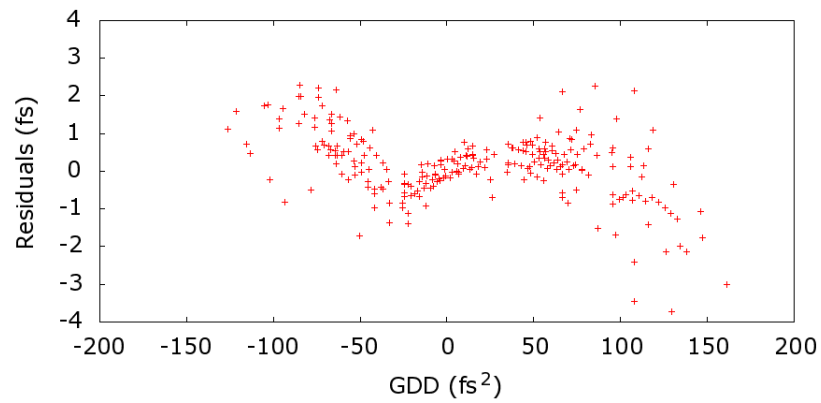
12.4 Coupling into the photonic crystal fibre

In this section I will describe some of the challenges encountered in coupling the light into the PCF and solutions to these challenges. A number of factors including the spectrally broad input pulses and the short PCFs used mean that the coupling process is not as simple as in other PCF set-ups and requires some detailed explanation.

The first coupling issues arise from the use of pulses with very broad spectra. The main difficulty is that such pulses are extremely susceptible to dispersion. In passing through any medium the pulse length will change due to the different velocities of the various frequency components in the pulse. Therefore it is not possible to use lenses to focus the beam as the large thickness of glass involved would broaden the pulse to an unacceptable degree. This solution to this is to use an Off-axis Parabolic Mirror (OAP) to focus the beam. These are a well known type of focusing



(a) Pulse length as the GDD is varied: theoretical and fitted experimental results - the fitting is accomplished by varying the GDD of the elements and using (12.6)



(b) Residuals - deviations of the measured pulse length from the fitted pulse length as a function of the GDD

Figure 23: Measuring the GDD of the optical elements (a) Pulse length as the GDD is varied, (b) Residuals

mirror, which introduces much less GDD into the beam path and is free of spherical aberrations (all parallel light rays focus to one point).

An additional problem with the use of lenses for focusing is chromatic aberration. This arises because different frequencies of light will be focused to different spatial positions by a lens. Again this issue is resolved by using an OAP to focus the beam. As the OAP relies on reflection to produce a focus, all frequencies will be focused to the same point.

The OAP we use for coupling into the PCF has a gold coating. The coating is used to optimise the reflectance in the region of the spectrum where the input pulse lies, i.e. the near IR.

When the beam is being focused as part of the initial experimental set-up or after significant changes have been made in the set-up, the focus spot will at first be reasonably large. In this case it is possible to use a commercial beam scanning device to measure the size of the focus and start to reduce its size by adjustments of the OAP and the mirrors steering the beam onto the OAP. The beam scanning device is only specified to measure beam sizes down to $2.5\ \mu\text{m}$ in diameter. In order to optimise smaller focal spots a different method is required.

The focus size is further optimised using a two photon technique. A silicon photo-diode is placed in the focus to detect the incoming photons. The photo-diode is sensitive in the range 220 nm to 360 nm, hence it can only detect two photon events from the input beam. These are non-linear events and therefore very sensitive to the intensity in the focal spot (and hence to the size of the focal spot). The photo-diode signal produced by the input beam is very weak compared to background light, it is distinguished using a Lock in Amplifier (LIA). This device, developed in the 1930s and 1940s [32, 93], is used to pick out small signals from a very noisy background. It uses the fact that, if two sinusoidal functions of different frequencies are multiplied together and integrated over a much longer time than the period of either function, the result will be zero. If however the two functions have the same frequency, the result of the integration will be half the multiple of the two amplitudes. In our case, a chopping wheel placed in the input beam before the PCF modulates the beam, and therefore the photo-diode signal, sinusoidally. The chopping wheel frequency is sent to the LIA as a reference and the LIA integrates over the product of the photo-diode signal and a sinusoidal function at the reference frequency. Any non-zero component in the result is due to the input beam rather than noise. In this way the focus size is adjusted to maximize the photo-diode signal by adjusting the optical elements before the beam focus. One drawback of this method is

that it does not give an absolute size for the focus, only relative improvement can be seen.

Once the focus has been optimized, a piezo stage is used to position the PCF in the focus. This positioning is aided by the use of a microscope positioned above the PCF. For a long piece of PCF the output power is easily measured using a power meter. The coupling efficiency is typically found to be around 20 – 30%. Thus for an 100 mW average power beam before the PCF (the laser output power is reduced after passing through all other optical components) the average power level in the PCF is estimated to be 20 – 30 mW . For a 12 fs input pulse (full width half maximum) and an 77 MHz repetition rate this leads to a peak power of 22 – 32 kW.

For shorter pieces of PCF the power meter is no longer suitable as a coupling aid. A significant proportion of the input light is able to pass around the PCF or through the cladding and is therefore detected by the power meter. In this case the microscope is used to move the PCF end towards the focus and rough alignment is achieved by observing the output from the PCF and looking for a characteristic pattern as the piezo stage is adjusted. I developed this pattern observation technique as a quick and simple way to achieve a high enough coupling efficiency to observe signals such as RR in the output which could then be used for further coupling improvement.

The characteristic pattern observed in the output as the PCF end passes through the focus is as follows, as the PCF cladding moves into the focus a bright red output is observed, as the core then moves into the focus the output dims, then brightens again as the cladding on the other side of the core moves into the focus. By looking for this characteristic dimming the core can be found. Once in this region where the output is dim, fine adjustments lead to a bright output in colours ranging from yellow to purple depending on the input pulse properties and degree of coupling. Further improvement in the coupling is achieved by observing the RR signal in the PCF output using a CCD spectrometer, this process is discussed further in section 12.5. After this series of steps the coupling efficiency is expected to be around 20 – 30 %, similar to the result for the long PCF. The uncertainty in the exact power coupled into the PCF will later be taken into account when quantitative results from the experiments are compared to simulation results acquired using specific input powers.

As an aside it is interesting to note that when a short piece of PCF is placed in the input focal point with the core slightly offset from the focus, for various discrete offset positions a particular “star” shaped mode appears in the output. The shape of the mode is exactly reproduced for the

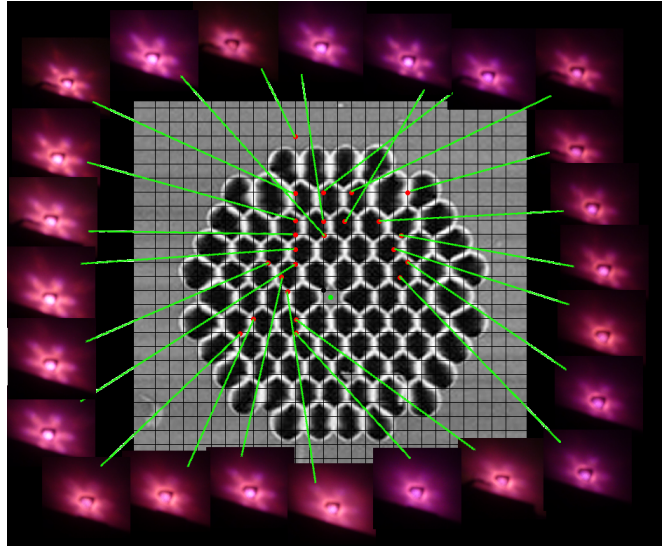


Figure 24: Beam shapes at the output of the NL-1.5-670 PCF as the PCF end is scanned across the focus

different positions although with varying levels of brightness. This may be due to a form of guiding through other secondary channels in the periodic structure of air holes in the cladding. Such guiding has previously been seen in a paper by Efimov et al. [6]. As in our experiment, they keep the focus spot in the same place and raster the PCF tip across. Rather than photographing the output spot, as we do, they measure the transmitted power. Their results clearly show that it is possible for light to be guided in the supporting structures between the holes in the cladding.

The photographic results from my experiment are shown in figure 24, along with an SEM image of the PCF end and the approximate position of the focus spot relative to the PCF core. Note that, in the output spot pictures, the central part of the beam has been blocked as it is considerably brighter than the rest of the spot and that the pattern only appears at the marked positions. The irregular distribution of the marked positions suggests that the PCF end may be damaged in some way such that light is not able to be guided in all supporting structures. In particular it appears that the lower right hand side of the PCF is not guiding any light. Another possible cause for the irregular distribution is that the piezo stage used to position the PCF drifted slightly during the

measurements, hence the positions recorded are only approximate.

12.5 Output detection

In this section some technical details will be described relating to the detection of signals from the PCF. Two sets of detection apparatus are used - one for the UV and one for the visible and near IR. Each has to fulfil certain criteria. They are required to have high and uniform spectral sensitivity over the regions of interest. In addition, for measurements of signal polarisation, it is desirable that they have the same sensitivity to each polarisation component.

The output from the PCF is collimated using an aluminium coated off OAP. The coating is a thin layer of protected aluminium on a substrate of non-protected aluminium designed to increase the reflectivity of the mirror over the UV, visible and near IR. In this case the OAP used (Edmund Optics) has reflectivity greater than 85% over the relevant spectral regions. As with the OAP used to focus the input light, using an OAP in the output rather than a lens removes the problems of spherical and chromatic aberration.

The beam is then directed either to a CCD spectrometer (Avantes AvaSpec) to measure signals in the visible and near IR or to a monochromator (Princeton Instruments) with attached single photon counter to measure signals in the UV. The CCD spectrometer allows real time measurements of the whole spectrum. The data acquisition system for the monochromator allows either the monitoring of the signal at a small range of wavelengths in real time or scans to be taken over a wider range of wavelengths.

A flip mirror is used in the output beam path to allow an easy transfer between coupling into the CCD spectrometer and coupling into the monochromator. In addition the mirrors used for the UV beam path are partially transparent to the visible and IR. It is therefore possible to couple the transmitted beam from one of these mirrors into a CCD spectrometer. This allows the coupling into the PCF to be monitored by observing the RR signal in the visible, whilst a monochromator scan is taking place.

The CCD spectrometer and its accompanying optics have a high sensitivity over the required spectral regions. The spectral response of the spectrometer grating is not completely uniform however the device has been previously calibrated by the manufacturer to take into account any

variation in sensitivity. In addition the spectrometer and coupling optics display negligible sensitivity to polarisation.

In the case of the monochromator and its accompanying optics the detection criteria are not so easily met. The edge of the spectral sensitivity of the monochromator and its coupling optics lies close to the phase matched wavelength of the NRR for some of the PCFs used. At this edge the spectral response becomes highly non-uniform and therefore a calibration procedure is required.

Measurements of the spectral sensitivity are taken using a Deuterium Halogen light source. This is initially measured using the CCD spectrometer (pre-calibrated) and then measured using the monochromator and its coupling optics. The results for an early experimental set-up are shown in figure 25(a). As can be seen, the high sensitivity region of the detection set-up is between 240 nm and 350 nm. This means that any phase matched NRR outside of this range may not be detectable. This initial calibration measurement also displays a series of fringes from 225 nm to 240 nm.

The non-uniformity and cut-off in the sensitivity in that region of the UV is unacceptable as this is the region in which most of the NRR signals lie. Therefore a new detection set-up was required using different optics to couple into the monochromator. A calibration of this set-up yields the results seen in figure 25(b). For longer wavelengths the results are similar to figure 25(a) hence only the short wavelength region of interest has been included. In addition the results are taken using a Glan-Taylor polariser in the beam to produce a beam horizontally polarised with respect to the optical table. The sensitivity cut off is now at a shorter wavelength and the variation in sensitivity is greatly reduced. The main improvement came from changing the mirrors used to direct the beam into the monochromator for a new set with a different reflective coating which have higher and more uniform reflectivity in the spectral region of interest.

The sensitivity of the detection set-up to different polarisations is also checked using the Deuterium Halogen light source (unpolarised) and the Glan-Taylor polariser. It is found that for light polarised horizontally with respect to the optical table the short wavelength decline in sensitivity occurs at a very slightly longer wavelength than for light polarised vertically with respect to the table. For longer wavelengths the sensitivity to each polarisation is approximately the same.

This sensitivity to different polarisations would be unacceptable if measurements of the NRR polarisation were to be carried out. However such measurements are not possible due to the small NRR signal strength combined with poor transmission of the Glan-Taylor polariser in that

spectral region. If it had been possible to take polarisation measurements then the detection set-up would have had to be modified to reduce the sensitivity to polarisation. Further measurements would be required to locate the optical elements responsible for the sensitivity and to replace them. Alternatively the polarisation sensitivity could be measured and all results corrected to take account of it.

As mentioned in section 12.4 the coupling efficiency could be optimised up to 20–30% efficiency using the RR signal. Both the production of the RR and the NRR increase with increasing power coupled into the PCF and therefore optimisation of their output indicates an improved coupling. However the RR is a considerably larger signal than the NRR and could be monitored in real time using the CCD spectrometer. In addition the NRR output signal strength was further complicated by factors such as loss which will be discussed in section 13.3. Hence the RR was the best signal to optimise and monitor the coupling efficiency. This could be achieved by observing the RR signal on the CCD spectrometer and adjusting the piezo stage to move the PCF into the focus.

12.6 Measuring the photonic crystal fibre properties

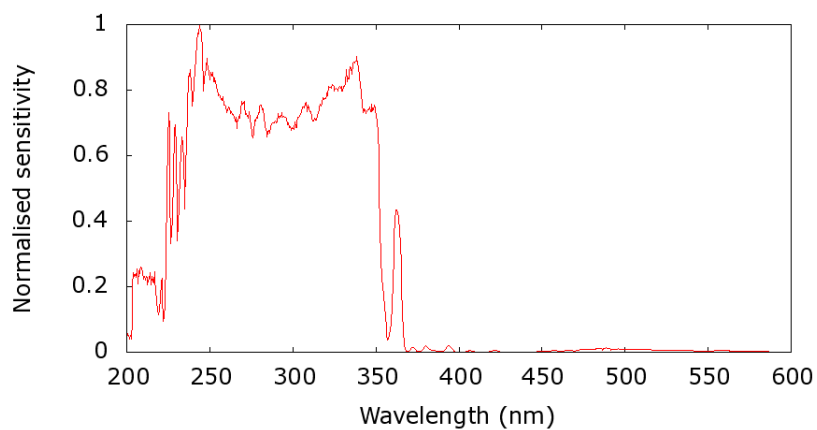
Accurate predictions of the pulse evolution in the PCF require knowledge of the dispersive properties of the PCF. This is particularly important in predicting where in the spectrum signals such as the RR and NRR will occur. In this section I will describe the methods employed to measure the dispersion profiles of the PCFs we use.

All of the PCFs are labelled with a particular ZDW, however this is an approximate value which usually does not correspond to measured values. Hence although the PCFs will be referred to by these labels, they do not reflect the actual PCF properties.

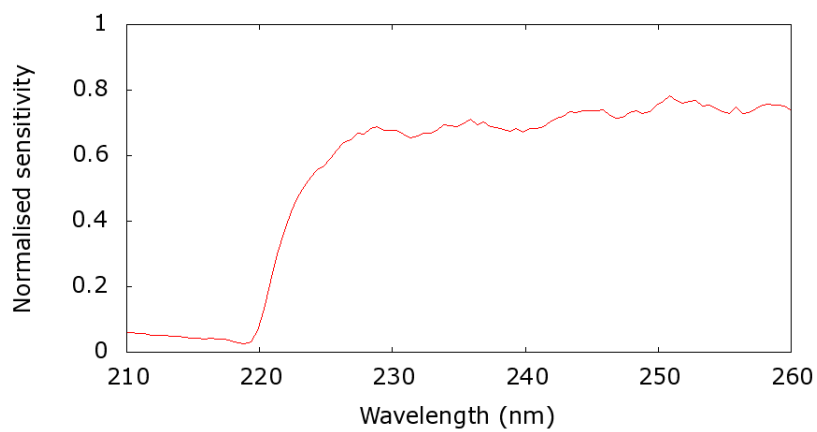
The two methods used to measure the dispersion profiles of the PCFs employed in the experiments are: fitting to the RR peak at threshold and using external data. All of the measurements and calculations were carried out by other people in the research group or in other research groups, therefore they will only be briefly outlined.

12.6.1 Method one - Resonant Radiation phase matching

This method involves recording the PCF output spectrum and measuring the wavelength of the



(a) Old detection set-up



(b) New detection set-up

Figure 25: Normalised UV detection set-up sensitivity. (a) Sensitivity using old detection set-up. (b) Sensitivity using new detection set-up, horizontal polarisation only

RR signal as a function of the input pulse wavelength.

As described in part II the RR obeys a phase matching condition. This is expressed as in (8.15) or (10.2). In the case of the former if the input power is negligible the equation becomes

$$\sum_{n \geq 2} \frac{\beta_n}{n!} (\omega_{RR} - \omega_S)^n = 0. \quad (12.8)$$

The lowest input power for which an RR signal is seen, will produce a signal at a wavelength (frequency) which to a very good approximation solves the above equation. As the equation shows the wavelength (frequency) of the RR signal will depend on the frequency of the input pulse ω_s .

A femtosecond laser (Delmar Trestles) is used for this experiment. The laser produces pulses of approximately 70 fs duration, which can be varied in wavelength from 750 – 900 nm. It is this ability to vary the wavelength which means that this laser is used rather than the FemtoSource Rainbow laser used in most of the experiments. For the PCF under test a series of output spectra are recorded for different input pulse wavelengths. At each wavelength the power is increased until the first appearance of the RR signal in the output.

The results for ω_{RR} as a function of ω_S are then fitted using a model for the PCF dispersion. The model used treats the PCF as a single strand of silica in air with a particular radius [13, 141]. The propagation constants β of the modes of the PCF are found from the eigenvalue equation (3.1) discussed in section 3. In this case n_2 the cladding refractive index is set to the index of air. Once β is known (12.8) is used to find the RR phase matched frequency. The core radius a from (3.1) is used to fit the RR frequencies from the model to the measured values.

An example of the results from this experiment for one PCF is shown in figure 26 (data measured in our lab by Sven Rohr). The figure shows the measured and fitted RR wavelengths as a function of the input pulse wavelength. The data shows excellent agreement with the fit even though only one fitting parameter (the strand diameter) has been used. The standard deviation of the data is less than 2.5 nm.

This method has a few sources of uncertainty, the RR signals at threshold are very small and can be difficult to measure and the pump pulse has a bandwidth of about 10 nm introducing some uncertainty into its measured wavelength. Also the model used to fit the measured data has only one fitting parameter and relies on the PCF having a high air fill fraction in the cladding. Therefore

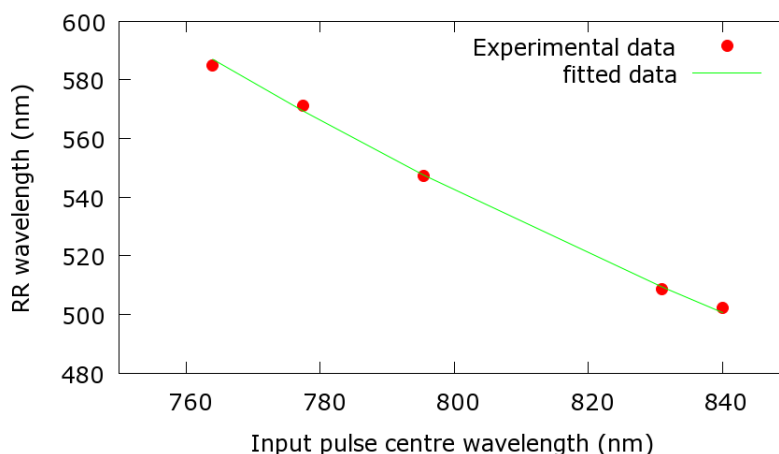


Figure 26: Measured peak wavelengths (wavelength at the maximum spectral density) and fitted data for the RR method. NL-1.6-615 PCF

not all of the PCFs used in the experiments can be fitted using this model. If the air holes in the photonic crystal cladding are too small then the struts connecting to the core cannot be neglected and it is not possible to treat the core as an isolated strand. One example of a PCF which could not be measured with this method is the NL-PM-750B. Its dispersion curve was measured using method two described below.

Despite the sources of uncertainty the method is still expected to lead to accurate predictions of the NRR wavelength. This is because the NRR lies in the UV and the refractive index in this spectral region changes rapidly with wavelength, leading to good wavelength discrimination. This effect reduces the impact of the uncertainty in the input pulse wavelength leading to an estimated uncertainty of only 1 nm in the UV.

12.6.2 Method two - external data

For some PCFs it is not possible to use method one to measure the dispersion. For these PCFs the strand model used in method one is not applicable. The GVD parameter β_2 of one of these PCFs (NL-PM-750B) has been measured by the group of Biancalana in Erlangen and also by the manufacturer (Crystal Fiber - now part of Blaze photonics), in both cases for the spectral region 600 – 1500 nm. The refractive index of the PCF is estimated using the measured data and the refractive index in the UV, calculated using the Sellmeier equation, to fit the index. The index in

the UV is expected to be close to the index for bulk silica as the waveguide contribution will be small, hence the Sellmeier equation can be used. This dispersion curve is expected to be highly accurate due to the very precise measurements taken by the Erlangen group.

13 Results

In this section I first present one of the key results in this thesis, the first experimental observations of NRR. This demonstrates the first example in optics of a mixing between positive and negative frequencies. Signals at both the RR and NRR predicted wavelengths are observable in the output spectra of a PCF.

Having presented results showing a signal at the expected NRR wavelength we would then like to investigate the signal further. As a first step I will discuss various other potential sources of radiation in the UV and explain why the signal cannot be due to any of these. Once this has been established we would like to know how the generation of NRR depends on the compression of the input pulse. We postulate that in order to drive the NRR a component of the pulse oscillating at its phase matched wavelength is required. To investigate this we need to be able to observe the spectral broadening occurring as the pulse compresses in the PCF. We would also like to be able to control the degree to which the pulse compresses and hence how far its spectrum broadens in order to see the impact of this on the NRR.

There are several different methods to achieve both of these aims and these will be discussed in the next few sections. Observation of the extent of the spectral broadening is difficult to achieve as the effect is transient. We need compression to occur at the end of the PCF in order to measure the maximally broadened spectrum in the output. We can cut the PCF to an appropriate length although this is inefficient and requires a different PCF length every time the input pulse parameters are varied. Alternatively by varying the input power or input chirp we can move the position of compression in the PCF, this is a more efficient method and variation of both can also be used to control the degree of pulse compression. In sections 13.3 and 13.4 we will see which out of power and chirp is the best method to use to investigate and control pulse compression. A further subsection looks at the impact of polarisation providing further insights into the nature of the NRR and RR.

It is important to note at this point that the focus of most of the experiments is NRR not RR.

PCF	Axis	ZDW (nm)	RR wavelength (nm)	NRR wavelength (nm)
NL-1.5-590	1	685 ± 13	516 ± 18	229 ± 2
NL-1.6-615	1	694 ± 10	534 ± 10	232 ± 1
NL-1.6-615	2	697 ± 10	542 ± 10	233 ± 1
NL-1.5-670	1	665 ± 10	478 ± 10	221 ± 1
NL-1.5-670	2	666 ± 10	480 ± 10	222 ± 1
NL-PM-750B	1	733 ± 10	582 ± 10	247 ± 1

Table 2: ZDWs and the predicted RR and NRR wavelengths for negligible input power, calculated using method one (NL-1.5-590, NL-1.6-615, NL-1.5-670) or two (NL-PM-750B)

As discussed in section 5.1 RR is a strong signal which has been measured many times before. Results for RR will be presented alongside results for NRR for comparison and to provide a link with the established work in the field of RR however greater critical analysis will be applied to the NRR as it is a new discovery.

13.1 Examples of RR and NRR

In this section for one PCF I present output spectra showing the NRR at the predicted wavelength (figure 27). This measurements lends support to the idea that a coupling can exist between positive and negative frequencies leading to previously undiscovered phenomena such as NRR. For the same PCF I also show the RR signal (figure 28) and compare its wavelength shift with power to theoretical expectations.

Predictions for the NRR and RR wavelengths (at negligible power) for different PCFs are shown in table 2. These predictions are made using the phase matching condition and the dispersion profiles measured using method one or two from section 12.6. Although data from only one PCF (NL-1.6-615) is presented in this section we also measured NRR at the predicted wavelength for three of the four PCFs listed. The predicted NRR wavelength for the NL-PM-750B is at longer wavelengths than the other PCFs and lies in a region with other stronger signals hence it was not possible to measure the NRR from this PCF.

As a note on the predictions in table 2, the PCFs are slightly birefringent thus each principal axis has a different dispersion profile and hence different predicted phase matched RR and NRR wavelengths. For the NL-PM-750B and the NL-1.5-590 we only have data for one axis of the PCF. In the latter case the PCF is expected to have a similar birefringence to the NL-1.6-615 and

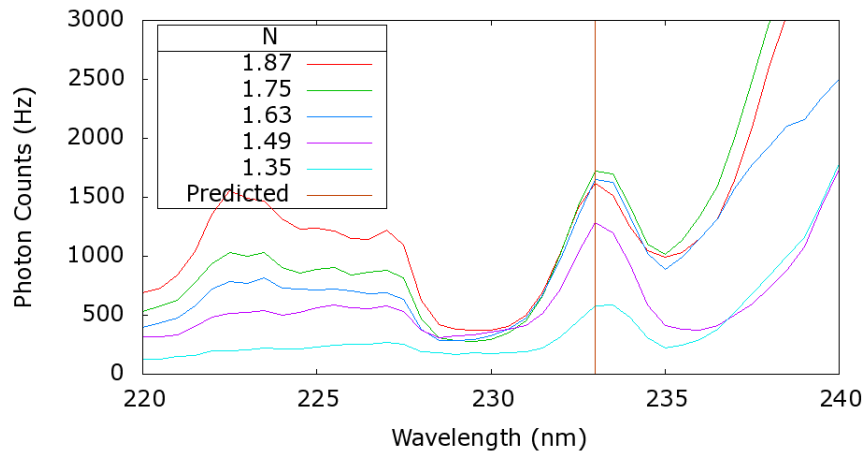


Figure 27: Experimental UV output spectra for the NL-1.5-615 PCF with varying input pulse soliton order N

the NL-1.5-670 PCFs and hence a similar small difference for the axis two ZDW, RR and NRR wavelengths. The uncertainty for each of these values has been listed as larger than for the NL-1.6-615 and the NL-1.5-670 PCFs in order to take into account the uncertainty in which axis is being used experimentally.

The NL-PM-750B is a polarisation maintaining PCF so it will have a deliberately higher birefringence and larger differences are expected between axis one and axis two.

Figure 27 shows example UV output spectra from the NL-1.6-615 PCF for different input pulse powers (shown in terms of N as defined in (8.4)). The vertical line indicates the predicted NRR wavelength for this PCF and a clear signal is seen at this wavelength. The signal is small for low values of N and initially grows as N increases before decreasing in height slightly for the largest N value. The variation in the centre wavelength of the peak is negligible over the range of N investigated. The variation of the NRR with power will be discussed in section 13.3, the key point from these results is that there is a signal at the predicted wavelength. In section 13.2 I discuss why this signal cannot be due to other sources of radiation in the UV which allows us to conclude with reasonable certainty that it is NRR.

The UV output spectra for the NL-1.5-590 PCF and the NL-1.5-670 PCF also have a signal at the predicted NRR wavelengths for those PCFs. The signal behaves in a similar way to the peak in figure 27 when the power is varied.

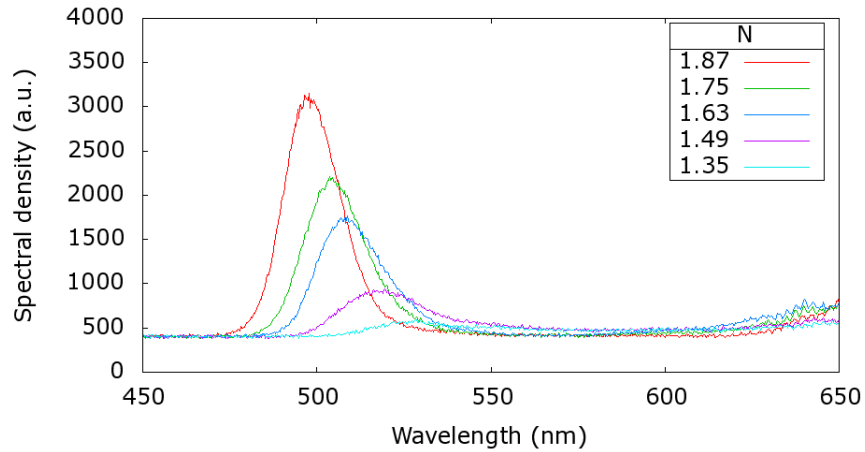


Figure 28: Experimental visible output spectra for the NL-1.6-615 PCF with varying input pulse soliton order N

Figure 28 shows example visible output spectra from the NL-1.6-615 PCF also for different input pulse powers. An isolated peak can be seen which grows and shifts to shorter wavelengths as the power increases. Similar results are found for the other PCFs listed in table 2.

In both of the above figures the powers are expressed in terms of N (as defined in (8.4)) the order of soliton that would be produced for that power. In that equation P_0 is the peak power of the pulse calculated from $P_0 = P_{av}/\nu T_{FWHM}$, where P_{av} is the average power of the light coupled into the PCF estimated from the measured input power and a 20% coupling, ν is the laser repetition rate and T_{FWHM} is the full width half maximum of the pulse intensity related to T_0 by $T_{FWHM} = 2\ln(1 + \sqrt{2}) T_0$. In each case a PCF of approximately 5 mm length was used ¹¹. As described in section 12.2 the input light is linearly polarized and the PCFs are aligned so as to excite only one principal axis. The input chirp is kept constant and close to zero as the power is varied.

The variation in the RR wavelength with power was discussed in section 10 and has been measured by many different research groups over the years. In figure 29 I present results from one PCF for measured and theoretical RR wavelengths as the power varies. The theoretical results are calculated using the dispersion profile from method one of section 12.6 and the good match between data and theory suggests that the dispersion profile is reasonably accurate. Similar results

¹¹The justification for using such short pieces of PCF will be discussed further in section 13.4

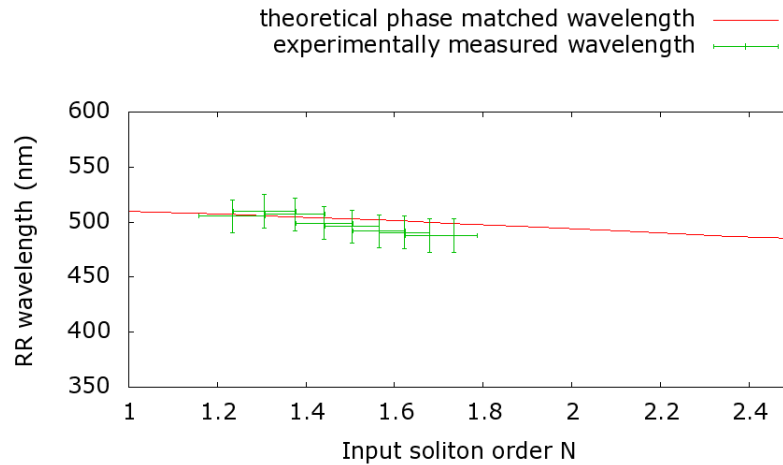


Figure 29: Experimental results for the RR peak wavelength (wavelength at the maximum spectral density) with varying input pulse soliton order N along with the predicted RR values for the NL-1.5-590

are found for the other PCFs in table 2. The error bars are a result of uncertainty in the exact coupling into the PCF and also uncertainty in the exact wavelength of the RR peak. Discrepancies between the data and the theory may also arise from limits in the model used in method one. As discussed in section 12.6 method one only uses one parameter for fitting and its assumption relies on a high air fill factor in the cladding.

13.2 Alternative explanations for the UV peak

In order to lend further weight to the theory that the peak in the UV is NRR it is necessary to show that the signal is not due to other effects which can produce light in the UV. One such alternative explanation is that the UV peaks are due to scattering in the monochromator and arise from radiation at longer wavelengths entering the detector. Another is that the signal is produced by THG and a third explanation is that the signal is produced by FWM.

The first of these explanations is unlikely as an intense beam would be required to scatter enough light to produce the signals seen in the UV and the amount of light entering the monochromator is very small. We can rule it out using narrow band UV filters in the PCF output. If the UV output is due to spurious monochromator signals from longer wavelengths then with the filter in we would expect a negligible UV signal. An example of such a measurement is shown in figure 30. A

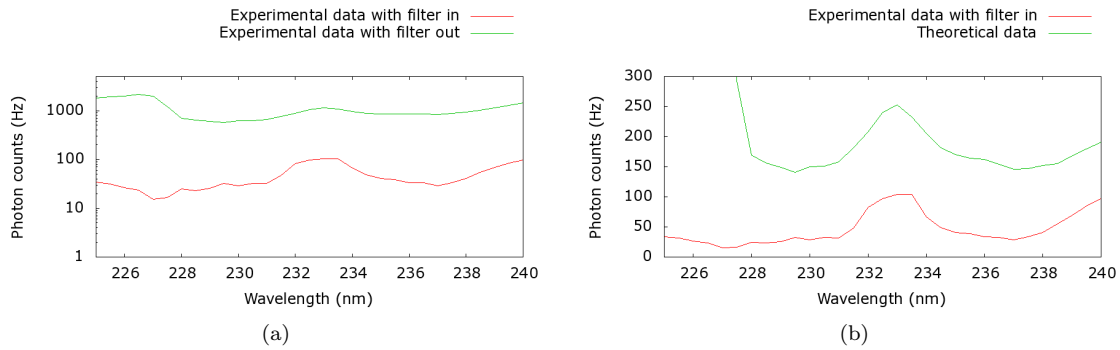


Figure 30: Experimental UV spectra NL-1.6-615 PCF. (a) Spectra with and without the 229 nm bandpass filter in the output. (b) Spectrum with the filter in compared to the spectrum without the filter multiplied by the specified filter transmission.

5 mm piece of the NL-1.6-615 PCF is used and UV output spectra are recorded with and without a bandpass filter in the output (Andover filter centred at 229 nm with a bandwidth of 21 nm and a peak transmission of 25%).

The results in figure 30(a) show that without the filter there is a peak in the UV at the predicted NRR wavelength. With the addition of the filter this peak decreases in height by approximately a factor of 10. In order to determine whether this decrease points to spurious longer wavelength signals we also need to compare the results to the transmission of the filter over that wavelength range in the UV. This is done in figure 30(b), which compares the spectrum with the filter in, to the spectrum with the filter out multiplied by the specified filter transmission. There is a small discrepancy between the results, the experimentally measured peak height with the filter in is approximately 2.5 times smaller than expected from the filter transmission. However the results are close enough to indicate that at least a large proportion of the UV peak is not due to longer wavelengths scattering in the monochromator. The discrepancy may be partially due to a change in the coupling into the monochromator when the filter is inserted. As noted in section 12.2 figure 22, small deviations in the beam direction caused by rotating the Glan-Taylor polariser cause significant changes in the coupling into the monochromator. Likewise inserting a filter will cause some beam deviation and reduce the coupling. However the results in figure 30 may also indicate that there is a small component in the signal at the NRR wavelength which is due to scattering.

A second alternative process is THG where three input pulse photons combine to produce one photon at a higher frequency. This process, including its phase matching condition, is discussed in

more detail in section 4.2. The process can be phase matched in our PCFs if the pulse photons are in the fundamental mode and produce a third harmonic in a higher order mode. Alternatively the pulse photons could be in a higher order mode and produced third harmonic in an even higher order mode.

In order to produce third harmonic radiation via $3\omega_1 = \omega_3$ in the region of the UV where the NRR lies (220 – 245 nm) the input pulse must have a component between 660 nm and 735 nm. The laser output does have components in this spectral region however these are mostly removed by inserting a long pass filter into the input beam (Comar 695 nm filter).

Figure 31(a) shows the IR output spectra from the NL-1.5-590 PCF with and without the filter in the input. The filter introduces additional chirp but this has been compensated for to ensure that in both cases the chirp is equal. The spectra show that the filter removes the short wavelength edge of the output pulse spectrum. Figure 31(b) shows the corresponding UV output spectra. Some components in the UV also reduce when the filter is added however the peak at the NRR wavelength remains and changes little in height. This indicates that the signal is not due to THG. Further evidence for this could be found by studying the mode of the output light at the NRR wavelength. The programme mentioned in section 4.2 can be used to calculate, for the fundamental and higher order modes, the variation in the PCF refractive index with wavelength. This can be combined with the phase matching condition to find out if there is a solution to the THG phase matching condition at the NRR wavelength and if so in which higher order mode it would have to be. The programme can also be used to find the shape of the mode and this could be compared to experimental results.

A third alternative source of radiation driven by pulses would be FWM, this type of process was discussed further in section 4.3. Two degenerate pump waves in the IR would have to produce a signal in the UV and an idler at longer wavelengths. By studying the dispersion relations of our fibre we can conclude that it is not possible that FWM is responsible for the UV peak at the NRR wavelength because energy conservation and phase matching cannot be achieved for the PCFs and the input pulses used.

In conclusion we have seen that the signal in the UV cannot be explained by scattering, THG or FWM. This together with the fact that for different PCFs the signal appears at the predicted NRR wavelength lends support to the idea that it is NRR generated by higher order dispersion

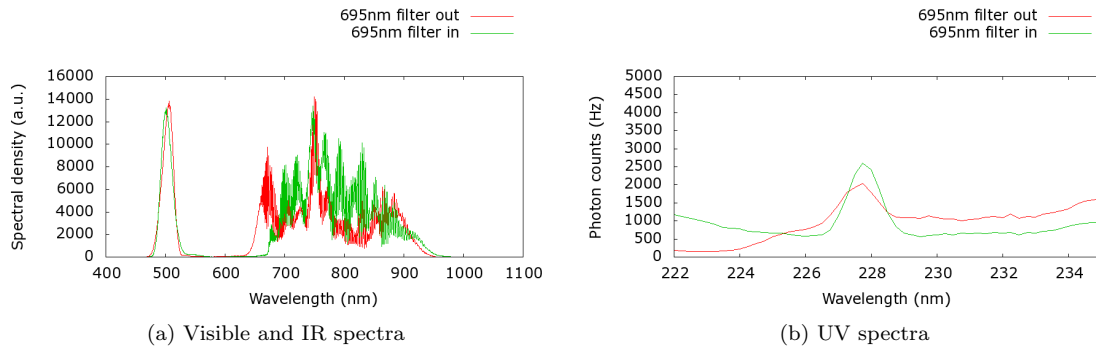


Figure 31: Experimental visible, IR and UV spectra with and without the 695 nm long pass filter in the input beam. NL-1.5-590 PCF

acting on the input pulse.

13.3 The effects of input power on pulse compression, NRR and RR

In this section I will describe the results of some experiments varying the input pulse power. We expect the power to affect pulse compression, which can be used to achieve the goals stated at the start of section 13. Specifically we expect to be able to use the power to affect the position of maximum pulse compression in the PCF and the degree to which the pulse compresses. This can be used to investigate the dependence on NRR on spectral broadening and also to observe its evolution. In the latter case it is at the point of maximum compression that the RR and NRR are generated hence by moving its position we vary how far the two types of radiation must propagate before the PCF output. Additionally, moving the point of compression towards the end of the PCF allows us to minimise the distance propagated by the NRR and RR and hence minimise the loss experienced by the radiation. This is particularly important in the case of NRR as it experiences high losses, this will be discussed further in section 13.4.4. This method of moving the compression point by tuning the input power has been used previously by other groups to investigate pulse evolution and compression and to ensure that the shortest pulse length is reached at the end of the compressing medium [45, 81].

The impact of power on RR has been studied by many groups and has been seen to shift the RR phase matched wavelength and to affect the generation efficiency of the RR. The interesting question is whether it will affect NRR in the same way. We have already seen in section 13.1

that the wavelength of the NRR does not shift significantly with varying input power and that the height of the NRR peak does not always increase with increasing input power. These results must be compared to the expectation that generation efficiency of both RR and NRR will increase with increasing pulse power. This is due to the increased effect of SPM for higher peak powers which leads to greater pulse spectral broadening. The link between SPM and spectral broadening has been explored previously in part II. As the generation efficiencies of RR and NRR are both expected to depend critically on there being a component of the input pulse oscillating at their phase matched frequencies, increased spectral broadening will lead to greater production rates of RR and NRR.

As we will see in this section, varying the power to move the point of maximum pulse compression can only be used to qualitatively investigate pulse compression and RR and NRR evolution because, as explained previously, any change in the power will also impact the spectral broadening and generation efficiency of NRR and RR. This limits the usefulness of the power variation as a method for moving the compression point. In addition the range of powers required to move the compression point over more than a few millimetres exceed those capable of being produced by the laser. This power range will be investigated using the pulse simulation programme. A better method for moving the compression point is to vary the pulse chirp which will be described in section 13.4.

13.3.1 Simulation results

In order to demonstrate how the power affects the pulse compression and spectral broadening I will present simulations showing the evolution of a pulse over a short piece of PCF. I will first discuss how the input pulse spectrum changes as the pulse propagates and then look at the generation of RR and some other features of the evolution.

Figure 32 shows the spectral evolution of a pulse for different input pulse powers (labelled in terms of the parameter N). For the lowest N the spectrum width remains approximately constant over the whole propagation distance. In this case the effect of SPM is weak and the PCF dispersion dominates the pulse evolution. The pulse broadens in time due to the dispersion further reducing the peak power and the effect of SPM, hence no spectral broadening occurs. For $N = 1$ the spectrum again does not expand, this is expected and is due to the exact balance between SPM

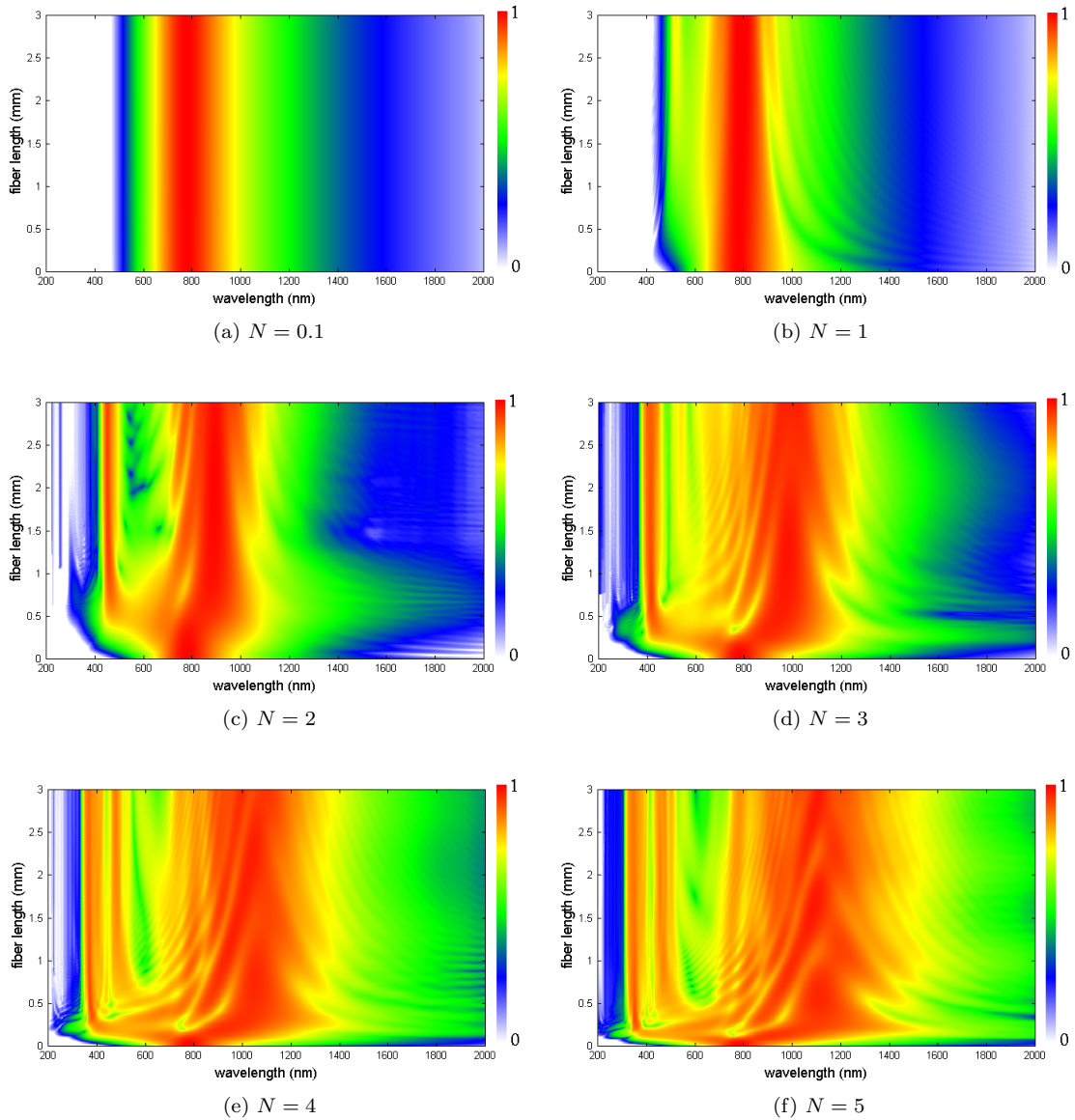


Figure 32: Simulation results - Log scale spectral evolution of a 7 fs hyperbolic secant pulse over 3 mm for different input pulse soliton orders (N). For each plot the colour scale runs from 0 to 1 where 1 is the maximum recorded spectral density for the individual plot

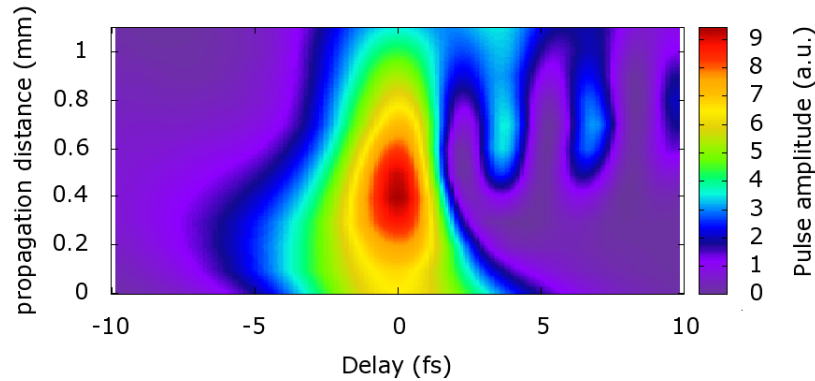


Figure 33: Simulation results - Colour scale plot of the temporal evolution of the pulse amplitude over 1.1 mm for a hyperbolic secant input pulse with an initial length of 7 fs, a soliton order of $N = 2.25$ and zero initial chirp

and GVD.

For $N > 1$ the spectrum expands over a short propagation distance and then contracts again. The extent of the spectral broadening becomes larger as N increases due to the increased effect of SPM. The position of the broadest spectrum also varies, as N increases it moves towards the start of the PCF. After the first spectral broadening the evolution in figure 32 becomes more complicated for increasing N as higher order effects start to play more of a role. The spectrum broadens and contracts multiple times in an effect known as breathing. The periodic evolution of higher order solitons has been discussed in section 8.2 although in our case the higher order effects further complicate matters by perturbing the soliton and potentially leading to soliton fission, which will be discussed shortly.

The spectral broadening and contraction occur as the pulse temporally compresses and then expands again. This is shown in the colour scale plot in figure 33 which shows the temporal evolution of an $N = 2.25$ pulse over 1.1 mm or propagation. The initial pulse has a full width half maximum of 7 fs, which decreases to just under 3.4 fs by 0.6 mm and then increases again ¹².

We now turn to the generation of RR in figure 32. A narrowband spectral component appears in the visible as the pulse propagates. This is the RR, which is driven by the pulse when its spectrum

¹²It must be noted that the simulation programme is only designed for pulses down to 10 fs in length, however the compression behaviour is as expected and agrees with the experimental results that will be presented later

includes a component at the RR phase matched wavelength. As explained in section 10 the RR phase matched wavelength decreases as the input pulse power increases hence for larger N the RR occurs at shorter wavelengths. The RR is generated in all cases except $N = 0.1$. For $N = 1$ even though no spectral expansion occurs the original pulse spectrum is wide enough to overlap the RR wavelength and drive the radiation.

Initially the RR is spectrally connected to the pulse however within half a millimetre of propagation the pulse spectrum has contracted again leaving the RR as an isolated peak. Once generated the RR remains at the same wavelength throughout its propagation. The RR will be affected by dispersion and hence its peak power will decrease as it continues to propagate, however over the distances shown in figure 32 this decrease is not noticeable.

The generation of RR from input pulses with $N > 1$ is complicated by soliton fission. As discussed in section 4.1 a higher order soliton (of order N) is composed of N fundamental solitons. Effects such as higher order dispersion and higher order non-linearities cause the pulse to break apart releasing its constituent fundamental solitons. Each of these will drive the generation of RR and NRR if they have components oscillating at the phase matched frequencies. The first soliton released in the breakup will have the greatest peak power [62], therefore the largest RR and NRR signals are expected to be due to this pulse. Additionally each constituent soliton released will have a slightly different central wavelength and hence phase match to RR and NRR at different wavelengths.

Soliton fission is expected to occur after a propagation distance of approximately $L_{fission} = L_D/N$ [136]. For the PCF and pulse parameters used in the simulation this means that the fission will occur between 0.12 mm for $N = 5$ and 0.30 mm for $N = 2$. In the spectra for $N > 1$ we see SPM induced spectral broadening starting at distances less than $L_{fission}$ and then the generation of an RR signal. At further propagation distances we see additional signals generated in the visible at longer wavelengths compared to the original RR signal. This is the expected behaviour for a higher order soliton undergoing fission into multiple pulses which can each drive RR. For large values of N we do not see N visible signals, either the original pulse has not completely broken apart yet or it has and the resulting fundamental solitons are too weak to generate observable RR.

The NRR is not present in the simulation results. This is because in its current form it is not possible to include the negative branch of the dispersion relation in the PCF parameters used

in the simulation. Therefore the NRR solution to the phase matching condition cannot be found. However the simulations do demonstrate qualitatively that it is possible for the input pulse spectrum to expand into the UV and therefore to drive the generation of NRR.

Over longer propagation distances we would expect to see other effects occurring such as a further shift of the pulse to longer wavelengths due to Raman scattering. In the simulation programme it is possible to turn the Raman effect off and this made little difference to the spectral evolution over the propagation distance being considered here. In addition the effect of self-steepening could be turned off in the simulation programme. As with the Raman effect this had little impact for the parameters and propagation lengths used.

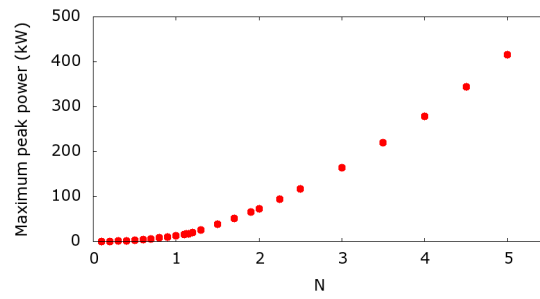
We now turn to further analysis of the effect of power on pulse compression. In the next section I compare these results from the simulations to the pulse compression observed in the experiments and the generation of RR and NRR.

We characterise the pulse compression in a PCF by three parameters - the compression factor $F = T_i/T_{min}$, the quality factor $Q = P_{max}/P_0F = P_{max}T_{min}/T_i$, and the position in the PCF at which the maximum compression occurs. Here T_i is the initial pulse length, T_{min} is the minimum pulse length reached when the pulse compresses, P_0 is the initial peak power and P_{max} is the maximum peak power reached. The quality factor is a measure of the total energy contained in the compressed pulse relative to the energy in the original pulse.

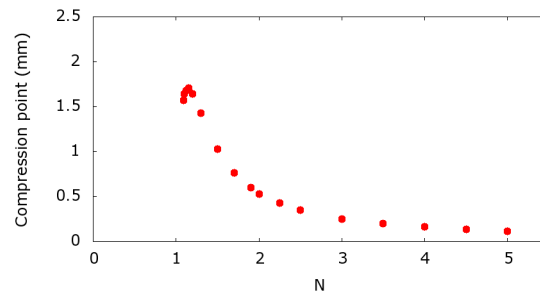
The variation of P_{max} , the position of compression, F and Q with N are shown in figure 34. For $N < 1$ there is no pulse compression and the minimum pulse length and maximum peak power are those of the input pulse. As N increases above $N = 1$ the minimum pulse length sharply decreases and F increases, indicating that the pulse is now able to temporally compress due to the combined effects of SPM and GDD. Further increases in N lead to the minimum pulse length reaching a steady value just below 3 fs¹³ and F reaching a steady value of about 2.5.

If the NLSE is used to predict the variation of F with N , the result is $F \sim 4.1N$ [1], which is clearly not the case in the simulations. This is due to the presence of higher order effects in particular higher order dispersion which causes soliton fission limiting the degree of pulse compression that is possible [135]. Raman shifting and self-steepening will also play a role but, as mentioned previously these can be turned off in the programme with minimal effects on the pulse compression.

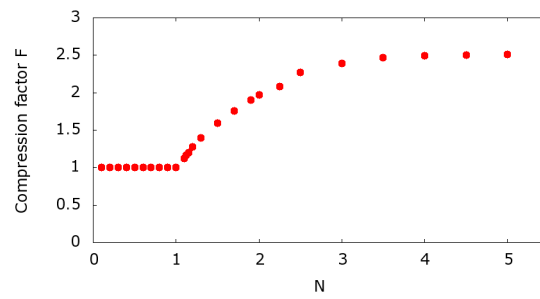
¹³Again it must be noted that such short pulse lengths are beyond the range the programme is designed for



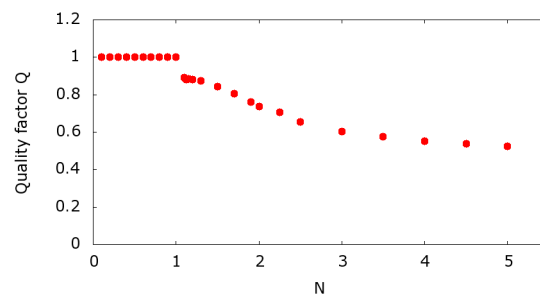
(a)



(b)



(c)



(d)

Figure 34: Simulation results - Variation in the pulse compression parameters with N . (a) Maximum peak power. (b) Position of maximum compression in the PCF. (c) Compression factor F . (d) Quality factor Q

As a side note this shows that simply increasing the pulse power is not a suitable method to achieve the steepest pulses. This is of particular importance in designing experiments to generate radiation which depends critically on the driving pulse steepness. One such type of radiation is the optical analogue of HR which was discussed in section 6. As the higher order dispersion is the main factor limiting compression PCFs with flat dispersion are required to produce the shortest pulses.

As would be expected the maximum peak power increases with increasing input N . The quality factor decreases, tending towards a steady value below 0.5. This is due to a pedestal forming around the pulse as it compresses, which will contain some of the original energy [2]. The pedestal forms because the GVD introduces a linear chirp across the whole pulse whilst the SPM induced chirp is only linear across the central region, therefore it is only in this region that the two effects can ever perfectly balance allowing efficient compression. The quality factor will affect the RR and NRR generation as the energy of the spectral component of the pulse at the RR and NRR phase matched wavelengths will be affected by the total energy of the compressed pulse.

The position of maximum compression displays an interesting behaviour. As N increases above 1 and the pulse is first able to compress, the point of compression initially moves to longer propagation distances. The greatest propagation distance for the compression is for $N = 1.15$ - the pulse reaches a minimum length of about 5.8fs at a distance of just over 1.7mm from the start of the PCF. Further increases in N move the compression point back towards the start of the PCF levelling off below 0.15 mm. This pattern occurs due to the changing balance between SPM and GDD as N increases.

The variation seen in figure 34(b) indicates how it is possible to use the power to qualitatively investigate the RR and NRR evolution. By varying the input power to change from $N = 1.15$ to $N = 2$ (achievable with the experimental equipment available) it is possible to move the compression point by almost 1.2 mm. This distance can be increased by using different input pulse parameters. For example, the same simulations were carried out using a 12 fs pulse length and over the same input power range the compression point could be moved by almost 3.5 mm. Also using a large positive input chirp increases the effect on the compression point of varying the power. However even with these increases the distance over which the compression point can be moved is still significantly smaller than that which is possible by varying the chirp, this will be seen in section 13.4.

A further issue with using the power to move the compression point is that as seen in figure

34(a) and figure 32, the peak power and the extent of the spectral broadening change significantly with changing input power. Hence the method is limited as a means of investigating RR and NRR evolution unless corrections can be made for the variation in their generation efficiency. However these large changes mean that varying the power is a useful tool for investigating the effect of the degree of pulse compression on the generation of NRR and RR.

The simulations in this section are achieved using a split step Fourier tool (RP ProPulse) [101]. The input pulse used is a 7 fs long hyperbolic secant pulse with zero chirp chosen to match the experiments as closely as possible. The evolution is only recorded over 3 mm, this is sufficient to capture the pulse temporal compression for the range of pulse parameters used. The PCF parameters used in the simulations (i.e. the dispersion curve) are taken from the NL-1.5-590 PCF, qualitatively similar results are obtained using the other PCFs.

In conclusion the simulation results have qualitatively matched our expectations in terms of spectral broadening and RR generation. The broadening is mainly due to SPM for small N and for large N it is also influenced by higher order dispersion which limits the extent of the pulse compression. RR is generated when the pulse spectrum overlaps with its phase matched wavelength and will form an isolated peak which propagates with little change over the distances considered.

13.3.2 Experimental results

Having investigated pulse compression and RR generation using simulations we now turn to experimental results. These demonstrate how the NRR and RR output change as the input power increases and how the output spectrum of the pulse varies. The results show that for powers below a threshold value corresponding to $N = 1$ the pulse does not compress in the PCF and hence there is limited overlap between the pulse spectrum and the RR wavelength and negligible overlap with the NRR wavelength. Therefore in the output there is some RR but no NRR. As the power increases spectral broadening occurs and hence there is an increase in the production of RR and if the spectral broadening is large enough NRR is also produced. In the case of RR this will result in an increased output of the radiation. However the NRR results are complicated by loss and in order to obtain an accurate picture of how the power is affecting the generation of the NRR the output must be corrected for loss, this will be addressed in section 13.4.4.

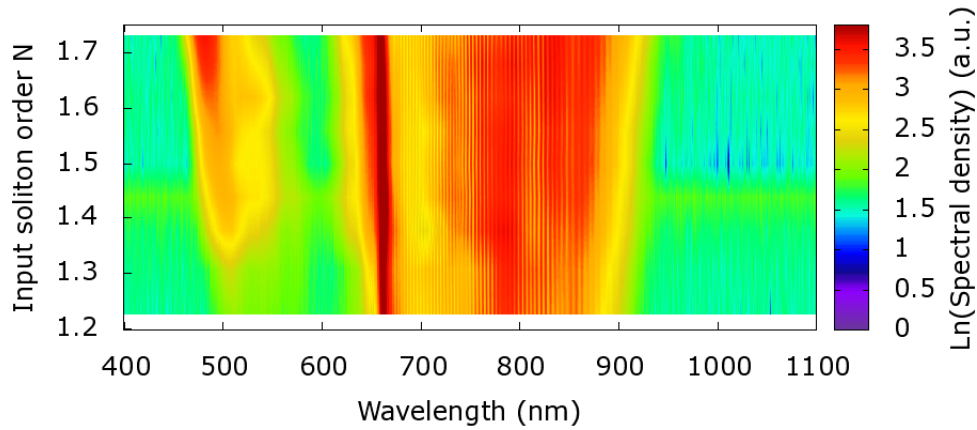


Figure 35: Experimental results - Colour scale plot of the visible and IR output spectra (logarithmic values) from a 5 mm piece of the NL-1.5-590 PCF as the input pulse power (N) is varied. The power is varied in small discrete steps

Direct investigation of the variation in the pulse spectral broadening with power is difficult. As seen in figure 32 the broadening is a transient effect and will therefore only be seen in the output if the compression occurs at the end of the PCF. For a pulse with zero input chirp figure 34(b) demonstrates that the furthest position along the PCF for the point of compression is about 1.7 mm for $N = 1.15$. We see in figure 34(b) that small changes from $N = 1.15$ result in large changes in the position of compression. So only for a very small range of input powers will the spectral broadening be visible in the output of a 1.7 mm PCF. Different PCF lengths could be used to observe the full extent of the spectral broadening for different input powers, however cutting many lengths is inefficient and leads to issues with maintaining the same coupling into each piece.

The experiments use either 7 fs or 12 fs pulses. The longer pulses are generated when a long pass filter (Comar 695 nm) is used to clean up the laser output spectrum as explained in section 12. The input pulse chirp is 90 fs^2 , this is different to the zero chirp used in the simulations but the qualitative behaviour is the same. The chirp arises from the insertion of a HWP and POL to control the input pulse power. The PCF is a 5 mm piece of the NL-1.5-590. The power is varied and the output spectra in the visible, IR and UV recorded.

The results for the visible and IR using a 7 fs input pulse are shown in figure 35. The strong

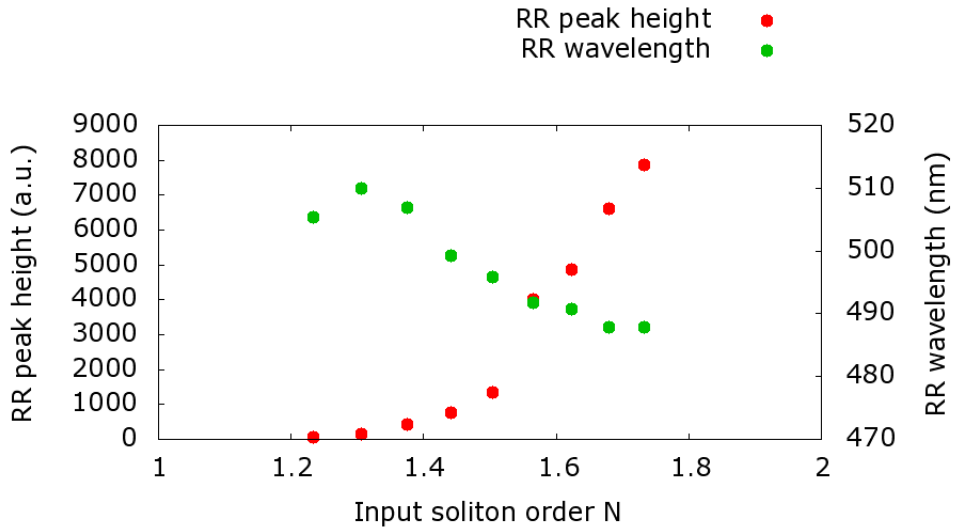
spectral feature at approximately 500 nm is the RR. As expected we see an increase in the RR signal as N is increased and also a slight shift to shorter wavelengths. The main pulse spectrum broadens slightly for larger N . Increased broadening is expected for larger N , however as discussed this is complicated by the affect of N on the position of compression.

The feature at 670 nm is the aforementioned component that does not form part of the pulse and is later removed using the long pass filter. The fringes in the IR are believed to be due to interference between different modes in the PCF.

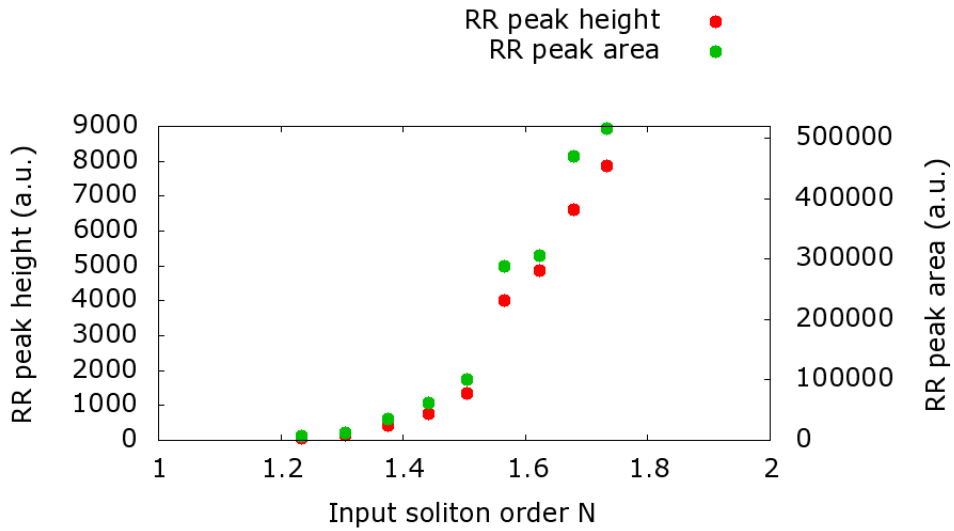
The variation with N of the height of the RR peak and its wavelength are shown in figure 36(a). As expected the RR peak height is small for low N and increases monotonically as N increases. The RR wavelength behaviour has been discussed previously and compared to theoretical values with good agreement. In figure 36(b) the area of the RR peak has been plotted along with the peak height. This allows comparison of the total amount of RR generated for different powers. The two sets of results have a very similar shape indicating that the RR peak for different powers has approximately the same width, this is in agreement with the shape of the RR peak seen in figure 35.

The corresponding results for the NRR as the input power varies are shown in figures 37 and 38(a). The colour scale plot shows the NRR signal at the expected wavelength of 229 ± 2 nm. Similarly to the RR, the NRR is negligible for smaller N and increases in height as N increases. In figure 37, it is also possible to see the spectral broadening of the input pulse as N reaches its largest values. This supports the results from the simulation which indicated that the extent of the spectral broadening is sufficient to produce a component in the UV to drive the NRR.

The variation in the height of the NRR with N has been plotted in figure 38(a). The loss experienced by the NRR is estimated to be $1.5 - 2.5$ dBmm⁻¹, an explanation of how this was estimated and reasons for the loss will be given in section 13.4.4. In order to take the loss into account the distance propagated by the NRR after its generation is calculated. The NRR is driven at the point of maximum compression in the PCF and this position for different values of N is estimated from the simulations. The output NRR is then calibrated for loss, the results are shown in figure 38(a). The difference is small but the uncalibrated peak heights appear to be levelling off slightly at higher N values. This is due to the compression point moving closer towards the start of the PCF for larger N and hence the loss increasing and reducing the output peak height, the



(a) Height (maximum spectral density) and wavelength (at the maximum spectral density) of the RR peak as the input power (N) is varied



(b) Height (maximum spectral density) and area of the RR peak as the input power (N) is varied

Figure 36: Experimental results - wavelength, height and area of the RR peak as the input power is varied

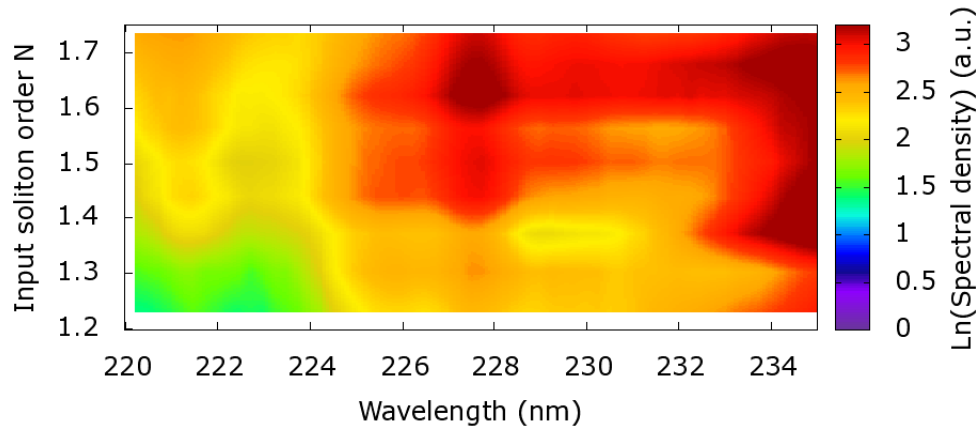
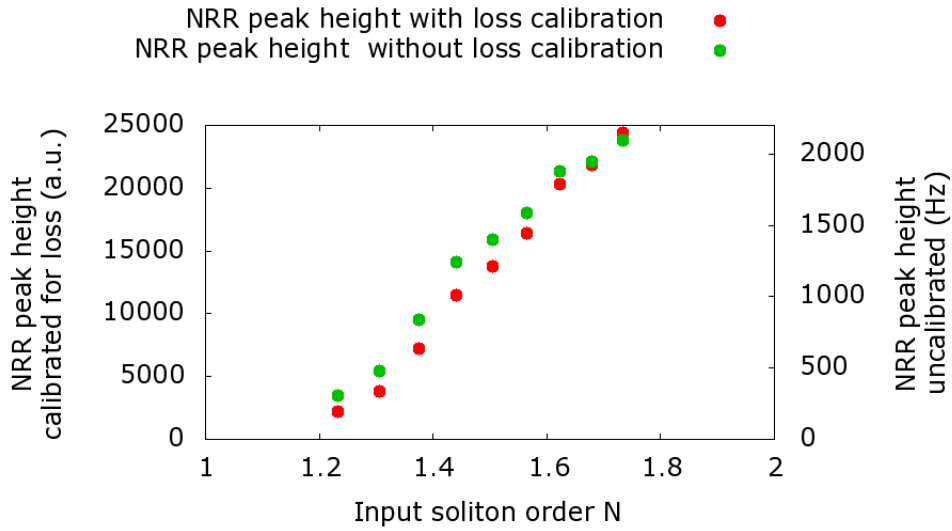


Figure 37: Experimental results - Colour scale plot of part of the UV output spectra (logarithmic values) from a 5 mm piece of the NL-1.5-590 PCF as the input pulse power (N) is varied

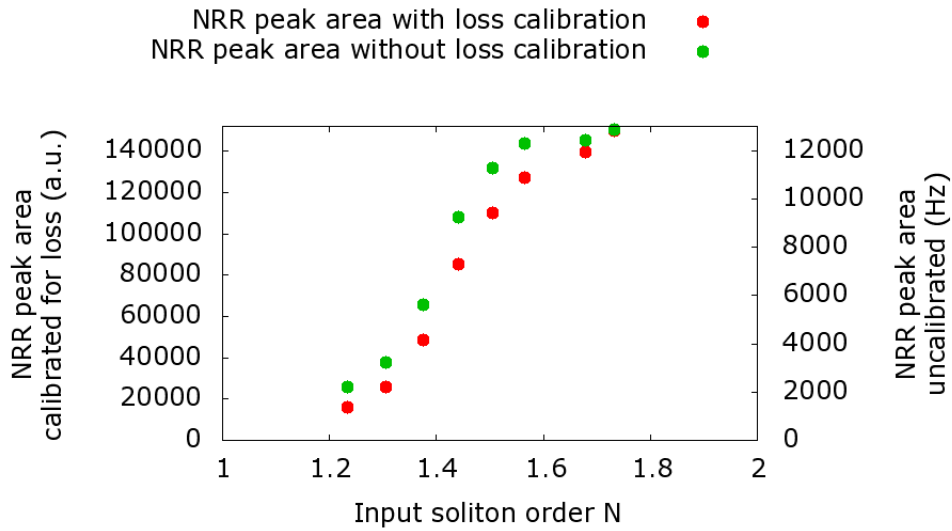
calibration removes this effect.

The variation in the area of the NRR with N has been plotted in figure 38(b). Unlike the RR peak height and peak area comparison, there is a slight difference between the NRR peak height and peak area variations as the power is increased. The peak area (both with and without loss calibration) levels off for larger N values whilst the peak height continues to increase almost linearly. This requires further investigation. It could be an effect due to inaccurate determination of how much of the signal at the NRR wavelength is part of the NRR and how much is due to other sources. As we have seen in section 13.2 there is some light at that wavelength which may be due to scattering. Also some of the signal will be due to the expansion of the pulse spectrum. However it could also indicate that the generation of the NRR does not improve linearly as the power increases but instead reaches a steady generation efficiency which does not improve with increased power. This would have implications for optimising the generation of NRR.

The dependence of the NRR peak height on N is not easy to determine experimentally from the small range of N values used. If the RR and NRR are generated by a fundamental soliton then from the theory in section 9 we expect both to vary as



(a) Height (maximum counts) of the NRR peak as the input power (N) is varied both with and without loss calibration



(b) Area of the NRR peak as the input power (N) is varied both with and without loss calibration

Figure 38: Experimental results - height and area of the NRR peak, with and without loss calibration

$$|A'|^2 = \left(\frac{\pi\gamma\beta_0\omega^2 T_0 P_0 \sqrt{P_0} \chi^{(3)}}{\omega_0^2 \beta \chi_0^{(3)}} \right)^2 \left(T_0^2 (\omega - \omega_0)^2 + 1 \right)^2 \operatorname{sech}^2 \left(\frac{\pi T_0}{2} (\omega - \omega_0) \right). \quad (13.1)$$

This will not be valid for higher order solitons however the range of N for which we have experimental results is close to 1 so as an approximation we can use the above formula for the intensity variation.

It must be noted at this point that, as we have seen before, the simulation programme cannot predict the NRR whereas the theory derived in part II can. In both cases the starting point is Maxwell's equations and from these a wave equation is derived. The simulation programme uses a split step Fourier method to find the pulse amplitude in either the time or frequency domain at a particular location in the system. In order to achieve this the user must input the input pulse and fibre parameters, in particular the dispersion data for the fibre. Currently the programme (which is a commercial piece of software) will only take into account positive frequencies i.e. only the positive branch of the dispersion relation. Therefore only the positive frequency solution to the resonant dispersive radiation phase matching condition is found (RR). Possible further work would involve adapting the programme to take into account negative frequencies and therefore allow the NRR to be found. This would enable predictions for the variation in the NRR intensity with power and chirp to be made. In part II two different wave equations are discussed (the NLSE and the more detailed pulse propagation equation). From each the phase matching condition for resonant dispersive radiation is found. We can then use this together with both the positive and negative branches of the dispersion relation to find the RR and the NRR. We use more detailed pulse propagation equation to find an estimate for the amplitude of the RR and NRR (see (13.1) above) and compare this to experimental results. As we will see for the NRR there are large discrepancies which are at least in part due to the assumptions made in calculating the theoretical values. These will be discussed after the results have been presented.

In order to compare theoretical and experimental results we use the temporal width from the simulation results for the minimum pulse length T_0 . From this the approximate variation in the spectral amplitudes at the RR and NRR phase matched frequencies with N are calculated using (13.1). This is simple for the NRR which does not shift with power. For the RR the phase matched

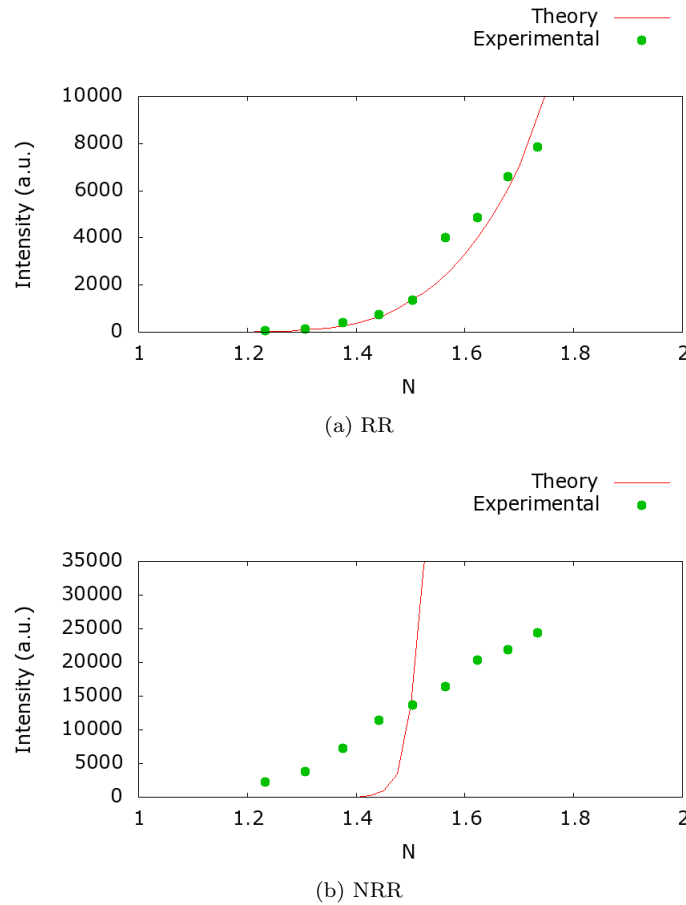


Figure 39: Theoretical and experimental NRR and RR intensities as a function of N . The experimental results are the maximum spectral densities of the RR and NRR signals.

wavelength must be calculated for each N . Using these spectral amplitudes we find the approximate theoretical dependence of the RR and NRR intensities on N - this is shown in figure 39 where the results have been scaled by the experimental result at $N = 1.5$. In both cases the experimentally measure peak heights have been used. In the case of RR there is little difference between peak are and peak height variation. In the case of NRR there is a small variation at the largest N values. Using the peak area would produce a slightly worse fit to the theoretical predictions.

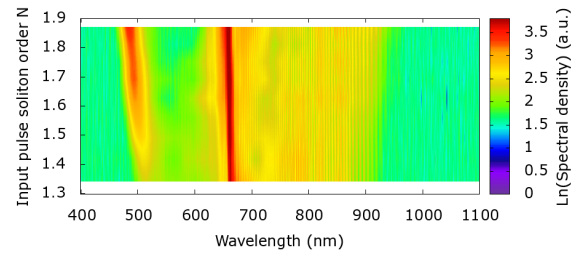
A comparison of the theoretical and experimental RR intensities in figure 39(a) shows that they follow a similar pattern as N increases even with the approximations made in deriving the theoretical amplitude. For the larger N values in figure 39(a) the theoretical intensities increase faster than the experimental values. This discrepancy may be due to the fact that loss has not

been taken into account in the theoretical intensity derivation and also the fact that the derivation was for the $N = 1$ case.

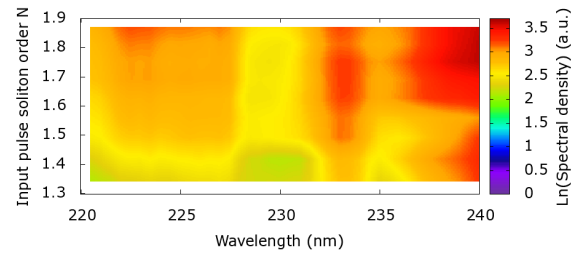
Figure 39(b) shows that the NRR fits much less well. Experimentally it starts to appear for smaller N than would be suggested by the theory and then grows almost linearly with N compared to the almost exponential theoretical growth. This former discrepancy may indicate that it is being seeded by other sources of light in the UV. Another explanation is that the pulse compresses more for smaller N in the experiments than predicted by the simulations.

Considering the latter discrepancy - the same issues discussed for the RR case will also apply, i.e. loss and the use of the fundamental soliton in the derivation. Another major issue is likely to be the degree of pulse compression predicted by the simulations. The simulations are not expected to perfectly reproduce the pulse dynamics. One reason for this is that the input pulse in the experiments is not the perfect hyperbolic secant assumed in the simulations thus it will be affected differently by higher order effects. Also as discussed previously there is some uncertainty in the dispersion profile used in the simulations (measured using method one in section 12.6). This will lead to differences between the simulated and actual pulse evolution.

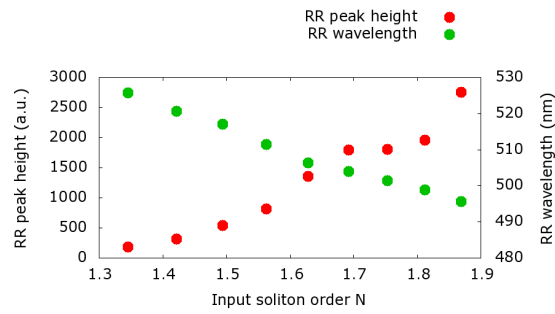
As a comparison to the NL-1.5-590 PCF, results for the NL-1.6-615 PCF are displayed in figure 40. The input pulse parameters are the same as for the NL-1.5-590 experiment. The results are qualitatively similar to the NL-1.5-590 PCF. The RR and loss calibrated NRR both increase in height with increasing input pulse power and the pulse spectrum becomes increasingly broad. Results for the RR and NRR peak areas are not shown. As in the case of the NL-1.5-590 the RR peak height and peak areas vary in approximately the same way. The NRR peak area also varies in approximately the same way as the peak height - both increase with power but the rate of increase decreases for larger N . This behaviour is similar to that seen for the NRR peak area using the NL-1.5-590 PCF. Again this suggests that more care is needed to separate the NRR from other sources of light at that wavelength. This could partially be achieved using filters to block scattered light. Additionally an investigation into the modes produced in the UV could help to distinguish the NRR from the expanded pulse spectrum. If the levelling off at higher powers is still measured then further investigation is required into why this is the case.



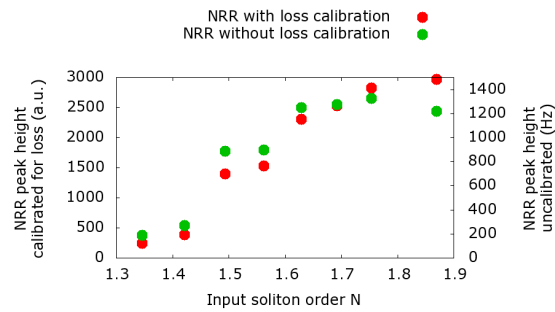
(a)



(b)



(c)



(d)

Figure 40: Experimental results - Output from the NL-1.6-615 PCF as the power is varied for a 7 fs input pulse with a chirp of 90 fs^2 , (a) Visible and IR colour scale plot. (b) UV colour scale plot. (c) RR peak height (maximum spectral density) and wavelength (at the maximum spectral density). (d) NRR peak height (maximum counts) with and without loss calibration

As explained previously, in some of the experiments a long pass filter was used to clean up the input pulse spectrum which increased the transform limited pulse length to 12 fs. The behaviour is qualitatively similar to that seen in figure 40(a). However the RR and NRR are not generated until slightly higher input powers are used. This is because the longer input pulse for the same N has a lower peak power and hence the effect of SPM induced spectral broadening is reduced which in turn reduces the generation efficiency of the RR and NRR.

13.4 The effects of input chirp on pulse compression, NRR and RR

In this section I describe the other main tool at our disposal for controlling the position and degree of pulse compression. As explained before this allows us to investigate pulse spectral broadening and its influence on NRR, and to observe the evolution of NRR

In section 13.3, the simulations showed that by varying the power of the input pulse, the position of maximum pulse compression is moved through the PCF. This had limited use as a method for investigating RR, NRR and pulse evolution as the generation efficiency of the RR and NRR depend critically on the pulse power as does the extent of pulse compression. A more useful tool to move the compression point is the input pulse chirp. Before the pulse maximally compresses in the PCF the linear input pulse chirp must be compensated by the PCF dispersion¹⁴. The greater the chirp the longer the propagation distance required to compensate it and hence the further along the PCF the point of maximum compression occurs.

The key advantage of using the chirp over power is that it can be used to move the compression point over several millimetres with limited changes in the degree of pulse compression in the PCF compared to using the power. For example, as seen in figure 34(b) when N is increased from 1.15 to 5 the compression point moves by only 1.6 mm. Over the same N range the maximum peak power reached in the PCF increases by a factor of about 24. This will lead to a large change in the generation efficiency of RR and NRR. Simulation results show that it is possible to use the chirp to move the point of compression over 10 mm whilst changing the maximum peak power reached by only a factor of 1.5. This indicates a much smaller change in the degree of pulse compression

¹⁴In the experiments the input pulse lies in the anomalous dispersion region of the spectrum for all of the PCFs used hence such compensation only occurs for positively chirped input pulses

and hence the generation efficiency of the RR and NRR will be much less affected. Therefore the chirp is a better tool than power for moving the point of pulse compression whilst the power is more useful for investigating the effect of the degree of compression on NRR and RR generation.

In this section I will first present simulation results showing how the chirp is expected to affect the pulse dynamics. I will then describe the results of experiments varying both the input pulse chirp and the PCF length.

13.4.1 Simulation results

In order to demonstrate how the input pulse chirp affects the pulse compression and spectral broadening I present similar simulations to those in section 13.3. However in this case the input power is kept constant to give $N = 2.25$ and the chirp is varied. The power level is chosen to match that used in the bulk of the experiments in this section. As before the dispersion parameters of the NL-1.5-590 PCF are used.

Many of the experiments varying the chirp are carried out with 12 fs input pulses (particularly those in section 13.4.3) hence most of the simulations use this pulse length rather than 7 fs. Later in this section I will present some simulation results for different input pulse lengths which show that the behaviour is qualitatively the same for shorter pulses.

In figures 41 and 42, for different input pulse chirps the spectra at different propagation distances are plotted in a log scale colour plot, this shows how the pulse and RR evolve in the PCF. As in the simulation results from section 13.3 the initial pulse spectrum expands and then contracts again as the pulse temporally compresses and expands.

The main impact of varying the chirp is that it moves the point of pulse compression further along the PCF for increasing chirp. Additionally the degree of pulse broadening decreases with increasing chirp, although this effect is small. These two effects clearly demonstrate why the chirp is the ideal tool to investigate pulse and driven radiation evolution. The position of compression can easily be moved over 10 mm with only very small changes in the degree of compression. Later in this section I look in more detail at how small the change in the degree of compression is.

The spectral features in figures 41 and 42, are the same as those seen in figure 32 and therefore do not need to be explained in detail again. The pulse broadens due to the effects discussed in the

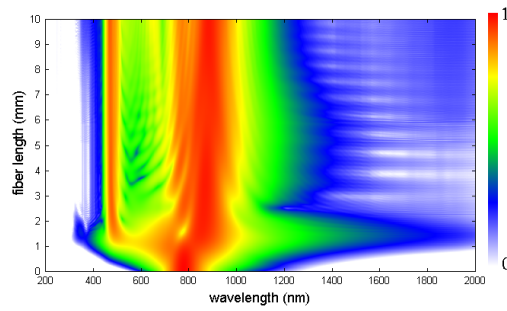
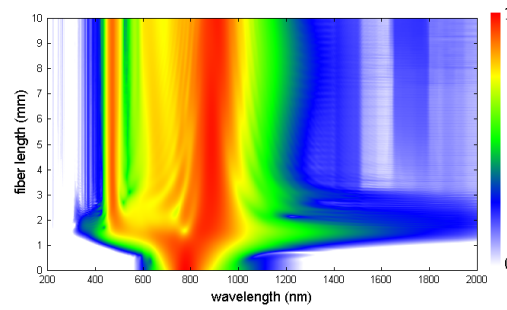
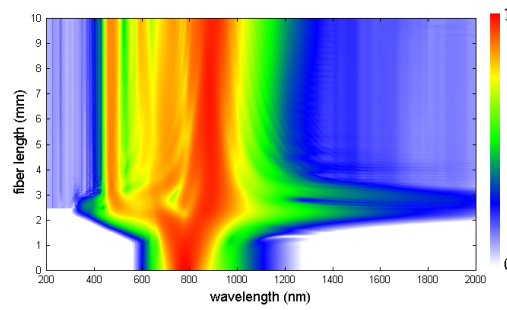
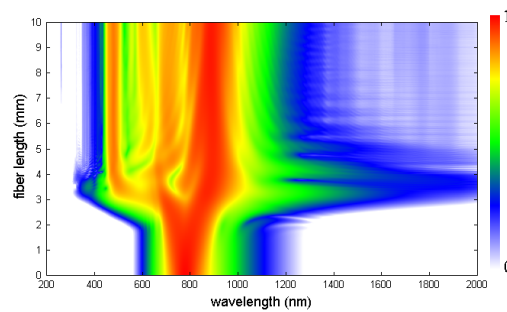
(a) 0 fs^2 (b) 41 fs^2 (c) 81 fs^2 (d) 122 fs^2

Figure 41: Simulation results 1 - Log scale spectral evolution of a 12 fs, $N = 2.25$ hyperbolic secant pulse for different input pulse chirps. For each plot the colour scale runs from 0 to 1 where 1 is the maximum recorded spectral density for the individual plot

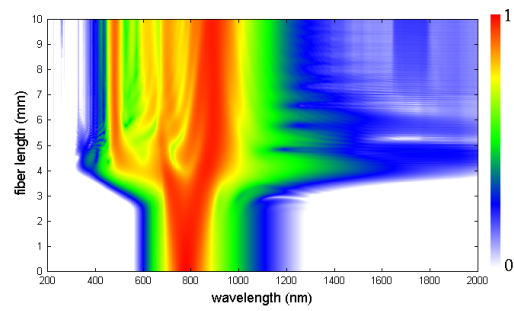
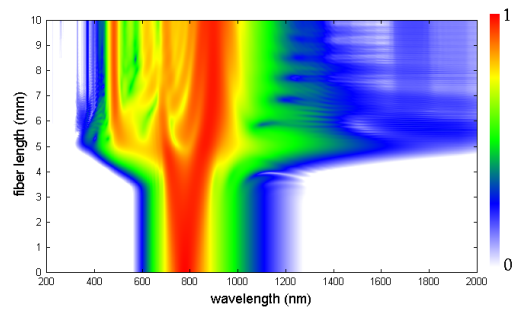
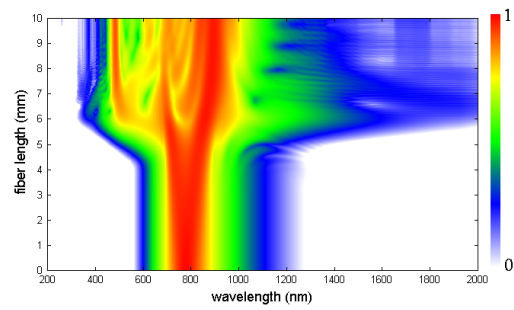
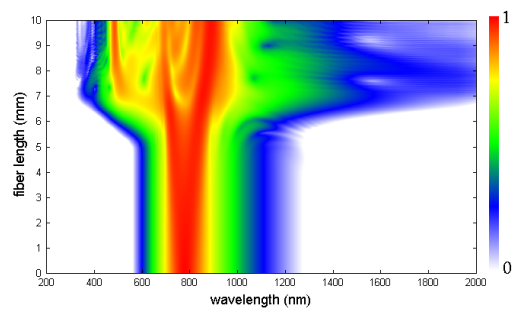
(a) 162 fs^2 (b) 203 fs^2 (c) 244 fs^2 (d) 284 fs^2

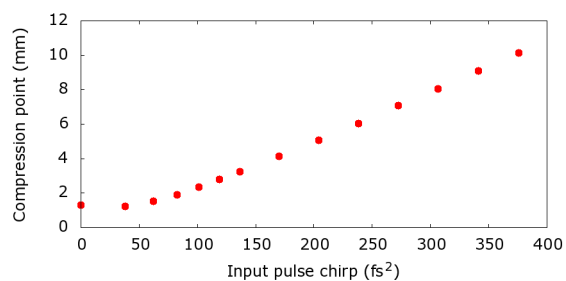
Figure 42: Simulation results 2 - Log scale spectral evolution of a 12 fs, $N = 2.25$ hyperbolic secant pulse for different input pulse chirps. For each plot the colour scale runs from 0 to 1 where 1 is the maximum recorded spectral density for the individual plot

previous section and drives the RR signal in the visible.

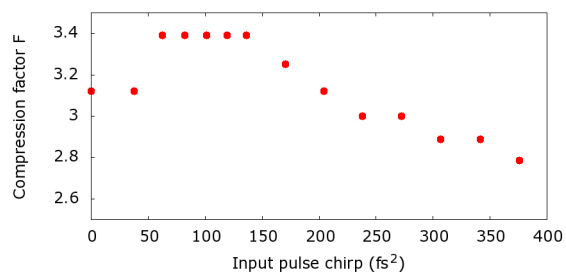
Figure 43 shows how the parameters of the pulse compression - position of pulse compression, compression factor F , maximum peak power and quality factor, vary with input pulse chirp. The results display several interesting features. The first and most important feature to note is that, as also seen in figure 41, increasing the input chirp moves the compression point along the PCF due to the increased propagation distance required to compensate the initial chirp. For higher chirp values the dependence of the compression point on the chirp is almost linear, for every extra fs^2 of input chirp the compression point moves by about 0.03 mm. For low chirp values there is an offset from zero because even with no initial chirp to compensate the pulse compression still takes a finite propagation distance.

Another interesting feature is the slight variation in the degree of pulse compression as the chirp varies. This is shown by the decrease in the maximum peak power as the chirp becomes large and the corresponding decrease in the compression factor F . A naive theory of chirp compensation would suggest that the PCF GVD compensates the input chirp resulting in a pulse which is identical to an initially unchirped pulse at the start of propagation. If this were the case the degree of pulse compression would be unaffected by the input chirp and only the position of compression would change. This is clearly not the case. One reason for this is that the naive theory assumes that the GVD acts in isolation. In reality SPM and higher order effects also affect the pulse and reduce the extent of pulse compression. Another possible reason is that the presence of an initial chirp can assist in the breakup of a higher order soliton [81]. The larger the chirp the faster this breakup happens and the smaller the extent of SPM induced spectral broadening. The impact of these effects also leads to a slight decrease in the quality factor indicating that less of the input pulse energy is ending up in the compressed pulse.

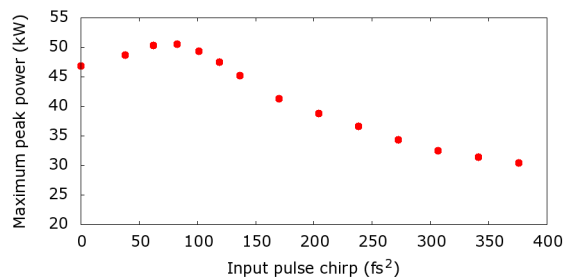
One further interesting feature is the increase in the degree of pulse compression for a small positive chirp compared to zero chirp. This is indicated by the larger maximum peak power and compression factor for a small positive chirp. It appears that there is an optimum chirp for pulse compression which is not quite zero. The reason for this is not fully understood. Other investigations into the effect of chirp on pulse evolution have not mentioned seeing this particular effect [134, 31, 81]. However this may be because the focus of their investigations was on other aspects of pulse evolution such as the break-up of higher order solitons, or that their chirp steps were larger



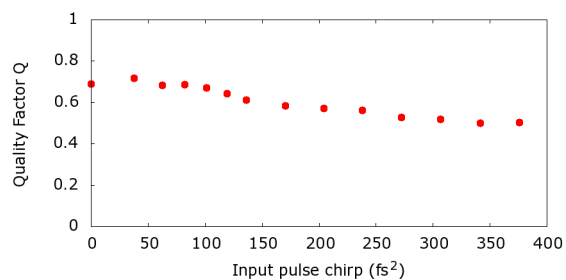
(a)



(b)



(c)



(d)

Figure 43: Simulation results - Variation in the pulse compression parameters with input pulse chirp for an $N = 2.25$, 12 fs pulse. (a) Position of maximum compression in the PCF. (b) Compression factor F. (c) Maximum peak power. (d) Quality factor Q

or had too large an error to notice the effect.

The optimal chirp could possibly be due to the fact that the SPM acts to both broaden the spectrum and introduce a positive chirp - thus a pulse with an initial positive chirp has similarities to a pulse which has already undergone some SPM. This pseudo SPM effect enhances the pulse compression. For input chirps larger than the optimum chirp the decreased initial pulse peak power becomes the dominant effect cancelling out any enhancement in pulse compression from the initial chirp and hence the degree of compression starts to decrease again.

The presence of an optimum chirp is interesting because it can be used to optimise the generation of NRR and RR by maximising the pulse compression. In the next section I present experimental results for the variation in the NRR and RR peak heights with chirp, this will show if there is an improvement in the NRR and RR generation at the optimum chirp.

The results in figure 43 indicate that there is an optimum chirp for one particular set of pulse parameters. Further simulations were carried out to investigate whether or not this effect persisted for different input pulse powers and pulse lengths. The results from this are shown in figure 44, which plots the optimum chirp (chirp for the maximum peak power reached when the pulse compresses) as a function of both input pulse length and input N . It can be seen that there is indeed a non-zero optimum chirp for a range of pulse lengths up to at least 200 fs and for values of N ranging from 0.6 up to at least 5. Also shown in figure 44, is the improvement in the maximum peak power for the optimum chirp as compared to zero chirp. When the power is varied this improvement peaks sharply and is greatest for a pulse with $N = 1.1$. When the pulse length is varied the change in the improvement is more gradual peaking for about 60 fs and then gradually declining as the pulse length increases.

A reason for the existence of a non-zero optimum chirp has been briefly suggested above, however further work is required into exactly why it occurs and why it varies with pulse length and pulse power in the way shown in figure 44. The key point to note is that simulations show it to be a persistent feature and therefore it needs to be considered when interpreting the experimental results.

The simulations for different pulse lengths show that qualitatively the behaviour as the chirp is varied is the same as for 12 fs. The position of compression moves along the fibre axis as the chirp increases. The longer the pulse length the larger the distances required for pulse compression. This

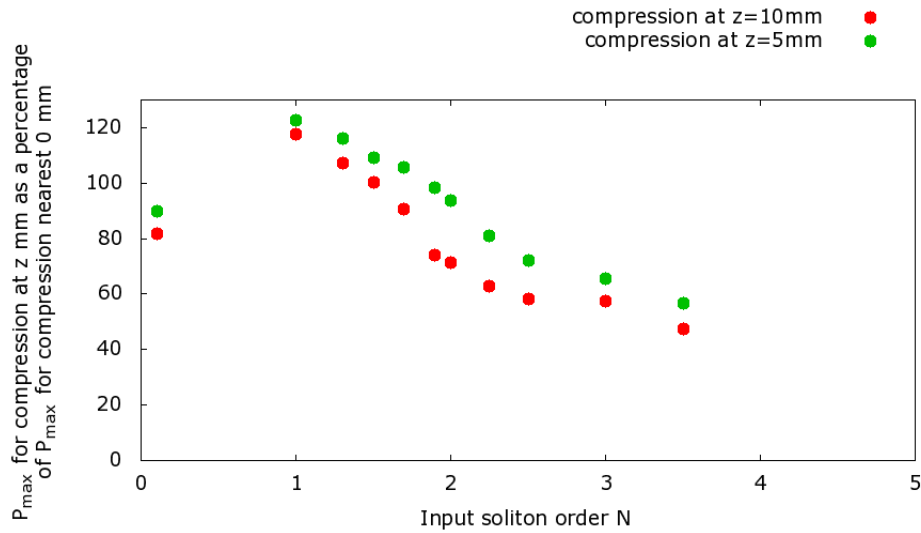


Figure 45: Simulation results - maximum peak power for a chirp where compression occurs at 5 mm or 10 mm as a percentage of the maximum peak power for compression as close to the start of the PCF as possible, as a function of N

is as expected because the effects of GVD and SPM will both depend on the pulse length.

As mentioned previously if we want to use the chirp to investigate the pulse and driven radiation evolution, we ideally want no change in the degree of pulse compression as the chirp varies. As seen in figure 43, this is not quite the case. Figure 45 shows the variation with N of the change in the maximum peak power reached in the PCF when the chirp is changed from the value required for compression as close to the start of the PCF as possible, and the chirp for compression at 5 mm. The same is also plotted for 10 mm. We choose 5 mm as we are particularly interested in investigating the generation of NRR, and movement of the compression point over 5 mm is more than sufficient to achieve this. The NRR is generated when the pulse compresses and, as seen in the simulations, this occurs over only 2 – 3 mm. We also consider 10 mm to see to what extent we can investigate the subsequent evolution of the NRR. This can be measured by moving the compression point back towards the start of the PCF. However due to high losses at the NRR wavelength, if the NRR has to propagate over longer distances, the signal in the output becomes increasingly small. Therefore we only need to consider PCF lengths up to about 10 mm.

The figure shows that for low N the peak power is slightly higher for compression at the start of the PCF. As N approaches 1 the peak power becomes greater for compression at 5 mm (or 10 mm).

This is due to the existence of the non-zero optimum chirp. Further increases in N lead to the peak power becoming greater for compression at the start of the PCF. Hence the smallest differences in the peak power, as the compression point is moved, are for $N \sim 0.5$ and $N \sim 1.5$. In the experiments we use an $N = 2.25$ pulse and hence the maximum peak power when the compression occurs at the end of a 5 mm PCF is about 80% of the maximum peak power for compression close to the start. This is small enough to mean that we can use the chirp as a tool to investigate pulse compression and NRR generation.

13.4.2 Experimental results

In this section I present experimental results showing the effect of chirp on pulse compression and the generation of NRR and RR. These can be compared to the simulation results in the previous section. The first results show how the chirp can be used to move the compression point to the end of the PCF and therefore observe the full extent of the pulse broadening. I then present results showing how the RR varies with pulse chirp. As discussed previously, the chirp can be used to investigate how the RR evolves. Finally I show results from a series of experiments where the chirp is varied for different PCF lengths. This investigation allows us to see how the slight variation in the degree of pulse compression as the chirp is changed affects the RR and the NRR generation. In particular the existence of the optimum chirp can be investigated. I also include details of the calculations for the loss experienced by the NRR.

The first set of experimental results looks at the combined influences of pulse power and chirp on pulse evolution in a PCF. For a series of constant chirp values the input pulse power is varied and the PCF output spectra recorded. The data sets in figures 46 and 47 are recorded using the NL-1.6-615 PCF. In each case the input pulse has a length of 7 fs and is coupled into a 5 mm long piece of PCF. As before the power is expressed in terms of N , as defined in (8.4), where for each plot all parameters apart from P_0 are constant.

We see that for the largest negative chirp (-78 fs^2) the pulse appears to broaden slightly for

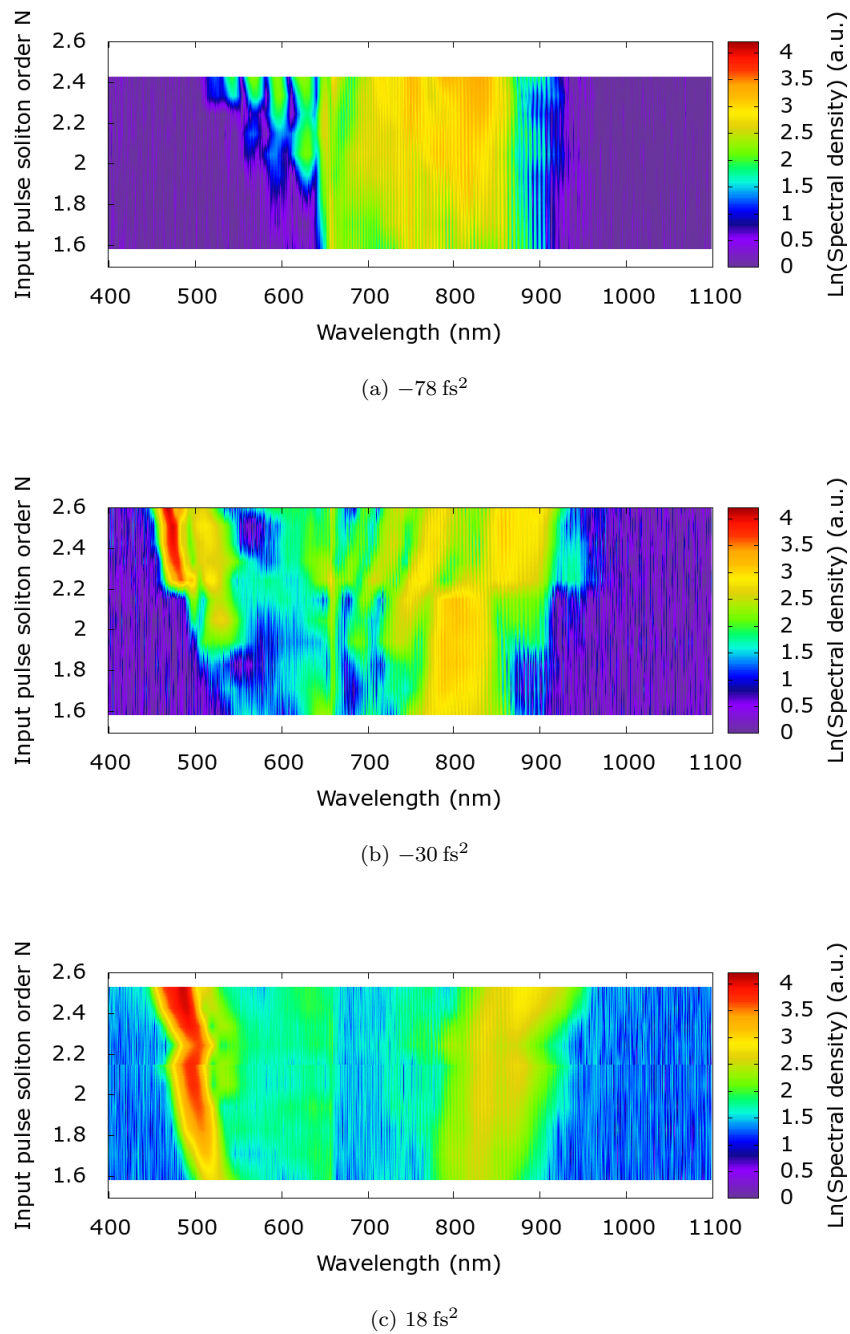


Figure 46: Experimental results 1 - Colour scale plots for the visible and IR output spectra (logarithmic values) as the input power is varied for different chirps. NL-1.6-615 PCF with 7 fs input pulses

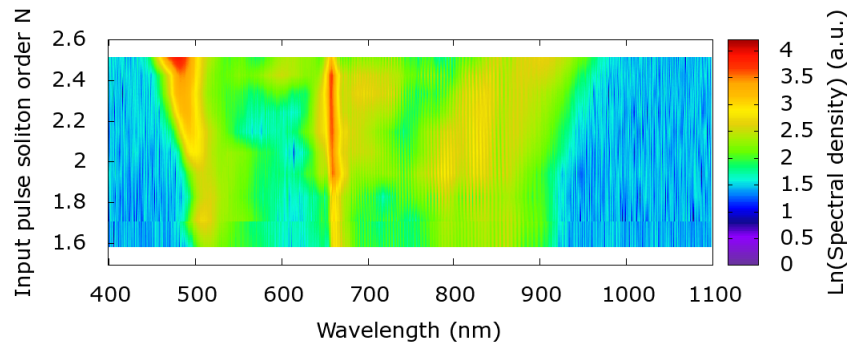
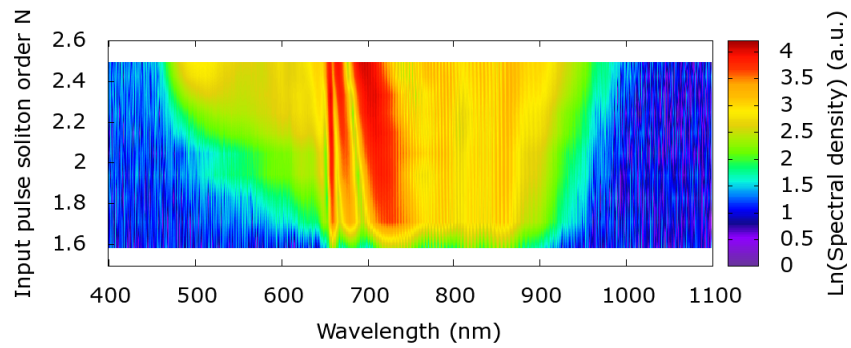
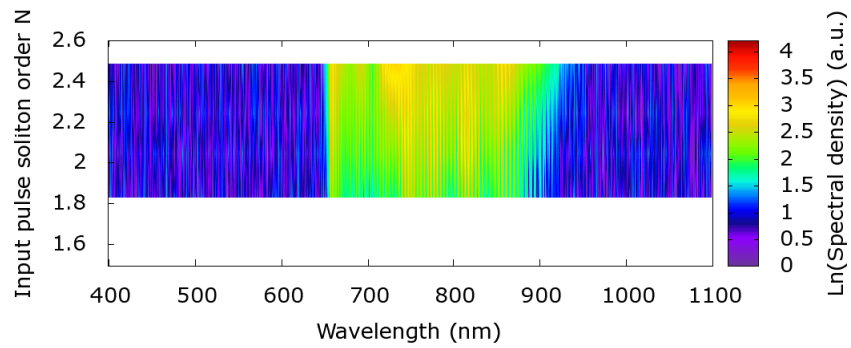
(a) 119 fs^2 (b) 201 fs^2 (c) 303 fs^2

Figure 47: Experimental results 2 - Colour scale plots for the visible and IR output spectra (logarithmic values) as the input power is varied for different chirps. NL-1.6-615 PCF with 7 fs input pulses

higher powers with a few peaks appearing in the visible. However it is unclear whether or not any of these is RR. It is expected that for large negative input chirps compression will not occur as the pulse peak power will be low and the effect of SPM small. The PCF GVD will temporally broaden the pulse decreasing the power further.

For the smaller negative chirp (-30fs^2) there is clear spectral broadening as the power increases and an RR peak can be seen for the higher powers. The spectral broadening occurs because the input pulse has a sufficiently high peak power (for the higher N values) to allow SPM to generate new frequencies. This also explains the very slight broadening for the highest N values in the -78fs^2 case.

For all of the positive input chirps, except the largest, the pulse spectrum can be seen to broaden and drive the RR in the visible. As the chirp increases the RR peak first appears for higher input powers.

We expect that for the same input power the position of pulse compression will move further along the PCF for increased input chirp. We have also seen, in section 13.3, that increasing the power will, in general, move the compression point towards the start of the PCF. The results for positive chirp can be explained using these two ideas. For the larger chirps, at low power compression will not be able to occur inside the PCF, hence negligible RR will be generated. Increasing the power means that the compression can occur inside the PCF and a non-negligible amount of RR can be generated. Additionally, as we have seen in the simulations, the degree of compression decreases slightly at the input chirp increases. Therefore higher powers are required to compress the pulse enough to generate RR. In the plot for the largest input chirp (303fs^2) no RR is visible. In this case, with the available power range, either the deterioration in the degree of pulse compression due to the increased chirp is too large to be compensated, or the pulse cannot compress inside the PCF.

The variation in the height of the RR peak with N for the different input pulse chirps is shown in figure 48. For all input chirps the RR height generally increases with increasing power as expected¹⁵. The greatest RR output is measured for small positive and negative chirps. The variation in the RR peak area with power and chirp is not shown but follows a similar pattern.

These results give an indication of the impact of chirp on the degree of pulse compression, and

¹⁵There are slight deviations from this trend at low N , which are likely to be due to noise in the data

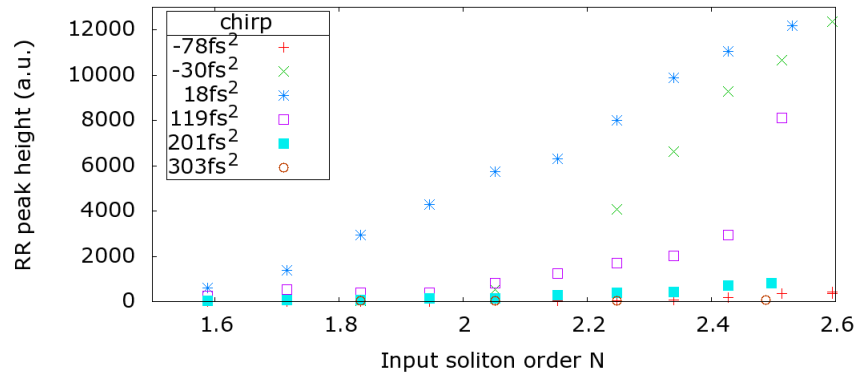


Figure 48: Experimental results - RR peak height (maximum spectral density) as the input power is varied for different pulse chirps. NL-1.6-615 PCF with 7 fs input pulses

therefore the generation of RR. This can be compared to the impact on the pulse compression when we use the power to move the point of compression. From the simulations, for a 12 fs pulse with $N = 2.25$, the point of compression will move by approximately 6.7 mm when the chirp is changed from 0 fs^2 to 303 fs^2 . From the simulations, using the power to vary the pulse compression over a similar distance for a small constant chirp would require a power range of more than $N = 1$ to $N = 5$. With a larger, constant input chirp the power range could be reduced, for example, using a chirp of 303 fs^2 the compression point could be moved by 6.7 mm by varying the power from $N = 1$ to less than $N = 3$. However, this is still beyond the range achievable in our experiments and, as we have seen using higher chirps will further deteriorate the degree of compression. Longer initial pulse lengths (with no chirp) also allow power variation to move the compression point over longer distances, but again this comes at the expense of greater compression.

This comparison shows that the chirp is a better tool to move the point of compression than the power. However we have seen that changing the chirp does cause a significant change in the RR generation, which indicates that it significantly changes the degree of pulse compression. We need to take this change in pulse compression and the generation of RR (and NRR) into account when using the chirp to investigate pulse evolution and NRR and RR generation.

Additionally, we have seen that the RR output and spectral broadening are greatest for small positive and negative chirps. This may be useful - for example when the power of the RR needs to be maximised for use in practical applications or when a high degree of spectral broadening is required to drive UV radiation such as the NRR or the optical analogue of HR. This latter point

is considered further when we look at the NRR output whilst varying the GDD.

We now turn to experimental results where the chirp is varied at constant input power. As we increase the chirp the compression point moves along the PCF and the output RR and pulse spectra evolve over a smaller propagation distance before the PCF end. Thus the output spectra for decreasing pulse chirp are qualitatively similar to those for increasing propagation distances, with the caveat that the chirp also alters the degree of pulse compression.

Figure 49 shows one example of varying the chirp for an input pulse of 7 fs length and $N=2.06$. Once again the NL-1.6-615 PCF is used with a length of 5 mm. The colour scale plot shows that for large chirps the pulse spectrum remains fairly narrow and there is no RR. At this point the chirp is too large to be fully compensated for inside the PCF and the pulse is not able to compress completely. As the chirp decreases we see the pulse spectrum broadening and starting to drive the RR. Here the compression point is close to the end of the PCF and so we are able to observe the transient spectral broadening effect. Further decrease in the chirp causes a narrowing of the pulse spectrum leaving an isolated RR peak. The compression point is now closer to the start of the PCF, hence by the output the spectrum has narrowed again. Below zero input chirp the pulse spectral width and the RR peak height decrease. This is because as seen in figure 46 the pulse is less effectively compressed as the chirp becomes negative.

The RR peak heights and areas as a function of the input chirp are shown in figure 49(b). This shows there is an RR peak for a range of chirps from approximately zero to the largest chirp that can be compensated in the PCF. The height and area vary in the same way, both are greatest for a small positive chirp and then decrease as the chirp becomes large. This is in agreement with the simulation results which indicate that the degree of pulse compression should be greatest for a small positive optimum chirp and decrease with increasing chirp (see figure 43).

The results in figure 49(a) can be compared to the simulation results in figures 32 and 41. The experimental results display qualitatively the same behaviour indicating that the chirp can be used as a method to investigate pulse evolution. Further qualitative evaluation and comparison with simulations will be carried out in section 13.4.3.

Figure 50 shows how the output spectra vary with pulse chirp for several different input pulse powers. All display qualitatively similar behaviour to figure 49(a). For the lowest power ($N=0.9$) the spectral broadening is not sufficient to drive the RR and there is little change in the spectrum

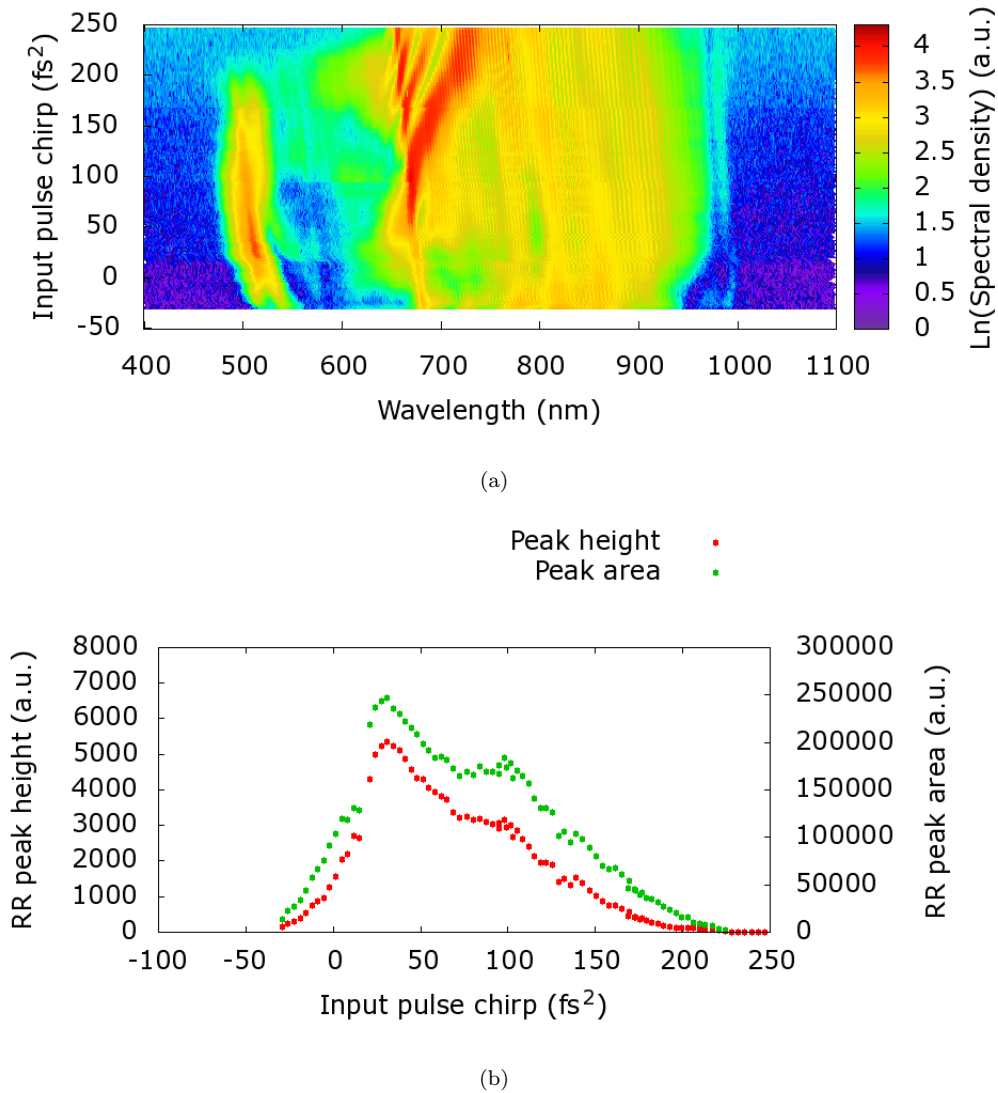


Figure 49: Experimental results - Visible and IR output spectra and RR peak heights (maximum spectral density) and areas as the input pulse chirp is varied. NL-1.6-615 PCF with an input pulse of 7 fs length and $N=2.06$. (a) Colour scale plot (logarithmic values). (b) RR peak heights and areas

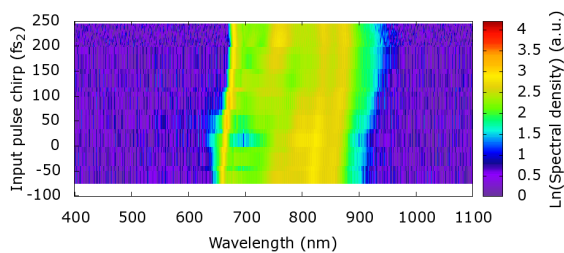
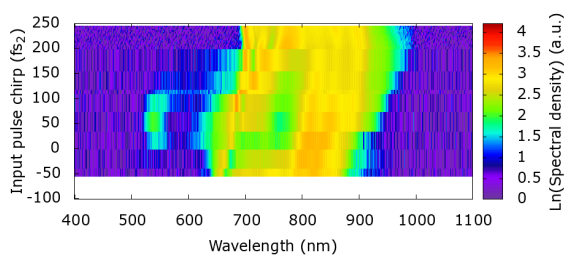
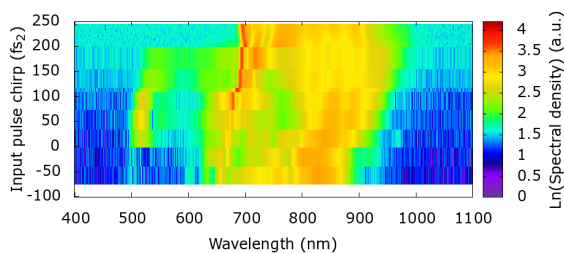
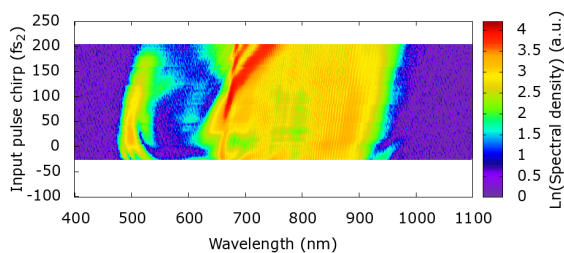
(a) $N = 0.9$ (b) $N = 1.3$ (c) $N = 1.6$ (d) $N = 1.8$

Figure 50: Experimental results - Visible and IR output spectra as the input pulse chirp is varied for different input pulse powers. NL-1.6-615 PCF with an input pulse of 7 fs length

for different chirps. As the power increases the RR signal becomes stronger as expected. In addition it is present for larger chirp values. This is because as seen in the simulations an increase in power will move the compression point closer to the start of the PCF. Or in other words for the same length of PCF increasing the input power allows larger chirps to be compensated over the PCF length.

13.4.3 Varying chirp and PCF length

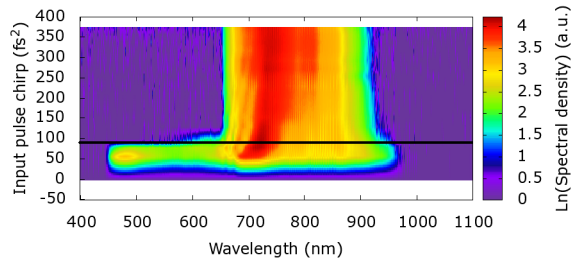
In the previous section I presented results showing the change in spectral expansion and RR generation as the chirp (and power) varied. In this section I extend the results by varying the PCF length as well. I look at the NRR generation as well as the pulse expansion and RR generation.

The purpose of varying the PCF length is twofold. Firstly it is used as a method to estimate the loss experienced by the NRR by comparing output spectra from experiments with the same input pulse parameters but different PCF lengths. As long as the pulse is able to compress within the PCF we expect the compression to occur identically regardless of the length. Therefore the same amounts of RR and NRR will be generated. Any differences in the output spectra are due to how the RR and NRR propagate through the PCF and in particular to how much loss they experience.

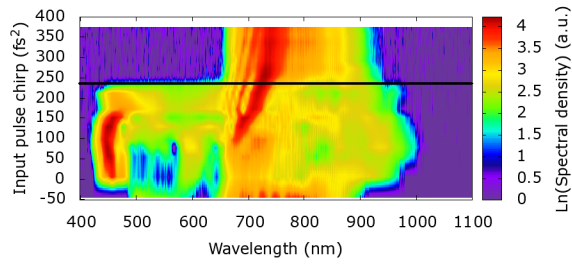
Secondly varying the PCF length can be used to investigate the pulse, RR and NRR at different stages in their evolution and the results can be compared to the results from varying the chirp to move the compression point and also those calculated using the simulation programme. If the former comparison indicates a good match then it shows that the chirp can be used as a tool to investigate pulse dynamics.

The PCF length is varied from 14 mm to 2 mm in 1 mm steps. Then, as before, the input pulse chirp is varied and the output spectra recorded. In these experiments the NL-1.5-590 PCF is used, instead of the NL-1.6-615 used in the previous section, to demonstrate that the same qualitative behaviour occurs for different PCFs (with similar dispersion profiles). The input pulse power is kept constant during each set of measurements and corresponds to $N = 2.25$. This power level is used as it is the maximum power available after sufficient optical elements has been placed in the beam to move the compression point to the end of the PCF.

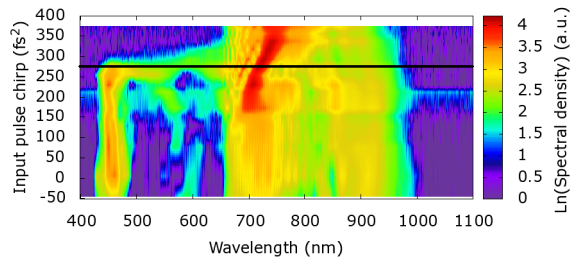
The results presented in figure 51 show how the visible and IR output spectra vary as a function



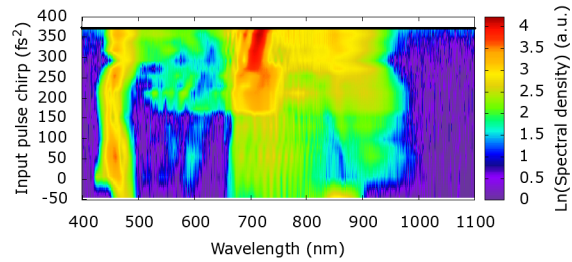
(a) 3 mm



(b) 6 mm



(c) 8 mm



(d) 10 mm

Figure 51: Experimental results - Colour scale plots of the visible and IR output spectra (logarithmic values) as the input pulse chirp is varied for different PCF lengths. NL-1.5-590 PCF with an input pulse of 12 fs length and $N = 2.25$

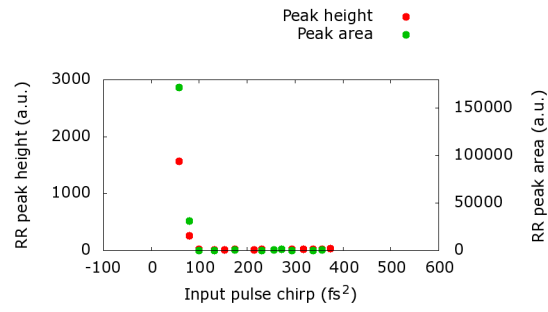
of input pulse chirp for a selection of four different PCF lengths. In all cases the behaviour is qualitatively similar to that seen in figure 49(a). For large chirps where the pulse does not compress in the PCF the spectrum remains narrow. As the chirp decreases to the point where compression occurs at the end of the PCF the spectrum broadens and the initial generation of RR is seen. For the 10 mm PCF length, the chirp range used is only just sufficient to see the pulse compression at the end of the PCF.

The value of the input chirp at which the spectral broadening and the generation of RR occur varies with the PCF length. It is marked with a horizontal line in the plots in figure 51. The variation is as expected - the longer the PCF the greater the input chirp required for compression at the PCF end. Table 3 compares input pulse chirps that lead to observable pulse compression at the PCF end, based on different mechanisms: linear indicates the chirp that would compensate the linear dispersion of the whole PCF length (i.e. $\beta_2 L$, where L is the PCF length). In order to facilitate comparison with experimental results the errors indicate a range of values for slightly longer or shorter PCFs reflecting the experimental uncertainty in the PCF length. The simulated chirp values for compression at the PCF end are calculated using the same parameters as the experiment.

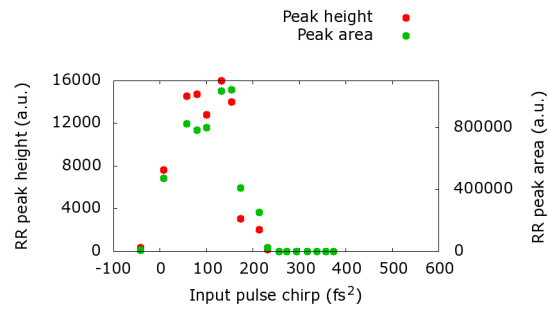
The simulation and linear results differ due to the effect of SPM. This generates new frequencies leading to faster pulse compression. The linear result does not take account of SPM so the chirp for compression at the end of the fibre is smaller than that predicted by the simulations. To allow comparison between simulation and experiment we need to take into account the uncertainty in the exact experimental coupling into each PCF. Therefore we include error values for the simulation results indicating how the chirp value varies for a small range of input pulse powers.

As can be seen in the table the experimental results agree reasonably well with the simulations within the uncertainties. A better match could hopefully be achieved if the coupling into the PCF were known more accurately.

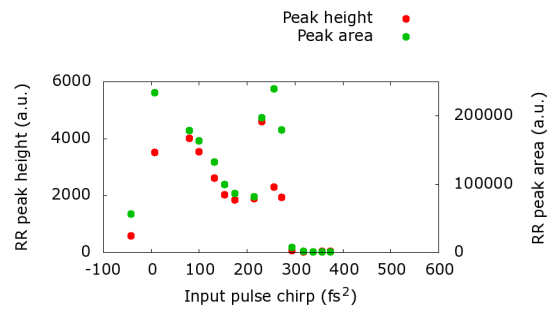
The plots in figure 52 show how the RR peak height and peak area in the output spectra varied with chirp for different PCF lengths. The data is not as clear as in figure 49(b). In general both the height and the area are small for negative chirp and increases to a peak for a small positive chirp ($\sim 80 \text{ fs}^2$). It then decreases with increasing chirp. For the two longest PCF lengths there is a second peak at a larger chirp value and in all cases for the largest chirp values the RR signal



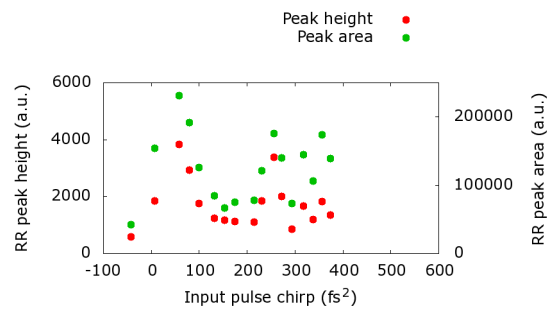
(a) 4 mm



(b) 6 mm



(c) 8 mm



(d) 10 mm

Figure 52: Experimental results - RR peak heights (maximum spectral density) and peak areas as the input pulse chirp is varied for different PCF lengths. NL-1.5-590 PCF with an input pulse of 12 fs length and $N = 2.25$

PCF length (L)	Linear	Simulation	Experimental result (figure 51)
4 mm	$108 \pm 13 \text{ fs}^2$	$124 \pm 20 \text{ fs}^2$	$87 \pm 20 \text{ fs}^2$
6 mm	$161 \pm 13 \text{ fs}^2$	$234 \pm 30 \text{ fs}^2$	$231 \pm 20 \text{ fs}^2$
8 mm	$215 \pm 13 \text{ fs}^2$	$305 \pm 37 \text{ fs}^2$	$272 \pm 20 \text{ fs}^2$
10 mm	$269 \pm 13 \text{ fs}^2$	$376 \pm 44 \text{ fs}^2$	$374 \pm 20 \text{ fs}^2$

Table 3: Chirp values for compression at the end of the PCF: linear results $\beta_2 L$ where β_2 is the PCF GDD parameter and L is the PCF length, results from the simulations and results from the experiments in figure. The linear results indicate the chirp for compression at the PCF end if non-linear effects are negligible 51

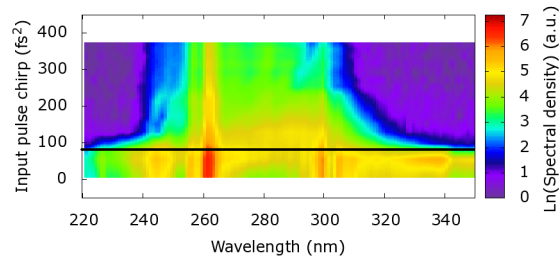
decreases again.

As explained previously, for negative chirp there is limited pulse compression, hence little RR is generated. As the chirp increases to the optimum small positive chirp the degree of compression is greatest and the RR signal peaks. Further increases in chirp lead to the decrease in pulse compression observed in the simulations. The fact that there is no RR signal for the largest chirp values for the three shorter PCF lengths is due to the pulse not compressing fully in the PCF. For the longest PCF there is still a small signal indicating that sufficient compression is occurring to drive the RR.

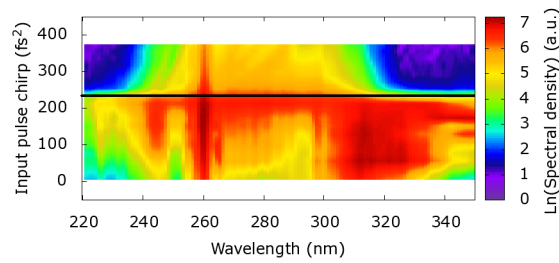
The second maximum in the RR signal at larger chirp is an interesting feature. It may indicate that for that input chirp the pulse is compressing at the end of the PCF. In this case there would be a component of the pulse spectrum at the RR wavelength which would increase the measured signal. The pulse compression and spectral broadening is a transient effect, hence the second peak only occurs for a small range of chirp values. For the shorter PCFs the optimum chirp and the chirp for compression at the PCF end are close, which could explain why there is no obvious second peak for the 4 mm and 6 mm PCFs (and why no clear second peak was seen in figure 49(b)).

This theory is weakened by the fact that the second peak for the 10 mm PCF occurs at smaller chirp values than the chirp for compression at the PCF end. There does however appear to be a third peak at the chirp for compression at the PCF end - this is more obvious from the peak area data than from the peak height data. One possible explanation for the second peak is that the pulse is compressing more than one in the PCF and each compression is broadening the spectrum and creating a peak at the RR wavelength.

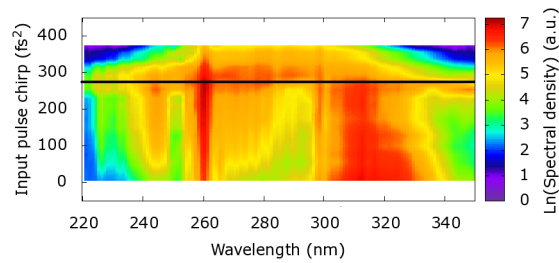
Having looked at the impact of chirp on pulse broadening in the IR and visible and on the



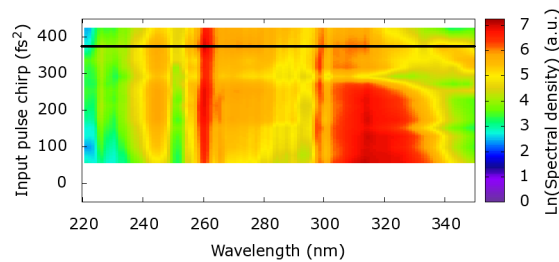
(a) 4 mm



(b) 6 mm



(c) 8 mm



(d) 10 mm

Figure 53: Experimental results - Colour scale plots of the UV output spectra (logarithmic values) as the input pulse chirp is varied for different input pulse powers. NL-1.5-590 PCF with an input pulse of 12 fs length and $N = 2.25$

generation of RR, I now turn to look at the effects in the UV, in particular the impact of chirp on the generation of NRR.

The colour scale plots in figure 53 show how the UV output spectra vary with input chirp for the same four PCF lengths as before. In these plots we are looking for evidence of spectral broadening into the UV when the input chirp corresponds to pulse compression at the PCF end. Such broadening is seen clearly for the three shorter lengths (marked by a horizontal line). This means that when the pulse compresses there will be a component of the pulse oscillating at the NRR wavelength which drives the radiation. The chirp values at which the broadening occurs match those seen in the visible and IR and listed in table 3. For the 10 nm plot the broadening is less obvious, this is likely to be due to the decrease in the degree of pulse compression for larger chirps.

As in the visible and IR plots in figure 51 the spectrum is narrow for large chirps which cannot be compensated inside the PCF. It then broadens for compression at the PCF end and re-contracts as the chirp decreases further.

As well as the spectral broadening the plots display a few other interesting features. The first thing to note is that the NRR appears in these plots as a weak spectral feature at about 227 nm. More detailed spectra for the NRR will be shown next. The next features to note are the high intensity narrow band radiation at approximately 260nm and the broader bandwidth signal between 300nm. and 340nm. These are both due to THG between the fundamental and higher order modes, as discussed in section 4.2. One contrast between the two spectral features is that the narrow band feature is strongest when the spectral broadening occurs i.e. when the compression is at the end of the PCF whilst the broad band feature is strongest for small chirp values. This could be related to the different loss experienced by each radiation. If the loss is high then the peak height of the radiation in the output would be expected for compression at the PCF end. If on the other hand the loss is lower then the peak would be expected for small positive chirps corresponding to the optimum pulse compression. Whilst these features are interesting they are not the subject of this investigation and will not be considered in more detail here. However the discussion of loss is also applicable to the NRR.

We now turn to focusing on the variation in the NRR output with chirp. Figure 54 shows the output spectra around the NRR wavelength with varying chirp. In all cases the NRR forms a peak

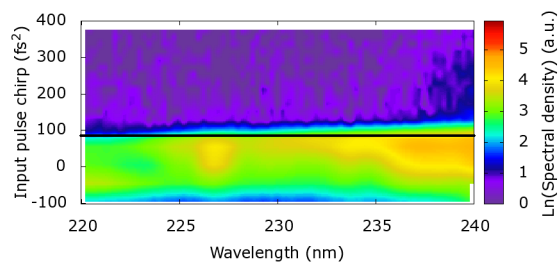
at 227 nm. The peak height decreases for chirps less than zero and also for large chirps. Working backwards from large chirps the first appearance of the NRR occurs at the same point as spectral broadening is seen. This is the short wavelength edge of the broadening seen in figures 51 and 53. Again this point has been marked with a horizontal line, corresponding to the values in table 3.

The height of the NRR in the output spectra as a function of chirp is shown in figure 55. As in figure 40(d) the heights have been plotted both calibrated and uncalibrated for loss. In this case the variation in the peak area has not been included, this follows almost the same pattern as the variation in the peak height for all PCF lengths.

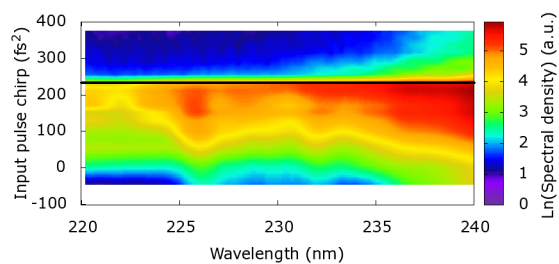
First we consider the uncalibrated results. The key aspect to note is that the variation in height with chirp is different to that of RR. The RR reached a maximum peak height for approximately the same small chirp value for all PCF lengths as seen in figure 52. In contrast the uncalibrated NRR peak heights reach a maximum for a chirp value which increases with increasing PCF length. This difference can be explained if the loss experienced by the NRR is much larger than that experienced by the RR. The high loss means that the NRR height reaches a peak in the output when the pulse compresses at the PCF end and therefore the loss is minimised.

An additional feature is that in the 10 mm plot there are two peaks in the NRR height. This could be another indicator that the pulse is compressing more than once in the PCF. The peak at the larger chirp value corresponds to the first compression occurring at the PCF end and the peak at the smaller chirp value corresponds to the second compression occurring at the PCF end.

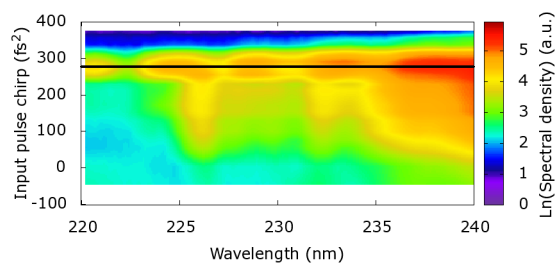
In the next section (section 13.4.4) the loss experienced by the NRR is calculated to be approximately $1.5 - 2.5 \text{ dBmm}^{-1}$. Using this to calibrate the data produces the other plots in figure 55. In all cases the NRR peak height now reaches a maximum for a smaller input chirp between 0 fs^2 and 150 fs^2 . Whilst the broad range suggests that the loss calculations require improvement the data now qualitatively match the behaviour of the RR. Specifically the NRR height is small for negative chirp corresponding to minimal pulse compression. As the chirp increases the NRR height increases to a maximum at the optimal chirp for compression. Further chirp increases lead to a decrease in the NRR height as the degree of compression deteriorates until eventually the chirp



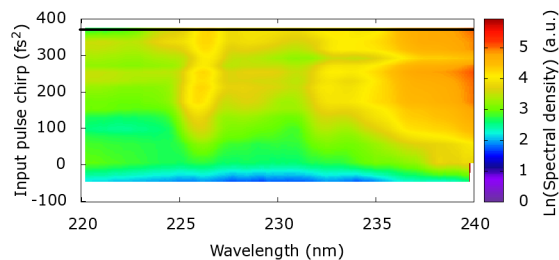
(a) 4 mm



(b) 6 mm

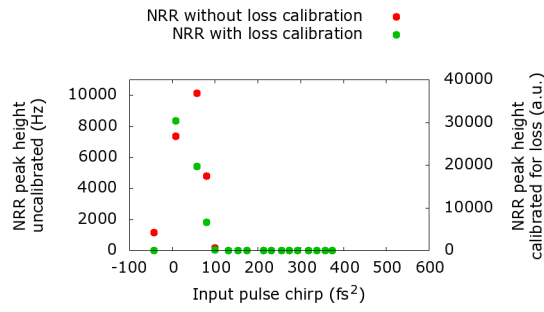


(c) 8 mm

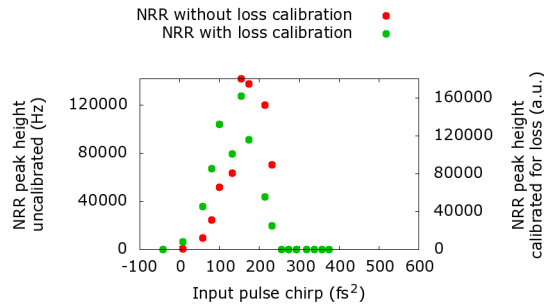


(d) 10 mm

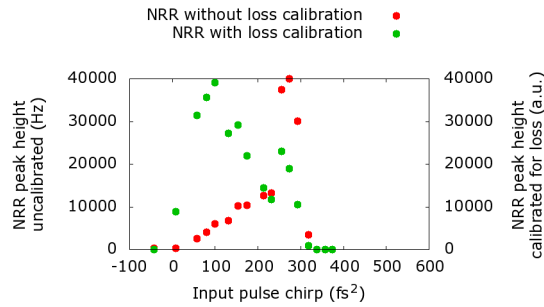
Figure 54: Experimental results - Colour scale plots of the NRR output spectra (logarithmic values) as the input pulse chirp is varied for different input pulse powers. NL-1.5-590 PCF with an input pulse of 12 fs length and $N = 2.25$



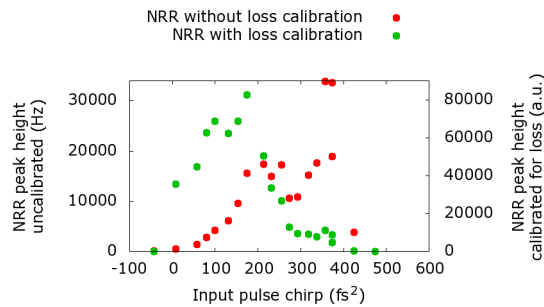
(a) 4 mm



(b) 6 mm



(c) 8 mm



(d) 10 mm

Figure 55: Experimental results - NRR peak heights (maximum counts) as the input pulse chirp is varied for different PCF lengths. NL-1.5-590 PCF with an input pulse of 12 fs length and $N = 2.25$

becomes too large to be compensated in the PCF.

13.4.4 Loss calculations

The high loss experienced by the NRR has been mentioned in the previous sections and results have been calibrated to take account of this loss. In this section I show how this loss was calculated. I present results showing how the peak height of the NRR changed for the same input chirp (and other pulse parameters) but for different PCF lengths. These results will then be used to calculate the loss experienced by the NRR.

The accuracy of the calculation will be limited by several factors. One is that the coupling into each PCF length may be different and hence even with the same input pulse parameters the generation efficiency of the NRR will vary. The second is that only some of the light at the NRR wavelength is part of the NRR radiation. Other sources of light at that wavelength include spurious higher order monochromator signals, THG and the broadened spectrum of the pulse itself. The light from other sources may be in a different mode to the NRR and therefore experience very different loss. Efforts can be made with filters to remove third harmonic light as seen in section 13.2. The higher order monochromator signals can also be removed with narrowband UV filters however these reduce further an already small signal. The spectral broadening is necessary to drive the NRR and therefore it cannot be removed.

In order to calculate the loss we assume that it can be expressed as an exponential loss (this may not be true if the NRR does not form in a guided mode)

$$I = I_0 e^{-\alpha(L-z_c)}. \quad (13.2)$$

Here I is the output NRR intensity and I_0 is the intensity of the NRR when it is generated at the point of maximum pulse compression. The loss is represented by the parameter α , and L and z_c are respectively the PCF length and the propagation distance between the start of the PCF and the

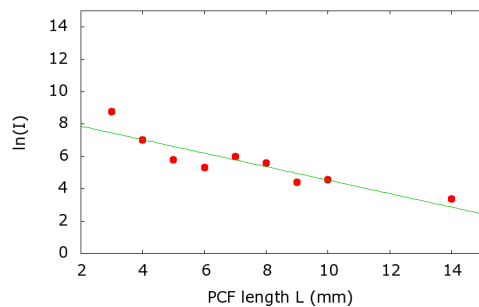
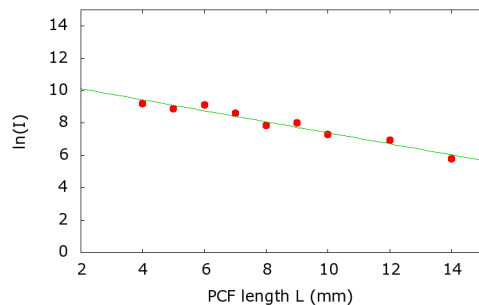
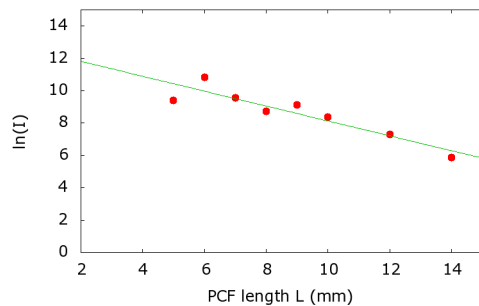
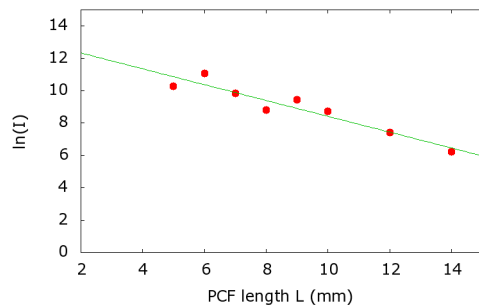
(a) -42 fs^2 (b) 57 fs^2 (c) 100 fs^2 (d) 131 fs^2

Figure 56: Experimental results 1 - Graphs of the natural logarithm of the NRR peak height (maximum counts) in the output as a function of the PCF length for different input pulse chirps. NL-1.5-590 PCF, $N = 2.25$, pulse length 12 fs

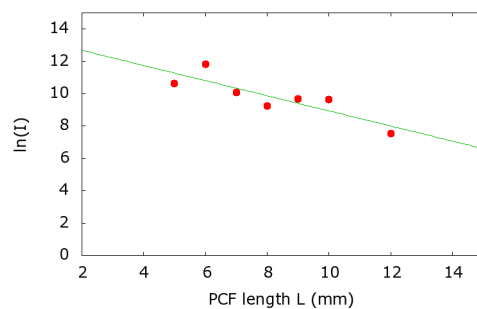
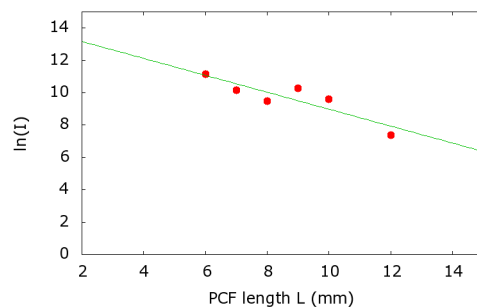
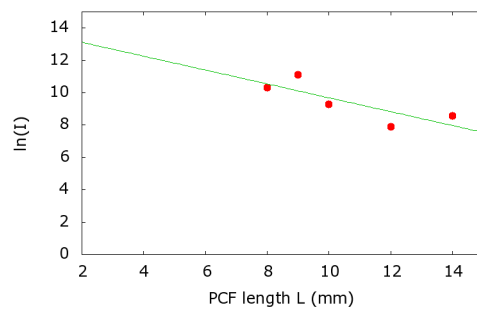
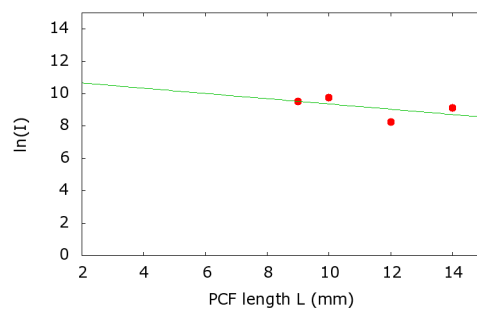
(a) 174 fs²(b) 231 fs²(c) 293 fs²(d) 338 fs²

Figure 57: Experimental results 2 - Graphs of the natural logarithm of the NRR peak height (maximum counts) in the output as a function of the PCF length for different input pulse chirps. NL-1.5-590 PCF, $N = 2.25$, pulse length 12 fs

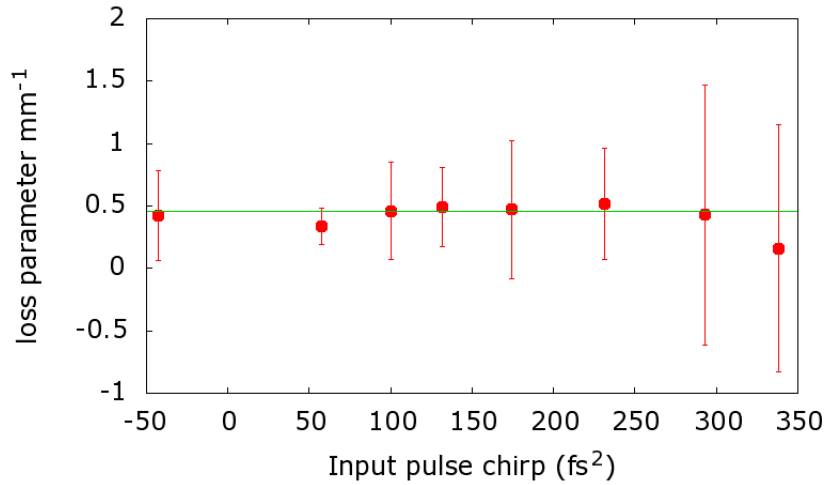


Figure 58: Experimental results - Calculated values of α as a function of input pulse chirp

point of compression. This is rearranged to give

$$\ln(I) = -\alpha L + \alpha z_0 + \ln(I_0). \quad (13.3)$$

We assume that the loss parameter α remains approximately constant for all input pulse parameters (i.e. we ignore non-linear loss). If the same input chirp is used then the pulse evolution will occur in the same way regardless of PCF length so z_c will be independent of PCF length. If the pulse compresses in the PCF then the same amount of NRR will be generated, hence for any one chirp I_0 will be also constant.

The graphs in figure 56 show the variation in $\ln(I)$ with PCF length for a several different chirps. For the larger chirps there are fewer points plotted as compression and NRR generation were only able to occur in the longer PCFs. For each chirp value, if there is a PCF length where compression occurs very close to the end of the PCF I have removed that value. This is to try to reduce the issue mentioned earlier of spectral components from the compressed pulse affecting the results. The gradient of the graphs will give the value of $-\alpha$.

The values of α from the graphs in figure 13.4.4 are shown in figure 58, as a function of the input pulse chirp. Taking a weighted average of the results gives a value for α of 0.46 mm^{-1} or $1.99 \pm 0.5 \text{ dBmm}^{-1}$. This is an extremely high loss, as a comparison the dominant contributions

to loss in the PCFs over a broad range of wavelengths from the UV to the IR are expected to be absorption and Rayleigh scattering (from density fluctuations in the silica). Absorption is largest in the UV (due to electronic resonances) and in the far IR (due to vibrational resonances). In the UV total losses can be of the order of 1 dBm^{-1} . At the NRR wavelength the contribution to this due to Rayleigh scattering will be of the order 300 dBkm^{-1} (proportional to $1/\lambda^4$).

The high losses suggest that the NRR is in a non-guided mode which radiates into the cladding of the PCF. However, if the NRR were generated in a higher order mode, this mode would have to satisfy the phase matching condition for NRR. As we have seen the NRR at a wavelength predicted using the phase matching condition and the fundamental mode, it appears that the NRR must be generated in the fundamental mode. Further work is required to investigate which mode the NRR may be forming in. Using SEM images of the PCF end and the mode calculation programme as described section 3, the different modes of each PCF can be calculated. This along with further experimental work can be used to investigate the NRR loss further.

One potential use for the results from these loss calculations is in the design of experiments to detect the optical analogue of HR. As mentioned in section 6 this is expected to be generated in the UV near to the NRR wavelength. It is possible that the HR will also experience high losses. Therefore, as seen in the NRR experiments, it may be necessary to choose the PCF length and input chirp such that the pulse compression occurs at the end of the PCF. In addition as seen in both the simulations and the experiments the greatest degree of pulse compression occurs for small chirps. The generation of the optical analogue of HR is expected to depend critically on the steepness of the pulse and therefore it will be favoured by a high degree of pulse compression. This suggests that using a short PCF where the chirp for compression at the PCF end is small will increase the probability of detecting the radiation.

13.5 Polarization experiments

This section describes a set of measurements investigating the polarisation state of both the pulse and the driven radiation. The results display some interesting features but further investigation is required to fully explain what is seen.

It was noted in the section 12.2 that the output light from the laser is horizontally polarised

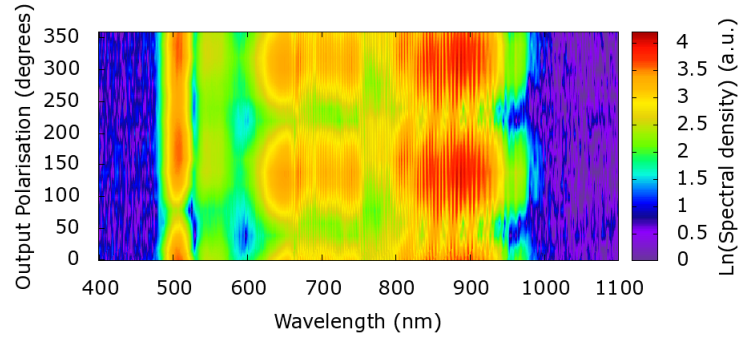
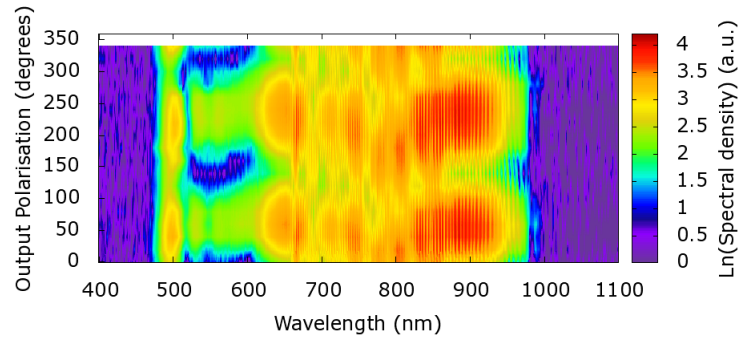
(a) Input polarisation 0° (b) Input polarisation 90°

Figure 59: Experimental results - Colour scale plots showing the variation in the visible and IR output spectra (logarithmic values) as a polariser in the output is rotated for input polarisations aligned on the two principal PCF axes. NL-1.6-615 PCF with $N = 2.1$, PCF length 2 mm

and that the PCFs are rotated to align with the input polarization so that only one principal axis is excited. This has the benefit of maximising the power along one axis and also removing extra signals in the output spectra. These occur due to the slight birefringence of the PCF.

We vary the input polarisation as it is expected to impact the peak power in each axis and therefore the pulse spectral broadening and the generation of RR and NRR. We look at different polarizations in the output to provide insights into the degree to which the input pulse polarization is maintained on propagation through the PCF and also into which of the driven radiation signals are co- or cross-polarised.

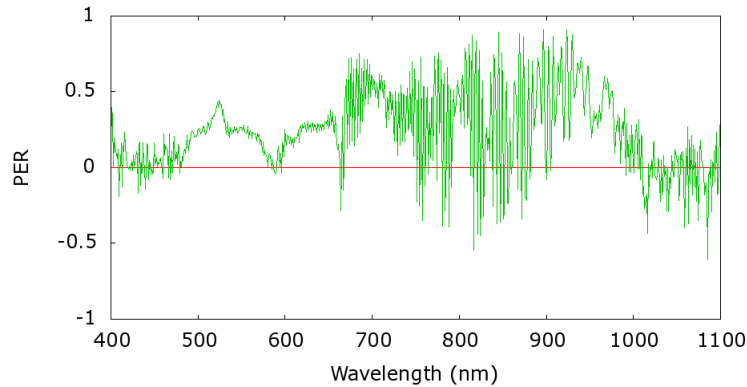


Figure 60: Experimental results - PER between the co- and cross-polarised output spectra. NL-1.6-615 PCF with $N = 2.1$, PCF length 2 mm. 0=signal is unpolarised, 1=signal is co-polarised, -1=signal is cross-polarised

As a first test we look at the visible and IR output spectra for different projections onto linear output polarisations. The purpose of this is to see to what extent the output pulse and RR are co-polarised with the input pulse. Figure 59, shows the output spectra as a polariser in the output beam is rotated for two different input polarisations. The input polarisation is rotated using a HWP and each polarisation aligns with a different PCF principal axis. The input power was kept constant in each case.

If the pulse and driven radiation remains co-polarised with the input pulse then we would expect the spectral density to be highest when the input and output polarisations coincide (i.e. at 0° for figure 59(a) and 90° for figure 59(b)). The data does not perfectly match this expectation. In both cases there are output polarisations for which the spectral density is higher across most of the bandwidth. However, these are slightly offset from the expected polarisation values. In both cases the output polariser for the stronger spectrum are slightly smaller than expected suggesting that the calibration of the output or input HWP angle may be slightly offset.

Using the results from figure 59(a), we correct for this offset by making the assumption that the output polariser angle corresponding to the highest overall spectral density is the angle co-polarised with the input. We then calculate the PER (see section 12.2 (12.1)) for each wavelength, using the co- and cross-polarised output spectra. The result is plotted in figure 60.

The results show that the PER varies considerably. The RR peak situated at about 500 nm is partially co-polarised as are large parts of the input pulse spectrum. However there are regions in

the pulse spectrum where the PER is very small or even slightly cross-polarised.

The PER of the input is at least 0.99 which is considerably higher than the output degree of polarisation. With the PCF removed from the experimental set-up we measure the PER in the focus and after collimation. These are found to have PER values of at least 0.95 suggesting that it is the PCF which is distorting the polarisation rather than the other optical elements in the beam path. Measurements of the visible and IR output spectra taken using various PCFs, fibre lengths and input pulse parameters all yield similar poor output PER values to those seen in figure 60.

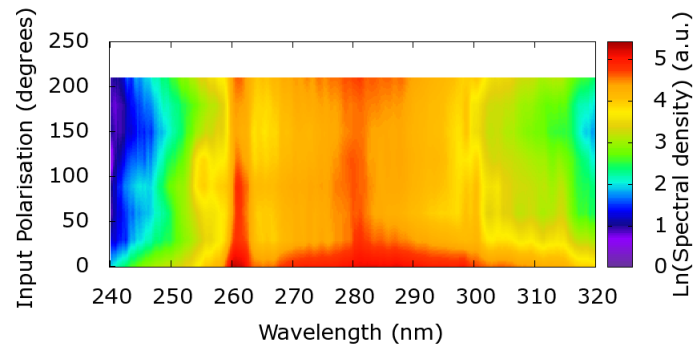
The results from the visible and IR indicate the the PER in the UV is also likely to be low as the UV radiation is driven by the pulse. To check this we record some results in the UV. In this case the input polarisation is rotated in the same way as before and different projections onto linear output polarisations are selected using a Glan-Taylor polariser. As in the visible and IR experiment, a very short piece of PCF is used (2 mm), in the hope that this will reduce the change in the polarisation. Results are presented for the NL-1.5-590 PCF as opposed to the NL-1.6-615 PCF used previously. However the results in the visible, IR and UV are qualitatively similar for both PCFs.

The results in figures 61(a) and 61(b), show respectively, how rotating the input polarisation and projecting onto different linear output polarisations affect the UV spectrum.

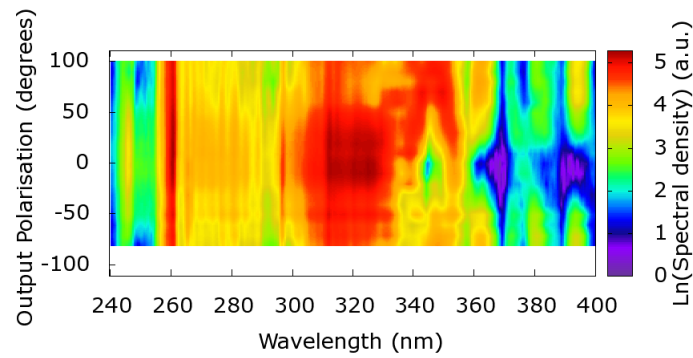
In figure 61(a) we see that the strongest output signal, across most of the spectrum, occurs when the input is aligned with one of the PCF principal axes. This is in agreement with the expectation that the signals driven by the pulse in the UV will be strongest when only one fibre axis is excited.

Aligning to the second axis produces a considerably smaller signal. A calibration of the monochromator shows differences, below 240nm, in the detection efficiency for horizontally and vertically polarised light. However at the wavelengths shown in figure 61(a), the differences are minimal. One possible explanation is that the coupling into the PCF varies when the input polarisation is rotated. As the peaks in the UV are sensitive to the peak power of the input pulse this could account for differences. Another explanation is that the PCF is damaged reducing coupling into one axis.

Figure 61(b), shows how the UV output spectrum varies as the output polariser is rotated. It is not possible to look in detail at the NRR as the transmission through the Glan-Taylor polariser is poor at that wavelength and the signal is too small. In addition, as mentioned previously, the detector sensitivity becomes polarisation sensitive close to the NRR wavelength. However results



(a)



(b)

Figure 61: Experimental results - Colour scale plots of the UV output spectra (logarithmic values). NL-1.5-590 PCF with $N = 2.1$, PCF length = 2 mm. (a) Constant output polarisation, rotating the input polarisation, 0^0 corresponds to the input polarisation aligned to a PCF axis. (b) Constant input polarisation, projecting onto different linear polarisations in the output, 0^0 corresponds to the same polarisation as the input

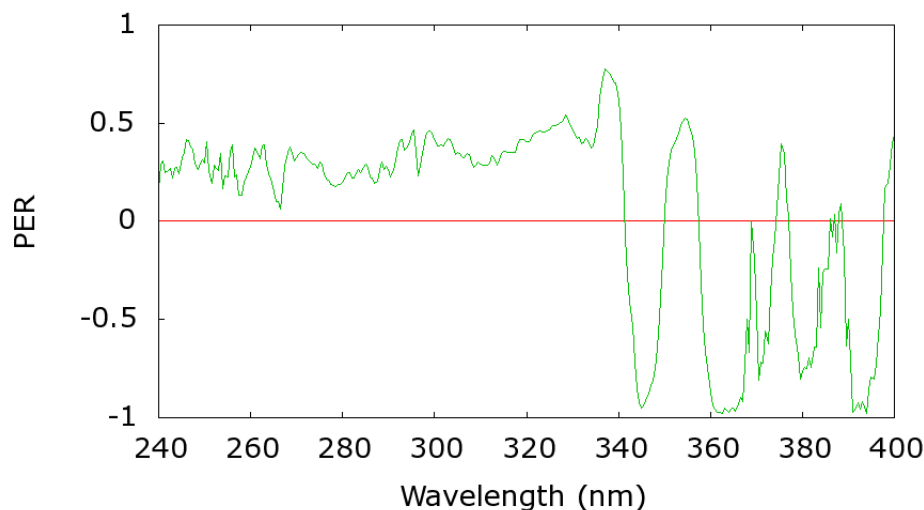


Figure 62: Experimental results - PER between the co- and cross-polarised output spectra. NL-1.5-590 PCF with $N = 2.1$, PCF length 2 mm. 0=signal is unpolarised, 1=signal is co-polarised, -1=signal is cross-polarised

for other signals in the UV can be investigated.

The plot shows that there are signals in the UV which are at least partially co-polarised. In particular the third harmonic radiation at 260nm and between 300nm and 340nm is strongest when the output polariser is aligned for co-polarised light. There is however some light which appears to be cross-polarised appearing in spectral bands between 360 nm and 400 nm. The origin of this radiation is not currently understood.

The UV equivalent of figure 60, showing the PER across the spectrum, is displayed in figure 62. Below 330 nm the output is partially co-polarised however above 330 nm there are parts of the spectrum which are strongly cross polarised.

In conclusion the results in this section have lead to many questions but few answers. The PER for the input light is high even in the focus. However the output light in the visible, IR and UV has a very low PER, and even in some cases indications that the output is cross-polarised compared to the input. Similar results have been found for all of the PCFs tested and for all fibre lengths. This is not in agreement with our expectations and we have not found similar results in the literature. This suggests that there is an issue with our measurement technique or that we need to improve our understanding of the polarisation behaviour in PCFs.

One possible explanation is that a large proportion of the input light is coupling into higher order modes, which have a lower degree of polarisation than the fundamental mode. However in cases where a large amount of RR is produced it is expected that a significant proportion of the input light must be coupled into the core of the PCF (in order to satisfy the phase matching condition), yet still there is a poor degree of polarization.

The PER does improve if the input power is reduced. As discussed in section 12.2, if a bandpass filter is used in the input the PER is larger, which is used to align the PCF axes with the input light polarisation. In this case the output spectrum is very similar to the input spectrum i.e. a narrow peak in the IR. The output PER values can reach up to 0.8. This suggests that the change in polarisation in the PCF is related to non-linear effects.

Further work is required to investigate the polarisation. If the changes are related to higher order modes then an analysis of the modes of the PCF using the programme described in section 3, and measurements of the modes in the fibre output, may provide some insights. The effect of input power on the polarisation can also be investigated further.

Part IV

Conclusions and outlook

In the literature review I describe the discovery and study of optical solitons and the types of radiation that can be driven by them, with a focus on the discovery of RR and some of the key research papers in the field. As mentioned before, RR is a well known phenomenon and its behaviour has been studied by many research groups over the years. The new development, which is the focus of this thesis, is the discovery of NRR. In the literature review I discuss the first paper relating to NRR, which I co-first authored [118]. In that paper the idea of coupling between negative and positive frequencies in optics is proposed and examples are shown in two different experiments. I also discussed another paper by Faccio et al. [117], which uses both analytical and numerical techniques to analyse the NRR and RR. The results show that, as in the well known case of RR, the NRR is expected to depend on the amplitude of the driving pulse spectrum at the phase matched wavelength.

The motivations behind the study of RR are discussed in section 5.1.1. Many different research groups have investigated RR and looked at various methods to control its generation. These methods focus on producing an optimised signal for practical uses i.e. a narrowband, tunable peak with high intensity and high stability. This contrasts with the motivations for the study of NRR, which is too small a signal to be of use in practical applications. NRR is interesting primarily because it indicates a coupling between positive and negative frequencies.

A conversion from positive to negative frequencies has been seen in water wave systems, which were discussed in section 5.2. However to the best of our knowledge, NRR is the first example in optics. Positive and negative frequencies are clearly present in the Fourier transform of a signal. However, experimental results can usually be described by considering only the positive frequencies. The NRR demonstrates that negative frequencies have a physical meaning as in order to describe the experimental results a conversion from positive to negative frequencies is required.

The first experimental results in this thesis are very similar to those in the first NRR paper [118]. They demonstrate for one PCF that a NRR signal is found at the wavelength predicted by the dispersion relation and the phase matching condition. Similar results have also found for two other PCFs. One limitation of this thesis is the small range of PCFs which we have used to measure NRR. These were selected for their dispersion characteristics, and to make use of the available laser source. As described in section 5.2, the phenomenon has been observed in bulk glass and simulation results suggest that it can be generated in quadratic media and from pulses in the normal dispersion

region. Further work in this field would include an investigation into NRR in other fibres and other optical systems. Also it would be interesting to see if there are other types of radiation which we can only explain using negative and positive frequencies. As suggested in the paper by Conforti et al. [92], systems described by similar equations to the NLSE do not take negative frequencies into account and therefore there may be scope in these fields to find new behaviour by considering negative frequencies. Examples of such systems include Bose Einstein condensates, plasmas and water waves.

Most of the other results in this thesis build on the initial discovery of NRR. They seek to confirm that it will only be generated when the input pulse spectrum expands to reach the phase matched wavelength and also to compare the growth of the NRR with theoretical predictions. This is achieved using the tools of pulse power and chirp to move the point of pulse compression and to vary the degree and quality of the compression. Simulation results help us to qualitatively see how the power and chirp affect pulse compression. Using these simulation results and our theoretical expectations we are able to interpret the experimental results for varying power and chirp. One key example of this is that we can use the chirp to move the point of compression to the end of the PCF and therefore see the full extent of the spectral broadening in the output. This allows us to see that the pulse spectrum can extend into the UV and drive the NRR. An extension to this would be to see if a steep pulse is required to drive the NRR or simply a broad spectrum.

In part II, a pulse propagation equation was derived without the use of the slowly varying envelope approximation and this was used to find an expression for the amplitude of the NRR. As expected from the work by Faccio et al. [117] and the body of research on RR, the amplitude was found to depend on the pulse spectral amplitude at the NRR wavelength. A rough comparison with experimental results could be made using pulse compression details from the simulations. This did not produce a good match, most likely due to the differences between the simulations and the experiments. Further work in the field of NRR would look into bringing experimental results and theoretical predictions into closer alignment. One approach to this would be to try to experimentally distinguish better between the NRR and other radiation in the UV, such as the expanded pulse spectrum. Also experimental measurements of the degree of pulse compression could be made using autocorrelation techniques. These could be used rather than simulation results for pulse compression.

Of the two tools used to study the pulse compression and NRR generation, we find that the chirp is considerably more useful for moving the point of pulse compression, whilst power is more useful for varying the degree of pulse compression. In the former case, compared to the power, the chirp causes a significantly smaller change in the degree of pulse compression when it is used to move the point of compression. In the latter case we can use the large changes in the degree of compression as the power varies to study the effect of compression and spectral broadening on NRR generation.

The chirp is therefore used to move the point of compression and study the pulse evolution and compression, and the NRR and RR generation and evolution. In the results we see some issues with this method. In particular the degree of compression does change to a small extent when the chirp is varied. This means that either the method only produces qualitatively comparable results or that the results have to be corrected for the change in pulse compression.

One positive effect of the change in the degree in pulse compression with chirp is that there appears to be an optimal small positive chirp for pulse compression. This can be clearly seen in the simulation results for a wide range of input pulse parameters and can also be seen in the experimental results. The optimum chirp can be used to optimise the RR and NRR generation by maximising the spectral broadening. This is an area which requires further work to investigate why the optimum chirp is non-zero and why it varies with power and pulse length.

One outcome from experiments using the chirp to move the compression point, is that we use this method with different PCF lengths to investigate the loss experienced by the NRR. This is found to be very high. We postulate that this could be due to the NRR forming in a higher order mode, although this would also have to satisfy the phase matching condition. Further investigation of the fibre modes for both the input and the NRR is required. This may also shed some light on the unexpected polarisation changes in the PCFs.

Part V

Appendix

14 Hollow core PCF guiding

In this section I briefly explain how guiding occurs in a hollow core PCF.

In a hollow core PCF the pattern of holes in the cladding is a type of photonic crystal. These have certain bands of frequencies which cannot propagate through them known as stop bands. Research into the field of photonic crystals has been extensive and the following references cover many of the developments, including the use of photonic crystals in fibre design [129, 119, 15, 60, 151, 14].

The stop bands of a photonic crystal are due to the periodic nature of the pattern. The same phenomenon is seen in Bragg diffraction from a crystal lattice. In the latter case the periodic structure is the crystal lattice which has a periodicity with a scale of a few angstroms. Incident light will scatter and interfere constructively if the path difference between rays reaching different lattice planes is an integer multiple of wavelengths [58]. For a particular wavelength of light this means that a discrete set of incoming ray angles will produce a reflection. Equivalently for a particular incoming ray angle only discrete wavelengths will be reflected. Mathematically this is expressed by Bragg's law,

$$2d_{h,k,l}\sin(\theta_{h,k,l}) = m\lambda,$$

where $d_{h,k,l}$ is the distance between lattice planes labelled by the Miller indices h, k, l , θ is the angle between the incident light and the normal to the set of lattice planes (h, k, l) (and hence also the angle of the reflected light), m is an integer and λ is the wavelength of the incident light. Incident light with an angle and a wavelength obeying the above equation will be totally reflected and therefore cannot propagate through the crystal. For lattice spacings of a few angstroms the wavelengths that are not allowed to propagate will be in the x-ray region of the spectrum.

Bragg's law will also apply in the case of a photonic crystal although, due to the larger scale of the periodicity, light of longer wavelengths will be unable to propagate through the crystal.

Unlike Bragg diffraction from crystals, the range of blocked wavelengths in a photonic crystal is quite large as for a particular h, k, l . Bragg's law can be satisfied for a range of wavelengths of order $\Delta\lambda/\lambda \sim 10^{-2}$ compared to $\Delta\lambda/\lambda \sim 10^{-6}$ for X-ray diffraction. This range of blocked wavelengths is known as a band gap and in photonic crystals the band gap for one h, k, l can be large enough to overlap with the band gap for another h, k, l . In particular this occurs if the symmetry of the photonic crystal is hexagonal, as in the case of PCFs. This overlap means that, for any incident

angle, a particular wavelength range of light will not be able to propagate. The properties of photonic crystals that have just been described will allow guided modes to form in a PCF which propagate in the hollow core but not in the photonic crystal cladding.

15 Derivation of the NLSE

The following derivation mostly follows Agrawal [2] and Boyd [18] with added emphasis on certain approximations which are not valid for short pulses and which will need to be removed in the more general pulse propagation equation.

We are considering electromagnetic radiation passing through a fibre. The electric and magnetic fields of the radiation will interact with the material of the fibre. Any treatment of the propagation of electromagnetic waves must start with Maxwell's equations

$$\nabla \cdot \mathbf{D} = \rho_f, \quad (15.1)$$

$$\nabla \cdot \mathbf{B} = 0, \quad (15.2)$$

$$\nabla \times \mathbf{E} = -\frac{\partial \mathbf{B}}{\partial t}, \quad (15.3)$$

$$\nabla \times \mathbf{H} = \frac{\partial \mathbf{D}}{\partial t} + \mathbf{J}. \quad (15.4)$$

Where \mathbf{D} and \mathbf{B} are respectively the electric and magnetic flux densities in the medium, and \mathbf{E} and \mathbf{H} are the electric and magnetic field vectors of the electromagnetic radiation.

For the case of light propagating in a fibre there are no free charges hence the free charge density ρ_f is zero and also no currents hence the current density vector (\mathbf{J}) is zero. Therefore the equations become

$$\nabla \cdot \mathbf{D} = 0, \quad (15.5)$$

$$\nabla \cdot \mathbf{B} = 0, \quad (15.6)$$

$$\nabla \times \mathbf{E} = -\frac{\partial \mathbf{B}}{\partial t}, \quad (15.7)$$

$$\nabla \times \mathbf{H} = \frac{\partial \mathbf{D}}{\partial t}. \quad (15.8)$$

The electric and magnetic flux densities are due to the electric and magnetic fields respectively and the response of the fibre material to these fields. They are expressed in terms of the electric and magnetic fields as:

$$\mathbf{D} = \epsilon_0 \mathbf{E} + \mathbf{P}, \quad (15.9)$$

$$\mathbf{B} = \mu_0 \mathbf{H} + \mathbf{M}. \quad (15.10)$$

Where \mathbf{P} is the induced electric polarization of the medium. The electric field causes the bound electrons in the medium (in our case the optical fibre) to realign. This produces a net charge distribution which leads to an additional contribution to the electric field in the medium. Similarly \mathbf{M} is the induced magnetic polarization of the medium due to the magnetic field. The other symbols are the vacuum permittivity ϵ_0 and the vacuum permeability μ_0 . For the following analysis only the electric field will be considered although a similar procedure can be used to analyse the magnetic field.

We can use the above equations to derive a wave equation for the electric field. First we replace \mathbf{B} in (15.7) with \mathbf{H} using (15.10)

$$\nabla \times \mathbf{E} = -\mu_0 \frac{\partial \mathbf{H}}{\partial t} - \frac{\partial \mathbf{M}}{\partial t} = -\mu_0 \frac{\partial \mathbf{H}}{\partial t}. \quad (15.11)$$

Where we have set \mathbf{M} to zero as an optical fibre is a non-magnetic medium and thus has no induced magnetic polarisation.

Taking the curl of (15.7) and substituting in (15.8) leads to

$$\nabla \times \nabla \times \mathbf{E} = -\mu_0 \frac{\partial^2 \mathbf{D}}{\partial t^2}, \quad (15.12)$$

$$\nabla \times \nabla \times \mathbf{E} = -\frac{1}{c^2} \frac{\partial^2 \mathbf{E}}{\partial t^2} - \mu_0 \frac{\partial^2 \mathbf{P}}{\partial t^2}, \quad (15.13)$$

where $c^2 = 1/\mu_0 \epsilon_0$. Using the familiar relation for the double curl we get

$$\nabla(\nabla \cdot \mathbf{E}) - \nabla^2 \mathbf{E} = -\frac{1}{c^2} \frac{\partial^2 \mathbf{E}}{\partial t^2} - \mu_0 \frac{\partial^2 \mathbf{P}}{\partial t^2}. \quad (15.14)$$

The first term on the LHS is rewritten using (15.5) and (15.9)

$$\nabla(\nabla \cdot \mathbf{E}) = \frac{1}{\epsilon_0} \nabla(\nabla \cdot \mathbf{D} - \nabla \cdot \mathbf{P}) = -\frac{1}{\epsilon_0} \nabla \cdot (\nabla \cdot \mathbf{P}). \quad (15.15)$$

Where we have used the fact that there are no free charges and hence the divergence of the electric

flux density \mathbf{D} is zero. Substituting this into (15.14) leads to an initial form of the wave equation

$$\frac{1}{\epsilon_0} \nabla (\nabla \cdot \mathbf{P}) + \nabla^2 \mathbf{E} = \frac{1}{c^2} \frac{\partial^2 \mathbf{E}}{\partial t^2} + \mu_0 \frac{\partial^2 \mathbf{P}}{\partial t^2}. \quad (15.16)$$

The charge density due to the realignment of bound electrons by the electric field is referred to as the bound or polarisation charge density $\rho_b = -\nabla \cdot \mathbf{P}$ [51]. For low intensity electric fields this term will be zero as \mathbf{P} will be a linear function of \mathbf{E} and therefore \mathbf{E} will be proportional to \mathbf{D} . However we wish to consider cases where the electric field will have a high intensity and \mathbf{P} will have a non-linear dependence on \mathbf{E} .

The next step in the derivation is to express \mathbf{P} phenomenologically in terms of \mathbf{E} . We start by writing \mathbf{P} as a power series expansion in \mathbf{E} . This approach is not valid if the frequency of the electric field is near to a resonance of the medium. This is a frequency which will lead to resonant oscillations of bound electrons and hence absorption of the electromagnetic radiation. For the fibres and the laser light that we use we are far from resonance so the power series expansion will be valid,

$$\begin{aligned} \frac{\mathbf{P}(\mathbf{r}, t)}{\epsilon_0} &= \int_{-\infty}^{\infty} \chi^{(1)}(t - t_1) \mathbf{E}(\mathbf{r}, t_1) dt_1 + \int_{-\infty}^{\infty} \int_{-\infty}^{\infty} \chi^{(2)}(t - t_1, t - t_2) \mathbf{E}(\mathbf{r}, t_1) \mathbf{E}(\mathbf{r}, t_2) dt_1 dt_2 \\ &+ \int_{-\infty}^{\infty} \int_{-\infty}^{\infty} \int_{-\infty}^{\infty} \chi^{(3)}(t - t_1, t - t_2, t - t_3) \mathbf{E}(\mathbf{r}, t_1) \mathbf{E}(\mathbf{r}, t_2) \mathbf{E}(\mathbf{r}, t_3) dt_1 dt_2 dt_3 + \dots \end{aligned} \quad (15.17)$$

The coefficients of (15.17) $\chi^{(n)}$ are known as the susceptibilities of the medium. As well as assuming that the frequency of the electric field is far from a resonance, (15.17) also assumes that the medium response is local. This means that \mathbf{P} at a particular point in the medium is only affected by the electric field at the same point [21].

Another feature of (15.17) is that it takes into account the fact that the response of the medium to the electric field may not be instantaneous. This is why in order to find \mathbf{P} at time t each term is a convolution of a time dependent susceptibility and the electric field at different times. This time dependence is only important if the propagating electromagnetic field is in the form of pulses with a temporal length which is comparable or shorter than the response time of the medium.

The order of magnitude of each of the susceptibility terms is found by considering that the electric polarisation is due to the movement of bound electrons. Therefore the size of each term

would be expected to be related to the approximate atomic field strength $E_{atom} = e / (4\pi\epsilon_0 a_0^2)$, where e is the electron charge and a_0 is the Bohr radius of the Hydrogen atom [18] [7]. The second term in the RHS of (15.17) (first non-linear term) will be of the same order of magnitude as the first term (linear term) when the applied electric field \mathbf{E} is of the same order as the atomic field strength. This means that $\chi^{(2)} \sim \chi^{(1)}/E_{atom}$ and similarly $\chi^{(3)} \sim \chi^{(2)}/E_{atom} \sim \chi^{(1)}/E_{atom}^2$ and $\chi^{(4)} \sim \chi^{(1)}/E_{atom}^3$. As explained in Boyd [18] the linear polarisation of the medium is given by the product of the density of atoms in the medium which is of order $1/a_0^3$, and to the atomic polarisability which is of order a_0^3 . Thus $\chi^{(1)}$ is approximately 1, $\chi^{(2)}$ is approximately $1.95 \times 10^{-12} \text{ V}^{-1}\text{m}$, $\chi^{(3)}$ is approximately $3.79 \times 10^{-24} \text{ V}^{-2}\text{m}^2$ and $\chi^{(4)}$ is approximately $7.39 \times 10^{-36} \text{ V}^{-2}\text{m}^2$. From these values we see that unless the electric field is very large i.e. of order the atomic field strength $E_{atom} = 5.13 \times 10^{11} \text{ Vm}^{-1}$, the linear term will dominate.

If the field is of the order of the atomic field strength then the expansion in (15.17) will not be valid and other methods to express \mathbf{P} in terms of \mathbf{E} will have to be used. In our case the maximum electric field used is of order 10^9 Vm^{-1} , considerably smaller than E_{atom} hence the expansion can be used. As the higher susceptibility terms become increasingly small it is sufficient to consider only terms up to $\chi^{(3)}$. Additionally for centro-symmetric materials the $\chi^{(2)}$ term will be identically zero.

To explain the last comment in more detail, centro-symmetric materials (such as silica the material of the fibres used) are formed of molecules with inversion symmetry. This means that if the molecule is inverted (all points (x, y, z) in the unit cell moved to $(-x, -y, -z)$) then it will have the same physical properties. This means that if the direction of the electric field is reversed then the direction of the polarisation should also reverse. however for the case of the second order susceptibility term in (15.17) the polarisation will depend on the square of the electric field and therefore it will not reverse [43]. For this reason the second order susceptibility must be zero.

We now simplify (15.17) further by assuming that the light propagating through the medium is in the form of pulses with a longer temporal length than the non-linear response time of the medium to the field. In this case it is possible to treat the response as instantaneous and replace the time dependence of the susceptibilities in the $\chi^{(3)}$ term with delta functions. This is valid for pulses of 1 ps or longer [2]. Removing all susceptibilities higher than third order and the second order susceptibility and treating the non-linear response as instantaneous leads to the following

equation

$$\begin{aligned} \frac{\mathbf{P}(\mathbf{r}, t)}{\varepsilon_0} &= \int_{-\infty}^{\infty} \chi^{(1)}(t - t_1) \mathbf{E}(\mathbf{r}, t_1) dt_1 + \chi^{(3)} \mathbf{E}(\mathbf{r}, t) \mathbf{E}(\mathbf{r}, t) \mathbf{E}(\mathbf{r}, t), \\ &= \mathbf{P}_L(\mathbf{r}, t) + \mathbf{P}_{NL}(\mathbf{r}, t). \end{aligned} \quad (15.18)$$

Where we have split the induced electric polarisation \mathbf{P} into a linear \mathbf{P}_L and a non-linear \mathbf{P}_{NL} response to the electric field.

As a further simplification we assume that the electric field is polarized along one axis initially and remains polarized along the same axis during propagation. An additional approximation assumes that the pulse consists of a slowly varying pulse envelope over a fast pulse oscillation (slowly varying envelope approximation). This is only valid for longer pulses and is one of the key features which invalidates the NLSE for use with few-cycle pulses. With these assumptions the electric field and the linear and non-linear polarizations are written as

$$\begin{aligned} \mathbf{E}(\mathbf{r}, t) &= \frac{1}{2} \hat{x} [E(\mathbf{r}, t) e^{-i\omega_0 t} + c.c], \\ \mathbf{P}_L(\mathbf{r}, t) &= \frac{1}{2} \hat{x} [P_L(\mathbf{r}, t) e^{-i\omega_0 t} + c.c], \\ \mathbf{P}_{NL}(\mathbf{r}, t) &= \frac{1}{2} \hat{x} [P_{NL}(\mathbf{r}, t) e^{-i\omega_0 t} + c.c]. \end{aligned} \quad (15.19)$$

Where $E(\mathbf{r}, t)$, $P_L(\mathbf{r}, t)$ and $P_{NL}(\mathbf{r}, t)$ represent the slowly varying envelope propagating at the group velocity $v_g = d\omega/dk$ where k is the wavenumber, and the exponential part represents the fast oscillations within the envelope with frequency ω_0 propagating at the phase velocity $v_p = \omega_0/k(\omega_0)$ where $k(\omega_0)$ is the wavenumber at frequency ω_0 .

Substituting the electric field into (15.18) and using Fourier transforms,

$E(\mathbf{r}, t) = (1/2\pi) \int_{-\infty}^{\infty} \tilde{E}(\mathbf{r}, \omega) \exp(-i\omega t) d\omega$ and similarly for $\chi^{(1)}(t)$, we find an expression for P_L

$$\begin{aligned}
 P_L(\mathbf{r}, t) e^{-i\omega_0 t} &= \varepsilon_0 \int_{-\infty}^{\infty} \chi^{(1)}(t-t_1) \cdot E(\mathbf{r}, t_1) e^{-i\omega_0 t_1} dt_1 \\
 \Rightarrow P_L(\mathbf{r}, t) &= \varepsilon_0 \int_{-\infty}^{\infty} \left[\frac{1}{2\pi} \int_{-\infty}^{\infty} \tilde{\chi}^{(1)}(\omega) e^{-i\omega(t-t_1)} d\omega \right] \cdot E(\mathbf{r}, t_1) e^{+i\omega_0(t-t_1)} dt_1 \\
 \Rightarrow P_L(\mathbf{r}, t) &= \frac{\varepsilon_0}{2\pi} \int_{-\infty}^{\infty} \tilde{\chi}^{(1)}(\omega) \left[\int_{-\infty}^{\infty} E(\mathbf{r}, t_1) e^{i(\omega-\omega_0)t_1} dt_1 \right] e^{-i(\omega-\omega_0)t} d\omega \\
 \Rightarrow P_L(\mathbf{r}, t) &= \frac{\varepsilon_0}{2\pi} \int_{-\infty}^{\infty} \tilde{\chi}^{(1)}(\omega) \tilde{E}(\mathbf{r}, \omega - \omega_0) e^{-i(\omega-\omega_0)t} d\omega. \tag{15.20}
 \end{aligned}$$

In the first line of (15.20) we use the parts of $\mathbf{E}(\mathbf{r}, t)$ and $\mathbf{P}_L(\mathbf{r}, t)$ oscillating with the same frequency ω_0 and (15.18). We replace $\chi^{(1)}(t-t_1)$ with its Fourier transform and rearrange to form a term equal to $\tilde{E}(\mathbf{r}, \omega - \omega_0)$. This form for $P_L(\mathbf{r}, t)$ in terms of Fourier transforms is useful as in a later step we will want to express the wave equation in the Fourier domain. This will remove the time derivatives in (15.16).

We carry out a slightly different procedure to find an expression for P_{NL} . As a first step we substitute the forms for $\mathbf{E}(\mathbf{r}, t)$ and $\mathbf{P}_{NL}(\mathbf{r}, t)$ from (15.19) into (15.18)

$$\begin{aligned}
 &P_{NL}(\mathbf{r}, t) e^{-i\omega_0 t} + P_{NL}^*(\mathbf{r}, t) e^{i\omega_0 t} \\
 &= \frac{1}{4} \varepsilon_0 \chi^{(3)} \left[E(\mathbf{r}, t)^3 e^{-3i\omega_0 t} + 3|E(\mathbf{r}, t)|^2 (E(\mathbf{r}, t) e^{-i\omega_0 t} + E^*(\mathbf{r}, t) e^{i\omega_0 t}) + E^*(\mathbf{r}, t)^3 e^{3i\omega_0 t} \right]. \tag{15.21}
 \end{aligned}$$

The terms oscillating at $3\omega_0$ and $-3\omega_0$ (third harmonic frequencies) will be neglected in this derivation. The justification for this is that in this derivation we are considering parametric processes where the interaction between the electromagnetic field and the medium happens instantaneously and does not change the state of the medium. This means that no energy can be transferred from the field to the medium or vice versa. All parametric processes which occur must therefore obey phase matching rules which allow conservation of energy and momentum within the field. The terms describing the third harmonic will require such phase matching and in most cases are small compared to the other terms in (15.21) [2]. As discussed in section 4.2 it is possible to achieve

phase matching between the pump pulse and a third harmonic but one or both of these has to be in a higher order mode.

Considering just the part of (15.21) oscillating with ω_0 leads to the following expression for $P_{NL}(\mathbf{r}, t)$,

$$\begin{aligned} P_{NL}(\mathbf{r}, t) &= \frac{3}{4}\varepsilon_0\chi^{(3)}|E(\mathbf{r}, t)|^2 E(\mathbf{r}, t) \\ \Rightarrow P_{NL}(\mathbf{r}, t) &= \varepsilon_0\varepsilon_{NL}E(\mathbf{r}, t). \end{aligned} \quad (15.22)$$

Where $\varepsilon_{NL} = (3/4)\chi^{(3)}|E|^2$. This is a simplified form for the non-linear polarisation but it is still non-linear in $E(\mathbf{r}, t)$, which means that we cannot easily convert to the Fourier domain where we can obtain a simpler version of the wave equation with no time derivatives.

We avoid this difficulty by considering ε_{NL} to be a constant. This is justified by the slowly varying envelope approximation where we defined $E(\mathbf{r}, t)$ as a slowly varying envelope. Additionally we assume that the non-linear contribution to the polarisation is small, which is a good approximation as seen from the previous discussion of the size of the susceptibilities.

In this case it is simple to Fourier transform the wave equation (15.16). We start by substituting the forms of $\mathbf{E}(\mathbf{r}, t)$, $\mathbf{P}_L(\mathbf{r}, t)$ and $\mathbf{P}_{NL}(\mathbf{r}, t)$ from (15.19), into (15.16) and considering only the parts oscillating at frequency ω_0 ,

$$\begin{aligned} &\frac{1}{\varepsilon_0}\nabla\cdot(\nabla\cdot(P_L(\mathbf{r}, t) + P_{NL}(\mathbf{r}, t))e^{-i\omega_0 t}) + \nabla^2 E(\mathbf{r}, t)e^{-i\omega_0 t} \\ &= \frac{1}{c^2}\frac{\partial^2}{\partial t^2}\left(E(\mathbf{r}, t)e^{-i\omega_0 t} + \frac{1}{\varepsilon_0}P_L(\mathbf{r}, t)e^{-i\omega_0 t} + \frac{1}{\varepsilon_0}P_{NL}(\mathbf{r}, t)e^{-i\omega_0 t}\right). \end{aligned} \quad (15.23)$$

As discussed previously the divergence of the linear part of the polarisation will be zero. Using the assumption that ε_{NL} is a constant that was discussed previously, we can now also set the divergence of the non-linear part of the polarisation to zero. We now insert the forms for $P_L(\mathbf{r}, t)$

and $P_{NL}(\mathbf{r}, t)$ from (15.20) and (15.22),

$$\begin{aligned} \nabla^2 E(\mathbf{r}, t) e^{-i\omega_0 t} &= \frac{1}{c^2} \frac{\partial^2}{\partial t^2} (E(\mathbf{r}, t) e^{-i\omega_0 t}) + \frac{1}{c^2} \frac{\partial^2}{\partial t^2} \left(\frac{1}{\varepsilon_0} \varepsilon_0 \varepsilon_{NL} E(\mathbf{r}, t) e^{-i\omega_0 t} \right) \\ &+ \frac{1}{c^2} \frac{\partial^2}{\partial t^2} \left(\frac{1}{\varepsilon_0} \left(\frac{\varepsilon_0}{2\pi} \int_{-\infty}^{\infty} \tilde{\chi}^{(1)}(\omega) \tilde{E}(\mathbf{r}, \omega - \omega_0) e^{-i(\omega - \omega_0)t} d\omega \right) e^{-i\omega_0 t} \right). \end{aligned} \quad (15.24)$$

The above equation is now expressed only in terms of the electric field. We now act with the time derivative on the term on the RHS allowing us to cancel the exponential terms and rearrange slightly

$$\begin{aligned} \nabla^2 E(\mathbf{r}, t) &= \frac{1}{c^2} \left(\frac{\partial^2}{\partial t^2} E(\mathbf{r}, t) - 2i\omega_0 \frac{\partial}{\partial t} E(\mathbf{r}, t) - \omega_0^2 E(\mathbf{r}, t) \right) (1 + \varepsilon_{NL}) \\ &- \frac{1}{c^2} \left(\frac{1}{2\pi} \int_{-\infty}^{\infty} \omega^2 \tilde{\chi}^{(1)}(\omega) \tilde{E}(\mathbf{r}, \omega - \omega_0) e^{-i(\omega - \omega_0)t} d\omega \right). \end{aligned} \quad (15.25)$$

The next step is to replace the remaining $E(\mathbf{r}, t)$ terms with their Fourier transform allowing us to remove the remaining time derivatives and collect the RHS terms under one integral,

$$\begin{aligned} &\int_{-\infty}^{\infty} \nabla^2 \tilde{E}(\mathbf{r}, \omega - \omega_0) e^{-i(\omega - \omega_0)t} d\omega \\ &= -\frac{1}{c^2} \int_{-\infty}^{\infty} \left((\omega - \omega_0)^2 + 2\omega_0(\omega - \omega_0) + \omega_0^2 \right) (1 + \varepsilon_{NL}) \tilde{E}(\mathbf{r}, \omega - \omega_0) e^{-i(\omega - \omega_0)t} d\omega \\ &\quad - \frac{1}{c^2} \int_{-\infty}^{\infty} \omega^2 \tilde{\chi}^{(1)}(\omega) \tilde{E}(\mathbf{r}, \omega - \omega_0) e^{-i(\omega - \omega_0)t} d\omega. \end{aligned} \quad (15.26)$$

Further rearrangement leads to

$$\nabla^2 \tilde{E}(\mathbf{r}, \omega - \omega_0) + \frac{\omega^2}{c^2} \left(1 + \varepsilon_{NL} + \tilde{\chi}^{(1)}(\omega) \right) \tilde{E}(\mathbf{r}, \omega - \omega_0) = 0. \quad (15.27)$$

We now use $k = \omega/c$ where k is the wavenumber and express the term in brackets as the dielectric constant $\varepsilon(\omega) = 1 + \varepsilon_{NL} + \tilde{\chi}^{(1)}(\omega)$ with a non-linear contribution ε_{NL} . The equation is now in a

form known as the Helmholtz equation,

$$(\nabla^2 + k^2 \varepsilon(\omega)) \tilde{E}(\mathbf{r}, \omega - \omega_0) = 0. \quad (15.28)$$

We can transform the Helmholtz equation into the NLSE in a few steps. The first is to express $\tilde{E}(\mathbf{r}, \omega - \omega_0)$ using a separation of variables,

$$\tilde{E}(\mathbf{r}, \omega - \omega_0) = F(x, y) \tilde{A}(z, \omega - \omega_0) e^{i\beta_0 z}. \quad (15.29)$$

Here $F(x, y)$ is the transverse modal distribution function. In a similar method to the slowly varying envelope approximation we take $\tilde{A}(z, \omega - \omega_0)$ to be a slowly varying function of z the propagation distance along the fibre and the exponential function to represent the part which varies faster with wave number β_0 . The form for the electric field in (15.29) is substituted into the Helmholtz equation

$$\begin{aligned} \tilde{A}(z, \omega - \omega_0) e^{i\beta_0 z} \nabla_{xy}^2 F(x, y) + F(x, y) e^{i\beta_0 z} \frac{d^2}{dz^2} \tilde{A}(z, \omega - \omega_0) + i\beta_0 F(x, y) \frac{d}{dz} \tilde{A}(z, \omega - \omega_0) e^{i\beta_0 z} \\ - \beta_0^2 F(x, y) \tilde{A}(z, \omega - \omega_0) e^{i\beta_0 z} + k^2 \varepsilon(\omega) F(x, y) \tilde{A}(z, \omega - \omega_0) e^{i\beta_0 z} = 0. \end{aligned} \quad (15.30)$$

Where $\nabla_{xy} = d^2/dx^2 + d^2/dy^2$. As mentioned $\tilde{A}(z, \omega - \omega_0)$ is a slowly varying function of z so we neglect the second time derivative with respect to z . We also cancel the exponential functions and split (15.30) into two equations for the modal distribution and $\tilde{A}(z, \omega - \omega_0)$. At the same time we introduce the wave number $\tilde{\beta}$ as an eigenvalue

$$\begin{aligned} \tilde{A}(z, \omega - \omega_0) \nabla_{xy}^2 F(x, y) + 2i\beta_0 F(x, y) \frac{d}{dz} \tilde{A}(z, \omega - \omega_0) \\ - \beta_0^2 F(x, y) \tilde{A}(z, \omega - \omega_0) + k^2 \varepsilon(\omega) F(x, y) \tilde{A}(z, \omega - \omega_0) = 0, \end{aligned} \quad (15.31)$$

$$\Rightarrow \frac{1}{F(x, y)} \nabla_{xy}^2 F(x, y) + \frac{2i\beta_0}{\tilde{A}(z, \omega - \omega_0)} \frac{d}{dz} \tilde{A}(z, \omega - \omega_0) - \beta_0^2 + k^2 \varepsilon(\omega) + \tilde{\beta}^2 - \tilde{\beta}^2 = 0. \quad (15.32)$$

This leads to two equations

$$\nabla_{xy}^2 F(x, y) + (k^2 \varepsilon(\omega) - \tilde{\beta}^2) F(x, y) = 0, \quad (15.33)$$

$$2i\beta_0 \frac{d}{dz} \tilde{A}(z, \omega - \omega_0) + (\tilde{\beta}^2 - \beta_0^2) \tilde{A}(z, \omega - \omega_0) = 0. \quad (15.34)$$

Equation (15.33), the modal distribution equation, is used to find the transverse profile of the electromagnetic field in the fibre. It can be used to find an approximation to the propagation constant $\beta(\omega)$. Equation (15.34) describes how the field changes as it propagates along the fibre. It is the latter equation that we can arrange into the form of the NLSE however to achieve this we need to analyse the linear and non-linear contributions to the propagation constant using (15.33).

The modal distribution equation is first approached by neglecting the non-linear contribution to the dielectric constant $\varepsilon(\omega)$, as discussed before this contribution is significantly smaller than the linear contribution. The equation is then solved to find a solution for the zeroth order eigenvalue $\beta(\omega)$. The inclusion of the non-linear contribution is treated using perturbation theory. To first order this will leave the form of $F(x, y)$ unchanged and alter the eigenvalue by a small amount $\Delta\beta$. With the inclusion of non-linearity to first order in perturbation theory the new propagation constant is [126],

$$\tilde{\beta}(\omega) = \beta(\omega) + \Delta\beta. \quad (15.35)$$

Rearranging (15.34) and then substituting in (15.35) leads to

$$\frac{\partial \tilde{A}}{\partial z} = -\frac{i}{2\beta_0} (\beta_0 - \tilde{\beta}) (\beta_0 + \tilde{\beta}) \tilde{A} \approx -i (\beta_0 - \tilde{\beta}) \tilde{A} = -i (\beta_0 - \beta(\omega) - \Delta\beta) \tilde{A}. \quad (15.36)$$

Where the notation has been simplified by dropping the dependence of \tilde{A} on z and $\omega - \omega_0$. Equation (15.36) shows that a pulse propagating along a fibre axis will gain a phase which will be dependent on frequency and on intensity through $\Delta\beta$.

In order to reach the NLSE we need to use a form for the propagation constant which makes explicit the frequency dependence. In order to do this we expand $\beta(\omega)$ in a Taylor series about the frequency ω_0 of the rapidly oscillating part of the electric field from (15.19). The result can be seen in (12.2) in section 12.3. Previously in this derivation we have used the assumption that the pulses under consideration are long (> 1 ps), this will also mean that they are spectrally narrow and hence the higher order terms in (12.2) will be negligible. In the derivation of the NLSE the Taylor series is cut off after the β_2 term.

Substituting this form for $\beta(\omega)$ into (15.36) and Fourier transforming

$(\tilde{A}(z, \omega) = \int_{-\infty}^{\infty} A(z, t) \exp(-i(\omega - \omega_0)t) dt)$ back into the time domain leads to a form of the NLSE

$$\begin{aligned} & \int_{-\infty}^{\infty} \frac{\partial}{\partial z} A(z, t) e^{-i(\omega - \omega_0)t} dt \\ &= -i \int_{-\infty}^{\infty} \left(\beta_0 - \left(\beta_0 + \beta_1(\omega - \omega_0) + \frac{\beta_2}{2!}(\omega - \omega_0)^2 \right) - \Delta\beta \right) A(z, t) e^{-i(\omega - \omega_0)t} dt, \end{aligned} \quad (15.37)$$

$$\int_{-\infty}^{\infty} \frac{\partial}{\partial z} A(z, t) e^{-i(\omega - \omega_0)t} dt = i \int_{-\infty}^{\infty} \left(\beta_1 i \frac{d}{dt} - \beta_2 \frac{d^2}{dt^2} + \Delta\beta \right) A(z, t) e^{-i(\omega - \omega_0)t} dt, \quad (15.38)$$

$$\frac{\partial}{\partial z} A(z, t) = \left(-\beta_1 \frac{\partial}{\partial t} - \frac{i\beta_2}{2} \frac{\partial^2}{\partial t^2} + i\Delta\beta \right) A(z, t). \quad (15.39)$$

The form of $\Delta\beta$ can be found using perturbation theory, here we will simply state that it can be expressed as [2],

$$\Delta\beta = \gamma |A|^2. \quad (15.40)$$

Where $\gamma = n_2\omega_0 / (cA_{eff})$ is the non-linear parameter, n_2 is the non-linear contribution to the refractive index and A_{eff} is the effective core area which is a measure of the area of the mode described by $F(x, y)$. The NLSE now becomes

$$\frac{\partial}{\partial z} A(z, t) + \beta_1 \frac{\partial}{\partial t} A(z, t) + \frac{i\beta_2}{2} \frac{\partial^2}{\partial t^2} A(z, t) = i\gamma |A|^2 A(z, t). \quad (15.41)$$

The NLSE is often seen written in different forms. One common practice is to convert to the frame co-moving with the group velocity of the central frequency ω_0 ,

$$T = t - z\beta_1, \quad z = \xi,$$

$$\frac{\partial}{\partial t} = \frac{\partial}{\partial T}, \quad \frac{\partial}{\partial z} = \frac{\partial}{\partial \xi} - \beta_1 \frac{\partial}{\partial T},$$

$$\frac{\partial A(\xi, T)}{\partial \xi} + \frac{i\beta_2}{2} \frac{\partial^2 A(\xi, T)}{\partial T^2} - i\gamma |A(\xi, T)|^2 A(\xi, T) = 0. \quad (15.42)$$

This is now the form of the NLSE that is used in section 8.

16 Equipment

16.1 Double chirped mirrors

As explained in section 12.3, the few-cycle pulses used in the experiments are extremely susceptible to the effects of dispersion. Early efforts to counteract the effects of dispersion in short pulse lasers used prism pairs to introduce negative dispersion to balance the positive material dispersion [44]. However these prisms were found to introduce higher order dispersive effects creating a limitation on the achievable pulse lengths.

An alternative to compensate positive dispersion is the Gires-Tournois interferometer [102]. This can be used to achieve tunable negative dispersion. It operates on the principle of trapping different frequencies of light for different durations of time in a resonant structure. However the resonant structure also introduces undesirable higher order dispersive effects due to variations in the GDD across the reflected bandwidth.

Chirped mirrors for dispersion control were developed in an attempt to avoid the issue of higher order dispersion. They make use of a different method to introduce negative dispersion. Layers of coatings of varying high and low indices are used (also known as Bragg mirrors) which led to wavelengths of light penetrating the multilayer structure to different depths [107]. Using this method the group delay experienced by each frequency can be made an approximately linear function of the frequency over a certain bandwidth. This in turn means that the GDD is constant across this bandwidth. As an alternative the GDD can be made to be a linear function of frequency which could then be used to compensate TOD introduced by the gain medium in the laser.

Further investigations into chirped mirrors found that partial reflections from the front surface of the mirror and reflections from the back surface of the mirror (Bragg reflections) create an interferometer effect leading to some of the same resonant design properties as the Gires-Tournois [47]. In the same 1997 paper Kärtner et al. developed a new design known as a DCM. The first chirp refers to the chirping of the center wavelength of the Bragg mirror. The second chirp refers to varying the ratio of the thicknesses of the high and low index layers of the mirror. In their work they identify the issue with the chirped mirrors as an impedance matching problem. Their second chirp is equivalent to tapering the impedance, which removes the problem leading to a uniform GDD across a broad bandwidth.

16.2 Autocorrelator

The Autocorrelator used in the experiments is an A.P.E pulseCheck. The primary use for the device was to measure the pulse length as part of the experiment described in section 12.3.1, where the GDD of various optical elements was being measured.

The basic design of an autocorrelator is as follows [102]: The input light is split into two by a beam splitter and each beam is incident on a pair of angled mirrors reflecting it back towards the beam splitter. For one beam path the distance to the mirrors is varied electronically. The two beams recombine on the beam-splitter and are then focused onto a BBO (Barium Borate) crystal. The $\chi^{(2)}$ non-linearity of the crystal allows sum frequency generation to take place $\omega_1 + \omega_2 = \omega_3$, where ω_1 and ω_2 are the frequencies of the two incident beams and ω_3 is the frequency of the generated light. The intensity $I(\tau)$ of the generated higher frequency signal will depend on the overlap of the two input beams:

$$I(\tau) = \int P(t) P(t + \tau) dt \quad (16.1)$$

By varying the beam path for one beam and hence the delay τ between the two beams, and monitoring the output signal from the non-linear crystal, the pulse length is found. This process is known as an intensity auto-correlation.

References

- [1] G. P. Agrawal. *Nonlinear Fiber Optics*. Academic Press, Elsevier, 1989.
- [2] Govind P. Agrawal. *Nonlinear Fiber Optics*. Optics and Photonics. Academic Press, 3rd edition, 2001.
- [3] Nail Akhmediev and Magnus Karlsson. Cherenkov radiation emitted by solitons in optical fibers. *Physical Review A*, 51(3):2602–2607, 03 1995.
- [4] R. R. Alfano and S. L. Shapiro. Emission in the region 4000 to 7000 Å via four-photon coupling in glass. *Phys. Rev. Lett.*, 24(11):584–587, March 1970.
- [5] AS. Kovalev AM. Kosevich, BA. Ivanov. Magnetic solitons. *Physical Reports*, 193:117–238, 1990.
- [6] Fiorenzo G. Omenetto Jonathan C. Knight William J. Wadsworth Philip St. J. Russell Anatoly Efimov, Antoinette J. Taylor. Nonlinear generation of very high-order uv modes in microstructured fibers. *Optics Express*, 11:910–918, 2003.
- [7] J. A. Armstrong, N. Bloembergen, J. Ducuing, and P. S. Pershan. Interactions between light waves in a nonlinear dielectric. *Phys. Rev.*, 127(6):1918–1939, September 1962.
- [8] Carlos Barceló, Stefano Liberati, and Matt Visser. Towards the observation of hawking radiation in bose–einstein condensates. *International Journal of Modern Physics A*, 18(21):3735–3745, 2003.
- [9] F. Begum, Y. Namihira, S.F. Kaijage, S. M A Razzak, N.H. Hai, T. Kinjo, K. Miyagi, and N. Zou. Design of broadband dispersion compensating photonic crystal fibers for high speed transmission systems. In *Optical Fiber Communication - includes post deadline papers, 2009. OFC 2009. Conference on*, pages 1–3, 2009.
- [10] Feroza Begum and Yoshinori Namihira. *Recent progress in optical fiber research*, chapter 11, pages 229–246. InTech, 2012.

- [11] F. Belgiorno, S. L. Cacciatori, M. Clerici, V. Gorini, G. Ortenzi, L. Rizzi, E. Rubino, V. G. Sala, and D. Faccio. Reply to comment on "hawking radiation from ultrashort laser pulse filaments". *Phys. Rev. Lett.*, 107(14):149402, September 2011.
- [12] J C Knight B J Mangan P S Russell Birks, T.A. Photonic crystal fibres: An endless variety. *IEICE TRANSACTIONS on Electronics*, E84C:585–592, 2001.
- [13] T.A. Birks, D. Mogilevtsev, J.C. Knight, and P.S.J. Russell. Dispersion compensation using single-material fibers. *Photonics Technology Letters, IEEE*, 11(6):674–676, 1999.
- [14] T.A. Birks, P.J. Roberts, P.S.J. Russell, D. M. Atkin, and T.J. Shepherd. Full 2-d photonic bandgaps in silica/air structures. *Electronics Letters*, 31(22):1941–1943, 1995.
- [15] R. Biswas, C.T. Chan, M. Sigalas, C.M. Soukoulis, and K.M. Ho. *Photonic Band Gap Materials, Volume 315 of NATO ASI series*, volume 315. Springer Netherlands, 1996.
- [16] N. Bloembergen. *Recent Progress in Four-Wave Mixing Spectroscopy*, volume 21 of *Springer Series in Optical Sciences*. Springer Berlin Heidelberg, 1979.
- [17] Joseph Boussinesq. Théorie de l'intumescence liquide appelée onde solitaire ou de translation, se propageant dans un canal rectangulaire. *Comptes rendus de l'Académie des sciences*, 72:755–759, 1871.
- [18] R.W. Boyd. *Nonlinear optics*. Academic Press, 2008.
- [19] T. Brabec, Ch. Spielmann, P. F. Curley, and F. Krausz. Kerr lens mode locking. *Opt. Lett.*, 17(18):1292–1294, 1992.
- [20] The British Association for the Advancement of Science. *Report of the Fourteenth Meeting of the British Association for the Advancement of Science*, Albemarle Street, London, September 1845. John Murray.
- [21] Paul N. Butcher and David Cotter. *The Element of Nonlinear Optics*. Cambridge University Press, 1990.
- [22] R. H. Stolen C. F. Mollenauer and J. P. Gordon. Experimental observation of picosecond pulse narrowing and solitons in optical fibers. *Physical Review Letters*, 45:1095–1098, 1980.

- [23] Guoqing Chang, Li-Jin Chen, and Franz X. Kärtner. Highly efficient cherenkov radiation in photonic crystal fibers for broadband visible wavelength generation. *Opt. Lett.*, 35(14):2361–2363, Jul 2010.
- [24] Guoqing Chang, Chih-Hao Li, A. Glenday, G. Furesz, N. Langellier, Li-Jin Chen, M.W. Webber, Jinkang Lim, Hung-Wen Chen, D.F. Phillips, A. Szentgyorgyi, R.L. Walsworth, and F.X. Kartner. Spectrally flat, broadband visible-wavelength astro-comb. In *Lasers and Electro-Optics (CLEO), 2012 Conference on*, pages 1–2, 2012.
- [25] H H Chen, Z L Chen, X F Zhou, and J Hou. Ultraviolet-extended flat supercontinuum generation in cascaded photonic crystal fiber tapers. *Laser Physics Letters*, 10(8):085401, 2013.
- [26] Wei Chen, Shiyu Li, and Peixiang Lu. Dispersion-flattened bragg photonic crystal fiber for large capacity optical communication system. *Frontiers of Optoelectronics in China*, 2(3):289–292, 2009.
- [27] Chunfu Cheng, Youqing Wang, and Qinghua Lv. Effect of initial frequency chirp on the supercontinuum generation in all-normal dispersion photonic crystal fibers. In *Photonics and Optoelectronics Meetings (POEM) 2011: Optical Communication Systems and Networking*, volume 8331, pages 833100–833100–8, 2011.
- [28] Amol Choudhary and Friedrich König. Efficient frequency shifting of dispersive waves at solitons. *Opt. Express*, 20(5):5538–5546, Feb 2012.
- [29] Stéphane Coen, Alvin Hing Lun Chau, Rainer Leonhardt, John D. Harvey, Jonathan C. Knight, William J. Wadsworth, and Philip St. J. Russell. White-light supercontinuum generation with 60-ps pump pulses in a photonic crystal fiber. *Opt. Lett.*, 26(17):1356–1358, 2001.
- [30] Matteo Conforti, Niclas Westerberg, Fabio Baronio, Stefano Trillo, and Daniele Faccio. Negative-frequency dispersive wave generation in quadratic media. *Phys. Rev. A*, 88(1):013829, July 2013.

- [31] K. L. Corwin, N. R. Newbury, J. M. Dudley, S. Coen, S. A. Diddams, K. Weber, and R. S. Windeler. Fundamental noise limitations to supercontinuum generation in microstructure fiber. *Phys. Rev. Lett.*, 90(11):113904, March 2003.
- [32] C R Cosens. A balance-detector for alternating-current bridges. *Proceedings of the Physical Society*, 46(6):818, 1934.
- [33] Andrea di Falco. *Matlab fiber mode calculation programme*. University of St Andrews.
- [34] Scott A. Diddams, David J. Jones, Jun Ye, Steven T. Cundiff, John L. Hall, Jinendra K. Ranka, Robert S. Windeler, Ronald Holzwarth, Thomas Udem, and T. W. Hänsch. Direct link between microwave and optical frequencies with a 300 thz femtosecond laser comb. *Phys. Rev. Lett.*, 84(22):5102–5105, May 2000.
- [35] G. de Vries D.J. Korteweg. On the change of form of long waves advancing in a rectangular canal, and on a new type of stationary waves. *Philosophical Magazine*, 39:422–443, 1895.
- [36] Ho P.P Manassah J.T. Dorsinville, R and R.R. Alfano. *The Supercontinuum Laser Source*, chapter 9, pages 377–398. Springer, 2006.
- [37] John M. Dudley and Stéphane Coen. Coherence properties of supercontinuum spectra generated in photonic crystal and tapered optical fibers. *Opt. Lett.*, 27(13):1180–1182, 2002.
- [38] John M. Dudley, Goëry Genty, and Stéphane Coen. Supercontinuum generation in photonic crystal fiber. *Reviews of Modern Physics*, 78(4):1135–1184, 10 2006.
- [39] Daniel J. Ehrlich. *Laser microfabrication: thin film processes and lithography*. Academic Press, 1989.
- [40] J. N. Elgin. Perturbations of optical solitons. *Phys. Rev. A*, 47(5):4331–4341, May 1993.
- [41] M.Clerici V.Gorini G.Ortenzi L. Rizzi E. Rubino V.G.Sala D. Faccio F.Belgiorno, S.L.Cacciatori. Hawking radiation from ultrashort laser pulse filaments. *Phys Rev Lett*, 105(20):203901, November 2010.
- [42] A. Ferrando, E. Silvestre, J. J. Miret, and P. Andrés. Nearly zero ultraflattened dispersion in photonic crystal fibers. *Opt. Lett.*, 25(11):790–792, 2000.

- [43] Mario F. Ferreira. *Nonlinear Effects in Optical Fibers*. John Wiley & Sons, 2011.
- [44] R. L. Fork, O. E. Martinez, and J. P. Gordon. Negative dispersion using pairs of prisms. *Opt. Lett.*, 9(5):150–152, 1984.
- [45] Mark Foster, Alexander Gaeta, Qiang Cao, and Rick Trebino. Soliton-effect compression of supercontinuum to few-cycle durations in photonic nanowires. *Opt. Express*, 13(18):6848–6855, 2005.
- [46] Xiquan Fu, Liejia Qian, Shuangchun Wen, and Dianyuan Fan. Nonlinear chirped pulse propagation and supercontinuum generation in microstructured optical fibre. *Journal of Optics A: Pure and Applied Optics*, 6(11):1012, 2004.
- [47] T Schibli U Keller FX Kärtner, N Matuschek. Design and fabrication of double-chirped mirrors. *Optics Letters*, 22:831–833, 1997.
- [48] Thierry Georges and Francois Favre. Wdm soliton transmission in dispersion-managed links. In *18th Congress of the International Commission for Optics*, volume 3749, pages 156–157, 1999.
- [49] R. Ghosh, A. Kumar, J.-P. Meunier, and E. Marin. Modal characteristics of few-mode silica-based photonic crystal fibres. *Optical and Quantum Electronics*, 32(6-8):963–970, 2000.
- [50] J. P. Gordon and H. A. Haus. Random walk of coherently amplified solitons in optical fiber transmission. *Opt. Lett.*, 11(10):665–667, 1986.
- [51] W.R Grant, I.S. Phillips. *Electromagnetism*. John Wiley & Sons, 1990.
- [52] Ning Guan, Shinji Habu, Katsuhiko Takenaga, Kuniharu Himeno, and Akira Wada. Boundary element method for analysis of holey optical fibers. *J. Lightwave Technol.*, 21(8):1787, 2003.
- [53] S. Guenneau, A. Nicolet, F. Zolla, and S. Lasquellec. Modeling of photonic crystal optical fibers with finite elements. *Magnetics, IEEE Transactions on*, 38(2):1261–1264, 2002.
- [54] Ariel Guerreiro, Aires Ferreira, and J. T. Mendonça. Production of bright entangled photons from moving optical boundaries. *Phys. Rev. A*, 83(5):052302, May 2011.

- [55] A. Glenday G. Furesz N. Langellier Li-Jin Chen M.W. Webber Jinkang Lim Hung-Wen Chen D.F. Phillips A. Szentgyorgyi R.L. Walsworth Guoqing Chang, Chih-Hao Li and Franz X. Kärtner. Spectrally flat, broadband visible-wavelength astrocomb. In *Lasers and Electro-Optics (CLEO), 2012 Conference on*, 2012.
- [56] I. Hartl, X. D. Li, C. Chudoba, R. K. Ghanta, T. H. Ko, J. G. Fujimoto, J. K. Ranka, and R. S. Windeler. Ultrahigh-resolution optical coherence tomography using continuum generation in an air-silica microstructure optical fiber. *Opt. Lett.*, 26(9):608–610, 2001.
- [57] A. Hasegawa and F. Tappert. Transmission of stationary nonlinear optical pulses in dispersive dielectric fibers. *Applied Physics Letters*, 23, 1973.
- [58] H.E. Hook, J.R. Hall. *Solid State Physics*. John Wiley & Sons, 1991.
- [59] Karlsson Magnus Höök, Anders. Ultrashort solitons at the minimum-dispersion wavelength: effects of fourth order dispersion. *Optics Letters*, 18(17):1388–1390, September 1993.
- [60] P.M. Hui and Neil F. Johnson. Photonic band-gap materials. volume Volume 49 of *Solid State Physics*, pages 151–203. Academic Press, 1996.
- [61] A V Husakou and J Herrmann. Supercontinuum generation of higher-order solitons by fission in photonic crystal fibers. *Phys Rev Lett*, 87(20):203901, Nov 2001.
- [62] A. V. Husakou and J. Herrmann. Supercontinuum generation of higher-order solitons by fission in photonic crystal fibers. *Phys. Rev. Lett.*, 87(20):203901, October 2001.
- [63] Anton V. Husakou and Joachim Herrmann. Supercontinuum generation, four-wave mixing, and fission of higher-order solitons in photonic-crystal fibers. *J. Opt. Soc. Am. B*, 19(9):2171–2182, 09 2002.
- [64] Luca Tartara Ilaria Cristiani, Riccardo Tediosi and Vittorio Degiorgio. Dispersive wave generation by solitons in microstructured optical fibers. *Optics Express*, 12:124–135, 2004.
- [65] Anatoly A. Ivanov, Mikhail V. Alfimov, Aleksei M. Zheltikov, Marcin Szpulak, Wacław Urbanczyk, and Jan Wójcik. Polarization-controlled vectorial spectral transformations of femto-second pulses in a birefringent photonic-crystal fiber. *J. Opt. Soc. Am. B*, 23(5):986–991, May 2006.

- [66] Ayodeji Coker Jay E. Sharping, Marco Fiorentino and Robert S. Windeler Prem Kumar. Four-wave mixing in microstructure fiber. *Optics Letters*, 26:1048–1050, 2001.
- [67] P.J. Caudrey R.K. Bullough J.C. Eilbeck, J.D. Gibbon. Solitons in nonlinear optics i. a more accurate description of the 2π pulse in self-induced transparency. *J. Phys. A: Math., Nucl. Gen*, 6:1337–1347, 1973.
- [68] Steven Johnson and John Joannopoulos. Block-iterative frequency-domain methods for Maxwell's equations in a planewave basis. *Opt. Express*, 8(3):173–190, 2001.
- [69] David J. Jones, Scott A. Diddams, Jinendra K. Ranka, Andrew Stentz, Robert S. Windeler, John L. Hall, and Steven T. Cundiff. Carrier-envelope phase control of femtosecond mode-locked lasers and direct optical frequency synthesis. *Science*, 288(5466):635–639, 2000.
- [70] V. I. Karpman. Radiation by solitons due to higher-order dispersion. *Physical Review E*, 47(3):2073–2082, 03 1993.
- [71] Do-Hyun Kim and Jin Kang. Sagnac loop interferometer based on polarization maintaining photonic crystal fiber with reduced temperature sensitivity. *Opt. Express*, 12(19):4490–4495, 2004.
- [72] J. C. Knight, T. A. Birks, P. St. J. Russell, and D. M. Atkin. All-silica single-mode optical fiber with photonic crystal cladding. *Opt. Lett.*, 21(19):1547–1549, 1996.
- [73] J.C. Knight, J. Arriaga, T.A. Birks, A. Ortigosa-Blanch, W.J. Wadsworth, and P.S.J. Russell. Anomalous dispersion in photonic crystal fiber. *Photonics Technology Letters, IEEE*, 12(7):807–809, 2000.
- [74] J.C. Knight, T.A. Birks, R. F. Cregan, P.S.J. Russell, and J. P. De Sandro. Large mode area photonic crystal fibre. *Electronics Letters*, 34(13):1347–1348, 1998.
- [75] Jonathan C. Knight. Photonic crystal fibres. *Nature*, 424:847–851, 2003.
- [76] Y. Kodama and Akira Hasegawa. Nonlinear pulse propagation in a monomode dielectric guide. *Quantum Electronics, IEEE Journal of*, 23(5):510–524, 1987.

- [77] Y. Kodama, M. Romagnoli, M. Midrio, and S. Wabnitz. Role of third-order dispersion on soliton instabilities and interactions in optical fibers. *Opt. Lett.*, 19(3):165–167, 1994.
- [78] M. Kolesik, J. V. Moloney, and M. Mlejnek. Unidirectional optical pulse propagation equation. *Phys. Rev. Lett.*, 89(28):283902, December 2002.
- [79] M. Kolesik, L. Tartara, and J. V. Moloney. Effective three-wave-mixing picture and first born approximation for femtosecond supercontinua from microstructured fibers. *Phys. Rev. A*, 82(4):045802, October 2010.
- [80] V. I. Kruglov, A. C. Peacock, and J. D. Harvey. Exact solutions of the generalized nonlinear schrödinger equation with distributed coefficients. *Physical Review E*, 71(5):056619, 05 2005.
- [81] D. Krylov, L. Leng, K. Bergman, Jared C. Bronski, and J. Nathan Kutz. Observation of the breakup of a prechirped n-soliton in an optical fiber. *Opt. Lett.*, 24(17):1191–1193, 1999.
- [82] H. H. Kuehl and C. Y. Zhang. Effects of higher-order dispersion on envelope solitons. *Phys. Fluids B*, 2(5):889–900, May 1990.
- [83] P.V. Mamyshev, L.F. Mollenauer, J.P. Gordon. *Solitons in High Bit-Rate Long-Distance Transmission, Optical Fiber Telecommunications*, volume 3A. Academic Press, 1997.
- [84] Chinlon Lin and R. H. Stolen. New nanosecond continuum for excited-state spectroscopy. *Appl. Phys. Lett.*, 28(4):216–218, February 1976.
- [85] X. Liu, G.E. Villanueva, J. Lægsgaard, Møller, U., H. Tu, S.A. Boppart, and D. Turchinovich. Low-noise operation of all-fiber femtosecond cherenkov laser. *Photonics Technology Letters, IEEE*, 25(9):892–895, May 2013.
- [86] X. Liu, C. Xu, W. H. Knox, J. K. Chandalia, B. J. Eggleton, S. G. Kosinski, and R. S. Windeler. Soliton self-frequency shift in a short tapered air?silica microstructure fiber. *Opt. Lett.*, 26(6):358–360, 2001.
- [87] Xiaomin Liu, Jesper Lægsgaard, Uffe Møller, Haohua Tu, Stephen A. Boppart, and Dmitry Turchinovich. All-fiber femtosecond cherenkov radiation source. *Opt. Lett.*, 37(13):2769–2771, Jul 2012.

- [88] Fei Lu, Yujun Deng, Larry E. Foulkrod, and Wayne H. Knox. Dispersion micro-managed holey fiber and coherent blue-violet continuum generation. In *Conference on Lasers and Electro-Optics/Quantum Electronics and Laser Science and Photonic Applications Systems Technologies*, page CWA2. Optical Society of America, 2005.
- [89] Fei Lu and Wayne H. Knox. Generation, characterization, and application of broadband coherent femtosecond visible pulses in dispersion micromanaged holey fibers. *J. Opt. Soc. Am. B*, 23(6):1221–1227, Jun 2006.
- [90] Michal Lucki. *Recent progress in optical fiber research*, chapter 9, pages 177–192. InTech, 2012.
- [91] L. Mandel and E. Wolf. *Optical Coherence and Quantum Optics*. Cambridge University Press, 1995.
- [92] Daniele Faccio Fabio Biancalana Matteo Conforti, Andrea Marini. Negative frequencies get real: a missing puzzle piece in nonlinear optics. *arXiv:1305.5264v2 [physics.optics]*, 2013.
- [93] Walter C. Michels and Norma L. Curtis. A pentode lock-in amplifier of high frequency selectivity. *Review of Scientific Instruments*, 12:444–447, 1941.
- [94] Aleksandr V. Mitrofanov, Yaroslav M. Linik, Ryszard Buczynski, Dariusz Pysz, Dusan Lorenc, Ignac Bugar, Anatoly A. Ivanov, Mikhail V. Alfimov, Andrei B. Fedotov, and Aleksei M. Zheltikov. Highly birefringent silicate glass photonic-crystal fiber with polarization-controlled frequency-shifted output: A promising fiber light source for nonlinear raman microspectroscopy. *Opt. Express*, 14(22):10645–10651, Oct 2006.
- [95] D. Mogilevtsev, T. A. Birks, and P. St. J. Russell. Group-velocity dispersion in photonic crystal fibers. *Opt. Lett.*, 23(21):1662–1664, 1998.
- [96] D. Mogilevtsev, T. A. Birks, and P. St. J. Russell. Localized function method for modeling defect modes in 2-d photonic crystals. *J. Lightwave Technol.*, 17(11):2078, 1999.
- [97] P. D. Nation, J. R. Johansson, M. P. Blencowe, and Franco Nori. Colloquium: Stimulating uncertainty: Amplifying the quantum vacuum with superconducting circuits. *Reviews of Modern Physics*, 84(1):1–24, 01 2012.

- [98] Newport. www.newport.com/the-effect-of-dispersion-on-ultrashort-pulses.
- [99] M.D. Kruskal N.J. Zabusky. Interaction of "solitons" in a collisionless plasma and the recurrence of initial states. *Physical Review Letters*, 15:240–243, 1965.
- [100] A. Ortigosa-Blanch, J. C. Knight, W. J. Wadsworth, J. Arriaga, B. J. Mangan, T. A. Birks, and P. St. J. Russell. Highly birefringent photonic crystal fibers. *Opt. Lett.*, 25(18):1325–1327, 2000.
- [101] R. Paschotta. *simulation software PROPULSE*. RP Photonics Consulting GmbH, Zurich, Switzerland.
- [102] Rüdiger Paschotta. *Encyclopedia of Laser Physics and Technology*. Wiley-VCH, 2008.
- [103] H. He P.D. Drummond, K.V Kheruntsyan. Coherent molecular solitons in bose-einstein condensates. *Physical Review Letters*, 81:3055–3058, 1998.
- [104] Thomas G. Philbin, Chris Kuklewicz, Scott Robertson, Stephen Hill, Friedrich König, and Ulf Leonhardt. Fiber-optical analog of the event horizon. *Science*, 319(5868):1367–1370, 03 2008.
- [105] NKT Photonics. www.nktphotonics.com.
- [106] Mikhail Polyanskiy. Refractive index database, 2013.
- [107] K. Ferencz R. Szipocs. Chirped multilayer coatings for broadband dispersion control in femtosecond lasers. *Optics Letters*, 19:201–203, 1994.
- [108] Jinendra K. Ranka, Robert S. Windeler, and Andrew J. Stentz. Optical properties of high-delta air silica microstructure optical fibers. *Opt. Lett.*, 25(11):796–798, 2000.
- [109] Jinendra K. Ranka, Robert S. Windeler, and Andrew J. Stentz. Visible continuum generation in air-silica microstructure optical fibers with anomalous dispersion at 800 nm. *Opt. Lett.*, 25(1):25–27, 2000.
- [110] William Reeves, J. Knight, P. Russell, and P. Roberts. Demonstration of ultra-flattened dispersion in photonic crystal fibers. *Opt. Express*, 10(14):609–613, 2002.

- [111] P.J. Roberts, B.J. Mangan, H. Sabert, F. Couny, T.A. Birks, J.C. Knight, and P.St.J. Russell. Control of dispersion in photonic crystal fibers. In *Optical and Fiber Communications Reports*, volume 5, pages 313–339. Springer New York, 2007.
- [112] Scott J Robertson. The theory of hawking radiation in laboratory analogues. *Journal of Physics B: Atomic, Molecular and Optical Physics*, 45(16):163001, 2012.
- [113] Scott James Robertson. *Hawking Radiation in Dispersive Media*. PhD thesis, School of Physics and Astronomy University of St Andrews, 2011.
- [114] Germain Rousseaux, Philippe Maïssa, Christian Mathis, Pierre Couillet, Thomas G Philbin, and Ulf Leonhardt. Horizon effects with surface waves on moving water. *New Journal of Physics*, 12(9):095018, 2010.
- [115] Germain Rousseaux, Christian Mathis, Philippe Maïssa, Thomas G Philbin, and Ulf Leonhardt. Observation of negative-frequency waves in a water tank: a classical analogue to the hawking effect? *New Journal of Physics*, 10(5):053015, 2008.
- [116] Samudra Roy, S. K. Bhadra, and Govind P. Agrawal. Dispersive waves emitted by solitons perturbed by third-order dispersion inside optical fibers. *Physical Review A*, 79(2):023824, 02 2009.
- [117] E. Rubino, A. Lotti, F. Belgiorno, S. L. Cacciatori, A. Couairon, U. Leonhardt, and D. Faccio. Soliton-induced relativistic-scattering and amplification. *Sci. Rep.*, 2, 12 2012.
- [118] E. Rubino, J. McLenaghan, S. C. Kehr, F. Belgiorno, D. Townsend, S. Rohr, C. E. Kuklewicz, U. Leonhardt, F. König, and D. Faccio. Negative-frequency resonant radiation. *Physical Review Letters*, 108(25):253901, 06 2012.
- [119] Philip Russell. Photonic crystal fibers. *Science*, 299(5605):358–362, January 2003.
- [120] Kunimasa Saitoh, M. Koshihara, T. Hasegawa, and E. Sasaoka. Chromatic dispersion control in photonic crystal fibers: application to ultra-flattened dispersion. *Opt. Express*, 11(8):843–852, 2003.

- [121] Kunimasa Saitoh and Masanori Koshihba. Highly nonlinear dispersion-flattened photonic crystal fibers for supercontinuum generation in a telecommunication window. *Opt. Express*, 12(10):2027–2032, 2004.
- [122] Thomas Schneider. *Nonlinear Optics in Telecommunications*. Advanced Texts in Physics. Springer, 2004.
- [123] Ralf Schützhold and William G. Unruh. Comment on "hawking radiation from ultrashort laser pulse filaments". *Phys. Rev. Lett.*, 107(14):149401, September 2011.
- [124] Jacek. Markowicz Przemyslaw. Prasad Paras. N. Shen, Shen. Swiatkiewicz. Near-field microscopy and spectroscopy of third-harmonic generation and two-photon excitation in nonlinear organic crystals. *Applied Physics Letters*, 79:2681–2683, 2001.
- [125] Ya.M. Shnir. Topological solitons. *Physics of Particles and Nuclei Letters*, 9(9-10):745–754, 2012.
- [126] James G. Simmonds. *A First Look at Perturbation Theory*. Dover Publications Inc, 1998.
- [127] D. V. Skryabin, F. Luan, J. C. Knight, and P. St. J. Russell. Soliton self-frequency shift cancellation in photonic crystal fibers. *Science*, 301(5640):1705–1708, 09 2003.
- [128] Love J Snyder, A.W. *Optical Waveguide Theory*. Springer, 1983.
- [129] C M Soukoulis. Photonic band gap materials: the "semiconductors" of the future? *Physica Scripta*, 1996(T66):146, 1996.
- [130] D. E. Spence, P. N. Kean, and W. Sibbett. 60-fsec pulse generation from a self-mode-locked ti:sapphire laser. *Opt. Lett.*, 16(1):42–44, 1991.
- [131] Lord Rayleigh (J.W. Strutt). On waves. *Philosophical Magazine*, 1:257–271, 1876.
- [132] Kazunori Suzuki, Hirokazu Kubota, Satoki Kawanishi, Masatoshi Tanaka, and Moriyuki Fujita. Optical properties of a low-loss polarization-maintaining photonic crystal fiber. *Opt. Express*, 9(13):676–680, 2001.
- [133] S.W.Hawking. Particle creation by black holes. *Communications in Mathematical Physics*, 43:199–220, 1975.

- [134] Montian Tianprateep, Junji Tada, and Fumihiko Kannari. Influence of polarization and pulse shape of femtosecond initial laser pulses on spectral broadening in microstructure fibers. *Optical Review*, 12(3):179–189, 2005.
- [135] Marco V. Tognetti and Helder M. Crespo. Sub-two-cycle soliton-effect pulse compression at 800 nm in photonic crystal fibers. *J. Opt. Soc. Am. B*, 24(6):1410–1415, 2007.
- [136] Truong X. Tran and Fabio Biancalana. Dynamics and control of the early stage of supercontinuum generation in submicron-core optical fibers. *Phys. Rev. A*, 79(6):065802, June 2009.
- [137] Truong X. Tran, Katuscia N. Cassemiro, Christoph Söller, Keith J. Blow, and Fabio Biancalana. Hybrid squeezing of solitonic resonant radiation in photonic crystal fibers. *Physical Review A*, 84(1):013824, 07 2011.
- [138] J C Travers. Blue extension of optical fibre supercontinuum generation. *Journal of Optics*, 12(11):113001, 2010.
- [139] H. Tu and S.A. Boppart. Coherent fiber supercontinuum for biophotonics. *Laser and Photonics Reviews*, 7:628–645, September 2013.
- [140] Haohua Tu and Stephen A. Boppart. Optical frequency up-conversion by supercontinuum-free widely-tunable fiber-optic cherenkov radiation. *Opt. Express*, 17(12):9858–9872, Jun 2009.
- [141] Haohua Tu and Stephen A. Boppart. Ultraviolet-visible non-supercontinuum ultrafast source enabled by switching single silicon strand-like photonic crystal fibers. *Opt. Express*, 17(20):17983–17988, Sep 2009.
- [142] Reichert J Holzwarth R Diddams S Jones D Ye J-Cundiff S Hansch T Hall J Udem, T. *The Hydrogen Atom: Precision Physics of Simple Atomic Systems, Lecture Notes in Physics*, volume 570, chapter A new type of frequency chain and its application to fundamental frequency metrology, pages 125–144. Springer Verlag, 2001.
- [143] W.G. Unruh. Experimental black-hole evaporation? *Physical Review Letters*, 46:1351–1353, 1981.

- [144] H. Valtna, G. Tamošauskas, A. Dubietis, and A. Piskarskas. High-energy broadband four-wave optical parametric amplification in bulk fused silica. *Opt. Lett.*, 33(9):971–973, 2008.
- [145] P. K. A. Wai, H. H. Chen, and Y. C. Lee. Radiations by "solitons" at the zero group-dispersion wavelength of single-mode optical fibers. *Physical Review A*, 41(1):426–439, 01 1990.
- [146] P. K. A. Wai, C. R. Menyuk, Y. C. Lee, and H. H. Chen. Nonlinear pulse propagation in the neighborhood of the zero-dispersion wavelength of monomode optical fibers. *Opt. Lett.*, 11(7):464–466, Jul 1986.
- [147] B.R. Washburn, S.E. Ralph, P.-A. Lacourt, J. M Dudley, W.T. Rhodes, R.S. Windeler, and S. Coen. Tunable near-infrared femtosecond soliton generation in photonic crystal fibres. *Electronics Letters*, 37(25):1510–1512, 2001.
- [148] K. E. Webb, Y. Q. Xu, M. Erkintalo, and S. G. Murdoch. Generalized dispersive wave emission in nonlinear fiber optics. *Opt. Lett.*, 38(2):151–153, 2013.
- [149] Silke Weinfurtner, Edmund W. Tedford, Matthew C. J. Penrice, William G. Unruh, and Gregory A. Lawrence. Measurement of stimulated hawking emission in an analogue system. *Physical Review Letters*, 106(2):021302, 01 2011.
- [150] T. P. White, B. T. Kuhlmey, R. C. McPhedran, D. Maystre, G. Renversez, C. Martijn de Sterke, and L. C. Botten. Multipole method for microstructured optical fibers. i. formulation. *J. Opt. Soc. Am. B*, 19(10):2322–2330, 2002.
- [151] E. Yablonovitch. Photonic band-gap structures. *J. Opt. Soc. Am. B*, 10(2):283–295, 1993.
- [152] Dvir Yelin and Yaron Silberberg. Laser scanning third-harmonic-generation microscopy in biology. *Opt. Express*, 5(8):169–175, 1999.
- [153] Shabat A.B Zakharov, V.F. Exact theory of two-dimensional self-focusing and one-dimensional self-modulation of wave in nonlinear media. *Journal of Experimental and Theoretical Physics*, 34:62–69, 1972.
- [154] Hua Zhang, Song Yu, Jie Zhang, and Wanyi Gu. Effect of frequency chirp on supercontinuum generation in photonic crystal fibers with two zero-dispersion wavelengths. *Opt. Express*, 15(3):1147–1154, 2007.

- [155] Xinyong. Fu H. Y. Zhao, Chun-Liu . Dong and H. Y. Tam. *Recent progress in optical fiber research*, chapter 10, pages 193–228. InTech, 2012.
- [156] Zhaoming Zhu and Thomas Brown. Effect of frequency chirping on supercontinuum generation in photonic crystal fibers. *Opt. Express*, 12(4):689–694, 2004.